

Simulation of Myocardium Motion and Blood Flow in the Heart with Fluid-structure Interaction

by

Matthew Gerard Doyle

A thesis presented to the
Faculty of Graduate and Postdoctoral Studies
in partial fulfilment of the
requirement for the degree of

Doctor of Philosophy
in
Mechanical Engineering

Ottawa-Carleton Institute for Mechanical and Aerospace Engineering
Department of Mechanical Engineering
University of Ottawa
Ottawa, Ontario, Canada
August 2011

©Matthew Gerard Doyle, Ottawa, Canada, 2011

Abstract

The heart is a complex organ and much is still unknown about its mechanical function. In order to use simulations to study heart mechanics, fluid and solid components and their interaction should be incorporated into any numerical model. Many previous studies have focused on myocardium motion or blood flow separately, while neglecting their interaction. Previous fluid-structure interaction (FSI) simulations of heart mechanics have made simplifying assumptions about their solid models, which prevented them from accurately predicting the stress-strain behaviour of the myocardium. In this work, a numerical model of the canine left ventricle (LV) is presented, which serves to address the limitations of previous studies. A canine LV myocardium material model was developed for use in conjunction with a commercial finite element code. The material model was modified from its original form to make it suitable for use in simulations. Further, numerical constraints were imposed when calculating the material parameter values, to ensure that the model would be strictly convex. An initial geometry and non-zero stress state are required to start cardiac cycle simulations. These were generated by the static inflation of a passive LV model to an end-diastolic pressure. Comparisons with previous measurements verified that the calculated geometry was representative of end diastole. Stresses calculated at the specified end diastolic pressure showed complex spatial variations, illustrating the superiority of the present approach over a specification of an arbitrary stress distribution to an end-diastolic geometry. In the third part of this study, FSI simulations of the mechanics of the LV were performed over the cardiac cycle. Calculated LV cavity pressures agreed well with previous measurements during most of the cardiac cycle, but deviated from them

during rapid filling, which resulted in non-physiological backflow. This study is the first one to present a detailed analysis of the temporal and spatial variations of the properties of both the solid and the fluid components of the canine LV. The observed development of non-uniform pressure distributions in the LV cavity confirms the advantage of performing FSI simulations rather than imposing a uniform fluid pressure on the inner surface of the myocardium during solid-only simulations.

For Kim and Kaelyn

Acknowledgments

I would like to thank my supervisors, Professor Stavros Tavoularis and Professor Yves Bourgault for all their help, encouragement, and guidance during my doctoral research.

I would also like to thank Professors Michel Labrosse and Edgar Matida for their help during the early phases of my work and their feedback on my thesis proposal.

I would like to acknowledge the Ontario Graduate Scholarship in Science and Technology, the University of Ottawa Faculty of Graduate and Postdoctoral Studies, and the HPCVL/Sun Microsystems Scholarship, as well as Professors Tavoularis and Bourgault for providing financial support during my doctoral studies.

I could not have performed my simulations without both software and hardware support. I would like to acknowledge ADINA support for promptly helping with my many inquiries about their software. I would also like to acknowledge the staff at the High Performance Computing Virtual Laboratory (HPCVL) for allowing me to run my simulations on their clusters for many years and for answering my questions about their systems. In particular, I would like to thank Hartmut Schmider and Chris MacPhee for all of their help.

I would also like to thank my wife Kim for all of her patience and support over the many years of my doctoral studies. Without her, the completion of this work would not have been possible.

Lastly, I would like to acknowledge the graduate students and postdoctoral fellows I have had the privilege of working with over the years, especially Dong-Il Chang, Warren Dunn, Pascal Tremblay, Sean Bailey, Tim Rennie, and the late Craig Smith. I will treasure the time we have spent together discussing research and many other topics.

Contents

Nomenclature	ix
List of Figures	xvi
List of Tables	xxi
1 Introduction	1
1.1 Motivation	1
1.2 Objectives	3
1.3 Organization	4
2 Background	6
2.1 Cardiovascular system	6
2.2 Heart anatomy and physiology	6
2.3 Cardiac cycle	9
2.4 Muscle fibre contraction and relaxation	13
3 Myocardium material model	16
3.1 Introduction	16
3.2 Material model development	21
3.2.1 Material model selection	21
3.2.2 Material model definition	24
3.2.3 Material model modifications	28
3.3 Available measurements	37
3.3.1 Passive stress-strain behaviour	37
3.3.2 Total stress-strain behaviour	41
3.4 Methods	41
3.4.1 Numerical simulations	41
3.4.2 Material parameter calculations	43
3.5 Results	49
3.5.1 Material model validation	49
3.5.2 Adjustment of material compressibility	50

3.5.3	Passive material parameter calculations	51
3.5.4	Active material parameter calculations	52
3.6	Discussion	55
3.7	Conclusions	57
4	Inflation of the passive left ventricle	59
4.1	Introduction	59
4.2	Methods	67
4.2.1	Geometry and mesh	67
4.2.2	Governing equations	72
4.2.3	Boundary and initial conditions	76
4.2.4	Procedure for principal stretch and stress calculations	77
4.3	Results	79
4.3.1	Material parameter selection	79
4.3.2	Mesh dependence	81
4.3.3	Verification of end-diastolic state	82
4.3.4	Deformations	84
4.3.5	Principal stresses	89
4.3.6	Effect of the number of myocardial layers	94
4.3.7	Effect of muscle fibre orientation	96
4.4	Discussion	97
4.4.1	Assessment of the geometry, material model, and boundary conditions	97
4.4.2	Residual stresses	101
4.5	Conclusions	104
5	Cardiac cycle simulations	107
5.1	Introduction	107
5.2	Literature review	110
5.2.1	Solid-only simulations	110
5.2.2	Fluid-only simulations	114
5.2.3	Fluid-structure interaction simulations	117
5.3	Methods	121
5.3.1	Cardiac cycle definitions	121
5.3.2	Geometry	122
5.3.3	Mesh	124
5.3.4	Numerical methods	126
5.4	Preliminary tests	137
5.4.1	Time step dependence	137
5.4.2	Fluid mesh dependence	138
5.4.3	Variation of multiplier for active material parameter values	138
5.4.4	Periodicity	139
5.5	Results	139
5.5.1	Left ventricle cavity volume and pressure changes	139
5.5.2	Myocardium deformations	144
5.5.3	Myocardium stresses	151

5.5.4	Left ventricle cavity pressure variations	157
5.5.5	Blood velocities	162
5.5.6	Representative times during the cardiac cycle	163
5.6	Discussion	186
5.6.1	Geometry and mesh	186
5.6.2	Other model inputs	189
5.6.3	Periodicity	192
5.6.4	Compressibility	193
5.6.5	Numerical methods	194
5.7	Conclusions	195
6	Conclusions and recommendations for future work	197
6.1	Conclusions	197
6.1.1	Myocardium material model	197
6.1.2	Inflation of the passive LV	198
6.1.3	Cardiac cycle simulations	198
6.2	Recommendations	199
6.2.1	Myocardium material model	199
6.2.2	Inflation of the passive LV	200
6.2.3	Cardiac cycle simulations	201
6.2.4	Extension to patient-specific models	203
A	Parallel processing	220
A.1	Introduction	220
A.2	Methods	221
A.2.1	Geometries	221
A.2.2	Meshes	222
A.2.3	Numerical methods	223
A.3	Results and discussion	225
A.4	Conclusions	229
B	Additional details on inflation of the passive left ventricle	231
B.1	Definition of the governing equations	231
B.2	Left ventricle cavity volume calculations	232
C	Extension to anatomical geometry	235
C.1	Introduction	235
C.2	Methods	236
C.2.1	Geometry and mesh	236
C.2.2	Boundary conditions	238
C.2.3	Numerical methods	238
C.3	Results	239
C.4	Discussion	240

D	Additional details on cardiac cycle simulations	244
D.1	Fluid geometry definition	244
D.2	Time integration	248
D.3	Fluid-structure interaction	248

Nomenclature

a	outer semi-major axis of ellipsoid
a_i	sigmoid function slope parameter
\mathbf{B}_L	linear strain-displacement matrix
\mathbf{B}_{NL}	non-linear strain-displacement matrix
b	outer semi-minor axis of ellipsoid
b_i	sigmoid function location parameter
\mathbf{C}	right Cauchy-Green deformation tensor; also damping matrix
C_i	passive material parameter
c	height from the apex of the myocardium in the deformed geometry
\mathbf{D}	tangent constitutive tensor
D	diameter
D_i	active material parameter
$D_{i,\max}$	active material parameter when muscle fibres are fully contracted

\mathbf{d}	displacement vector
\mathbf{E}	Green's strain tensor
\overline{E}_{ii}	principal strain
e	eccentricity
EF	ejection fraction
\mathbf{F}	deformation gradient tensor; also force vector equivalent to the element stresses
F	forcing function magnitude
f	fractional height above the equatorial plane of the ellipsoid
\mathbf{f}^B	body force per unit volume
h	height of the ellipsoid
\mathbf{I}	identity matrix
I_i	strain invariant
J	volume ratio
J_i	reduced strain invariant
\mathbf{K}	stiffness matrix
L	length
\mathbf{M}	sheet direction unit vector; also mass matrix
m	mass
\mathbf{N}	fibre direction unit vector
N	number of threads

$O()$	upper bound on the order of magnitude
P	fraction of the code that is parallelized
p	pressure
\mathbf{R}	external load vector
R	radius of the sphere
r	radial distance from centre of LV cavity in the deformed geometry
Re	Reynolds number
\mathbf{S}	second Piola-Kirchhoff stress tensor
Δs	load step
SU	speed-up factor
SV	stroke volume
\mathbf{T}	Cauchy stress tensor
T_e	effective stress
T_i	principal Cauchy stress
t	depth from the exterior surface of the myocardium in the deformed geometry; also time
t_a	thickness of myocardium at the apex
t_b	thickness of myocardium at the equator
\mathbf{U}	nodal displacement vector
$\dot{\mathbf{U}}$	nodal velocity vector
$\ddot{\mathbf{U}}$	nodal acceleration vector

V	volume
\mathbf{v}	fluid velocity vector
W	strain energy density function
W_i	derivative of the strain energy density function with respect to the i^{th} strain invariant
\mathbf{w}	fluid mesh velocity vector
w_i	width
x, y, z	global Cartesian coordinate axes
x_1, x_2, x_3	material axes, in the fibre, sheet, and sheet-normal directions, respectively
y_1, y_2, y_3	principal stress axes
z_c	height of the centre of the sphere

Greek symbols

α	angle between the left ventricle outflow tract and the basal plane
β	angle between the left ventricle inflow tract and the basal plane
Δ	least-square difference
δ	small number
ε_i	small positive number
θ	angle between the aortic and mitral valve planes

κ	bulk modulus
λ_i	principal stretch
μ	viscosity
ρ	density
ρ_m	density of the compressible fluid
σ_f	fluid stress tensor
τ	time normalized by the period
φ_1	angle between y_1 and the local circumferential direction
φ_2	angle between y_2 and the local circumferential direction
φ_3	angle between y_3 and the local radial direction
χ	fraction of rabbit active stress to be added to passive canine stress
χ_*	push-forward operator

Subscripts

a	active
Ao	aorta
AV	aortic valve
c	calculated
ED	end diastole

<i>ES</i>	end systole
<i>f</i>	fluid
inc	incompressible
<i>LA</i>	left atrium
<i>LV</i>	left ventricle
<i>m</i>	measured
<i>MV</i>	mitral valve
<i>p</i>	passive
<i>s</i>	solid
sc	slightly compressible
0	reference state

Acronyms

ALE	arbitrary-Lagrangian-Eulerian
CFD	computational fluid dynamics
DG	diastasis geometry
ESG	end-systolic geometry
FSI	fluid-structure interaction
HPCVL	High Performance Computing Virtual Laboratory
IBM	immersed boundary method
IVC	isovolumetric contraction
IVR	isovolumetric relaxation

MRI	magnetic resonance imaging
RA	right atrium
RV	right ventricle

List of Figures

2.1	Anatomy of the heart. Arrows indicate the direction of blood flow.	7
2.2	Heart muscle fibre orientations for the left and right ventricles of a porcine heart. For the left ventricle, the fibres are oriented at angles of -60° on the outer surface (a), 0° in the middle (b), and $+80^\circ$ on the inner surface (c) (from Stevens et al. (2003)).	9
2.3	Composition of a single muscle fibre.	10
2.4	Structure of a sarcomere.	11
2.5	(a) Canine LV pressure-time plot, based on previous measurements (Sabbah and Stein (1981)), (b) freehand sketch of the approximate change in canine LV cavity volume versus time, based on an ejection fraction of 0.44, and (c) approximated canine LV pressure-volume plot, based on values in (a) and (b). Circles denote the start of a phase of the cardiac cycle and the opening or closing of a valve.	14
3.1	Passive LV myocardium stresses for three rabbits and three dogs in the (a) fibre and (b) cross-fibre directions. Symbols indicate experimental values from Lin and Yin (1998) for the rabbit and Novak et al. (1994) for the dog, dashed lines represent results of calculations made using material parameter values from Lin and Yin (1998), and solid lines indicate results obtained through numerical simulation, to be discussed in Sections 3.5.1 for the rabbit and 3.5.3 for the dog.	38
3.2	Total LV myocardium stresses for three rabbits in the (a) fibre and (b) cross-fibre directions. Symbols indicate experimental values from Lin and Yin (1998), dashed lines represent results of calculations made using material parameter values from Lin and Yin (1998), and solid lines indicate results obtained through numerical simulation, to be discussed in Section 3.5.1.	42
3.3	Geometry used for equibiaxial tensile test simulations.	43
3.4	Calculated and simulated canine active stresses in the fibre (a) and cross-fibre (b) directions.	54

3.5	Passive and total stresses for the canine and rabbit LV myocardia in the fibre (a) and cross-fibre (b) directions. Canine passive stresses correspond to the lower case in Fig. 3.1, and rabbit passive and total stresses correspond to specimen 1 in Figs. 3.1 and 3.2, respectively. The solid symbols indicate experimental values from Novak et al. (1994), while the hollow symbols were added to distinguish between the passive and total rabbit curves. All lines represent computational results obtained from equibiaxial tensile test simulations performed in ADINA.	54
4.1	Diagram showing an isolated LV geometry; h is the total height; a is the outer semi-major axis; b is the outer semi-minor axis; t_a is the myocardium thickness at the apex; and t_b is the thickness at the equator. Dashed lines separate six layers of the myocardium, each with a distinct fibre orientation.	69
4.2	Coarse (a) and fine (b) finite element meshes.	72
4.3	Location of elements used for principal stretch and stress calculations. These elements are located at a relative elevation from the apex of $z/h = 0.5$	78
4.4	Normalized volume changes vs. pressure for three sets of material parameter values, along with three previous experimental studies (points), and one previous computational study (solid line) for (a) only.	81
4.5	End-diastolic displacement magnitudes at the centre of the left ventricle geometry in the y - z plane, calculated at $p = 2$ kPa.	84
4.6	Representative principal stretches versus normalized volume change (a) and pressure (b), calculated as described in Section 4.2.4.	85
4.7	Representative transmural (a,c) and longitudinal (b,d) variations of the principal stretches at $p = 1$ kPa (a,b) and $p = 2$ kPa (c,d), calculated as described in Section 4.2.4.	88
4.8	Representative principal Cauchy stresses versus normalized volume change (a) and pressure (b), calculated as described in Section 4.2.4.	90
4.9	Representative transmural (a,c) and longitudinal (b,d) variations of the principal Cauchy stresses at $p = 1$ kPa (a,b) and $p = 2$ kPa (c,d), calculated as described in Section 4.2.4.	91
4.10	Representative transmural variations of the in-plane angles at $p = 2$ kPa, corresponding to the average stresses shown in Fig. 4.9c.	95
4.11	Representative transmural variations of the principal stresses (a) and the in-plane angles (b) at $p = 2$ kPa for two models with different numbers of wall layers.	96
5.1	Diagram showing the solid (a) and fluid (b) geometries along with key dimensions and geometric landmarks.	124
5.2	Diagram showing the dimensions used to define the section of a sphere used to cap the fluid geometry	125
5.3	Mesh for the solid geometry (a) and mesh 1 for the fluid geometry (b). . . .	126
5.4	Forcing function.	130
5.5	Outflow and inflow pressure boundary conditions based on measurements from Sabbah and Stein (1981).	136

5.6	a) Temporal variation of LV cavity pressure from present simulations along with measured values of p_{LV} , p_{LA} , and p_{Ao} from Sabbah and Stein (1981); b) temporal variation of LV cavity volume; c) variation of LV cavity pressure with LV cavity volume. In these figures, volumes have been normalized by the end-diastolic volume at $\tau = 0$. Circles denote the start of a phase of the cardiac cycle and the opening or closing of a valve.	142
5.7	Displacement magnitudes in the myocardium in the y - z centre-plane at selected times during IVC, ejection, and IVR for period 1. Outline represents end-diastolic geometry at $\tau = 0$	145
5.8	Displacement magnitudes in the myocardium in the y - z centre-plane at selected times during filling for period 1. Outline represents end-diastolic geometry at $\tau = 0$	146
5.9	Displacement magnitudes in the myocardium in the y - z centre-plane at selected times during IVC, ejection, and IVR for period 2. Outline represents end-diastolic geometry at $\tau = 1.000$	147
5.10	Displacement magnitudes in the myocardium in the y - z centre-plane at selected times during filling for period 2. Outline represents end-diastolic geometry at $\tau = 1.000$	148
5.11	Representative temporal variations of principal stretches for two periods of the cardiac cycle.	150
5.12	Effective stresses in the myocardium in the y - z centre-plane at selected times during IVC, ejection, and IVR for period 1. Outline represents end-diastolic geometry at $\tau = 0$	152
5.13	Effective stresses in the myocardium in the y - z centre-plane at selected times during filling for period 1. Outline represents end-diastolic geometry at $\tau = 0$	153
5.14	Effective stresses in the myocardium in the y - z centre-plane at selected times during IVC, ejection, and IVR for period 2. Outline represents end-diastolic geometry at $\tau = 1.000$	154
5.15	Effective stresses in the myocardium in the y - z centre-plane at selected times during filling for period 2. Outline represents end-diastolic geometry at $\tau = 1.000$	155
5.16	Representative temporal variations of principal Cauchy stresses for two periods of the cardiac cycle, calculated as described in Section 5.5.2.	157
5.17	Pressures in the LV cavity in the y - z centre-plane at selected times during IVC, ejection, and IVR for period 1.	158
5.18	Pressures in the LV cavity in the y - z centre-plane at selected times during filling for period 1.	159
5.19	Pressures in the LV cavity in the y - z centre-plane at selected times during IVC, ejection, and IVR for period 2.	160
5.20	Pressures in the LV cavity in the y - z centre-plane at selected times during filling for period 2.	161
5.21	Blood velocities in LV cavity in the y - z centre-plane at selected times during IVC, ejection, and IVR for period 1.	164

5.22	Blood velocities in the LV cavity in the y - z centre-plane at selected times during filling for period 1.	165
5.23	Blood velocities in the LV cavity in the y - z centre-plane at selected times during IVC, ejection, and IVR for period 2.	166
5.24	Blood velocities in the LV cavity in the y - z centre-plane at selected times during filling for period 2.	167
5.25	Displacement and effective stress contours for the myocardium in the y - z centre-plane at mid-ejection for two periods ($\tau = 0.150$ and $\tau = 1.150$). . . .	170
5.26	Pressure contours and velocity vectors for the LV cavity in the y - z centre-plane at mid-ejection for two periods ($\tau = 0.150$ and $\tau = 1.150$).	171
5.27	Representative transmural (a,c,e) and longitudinal (b,d) variations of the principal stretches (a,b), principal stresses (c,d), and in-plane angles (e) in the myocardium during mid-ejection for two periods ($\tau = 0.150$ and $\tau = 1.150$), calculated as described in Section 5.5.6.	172
5.28	Representative radial (a,c) and longitudinal (b,d) variations of the LV cavity pressure (a,b) and blood velocities (c,d) during mid-ejection for two periods ($\tau = 0.150$ and $\tau = 1.150$), calculated as described in Section 5.5.6.	175
5.29	Displacement and effective stress contours for the myocardium in the y - z centre-plane at end systole for two periods ($\tau = 0.312$ and $\tau = 1.312$). . . .	176
5.30	Pressure contours and velocity vectors for the LV cavity in the y - z centre-plane at end systole for two periods ($\tau = 0.312$ and $\tau = 1.312$).	177
5.31	Representative transmural (a,c,e) and longitudinal (b,d) variations of the principal stretches (a,b), principal stresses (c,d), and in-plane angles (e) in the myocardium at end systole for two periods ($\tau = 0.312$ and $\tau = 1.312$), calculated as described in Section 5.5.6.	179
5.32	Representative radial (a,c) and longitudinal (b,d) variations of the LV cavity pressure (a,b) and blood velocities (c,d) at end systole for two periods ($\tau = 0.312$ and $\tau = 1.312$), calculated as described in Section 5.5.6.	180
5.33	Displacement and effective stress contours for the myocardium in the y - z centre-plane at end diastole for two periods ($\tau = 1.000$ and $\tau = 2.000$). . . .	182
5.34	Pressure contours and velocity vectors for the LV cavity in the y - z centre-plane at end diastole for two periods ($\tau = 1.000$ and $\tau = 2.000$).	183
5.35	Representative transmural (a,c,e) and longitudinal (b,d) variations of the principal stretches (a,b), principal stresses (c,d), and in-plane angles (e) in the myocardium at end diastole for two periods ($\tau = 1.00$ and $\tau = 2.00$), calculated as described in Section 5.5.6.	184
5.36	Representative radial (a,c) and longitudinal (b,d) variations of the LV cavity pressure (a,b) and blood velocities (c,d) at end diastole for two periods ($\tau = 1.00$ and $\tau = 2.00$), calculated as described in Section 5.5.6.	185
A.1	Solid (left) and fluid (right) parts of the isolated LV geometry.	222
A.2	Solid (left) and fluid (right) meshes with the coarse (a) and fine (b) mesh densities.	224
A.3	Speed-up of parallel FSI simulations with three difference fluid mesh densities versus the number of threads, plotted in logarithmic axes.	226

B.1	Zoomed-in view (right) of the cylinder added to the top of the left ventricle cavity in the solid geometry to allow for calculations of cavity volume to be performed for the results of solid-only simulations.	234
C.1	Front (a-b) and top (c-d) view of the fluid (left) and solid (right) LV-RV geometry based on surface geometries obtained from researchers at INRIA Rocquencourt in France (Coudiere (2005)), based on the measurements of Nielsen et al. (1991).	242
C.2	Cut plane through the centre of the left and right ventricle geometry. The leftmost image (a) is for the undeformed case, and the rightmost image (b) is for the case where $p = 2$ kPa, and depicts bands of nodal pressure in the fluid part of the geometry and bands of effective stresses in the solid part of the geometry.	243
C.3	Percentage volume change results for the left and right ventricle geometry, the first isolated left ventricle geometry, three previous experimental studies (points), and a previous computational study (solid line).	243

List of Tables

3.1	Passive material parameter constraints.	36
3.2	Active material parameter constraints.	37
3.3	Passive and active material parameter values for rabbit specimen 4 of Lin and Yin (1998).	43
3.4	Calculation results to determine appropriate value of material bulk modulus.	51
3.5	Material parameter values for passive canine LV myocardium material model.	51
3.6	Material parameter values for active canine LV myocardium material model.	53
4.1	Average volumes of the LV cavity and masses of the LV myocardium. . . .	70
4.2	Material parameter values for passive canine LV myocardium material model.	76
5.1	Durations of the phases of the cardiac cycle for a heart rate of 100 beats/min.	122
5.2	Parameter values for sigmoid forcing functions.	130
5.3	Active material parameter values.	131
A.1	CPU time for the parts of the simulations with the fine fluid mesh.	227
A.2	Maximum speed-up factors for the three fluid mesh densities.	227
D.1	Approximations of valve angles from several LV geometries.	246

Chapter 1

Introduction

1.1 Motivation

Heart disease is one of the leading causes of death in the industrialized world. To better understand heart disease and treatment options, more complete knowledge of the healthy heart is required. Numerical modelling can be used as a powerful tool to advance our understanding of the behaviour of a healthy heart. A complete numerical model of the heart would be required to contain anatomically and physiologically accurate models of four moving valves and four deformable chambers, blood flow, myocardium mechanics, electrophysiology, and cellular mechanics, as well as to simulate all coupled interactions among these components and mechanisms. Such a model has not yet been developed, but recent advances in high performance computing have enabled researchers to improve upon existing heart models by including two or more components and their coupling in their studies.

Studies of heart mechanics have generally focused on the left ventricle (LV), which

is the main pumping chamber of mammalian hearts and is responsible for pumping blood through the body, because it is the chamber that most commonly develops malfunction or failure. Many researchers have studied either the solid mechanics of the myocardium (Nash and Hunter (2000), Kroon et al. (2009)), the fluid mechanics of blood flow (Long et al. (2008), Schenkel et al. (2009)), or other aspects, such as electromechanical coupling (Chapelle et al. (2009)), but without considering the interaction between the flowing blood and the deforming myocardium.

Any research which fails to account for fluid-structure interaction (FSI), which is the coupling of the dynamics of fluid and solid components, misses an important aspect of heart mechanics. Oertel's research group at the Karlsruhe Institute of Technology, Karlsruhe, Germany has developed sophisticated computational fluid dynamics (CFD) models of the blood flow in the LV, in which the motion of the LV wall was specified from magnetic resonance imaging (MRI) models (e.g., Schenkel et al. (2009)). More recently (Krittian et al. (2010)), the same group has begun to include FSI effects, because their CFD-MRI models were unable to "capture the effects of out of plane movement or torsion". Other researchers (Peskin and McQueen (1996), Watanabe et al. (2004)) have also included FSI effects in their simulations of heart mechanics. Although these studies have been successful in predicting the blood flow, simplifications in their solid mechanics models have limited their abilities to predict accurately the stress-strain behaviour of the myocardium.

Blood flow and myocardium motion play an equally important role in the overall mechanical behaviour of the LV, as each has a significant influence on the other. Numerical models of the mechanics of the LV should therefore include both of these components as

well as the coupling between them. Further, researchers should strive to achieve the same level of uncertainty in their results for both the fluid and solid mechanics rather than overly simplifying one or the other.

1.2 Objectives

The overall objective of this work was to perform fully coupled FSI simulations of the mechanics of the canine LV during the cardiac cycle. Parameters used to define both the fluid and solid models for these simulations were chosen to be representative of an “average” canine LV so that results obtained for both the fluid and solid phases could be compared to previous measurements for validation. This study has been divided into three parts: development of a solid material model, simulations of filling of the passive LV, and simulations of the cardiac cycle. Specific objectives for each of these parts are described in the following.

Development of a material model for the myocardium of a canine LV: Because the material properties of the myocardium cannot be modelled using a readily available material model, it is necessary to define a specific material model, which is suitable for incorporation into an existing FSI code. The objectives of this first phase were to modify an existing myocardium material model from the literature so that it could be used for finite element analysis, to determine material parameter values that are representative of an average canine LV, and to implement this model in a computer subroutine that could be linked to a commercial finite element package.

Static inflation of the passive LV myocardium to an end-diastolic pressure: The

primary objective of this phase was to calculate an end-diastolic state that could be used as an initial condition for cardiac cycle simulations. A secondary objective was to compare results from simulations employing different values of several model parameters to results from previous experimental and computational studies in order to determine a suitable choice of each parameter.

FSI simulations of the mechanics of LV over the cardiac cycle: The primary objective of this phase was to compute results for the fluid and solid models over the cardiac cycle that would be consistent, to the greatest possible extent, with physiological expectations.

1.3 Organization

The thesis consists of six chapters. Chapter 2 provides background information on the anatomy and physiology of the heart and a description of the cardiac cycle. Each of the following three chapters reproduces a stand-alone published article or a manuscript submitted for publication or intended to be submitted. Chapter 3 is an article (Doyle et al. (2010a)) discussing the development of a material model for the canine LV myocardium. Chapter 4 is a manuscript describing simulations of the inflation of the passive LV. Chapter 5 is a manuscript on FSI simulations during the cardiac cycle. Lastly, Chapter 6 contains general conclusions for this study as well as recommendations for future work in material model development, mechanics of myocardium deformation and blood flow, and FSI simulations of the heart. Four appendices have also been included in this thesis. These appendices contain work that is complementary to the work presented in the body of the

thesis, but which has been placed in appendices to avoid distracting the reader from the main issues in this study. Appendix A is an excerpt of an article (Doyle et al. (2010b)) that contains details on parallelization of the FSI simulations. Appendix B contains additional mathematical details pertaining to the simulations of the inflation of the passive LV. Appendix C briefly addresses the extension of this work to an anatomical geometry of the left and right ventricles and the challenges with performing such an extension. Lastly, Appendix D provides additional details on the fluid geometry definition and the numerical methods used in the FSI simulations.

Chapter 2

Background

2.1 Cardiovascular system

The cardiovascular system is an organ system in the bodies of animals, comprising the heart, blood vessels, and blood, whose primary function is to transport blood. In this section, background on the anatomy and physiology of mammalian hearts is provided along with a descriptions of the cardiac cycle and the contraction and relaxation of heart muscle fibres.

2.2 Heart anatomy and physiology

The heart is a muscular organ responsible for pumping blood through the body. It consists of four chambers, the left and right atria (LA, RA), and the left and right ventricles (LV, RV), as shown in Fig. 2.1. Note that left and right are defined by the way a person views his or her own heart. The left and right sides of the heart are separated from each

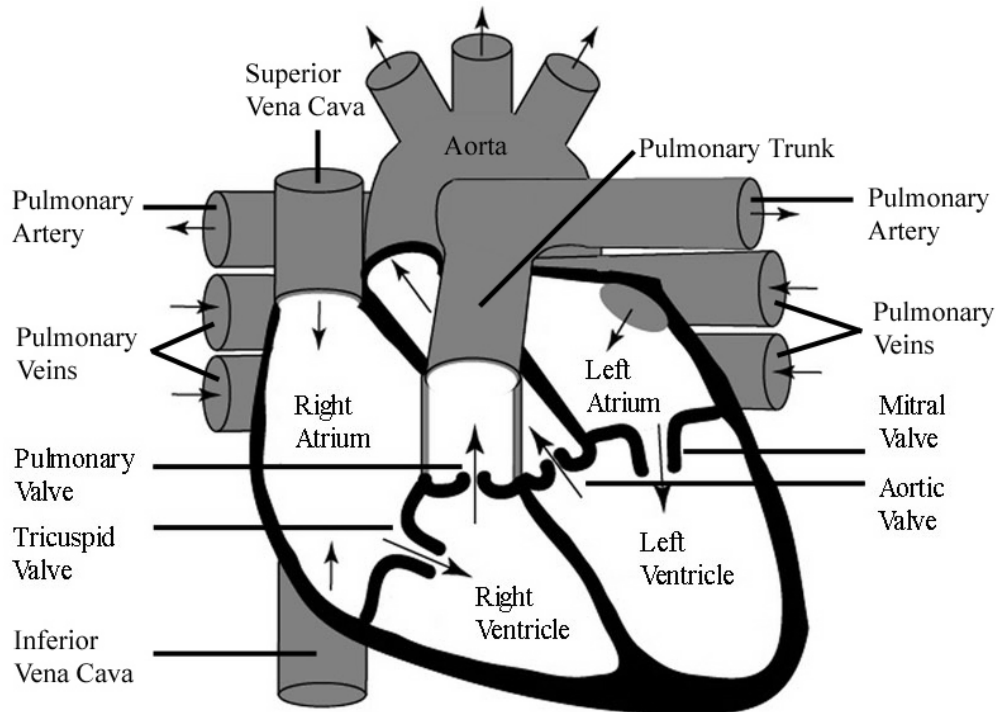


Figure 2.1: Anatomy of the heart. Arrows indicate the direction of blood flow.

other by two walls, the interatrial septum and the interventricular septum. The left side of the heart is responsible for pumping blood through the body, while the right side of the heart is responsible for pumping blood to the lungs. As shown in Fig. 2.1, the heart has four valves to control the flow direction; the pulmonary valve connects the RV to the pulmonary trunk, the tricuspid valve connects the RA and the RV, the aortic valve (AV) connects the LV and the aorta, and the mitral valve (MV) connects the LA and the LV. The mitral and tricuspid valves are called atrioventricular valves because they separate the atria from the ventricles. The other two valves, the pulmonary and aortic valves are called semilunar valves because of the shape of their leaflets.

The heart wall consists of three layers, which from the outside to the inside are the epicardium, the myocardium, and the endocardium. Both the epicardium and the endocardium are thin layers, containing epithelial cells and connective tissues. The myocardium is a thick layer that contains muscle fibres, extracellular matrix, interstitial fluid, blood vessels, and blood (Huyghe et al. (1991)). The extracellular matrix of the myocardium contains collagen fibres and other components such as elastin fibres and fibronectin (Opie (2004)). Myocardial thickness varies from chamber to chamber, according to the distance over which each chamber has to pump blood and the afterload it has to pump against. Accordingly, the atria have thinner myocardial layers than the ventricles. Further, the LV has a thicker myocardial layer than the RV, corresponding to the higher afterload of the body than that of the lungs. The relatively high afterload is also the reason for which the LV is the most commonly failing heart chamber.

The muscle fibres in the myocardium are arranged in layers of roughly constant fibre orientation, where the fibre angle, measured with respect to the local circumferential direction, changes from the epicardial surface to the endocardial surface. Pioneering work on quantifying the fibre angles in the myocardium was performed by Streeter et al. (1969), who found an almost linear change in fibre orientation through the myocardium of canine LVs. An example of the muscle fibre layers and angles can be found in Fig. 2.2¹, which is a representation of the LV and RV of a porcine heart.

Heart muscle fibres are arranged in bundles. As shown in Fig. 2.3, each muscle fibre can be divided into filaments, known as myofibrils, which are made up of repeating

¹Reprinted from *Journal of Biomechanics*, v. 36, Stevens, C., Remme, E., LeGrice, I., and Hunter, P., Ventricular mechanics in diastole: Material parameter sensitivity, p. 741, 2003, with permission from Elsevier.

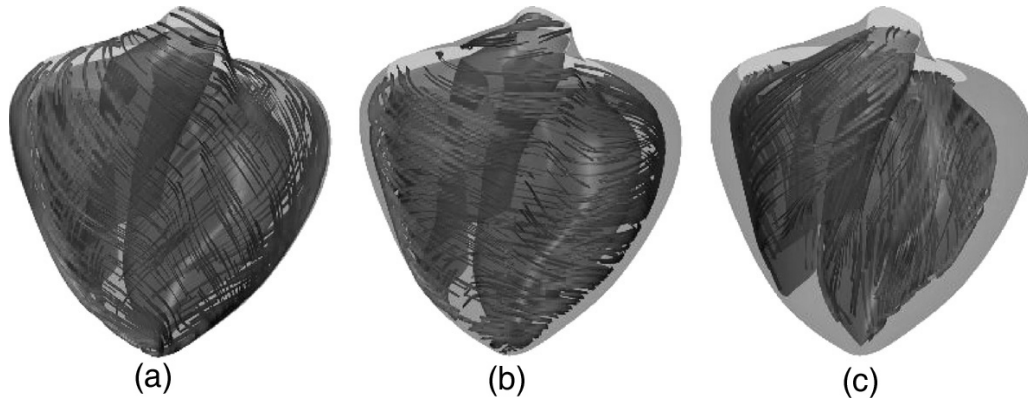


Figure 2.2: Heart muscle fibre orientations for the left and right ventricles of a porcine heart. For the left ventricle, the fibres are oriented at angles of -60° on the outer surface (a), 0° in the middle (b), and $+80^\circ$ on the inner surface (c) (from Stevens et al. (2003)).

units, referred to as sarcomeres. Sarcomeres are made up of two types of myofilaments, actin, which are thin, and myosin, which are thick, as shown in Fig. 2.4.

2.3 Cardiac cycle

During each heartbeat the heart undergoes several steps, in a process termed the cardiac cycle. At different parts of the cardiac cycle, each chamber of the heart contracts and relaxes; a chamber that is contracting is said to be in systole, whereas a chamber that is relaxing is said to be in diastole.

In this section, the cardiac cycle is described for the LV starting from end diastole, at which time the muscle fibres in the LV are fully relaxed, the AV and the MV are closed, and the volume V_f of the LV cavity reaches its maximum value. The cardiac cycle is divided into four phases, isovolumetric contraction (IVC), ejection, isovolumetric relaxation (IVR), and filling. These phases can be grouped together into two parts, ventricular systole, which

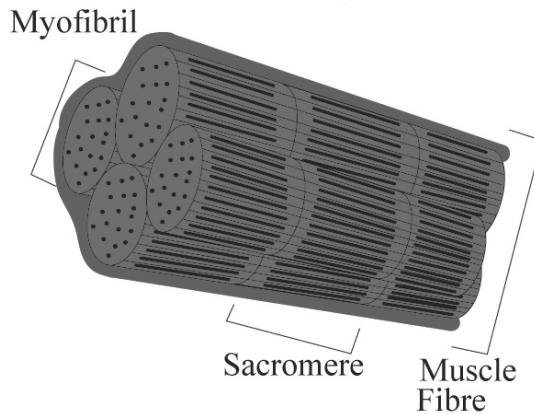


Figure 2.3: Composition of a single muscle fibre.

consists of the IVC and ejection phases, and ventricular diastole, which consists of the IVR and filling phases.

IVC begins at end diastole, when the MV closes. This phase is referred to as isovolumetric because V_f remains roughly constant during this phase when both valves are closed. During IVC, the muscle fibres contract and the pressure p_{LV} inside the LV cavity increases. Once p_{LV} exceeds the aortic pressure p_{Ao} , the AV opens and the ejection phase begins. Ejection is divided into two sub-phases, rapid ejection and reduced ejection (Opie (2004)). During rapid ejection, the muscle fibres continue to contract, p_{LV} continues to increase, and V_f decreases, as blood rapidly exits the LV during this phase because $p_{LV} > p_{Ao}$. When p_{LV} reaches a maximum, reduced ejection begins. During reduced ejection, the muscle fibres begin to relax, p_{LV} decreases, and V_f decreases, as blood continues to exit the LV, although at a slower rate because $p_{LV} < p_{Ao}$. When p_{LV} decreases sufficiently, the AV closes and IVR begins. During IVR, the muscle fibres continue to relax, p_{LV} decreases, and V_f remains roughly constant. IVR continues until p_{LV} is lower than the left atrial

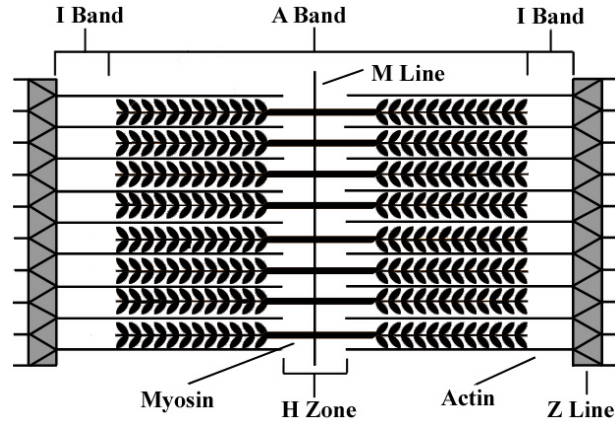


Figure 2.4: Structure of a sarcomere.

pressure p_{LA} at which time the MV opens and filling begins. Filling is divided into three sub-phases, rapid filling, diastasis, and atrial contraction (Opie (2004)). During rapid filling, muscle fibres complete their relaxation, p_{LV} continues to decrease and V_f increases as blood rapidly enters the LV. Once the muscle fibres have completed their relaxation, p_{LV} begins to increase and the rate of change of V_f decreases. As p_{LV} approaches p_{LA} , diastasis occurs. Diastasis is characterized by a small difference between p_{LV} and p_{LA} and a small increase in V_f . Lastly, the LA contracts, which marks the start of the atrial contraction sub-phase, during which p_{LV} and V_f increase as blood is driven into the LV from the LA. Once p_{LV} becomes equal to p_{LA} , the MV closes and the cardiac cycle begins again.

The overall mechanics of the LV during the cardiac cycle may be characterized by the changes in p_{LV} and V_f . Such changes may be plotted as functions of time or as functions of each other. The change in V_f during the cardiac cycle may be characterized by two parameters, the stroke volume SV and the ejection fraction EF . The stroke volume is the change in V_f from end diastole to end systole, that is $SV = V_{f,ED} - V_{f,ES}$. The ejection

fraction is the ratio of the stroke volume to the end-diastolic volume, i.e., $EF = SV/V_{f,ED}$. For comparison of results from different studies, it seems preferable to consider EF rather than SV , because SV depends on the initial value of V_f .

Available experimental information on the changes of physiological pressure and cavity volume of canine LV will be used for a partial validation of the present predictions. Figure 2.5a is plot of p_{LV} measured by Sabbah and Stein (1981) as a function of the normalized time τ , equal to the ratio of the actual time and the cardiac cycle period, for a period of 600 ms/heartbeat, which is equivalent to 100 beats/min. Considering that Sabbah and Stein (1981) did not measure the corresponding cavity volume changes for the measured pressures, the change in V_f will be estimated from EF taken from the literature. Previous studies of canine LVs have found ejection fractions of $EF = 0.43$ ($SV = 34$ ml) (Bovendeerd et al. (1996)) and 0.45 ($SV = 21$ ml) (Kerckhoffs et al. (2007)). One additional study, performed by Guccione et al. (1995) calculated $EF = 0.20$ ($SV = 10$ ml), which the authors suggest is representative of an “open-chest pentobarbital-anesthetized animal”. Disregarding the latter value as not corresponding to a natural *in vivo* state, one may consider the average value of EF for a canine LV to be $EF = 0.44$. Using this value and scaling changes in V_f during ejection and filling taken from volume-time plots from humans, such as the one presented by Parmley and Talbot (1979), a freehand sketch of V_f normalized by $V_{f,ED}$ as a function of τ was produced and is presented as Fig. 2.5b. The corresponding values of pressure and volume variations from Figs. 2.5a and b were used to construct a representative pressure-volume curve for the canine LV, which is plotted as Fig. 2.5c. In Figs. 2.5a-c, each of the four phases of the cardiac cycle is identified and the start

of each phase is denoted by an open circle, which signifies the opening or closing of a valve.

2.4 Muscle fibre contraction and relaxation

Heart muscle fibres contract and relax due to the propagation of an electrical potential through the heart. All muscle cells in the heart have an electric potential difference across their cell membranes. In diastole, during which the muscle fibres are relaxed, the extracellular space has a positive charge and the intracellular space has a negative charge. This is referred to as the polarized state. To contract the muscle fibres, the potential across the cell membrane must be reversed such that a sufficiently large positive charge exists inside the cell. A potential that exceeds the threshold value needed to cause the muscle fibres to contract is referred to as action potential. The change in the polarity across the cell membrane that leads to muscle fibre contraction is referred to as depolarization and is caused by the controlled transfer of calcium, sodium, and potassium ions across the cell membrane. The presence of calcium ions inside the cell causes a series of chemical reactions which drives the contraction of the muscle fibres. During muscle fibre contraction, the actin and myosin filaments slide past each other to decrease the length of each sarcomere, and consequently, of each muscle fibre, while the length of each filament remains constant. After the muscle fibres contract, the total ionic current is reversed, which restores a negative charge inside the cells and causes the muscle fibres to relax (Opie (2004)). This reversal phases is referred to as repolarization.

The propagation of the action potential through the heart is referred to as conduction and the study of the electric activity in the heart is referred to as cardiac electrophys-

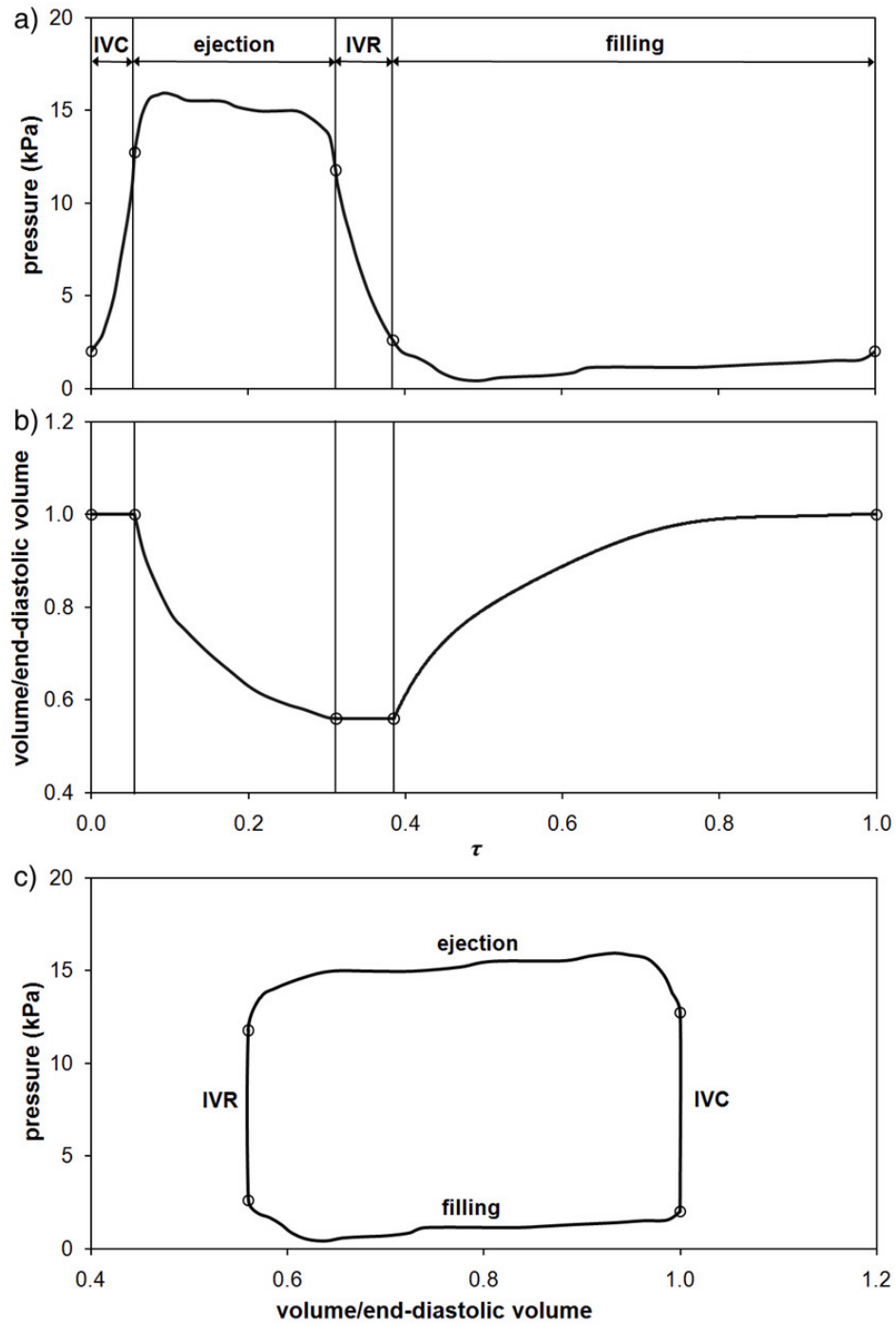


Figure 2.5: (a) Canine LV pressure-time plot, based on previous measurements (Sabbah and Stein (1981)), (b) freehand sketch of the approximate change in canine LV cavity volume versus time, based on an ejection fraction of 0.44, and (c) approximated canine LV pressure-volume plot, based on values in (a) and (b). Circles denote the start of a phase of the cardiac cycle and the opening or closing of a valve.

iology. Conduction begins in the sinoatrial (SA) node located in the right atrium. The SA node is the first natural pacemaker of the heart. Next, the action potential propagates along the muscle fibres of the two atria, causing them to contract. The action potential then travels to the atrioventricular (AV) node, which is the second natural pacemaker in the heart, and is located in the interatrial septum. From the AV node, the action potential moves down the interatrial septum and into the interventricular septum via the bundle of His. The action potential then travels down the interventricular septum to the apex, where it enters the Purkinje fibres and travels up the ventricular walls, causing them to contract (Tortora (2002)).

Chapter 3

Myocardium material model

3.1 Introduction

The myocardium, which is the thick muscular middle layer of the heart wall, comprises muscle fibres, extracellular matrix, blood vessels, blood, and interstitial fluid (Huyghe et al. (1991)). The extracellular matrix of the myocardium is mostly composed of collagen fibres, and also contains fibronectin and elastin (Opie (2004)). The muscle fibres in the myocardium are arranged in layers whose orientation changes gradually across the thickness of the wall. In developing material models for the wall of the left ventricle (LV) or other chambers of the heart, the general approach has been to neglect the epicardium and the endocardium, which are the outer and inner layers of the heart wall, respectively, and are much thinner than the myocardium.

It has previously been shown that the myocardium is a highly anisotropic material with three characteristic directions (LeGrice et al. (1995)), which are referred to as fibre, sheet, and sheet-normal (Nash and Hunter (2000)). The sheet direction is defined as being

perpendicular to the muscle fibres but tangential to the surface defined by the fibre axes, whereas the sheet-normal direction is defined as perpendicular to this surface. Therefore, any material model that is meant to describe the mechanical behaviour of the myocardium should ideally be orthotropic.

Additional complications in modeling the myocardium material arise by the fact that muscle fibres undergo successive contractions and relaxations during different parts of the cardiac cycle, as a result of the propagation of an electrical wave, known as action potential, through the myocardium. The action potential induces ion transfer across the cell membrane of the muscle cells, causing actin and myosin filaments to slide past each other, which shortens the length of the sarcomere units within the muscle fibre cells, and consequently reduces the overall length of the muscle fibres, resulting in muscle contraction. The contraction and relaxation of the muscle fibres can only be modeled with the use of a material model that is capable of changing during the cardiac cycle. When developing material models of the myocardium, two states of the muscle fibres are considered. The first is the “passive” state, in which the muscle fibres are fully relaxed, and the second is the “total” state, in which the muscle fibres are fully contracted. The total-state stresses are the sum of the passive-state stresses and additional “active” stresses, which are attributed to the fully-contracted muscle fibres. During the cardiac cycle, passive stresses are always present and fractions of the active stresses can be added to them to account for partially contracted muscle fibres.

The passive stress-strain relationship of the myocardium is highly non-linear. This relationship is dictated by the combined behaviours of collagen fibres and additional com-

ponents of the extracellular matrix, such as elastin (Opie (2004)). At low strains, the collagen fibers are crinkled like springs and the stress-strain behaviour of the myocardium is driven by the rest of the extracellular matrix, whose stiffness is much lower than that of collagen (Lanir (1979)). As the strain increases, the collagen fibres straighten out and the myocardium stiffness increases, eventually becoming dominated by the collagen fibre properties.

The LV myocardium has generally been modeled as a hyperelastic material, in which the stress-strain behaviour is defined in terms of a strain energy density function. Material models proposed in the literature for the passive LV myocardium can be classified into fully orthotropic ones with different material properties in the fibre, sheet, and sheet-normal directions (Nash and Hunter (2000); Usyk et al. (2000); Costa et al. (2001)) and transversely isotropic ones, with material properties differing only in two directions, fibre and cross-fibre (Humphrey et al. (1990b); Guccione et al. (1991); Lin and Yin (1998)). For the active myocardium, two types of models have been proposed: transversely isotropic models (Usyk et al. (2000); Lin and Yin (1998)), and models that are uniaxial in the fibre direction (Nash and Hunter (2000); Usyk et al. (2000); Guccione et al. (1993)). All material models necessarily contain adjustable parameters, whose determination should be based on appropriate experimental results, which are generally specific to a species and even to individuals within a species. All of these published models have been defined for the canine myocardium, with the exception of the one proposed by Lin and Yin (1998), which is for the rabbit myocardium.

Ideally, the measurement of material properties should be done with the undis-

turbed and functioning heart in its natural condition and should cover the entire cardiac cycle. This is currently impossible, and one may only resort to the measurement of stress-strain behaviour of excised myocardium specimens in the laboratory. Moreover, complete testing of the stress-strain behaviour of excised myocardium specimens, consisting of biaxial tests in the fibre and sheet direction, fibre and sheet-normal directions, and sheet and sheet-normal directions, along with shear tests, has not yet been carried out for a single set of specimens. In fact, in our literature survey we found no published biaxial tensile tests in the sheet and sheet-normal directions. Shear tests have been performed by Dokos et al. (2002) for pieces of porcine myocardium in the passive state, but have not yet been used for material model development.

Material model development generally makes use of equibiaxial tensile tests results, performed on pieces of the LV myocardium with the fibre axis for each piece aligned with one of the directions being stretched. The results of these tests are generally presented as plots of stress versus stretch, where stretch is the ratio of deformed and undeformed lengths. Equibiaxial tensile tests provide sufficient information for the determination of parameters in transversely isotropic models. Several sets of stress-stretch measurements for the passive canine LV myocardium, obtained from equibiaxial tensile tests, can be found in the literature (Humphrey et al. (1990b); Novak et al. (1994); Bovendeerd et al. (1996)). To our knowledge, the only published stress-stretch plots corresponding to both active and total material behaviour are those by Lin and Yin (1998), which have presented passive and total stress-stretch plots in the fibre and cross-fibre directions for the rabbit LV myocardium. To obtain the total stress-stretch results, Lin and Yin (1998) used a barium contracture

method to force the muscle fibres to contract. Both passive and total stress-stretch values have been proposed by McCulloch and Mazhari (2001) for a canine LV, with the latter representing an ischemic myocardium. However, these values were not based on direct measurements.

In the present study, our general objective was to perform finite element simulations of the mechanics of the heart, including both the blood flow and the wall motion. These simulations will focus on a canine LV, for which geometric information, stress-stretch measurements, and many previous experimental and computational results for various fluid and solid quantities over the cardiac cycle are available. The specific objective of this chapter is to implement a modified version of a previously defined material model for the passive and active behaviour of the LV myocardium that can be used in our finite element simulations, and to calculate appropriate material parameter values for this model. To achieve this goal, we faced a number of challenges and this chapter describes how we overcame some of them. First, we did not endeavour to devise a new material model, but rather to choose one from the literature. Our choice was based on the requirement that the model should cover the entire cycle, or be possible to modify in a way that it would so; moreover, any parameters present in the model should be possible to determine from available measurements, if not precisely, at least in a way that they would result in physiologically plausible predictions. The use of a fully orthotropic model was precluded by the lack of stress-strain results suitable for calculating material parameter values for such a model, so we chose a transversely isotropic model. Along the way, we also discovered that the mathematical form of the chosen model needed to be modified for purely numerical reasons and

we introduced modifications that allowed numerical convergence but without appreciably distorting its physical performance. Second, we calculated material parameter values for the passive LV myocardium based on available measurements on canines. Finally, in view of the lack of active stress-stretch measurements for the canine LV myocardium, we devised a method to adapt available measurements on rabbits so that they can serve as substitutes. In summary, work described in this article is the first step towards modeling the mechanics of the canine LV. It will be followed by detailed numerical simulations of the operation of an idealized canine heart with fluid-structure interaction between the deforming myocardium and the flowing blood.

3.2 Material model development

3.2.1 Material model selection

The choice of an appropriate material model of the LV myocardium was based on three selection criteria. First, the chosen material model should allow for the explicit definition of muscle fibre direction within the material model, rather than within the finite element model. This can be done by defining the strain energy density function in terms of strain invariants rather than strains, and introducing a strain invariant containing the fibre direction. Among the material models mentioned previously, only those of Humphrey et al. (1990b) and Lin and Yin (1998) are defined in terms of strain invariants. Meeting this criterion would facilitate the specification of fibre direction in our chosen finite element software, ADINA v. 8.5.2 (ADINA R & D, Inc., Watertown, MA, USA), because it was determined that defining the fibre direction within the material model would require no

modifications to the finite element code. Second, the chosen material model should have a number of independent material axes that would be equal to that of the available LV myocardium stress-stretch measurements to allow for validation and, if necessary, calculation of appropriate material parameters. As mentioned in the Introduction, stress-stretch measurements available in the literature are from equibiaxial tests, which specify properties for only the fibre and cross-fibre directions. This necessitates the use of a transversely isotropic material model, such as the models proposed by Humphrey et al. (1990b), Guccione et al. (1991), and Lin and Yin (1998). Third, the chosen material model should contain both passive and active components, preferably with the same number of independent material directions. Whereas the material models of Guccione et al. (1993), Nash and Hunter (2000), and Usyk et al. (2000) all have active parts with various numbers of independent material axes, only the material model of Lin and Yin (1998) satisfies this criterion as well as the other two. Therefore, the transversely isotropic material model proposed by Lin and Yin (1998) has been chosen as a starting point for the present work. A disadvantage of this approach is that the form of the material model and the associated parameter values are for rabbit rather than canine LVs.

In adapting the material model of Lin and Yin (1998) for simulations of the canine LV myocardium, two issues had to be addressed. First, whether the form of the material model, which was derived for a rabbit LV, is suitable for a canine LV; and second, whether there are suitable canine stress-stretch values in the literature from which one may calculate appropriate material parameter values for the canine LV. The first issue has been resolved by Kang and Yin (1996), who have compared their plots of $W_{p,i}$ versus I_i for rabbit LVs

with those for a canine LV by Humphrey et al. (1990a) ($W_{p,i} = \partial W_p / \partial I_i$, W_p is the passive strain energy density function and I_i is the i^{th} invariant of Green's strain tensor, to be defined in the next section). Kang and Yin (1996) concluded that these plots show comparable trends, which implies that the same functional form may be used to model both rabbit and canine LVs. In the absence of a suitable material model derived specifically for a dog, this evidence is deemed to justify the use of the Lin and Yin (1998) material model for canine LV myocardium simulations, provided that the material parameter values for rabbits are replaced by values appropriate for dogs. Although adapting properties measured for one species for use with another would obviously introduce some uncertainty, it has also been known that, when such properties are normalized by appropriate scales, they result in dimensionless values that are comparable for different mammals. For example, Li (1996) states that the LV ejection fractions (defined as the ratio of stroke volume to end diastolic volume) of four different mammals, including rabbits and dogs, are roughly the same. To address the second issue, one needs to examine separately the availabilities of passive and total stress-stretch measurements. For the passive canine LV, Novak et al. (1994) provide a range of stress-stretch measurements, which can be used to calculate appropriate material parameter values, as will be described in a following section. The issue becomes more difficult, however, when attempting to simulate the total material behaviour. As mentioned previously, the only known published total stress-stretch measurements for the LV myocardium are for the rabbit Lin and Yin (1998). In the absence of such measurements for a dog, rabbit measurements will be used to approximate canine LV myocardium total material behaviour. If total stress-stretch measurements for the canine LV myocardium

become available in the future, the material parameter values in the present model can be easily adapted to correspond to the new measurements instead of the ones used presently.

3.2.2 Material model definition

The material model is given in terms of the total strain energy density function W , from which one may calculate stresses from strains. More specifically, the components S_{ij} of the second Piola-Kirchhoff stress tensor \mathbf{S} can be calculated from the strain energy density function and the components E_{ij} of Green's strain tensor \mathbf{E} as

$$S_{ij} = \frac{\partial W}{\partial E_{ij}} - pC_{ij}^{-1}, \quad i, j = 1, 2, 3 \quad (3.1)$$

where p is a Lagrange multiplier, which is introduced to enforce material incompressibility and can be specified by considering the boundary conditions of each specific problem, and C_{ij}^{-1} are the components of the inverse of the matrix representing the right Cauchy-Green deformation tensor \mathbf{C} . \mathbf{C} can be defined in terms of the deformation gradient tensor \mathbf{F} as $\mathbf{C} = \mathbf{F}^T \mathbf{F}$ (Holzapfel (2000)). Because the experiments that will be used to evaluate the parameters in the material model were conducted along principal stretch axes, it is convenient to write the tensors \mathbf{F} and \mathbf{C} and \mathbf{C}^{-1} in terms of the principal stretches λ_i , $i = 1, 2, 3$ as

$$\mathbf{F} = \begin{bmatrix} \lambda_1 & 0 & 0 \\ 0 & \lambda_2 & 0 \\ 0 & 0 & \lambda_3 \end{bmatrix}, \quad \mathbf{C} = \begin{bmatrix} \lambda_1^2 & 0 & 0 \\ 0 & \lambda_2^2 & 0 \\ 0 & 0 & \lambda_3^2 \end{bmatrix}, \quad \text{and} \quad \mathbf{C}^{-1} = \begin{bmatrix} \lambda_2^2 \lambda_3^2 & 0 & 0 \\ 0 & \lambda_1^2 \lambda_3^2 & 0 \\ 0 & 0 & \lambda_1^2 \lambda_2^2 \end{bmatrix} \quad (3.2)$$

Alternatively, \mathbf{C} can be rewritten in terms of E_{ij} or principal strains \bar{E}_{ii} as

$$\mathbf{C} = \begin{bmatrix} 2E_{11} + 1 & E_{12} & E_{13} \\ E_{21} & 2E_{22} + 1 & E_{23} \\ E_{31} & E_{32} & 2E_{33} + 1 \end{bmatrix} = \begin{bmatrix} 2\bar{E}_{11} + 1 & 0 & 0 \\ 0 & 2\bar{E}_{22} + 1 & 0 \\ 0 & 0 & 2\bar{E}_{33} + 1 \end{bmatrix} \quad (3.3)$$

The principal strains are related to the principal stretches as $\lambda_i^2 = 2\bar{E}_{ii} + 1$, $i = 1, 2, 3$; in this and all subsequent equations containing repeating indices, Einstein's summation convention does not apply.

In order to compute the normal components of \mathbf{S} , the Lagrange multiplier p must be calculated using boundary conditions. In this study, calculations are performed for the case of equibiaxial tension, for which the material is stretched equally in the fibre (x_1) and cross-fibre (x_2) directions. For an incompressible material in equibiaxial tension, $S_{33} = 0$, from which p can be calculated as

$$S_{33} = \frac{\partial W}{\partial E_{33}} - pC_{33}^{-1} = 0 \Rightarrow p = \frac{1}{\lambda_1^2 \lambda_2^2} \left(\frac{\partial W}{\partial E_{33}} \right) \quad (3.4)$$

Substituting this value of p into Eq. (3.1) gives

$$S_{11} = \frac{\partial W}{\partial E_{11}} - \frac{\lambda_3^2}{\lambda_1^2} \frac{\partial W}{\partial E_{33}} \text{ and } S_{22} = \frac{\partial W}{\partial E_{22}} - \frac{\lambda_3^2}{\lambda_2^2} \frac{\partial W}{\partial E_{33}} \quad (3.5)$$

The stresses presented in most of the literature are Cauchy stresses \mathbf{T} , rather than second Piola-Kirchhoff stresses. The Cauchy stress tensor can be calculated from the second Piola-Kirchhoff stress tensor using a push-forward operator, denoted as χ_* , as follows

$$\mathbf{T} = \chi_*(\mathbf{S}) = \frac{1}{J} \mathbf{F} \mathbf{S} \mathbf{F}^T \quad (3.6)$$

where $J = \det \mathbf{F}$ is the volume ratio (Holzapfel (2000)).

Using Eq. (3.6), the definition of \mathbf{F} from Eq. (3.2), and the fact that for equibiaxial tensile tests $\lambda_1 = \lambda_2$, the normal components of \mathbf{T} can be calculated as

$$T_{ii} = S_{ii} \frac{\lambda_i^2}{\lambda_1 \lambda_2 \lambda_3} = \frac{S_{ii}}{\lambda_3}, \quad i = 1, 2 \quad (3.7)$$

$$T_{33} = 0 \quad (3.8)$$

The material model of Lin and Yin (1998), which serves as the basis for the model to be used in this study, decomposes the strain energy density function for the rabbit LV myocardium into a passive part W_p and an active part W_a , as

$$W = W_p + W_a \quad (3.9)$$

where

$$W_p = C_1 (e^Q - 1) \quad (3.10)$$

$$Q = C_2 (I_1 - 3)^2 + C_3 (I_1 - 3) (I_4 - 1) + C_4 (I_4 - 1)^2 \quad (3.11)$$

$$\begin{aligned} W_a = & D_0 + D_1 (I_1 - 3) (I_4 - 1) + D_2 (I_1 - 3)^2 \\ & + D_3 (I_4 - 1)^2 + D_4 (I_1 - 3) + D_5 (I_4 - 1) \end{aligned} \quad (3.12)$$

In these expressions, C_i and D_i are material parameters and I_1 and I_4 are invariants of Green's strain tensor, defined as

$$I_1 = \text{tr} \mathbf{C} = \lambda_1^2 + \lambda_2^2 + \lambda_3^2 \quad (3.13)$$

$$I_4 = \mathbf{N}^T \mathbf{C} \mathbf{N} = n_1^2 \lambda_1^2 + n_2^2 \lambda_2^2 + n_3^2 \lambda_3^2 \quad (3.14)$$

where \mathbf{N} is a unit vector along the muscle fibre direction ($\mathbf{N} = [n_1 \ n_2 \ n_3]^T$, $n_1^2 + n_2^2 + n_3^2 = 1$).

It should be noted that, in stress calculations, one does not need the value of W , but rather only its derivatives. For this reason, the value of the parameter D_0 is not required, and so D_0 is set to zero.

For a more complete definition of a transversely isotropic material, additional strain invariants, I_2 and I_5 , defined below, could have been included in Eqs. (3.11) and (3.12).

$$I_2 = \frac{1}{2} \left[(\text{tr} \mathbf{C})^2 - \text{tr} \mathbf{C}^2 \right] \quad (3.15)$$

$$I_5 = \mathbf{N}^T \mathbf{C}^2 \mathbf{N} \quad (3.16)$$

However, these invariants were neglected by the original authors of this model “because the determination of a specific form of a strain-energy function which depends on four invariants is extremely difficult” (Humphrey et al. (1990a)). In fact, Criscione et al. (2001) state that, because I_1 , I_2 , I_4 , and I_5 measure deformations that are not independent of each other, it is impossible to determine the appropriate form of W when considering all of these invariants, if only biaxial tests are performed. In their work, Criscione et al. (2001) define alternative invariants, which unlike I_1 , I_2 , I_4 , and I_5 , are nearly independent of each other, which in turn, could be used to determine a functional form of a transversely-isotropic constitutive equation for the LV myocardium. However, determining an appropriate form of

a constitutive equation would require performing experiments on pieces of LV myocardium that involve fixing one or more of these alternative invariants, while varying another to determine the influence of each one on the form of W . As the present study makes use of stress-stretch measurements from the literature, the determination of a new analytical form for the function W is beyond the current scope. Although we acknowledge that the analytical form of W defined by Eqs. (3.11) and (3.12) may not represent all aspects of the behaviour of the LV myocardium, due to the absence of these two strain invariants, we ensure that the model describes well the available data by choosing parameter values which fit well to existing stress-stretch measurements.

3.2.3 Material model modifications

Material compressibility

The previously defined model is fully incompressible. In many finite element codes, including ADINA, such models cannot be used because of the difficulty in enforcing conservation of volume in a geometry undergoing large deformations. It is therefore necessary to modify the expression for W to a slightly compressible form as described in the ADINA documentation (ADINA R & D, Inc. (2008a)). This is done by adding a volumetric term to represent the material compressibility, and converting the strain invariants to reduced strain invariants, as shown in the following.

$$W_p = C_1 (e^Q - 1) + \frac{1}{2} \kappa_s (J_3 - 1)^2 \quad (3.17)$$

$$Q = C_2 (J_1 - 3)^2 + C_3 (J_1 - 3) (J_4 - 1) + C_4 (J_4 - 1)^2 \quad (3.18)$$

$$W_a = D_0 + D_1 (J_1 - 3) (J_4 - 1) + D_2 (J_1 - 3)^2 \\ + D_3 (J_4 - 1)^2 + D_4 (J_1 - 3) + D_5 (J_4 - 1) \quad (3.19)$$

In the previous equations, κ_s is the material bulk modulus and J_i are reduced strain invariants, defined as $J_1 = I_1 I_3^{-\frac{1}{3}}$, $J_3 = I_3^{\frac{1}{2}}$, and $J_4 = I_4 I_3^{-\frac{1}{3}}$ where

$$I_3 = \det \mathbf{C} = \lambda_1^2 \lambda_2^2 \lambda_3^2 \quad (3.20)$$

For an incompressible material, $I_3 = 1$. As will be demonstrated further in this chapter, the volumetric term in Eq. (3.17) would vanish as $\kappa_s \rightarrow \infty$ and so compressibility effects would indeed become negligible when κ_s is sufficiently large. It is appropriate at this stage to provide a word of caution about this limit. Although the volumetric term vanishes as $\kappa_s \rightarrow \infty$ because $J_3 \rightarrow 1$, setting $J_3 = 1$ in Eq. (3.17) would lead to erroneous stress calculations due to differences in the derivatives of the invariants I_i and J_i with respect to E_{ij} ; to prevent this from happening, additional analysis would be required, but this is outside the scope of the present work.

For this slightly-compressible material, volumetric changes are accounted for by the second term on the right-hand side of Eq. (3.17), which eliminates the need for the Lagrange multiplier term in Eq. (3.1). Setting $p = 0$ in Eq. (3.1), leads to

$$S_{ij} = \frac{\partial W}{\partial E_{ij}}, \quad i, j = 1, 2, 3 \quad (3.21)$$

Solution convergence at zero strain

Further modification of the passive material model is necessary to achieve convergence of the simulations at zero strain. As described below, the adopted finite element procedure for stress calculations requires inversion of a matrix, which would cause the simulations to diverge when the strain is zero. This would happen at the first time step in dynamic simulations or the first load step in static simulations, if the undeformed state were taken as the initial condition. One approach for resolving this problem is to apply an initial condition for strain (which, in ADINA, would be introduced as an initial displacement), which would prevent the model from calculating a zero stress. For a simplified geometry, such as a cube, the appropriate initial displacements can be easily defined in all three directions. However, when performing simulations using a more complex geometry, such as the LV, an appropriate choice of initial conditions in all three directions is not so easy to make. For this reason, an alternative approach, in which additional terms are added to the passive material model, was used in the present work and is described below.

The tangent constitutive tensor \mathbf{D} is defined as

$$\begin{aligned}
 D_{ijkl} = & \left(\frac{\partial^2 W_p}{\partial J_1 \partial J_1} \frac{\partial J_1}{\partial E_{ij}} + \frac{\partial^2 W_p}{\partial J_1 \partial J_4} \frac{\partial J_4}{\partial E_{ij}} \right) \frac{\partial J_1}{\partial E_{kl}} \\
 & + \left(\frac{\partial^2 W_p}{\partial J_1 \partial J_4} \frac{\partial J_1}{\partial E_{ij}} + \frac{\partial^2 W_p}{\partial J_4 \partial J_4} \frac{\partial J_4}{\partial E_{ij}} \right) \frac{\partial J_4}{\partial E_{kl}} + \frac{\partial^2 W_p}{\partial J_3 \partial J_3} \frac{\partial J_3}{\partial E_{ij}} \frac{\partial J_3}{\partial E_{kl}} \\
 & + \frac{\partial W_p}{\partial J_1} \frac{\partial^2 J_1}{\partial E_{ij} \partial E_{kl}} + \frac{\partial W_p}{\partial J_3} \frac{\partial^2 J_3}{\partial E_{ij} \partial E_{kl}} + \frac{\partial W_p}{\partial J_4} \frac{\partial^2 J_4}{\partial E_{ij} \partial E_{kl}}
 \end{aligned} \tag{3.22}$$

Because of symmetry (indices 12 and 21, 13 and 31, and 23 and 32 are equal), \mathbf{D} can be represented as a 6×6 matrix. As will be shown in the following, at zero strain, some

of the diagonal terms of \mathbf{D} , namely, D_{1212} , D_{1313} , D_{2323} , are equal to zero, which causes the simulations to diverge during matrix inversion.

For the passive material model at zero strain, it can be shown that $\partial J_1 / \partial E_{kl} = \partial J_3 / \partial E_{kl} = \partial J_4 / \partial E_{kl} = 0$ for $kl = 12, 13, 23$, which makes the first three terms in Eq. (3.22) equal to zero for $kl = 12, 13, 23$. The second derivatives of $J_i, i = 1, 3, 4$ with respect to E_{ij} at zero strain are

$$\frac{\partial^2 J_1}{\partial E_{ij} \partial E_{kl}} = -2, \quad \frac{\partial^2 J_3}{\partial E_{ij} \partial E_{kl}} = -1, \quad \frac{\partial^2 J_4}{\partial E_{ij} \partial E_{kl}} = -2, \quad ij = kl = 12, 13, 23 \quad (3.23)$$

In view of these non-zero values, it is evident that, for D_{1212} , D_{1313} , and D_{2323} to be non-zero at zero strain, at least one of the last three terms in Eq. (3.22) must be non-zero, which means that at least one of the derivatives of W_p with respect to $J_i, i = 1, 3, 4$ must be non-zero. However, this is not the case as shown in the following. At zero strain, $\lambda_1 = \lambda_2 = \lambda_3 = 1$, $I_1 = 3$, $I_3 = 1$, $I_4 = 1$, $J_1 = 3$, $J_3 = 1$, and $J_4 = 1$. Consequently,

$$\begin{aligned} \frac{\partial W_p}{\partial J_1} &= C_1 e^Q [2C_2 (J_1 - 3) + C_3 (J_4 - 1)] = 0 \\ \frac{\partial W_p}{\partial J_3} &= \kappa_s (J_3 - 1) = 0 \\ \frac{\partial W_p}{\partial J_4} &= C_1 e^Q [C_3 (J_1 - 3) + 2C_4 (J_4 - 1)] = 0 \end{aligned} \quad (3.24)$$

By adding the terms $C_5 (J_1 - 3) + C_6 (J_4 - 1)$ to Q , the derivatives of W_p with respect to $J_i, i = 1, 3, 4$ at zero strain become

$$\begin{aligned}
\frac{\partial W_p}{\partial J_1} &= C_1 e^Q [2C_2 (J_1 - 3) + C_3 (J_4 - 1) + C_5] = C_1 C_5 \\
\frac{\partial W_p}{\partial J_3} &= \kappa_s (J_3 - 1) = 0 \\
\frac{\partial W_p}{\partial J_4} &= C_1 e^Q [C_3 (J_1 - 3) + 2C_4 (J_4 - 1) + C_6] = C_1 C_6
\end{aligned} \tag{3.25}$$

It is clear from Eq. (3.25) that model convergence should be achievable if either C_5 or C_6 have non-zero values in the model.

As explained above, the addition of two terms in the expression for the exponent Q , which are first order in J_1 and J_4 , would guarantee model convergence at zero strain, provided that at least one of the additional parameter values C_5 and C_6 is different from zero. The modified exponent can be written as

$$Q = C_2 (J_1 - 3)^2 + C_3 (J_1 - 3) (J_4 - 1) + C_4 (J_4 - 1)^2 + C_5 (J_1 - 3) + C_6 (J_4 - 1) \tag{3.26}$$

Passive material model constraints

When determining values for the various parameters for the passive and active material models, it becomes necessary to impose constraints on the signs and/or magnitudes of these parameters for physical or numerical reasons. The constraints defined in this section and the next one will be applied to the calculation of these material parameter values.

A natural way to ensure that the internal strain energy grows with increasing stretches is to require that W is a strictly convex function of the invariants J_1 and J_4 . Enforcement of the strict convexity of W also has a numerical benefit because it facilitates the convergence of the finite element computations. Although forcing W to be a strictly

convex function does not guarantee convergence, if W were not strictly convex, the simulations would diverge. For W_p to be strictly convex, sufficient but not necessary criteria are that $C_1 > 0$ and that e^Q be strictly convex. It is sufficient to enforce that Q be convex, because e^Q will also be convex if Q is convex. For Q to be convex, the second derivative of Q with respect to J_i must be positive definite (Bertsekas (1999)). This derivative can be written in matrix form as

$$\left[\frac{\partial^2 Q}{\partial J_i \partial J_j} \right]_{i,j=1,4} = \begin{bmatrix} 2C_2 & C_3 \\ C_3 & 2C_4 \end{bmatrix} \quad (3.27)$$

For the matrix in Eq. (3.27) to be positive definite, the principal minors must be strictly positive, which leads to the constraints $C_2 > 0$ and $4C_2C_4 - C_3^2 > 0$. Because optimization methods are used to estimate the model parameters and these methods only deal with inequality constraints instead of strict inequality constraints (Bertsekas (1999); Nocedal and Wright (1999)), these two strict positivity conditions must be restated as inequalities. In particular, the second constraint will be specified as $-4C_2C_4 + C_3^2 + \varepsilon_1 \leq 0$, where ε_1 is a small positive number.

Because of the addition of the two terms containing the parameters C_5 and C_6 in the expression for Q , stresses may no longer be equal to zero at zero strain ($\lambda_1 = \lambda_2 = \lambda_3 = 1$). To determine whether constraints on C_5 and/or C_6 would be required to ensure zero stress at zero strain, we will calculate the passive second Piola-Kirchhoff stresses in the x_1 and x_2 directions. Expanding the derivatives in Eq. (3.21), the passive parts of these stresses are defined as

$$S_{11} = \frac{\partial W_p}{\partial J_1} \frac{\partial J_1}{\partial E_{11}} + \frac{\partial W_p}{\partial J_3} \frac{\partial J_3}{\partial E_{11}} + \frac{\partial W_p}{\partial J_4} \frac{\partial J_4}{\partial E_{11}} \quad (3.28a)$$

$$S_{22} = \frac{\partial W_p}{\partial J_1} \frac{\partial J_1}{\partial E_{22}} + \frac{\partial W_p}{\partial J_3} \frac{\partial J_3}{\partial E_{22}} + \frac{\partial W_p}{\partial J_4} \frac{\partial J_4}{\partial E_{22}} \quad (3.28b)$$

The derivatives of W_p with respect to J_1 , J_3 , and J_4 are given in Eq. (3.25). Assuming that the muscle fibres are aligned with the x_1 axis, one may calculate the derivatives of J_1 and J_4 with respect to E_{11} and E_{22} as

$$\frac{\partial J_i}{\partial E_{jj}} = \frac{\partial J_i}{\partial I_1} \frac{\partial I_1}{\partial E_{jj}} + \frac{\partial J_i}{\partial I_3} \frac{\partial I_3}{\partial E_{jj}} = I_3^{-\frac{1}{3}} \left(\frac{\partial I_i}{\partial E_{jj}} - \frac{1}{3} \frac{I_i}{I_3} \frac{\partial I_3}{\partial E_{jj}} \right), i = 1, 4, j = 1, 2 \quad (3.29)$$

It can be shown that the derivatives of I_1 , I_3 , and I_4 with respect to E_{11} and E_{22} are

$$\begin{aligned} \frac{\partial I_1}{\partial E_{11}} &= 2, \quad \frac{\partial I_1}{\partial E_{22}} = 2 \\ \frac{\partial I_3}{\partial E_{11}} &= 2\lambda_2^2\lambda_3^2, \quad \frac{\partial I_3}{\partial E_{22}} = 2\lambda_3^2\lambda_1^2 \\ \frac{\partial I_4}{\partial E_{11}} &= 2, \quad \frac{\partial I_4}{\partial E_{22}} = 0 \end{aligned} \quad (3.30)$$

Substituting Eqs. (3.30) into Eq. (3.29) leads to

$$\begin{aligned} \frac{\partial J_1}{\partial E_{11}} &= I_3^{-\frac{1}{3}} \left(2 - \frac{2}{3} \frac{I_1}{I_3} \lambda_2^2 \lambda_3^2 \right), \quad \frac{\partial J_1}{\partial E_{22}} = I_3^{-\frac{1}{3}} \left(2 - \frac{2}{3} \frac{I_1}{I_3} \lambda_3^2 \lambda_1^2 \right) \\ \frac{\partial J_4}{\partial E_{11}} &= \frac{4}{3} I_3^{-\frac{1}{3}}, \quad \frac{\partial J_4}{\partial E_{22}} = -\frac{2}{3} I_3^{-\frac{1}{3}} \end{aligned} \quad (3.31)$$

Lastly, the derivatives of J_3 with respect to E_{11} and E_{22} can be shown to be

$$\frac{\partial J_3}{\partial E_{11}} = \lambda_2^2 \lambda_3^2 I_3^{-\frac{1}{2}}, \quad \frac{\partial J_3}{\partial E_{22}} = \lambda_3^2 \lambda_1^2 I_3^{-\frac{1}{2}} \quad (3.32)$$

Substituting Eqs. (3.25), (3.31), and (3.32) into Eqs. (3.28a,b) leads to

$$\begin{aligned} S_{11} = & C_1 e^Q [2C_2 (J_1 - 3) + C_3 (J_4 - 1) + C_5] \left[I_3^{-\frac{1}{3}} \left(2 - \frac{2}{3} \frac{I_1}{I_3} \lambda_2^2 \lambda_3^2 \right) \right] \\ & + \kappa_s (J_3 - 1) \left(\lambda_2^2 \lambda_3^2 I_3^{-\frac{1}{2}} \right) \end{aligned} \quad (3.33a)$$

$$\begin{aligned} & + C_1 e^Q [C_3 (J_1 - 3) + 2C_4 (J_4 - 1) + C_6] \left(\frac{4}{3} I_3^{-\frac{1}{3}} \right) \\ S_{22} = & C_1 e^Q [2C_2 (J_1 - 3) + C_3 (J_4 - 1) + C_5] \left[I_3^{-\frac{1}{3}} \left(2 - \frac{2}{3} \frac{I_1}{I_3} \lambda_3^2 \lambda_1^2 \right) \right] \\ & + \kappa_s (J_3 - 1) \left(\lambda_3^2 \lambda_1^2 I_3^{-\frac{1}{2}} \right) \end{aligned} \quad (3.33b)$$

$$+ C_1 e^Q [C_3 (J_1 - 3) + 2C_4 (J_4 - 1) + C_6] \left(-\frac{2}{3} I_3^{-\frac{1}{3}} \right)$$

At zero strain, $\lambda_1 = \lambda_2 = \lambda_3 = 1$, $I_3 = 1$, $I_1 = J_1 = 3$, $I_1 = J_4 = 1$, and $e^Q = 1$, reducing Eqs. (3.5a,b) to

$$S_{11} = \frac{4}{3} C_1 C_6 \quad (3.34a)$$

$$S_{22} = -\frac{2}{3} C_1 C_6 \quad (3.34b)$$

It is clear from Eqs. (3.34a,b) and the previously defined constraint $C_1 > 0$ that, for S_{11} and S_{22} to be zero at zero strain, $C_6 = 0$. Because only one of C_5 and C_6 needs to be different from zero in order to guarantee convergence and C_5 does not appear in Eqs. (3.34a,b), setting $C_6 = 0$ and specifying that $C_5 \neq 0$ means that the simulations will converge at zero strain while still allowing the passive stresses to be zero.

Table 3.1: Passive material parameter constraints.

Variable(s)	Constraint
C_1	$C_1 > 0$
C_2	$C_2 > 0$
C_2, C_3, C_4	$-4C_2C_4 + C_3^2 + \varepsilon_1 < 0$
C_5	$C_5 = \varepsilon_2$
C_6	$C_6 = 0$

Because C_5 was introduced to the material model to allow convergence at zero strain, its magnitude must be constrained in a way that its influence on the stress calculations is small for relatively large stretches. To achieve this objective, we will set $C_5 = \varepsilon_2$, where ε_2 is a small positive number. The value of ε_2 will be chosen during the parameter value calculations as to reduce the difference between the stresses calculated with and without C_5 to less than one percent for $\lambda_1 = \lambda_2 = 1.06$; with this choice, it is guaranteed that the effect of C_5 on the stresses will be even lower for higher stretches. A summary of all passive material parameter constraints is provided in Table 3.1.

Active material model constraints

Constraints on the active material parameter values are based on the incompressible form of the active material model, defined in Eq. (3.12), and were taken directly from the article of Lin and Yin (1998), in which they were based on plots of $W_{a,i} = \partial W_a / \partial I_i$ versus I_i for each of the seven rabbit specimens for which they took measurements. Because, for all specimens, $W_{a,1}$ increases with I_1 and $W_{a,4}$ increases with I_4 , both D_2 and D_3 must be positive. Furthermore, when examining plots of $W_{a,1}$ versus I_4 and $W_{a,4}$ versus I_1 , Lin and Yin (1998) found that in most cases $W_{a,i}$ decreases with increasing I_i . Although this trend may not necessarily be general, Lin and Yin (1998) proposed that D_1 should be

Table 3.2: Active material parameter constraints.

Variable(s)	Constraint
D_1	$D_1 < 0$
D_2	$D_2 > 0$
D_3	$D_3 > 0$
D_1, D_2, D_3	$4D_2D_3 - D_1^2 > 0$
D_4, D_5	$D_4 + D_5 > 0$

negative. Additionally, as the muscle fibres begin to contract during the active phase, a positive stress would be required at zero strain. For this reason, the sum of D_4 and D_5 must be positive. These constraints are summarized in Table 3.2. Constraints to ensure that the active material strain energy density function is strictly convex could be applied in a way similar to the one for the passive material function by calculating the second derivative of W_a with respect to the reduced strain invariants and enforcing that the matrix form of this derivative be positive definite, namely that $4D_2D_3 - D_1^2 > 0$ and $D_2 > 0$. The first constraint does not need to be enforced because it happens to be satisfied for all calculated sets of material parameter values; the second constraint is also of no consequence because it is a duplicate of one suggested by Lin and Yin (1998).

3.3 Available measurements

3.3.1 Passive stress-strain behaviour

Figure 3.1 is a stress-stretch plot showing the results of equibiaxial tensile tests performed in the fibre and cross-fibre directions on pieces of the passive LV myocardia from three rabbit (Lin and Yin (1998)) and three dog (Novak et al. (1994)) specimens. For the rabbit, measurements were extracted from Fig. 4 in the article by Lin and Yin (1998), and

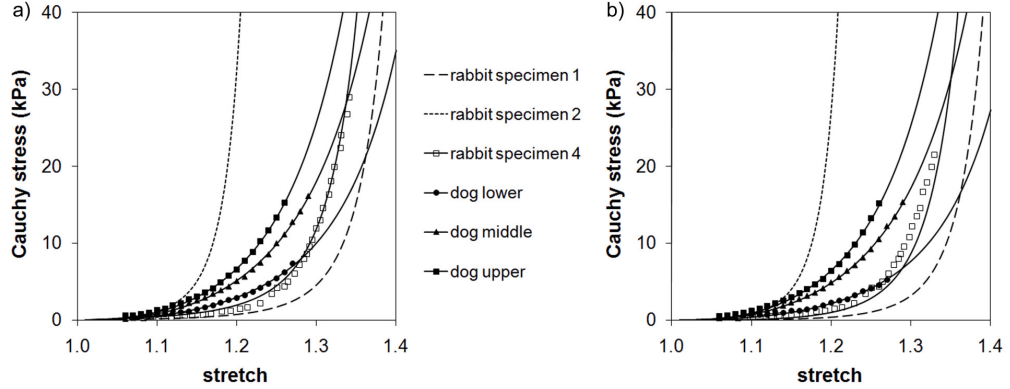


Figure 3.1: Passive LV myocardium stresses for three rabbits and three dogs in the (a) fibre and (b) cross-fibre directions. Symbols indicate experimental values from Lin and Yin (1998) for the rabbit and Novak et al. (1994) for the dog, dashed lines represent results of calculations made using material parameter values from Lin and Yin (1998), and solid lines indicate results obtained through numerical simulation, to be discussed in Sections 3.5.1 for the rabbit and 3.5.3 for the dog.

represent the only one of their seven specimens for which they published their measurements. By calculating stresses using the material model and parameter values provided by Lin and Yin (1998), it was determined that these measurements correspond to the material parameter values for specimen 4. The stress-stretch curves for rabbit specimens 1 and 2, shown in Fig. 3.1, were generated by calculating the stresses using material parameters given by Lin and Yin (1998) and represent the upper and lower bounds, respectively, of their seven rabbit specimens. The three sets of dog measurements were extracted from Figs. 1 and 2 in the article by Novak et al. (1994) for the fibre and cross-fibre directions, respectively, and represent the upper limit, the lower limit, and the middle of the range of stress-stretch curves from the middle part of the LV free wall.

As shown in Fig. 3.1, the stress-stretch curves of either species have two distinct parts, a slowly rising part at low stretches, and a steeper part at higher stretches. This

behaviour is attributed to the composite structure of the myocardium, which was discussed in the Introduction.

Whereas points in Fig. 3.1 presumably indicate actual experimental values and clearly demarcate the experimental range of stretches, the curves are approximate fits to the data and include parts computed by extrapolating the experimental ranges, although it is impossible to determine the stretch beyond which extrapolation has taken place. It is evident that extrapolated parts of all curves would be subject to additional uncertainty, which cannot be estimated but may be significantly larger than the measurement uncertainty. Moreover, all these plots represent a very small number of samples for each species, and, therefore, any observations based on these results should be treated as specific to individual specimens; thus these results have a qualitative significance rather than applying quantitatively to an entire species.

The reported range of each set of available experimental results extends between a minimum and a maximum stretch. It would have been helpful to know whether the bounds of these ranges are related to experimental limitations or reflect changes in material properties (e.g., elastic limits), but unfortunately the authors do not provide any relevant information. In contrast, any analytical model fitted to these data can be extrapolated to stretches both lower and higher than the experimental lower and upper bounds, respectively. It is obvious that, while extrapolating to lower stretches, the model must predict positive values for tensile tests. When extrapolating to higher stretches, the predictions will inevitably become devoid of physiological meaning as the model is extended to higher and higher stretches. However, when simulating heart operation, it is only necessary to

model stress-stretch behaviour within the expected stretch range. As typical of the range of strains experienced by the canine heart, measurements of stretches in an isolated LV undergoing passive filling performed by Omens et al. (1991) showed a maximum stretch of about 1.3, which is not much higher than the maximum stretches in the experiments by Novak et al. (1994); based on this observation, one may infer that, for cardiac cycle simulations, only minimal extrapolation, if any at all, may be required when the LV is at its maximum deformation. Although all specimens of a given species have qualitatively similar stress-stretch curves, the variability from one specimen to another is relatively large, particularly for the rabbit. Considering all plots in Fig. 3.1, one may note that, for a given stretch, the available stresses for all dog specimens fall well within the range of stresses for all rabbit specimens. Nevertheless, the high-stretch parts of all rabbit curves appear to have higher slopes than those of all dog curves. Although one may not exclude the possibility that steeper parts may have also been present in dog stress-stretch curves, if experiments at wider stretch ranges had been performed, the data indicate that, if one were to extrapolate the available measurements to higher stretches, the dog would likely have lower stresses in both the fibre and cross-fibre directions than the rabbit. The difference in slope between the rabbit and the dog curves, as well as the speculation that, at higher stretches, the dog stresses would be lower than the rabbit stresses are both consistent with Fig. 9 of Vetter and McCulloch (2000), which is a plot of values of passive fibre and cross-fibre stresses for various species, based on several published material models. Finally, comparison of the corresponding passive stress-stretch curves in the fibre and cross-fibre directions shows that both the rabbit and the dog myocardia exhibit stretch-dependent anisotropy. For example,

at a stretch of $\lambda = 1.15$, the ratio of fibre to cross-fibre stresses varies from 1.26 to 3.33 for the rabbit and from 1.03 to 1.18 for the dog, whereas at $\lambda = 1.25$, it varies from 1.15 to 1.65 for the rabbit and from 1.01 to 1.32 for the dog. The available information is not sufficient for one to determine conclusively whether the myocardium of one species is more anisotropic than that of the other.

3.3.2 Total stress-strain behaviour

Figure 3.2 contains plots of total stress-stretch behaviour for the rabbit LV myocardium for the same specimens presented in Fig. 3.1. These plots of total stresses show higher stresses for a given stretch than in the passive case, due to the additional active stresses caused by fibre contraction. The total stresses also show a greater degree of anisotropy than their corresponding passive values. For example, at $\lambda = 1.25$, the ratios of fibre to cross-fibre stresses for the total cases range from 1.18 to 2.70, which is wider than the range from 1.15 to 1.65 for the passive cases.

3.4 Methods

3.4.1 Numerical simulations

To validate our material model and computational procedures, we performed numerical simulations of equibiaxial tensile tests using material parameter values for rabbit specimen 4 proposed by Lin and Yin (1998), and then compared our passive and total stress-stretch results with values extracted from their Fig. 4. The equibiaxial tensile test simulations were performed using a cubic geometry, shown in Fig. 3.3, meshed using a sin-

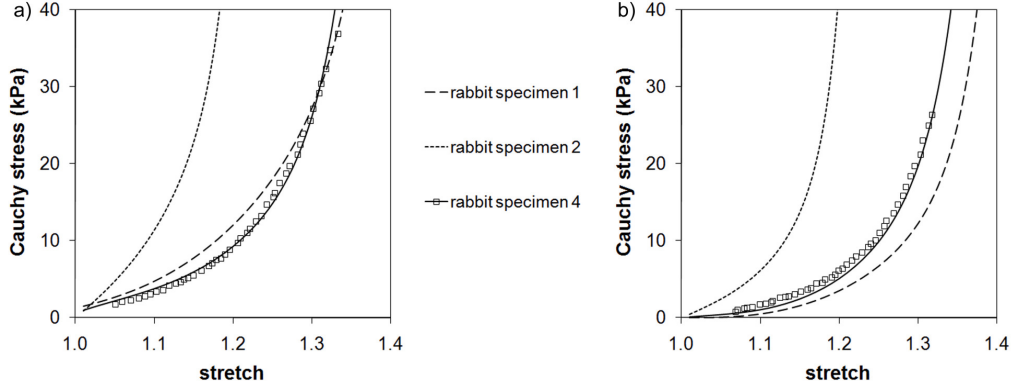


Figure 3.2: Total LV myocardium stresses for three rabbits in the (a) fibre and (b) cross-fibre directions. Symbols indicate experimental values from Lin and Yin (1998), dashed lines represent results of calculations made using material parameter values from Lin and Yin (1998), and solid lines indicate results obtained through numerical simulation, to be discussed in Section 3.5.1.

gle eight-node hexahedral element. The fibres were aligned with the x_1 direction, whereas x_2 and x_3 were cross-fibre directions. The geometry was constrained such that the surface normal to the negative x_3 axis was fixed in x_3 , the surface normal to the negative x_2 axis was fixed in x_2 , and the surface normal to the negative x_1 axis was fixed in x_1 . Equal displacements were applied to the surfaces normal to the positive x_1 and x_2 axes, corresponding to values of stretch from $\lambda_1 = \lambda_2 = 1$ to $\lambda_1 = \lambda_2 = 1.5$. The surface normal to the positive x_3 axis was free to deform according to the compressibility of the material. At each incremental displacement, the stresses were calculated using ADINA and our user-supplied material model.

The passive and active material parameter values used for these equibiaxial tensile test simulations were taken from Table 1 of Lin and Yin (1998) and are listed in Table 3.3. The passive parameter value C_1 and all of the active parameter values proposed by Lin and Yin (1998) were multiplied by a conversion factor of $98.1 \text{ kg} \cdot \text{cm}^2 / \text{g}_f \cdot \text{m} \cdot \text{s}^2$ to convert the

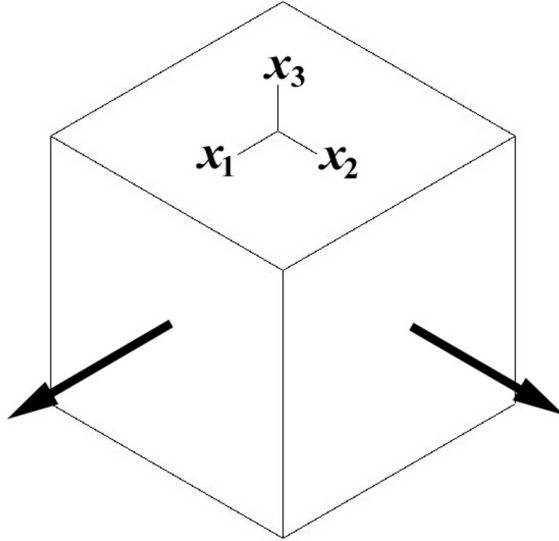


Figure 3.3: Geometry used for equibiaxial tensile test simulations.

Table 3.3: Passive and active material parameter values for rabbit specimen 4 of Lin and Yin (1998).

i	1	2	3	4	5	6
C_i (passive)	0.286 kPa	3.21	-2.60	2.01	0	0
D_i (active)	-3.80 kPa	4.01 kPa	2.45 kPa	0.933 kPa	0.301 kPa	n/a

units from g_f/cm^2 to Pa ($1 g_f = 9.81 \times 10^{-3} \text{N}$).

3.4.2 Material parameter calculations

Material parameter values for the passive and active material models were calculated using MatLab 7.4.0 (The MathWorks, Inc., Natick, MA, USA), and more specifically the “fmincon” function, which utilizes a sequential quadratic programming (SQP) method (Nocedal and Wright (1999)) to minimize a function of multiple variables. The function “fmincon” was chosen instead of the more widely used Levenberg-Marquardt method (Nocedal and Wright (1999)), because, unlike the latter, the former method allows one to

impose non-linear constraints that depend on several variables.

The passive and active material parameter values were calculated separately using the procedure described in the following. First, the measured Cauchy stresses $T_{11,m}$ and $T_{22,m}$, from equibiaxial stretching in the x_1 and x_2 directions, and their corresponding stretches were imported into MatLab. Next, initial estimates of the material parameter values were defined to calculate Cauchy stresses $T_{11,c}$ and $T_{22,c}$. In order to calculate these stresses, values of all three principal stretches are required. The stretches λ_1 and λ_2 in the fibre and cross-fibre directions are known from the imported measurements. Moreover, λ_3 can be determined as a function of κ_s by considering that, for biaxial tension with a free boundary normal to the x_3 -axis, the stress S_{33} must vanish. Although such calculation is possible, it would be cumbersome as well as unnecessary because the resulting stresses should be independent of κ_s in the weak compressibility limit. Therefore, instead of pursuing an exact procedure, we shall perform an order-of-magnitude analysis.

For a slightly compressible material, the procedure presented in Section 3.2.3 leads to the expression

$$\begin{aligned}
S_{22} = & C_1 e^Q [2C_2 (J_1 - 3) + C_3 (J_4 - 1) + C_5] \left[I_3^{-\frac{1}{3}} \left(2 - \frac{2}{3} \frac{I_1}{I_3} \lambda_1^2 \lambda_2^2 \right) \right] \\
& + \kappa_s (J_3 - 1) \left(\lambda_1^2 \lambda_2^2 I_3^{-\frac{1}{2}} \right) \\
& + C_1 e^Q [C_3 (J_1 - 3) + 2C_4 (J_4 - 1) + C_6] \left(-\frac{2}{3} I_3^{-\frac{1}{3}} \right)
\end{aligned} \tag{3.35}$$

which may be further simplified considering that $C_6 = 0$ and that for equibiaxial tension $\lambda_1 = \lambda_2$.

Under the assumption of weak compressibility, one may assume that volumetric

changes are small, so that

$$I_3 = \lambda_1^2 \lambda_2^2 \lambda_3^2 = 1 + \delta \quad (3.36)$$

where $|\delta| \ll 1$. Then, from Eq. (3.36) and the relation $\lambda_1 = \lambda_2$, one gets

$$\lambda_3 = \left(\frac{1 + \delta}{\lambda_1^4} \right)^{\frac{1}{2}} \quad (3.37)$$

Substituting Eq. (3.37) into the expressions for the derivatives of J_i with respect to E_{ij} , which are contained in the rightmost set of parentheses in each term in Eq. (3.35), leads to

$$I_3^{-\frac{1}{3}} \left(2 - \frac{2}{3} \frac{I_1}{I_3} \lambda_1^2 \lambda_2^2 \right) = (1 + \delta)^{-\frac{1}{3}} \left[\frac{4}{3} \left(1 - \frac{\lambda_1^6}{1 + \delta} \right) \right] = O(1) \quad (3.38a)$$

$$\left(\lambda_1^2 \lambda_2^2 I_3^{-\frac{1}{2}} \right) = \lambda_1^4 (1 + \delta)^{-\frac{1}{2}} = O(1) \quad (3.38b)$$

$$-\frac{2}{3} I_3^{-\frac{1}{3}} = -\frac{2}{3} (1 + \delta)^{-\frac{1}{3}} = O(1) \quad (3.38c)$$

where the notation $O()$ denotes the upper bound on the order of magnitude.

The orders of magnitude of the terms containing the invariants J_1 and J_4 are

$$J_1 - 3 = \left(2\lambda_1^2 + \frac{1 + \delta}{\lambda_1^4} \right) (1 + \delta)^{-\frac{1}{3}} - 3 = O(1) \quad (3.39a)$$

$$J_4 - 1 = \lambda_1^2 (1 + \delta)^{-\frac{1}{3}} - 1 = O(1) \quad (3.39b)$$

Substituting these orders of magnitude into Eq. (3.35) and considering that C_1 is a constant and that e^Q is bounded for stretches within the physiological limits, it is easy to

see that the three terms on the right-hand side of Eq. (3.35) are, respectively $O(1)$, $O(\kappa_s \delta)$, and $O(1)$. For the three terms in this equation to balance in orders of magnitude, it is necessary that the second term be at most of $O(1)$ which leads to

$$\delta = O\left(\frac{1}{\kappa_s}\right) \quad (3.40)$$

This relationship proves that, although at first glance it appears that the volumetric term $\frac{1}{2}\kappa_s (J_3 - 1)^2$ in Eq. (3.17) grows with increasing κ_s , it is actually of $O(1/\kappa_s)$ and therefore becomes negligible at sufficiently large κ_s , because $(J_3 - 1) = O(\delta) = O(1/\kappa_s)$. Furthermore, it is easy to show that

$$J_1 = I_1 \left[1 + O\left(\frac{1}{\kappa_s}\right) \right] \quad (3.41a)$$

$$J_4 = I_4 \left[1 + O\left(\frac{1}{\kappa_s}\right) \right] \quad (3.41b)$$

from which it follows that, in the limit as $\kappa_s \rightarrow \infty$, Eqs. (3.18) and (3.19) for the slightly compressible material model converge to Eqs. (3.11) and (3.12) for the incompressible material model. In conclusion, it is appropriate to compute the model parameters using incompressible relationships and then use the same parameters in the slightly compressible expressions, provided that κ_s is sufficiently large. The validity of this assumption for the stress calculations will be verified in Section 3.5.2, in which stresses are calculated in ADINA for various values of κ_s and compared to their corresponding incompressible stresses.

The stresses $T_{11,c}$ and $T_{22,c}$ will be calculated under the assumption of incompressibility in MatLab using Eqs. (3.5) and (3.7), as follows

$$T_{11,c} = \frac{2}{\lambda_3} \left[\begin{aligned} &\left(1 - \frac{\lambda_3^2}{\lambda_1^2}\right) C_1 e^Q [2C_2 (I_1 - 3) + C_3 (I_4 - 1) + C_5] \\ &+ C_1 e^Q [C_3 (I_1 - 3) + 2C_4 (I_4 - 1)] \end{aligned} \right] \quad (3.42a)$$

$$T_{22,c} = \frac{2}{\lambda_3} \left(1 - \frac{\lambda_3^2}{\lambda_2^2}\right) C_1 e^Q [2C_2 (I_1 - 3) + C_3 (I_4 - 1) + C_5] \quad (3.42b)$$

where $Q = C_2 (I_1 - 3)^2 + C_3 (I_1 - 3) (I_4 - 1) + C_4 (I_4 - 1)^2 + C_5 (I_1 - 3)$ and $\lambda_3 = \sqrt{1/\lambda_1^2 \lambda_2^2}$.

The next step in determining the material parameter values is to calculate the least-square difference between the calculated and measured stresses as

$$\Delta = \frac{1}{2} \left[(T_{11,c} - T_{11,m})^2 + (T_{22,c} - T_{22,m})^2 \right] \quad (3.43)$$

Lastly, optimal values for the material parameters, subject to both linear and non-linear constraints defined in Table 3.1 for the passive material parameters or Table 3.2 for the active material parameters, were computed such as to minimize Δ . For the constraints defined in Table 3.1, we have chosen $\varepsilon_1 = 0.01$ and have determined from stress calculations that $\varepsilon_2 = 0.0001$ is sufficiently small to satisfy the criteria defined in Section 3.2.3, as will be shown in Section 3.5.3.

For the passive material parameter value calculations, the three sets of stress-stretch measurements of Novak et al. (1994), which were presented in Fig. 3.1, were used for the calculations. For the active part, in the absence of measurements of canine active stresses, rabbit active stresses calculated using the material parameter values of Lin and Yin (1998) were used to approximate active canine material behaviour. A first, unsuccessful, attempt to estimate canine active material properties was made by assuming that the ratios of passive to total stresses for a given stretch were comparable for rabbits and dogs. This

ratio was calculated for each of the three rabbit specimens presented in Fig. 3.1 and used to calculate total stresses for each of the three dog cases in Fig. 3.1. The active stresses were then calculated as the difference between the total and passive stresses. The resulting active stress-stretch curves were clearly unacceptable because, in a range of large but physiologically plausible stretches, they predicted active stresses that decreased with increasing stretch. This non-physical behaviour is also found when examining the rabbit material models, but is not observed in the corresponding experimental results. For each rabbit case, there exists a critical stretch λ_{cr} above which the active stress begins to decrease with increasing stretch. This behaviour is due to the form of the material model and does not correspond to any physical phenomenon. For the three rabbit specimens in Fig. 3.2, λ_{cr} is approximately 1.5 for specimens 1 and 4 and 1.3 for specimen 2. In all three cases, λ_{cr} is greater than the maximum acceptable stretch for the passive part, which implies that this non-physical behaviour is not present in the material model within a physiologically relevant range. However, because the canine stress-stretch curves are less steep than those for the rabbits, when this approach is applied to the dog cases, it causes λ_{cr} to shift towards lower values of stretch, which are within the physiological range for the dog. Consequently, this method of scaling factors was deemed to be unsuitable for predicting active canine LV myocardium stresses.

To avoid the limitation of the scaling ratios, we propose an alternative approach, which uses a fraction of the rabbit active stress-stretch values directly, along with the passive canine stress-stretch values, to approximate the total canine stress-stretch behaviour. Considering that no total canine stress-stretch measurements are currently available, this

approximation may be an acceptable rough choice, particularly in view of the fact that there is a large variation of total stress-stretch behaviour from dog to dog. These active stresses are calculated as the difference between the total stresses and the passive stresses found in ADINA using the appropriate material parameter values. The active Cauchy stresses for the dog were then calculated using the following relation

$$T_{ij,a(\text{dog})} = \chi T_{ij,a(\text{rabbit})} \quad (3.44)$$

where χ is the fraction of the active rabbit stress that is added to the passive dog stress. Using values of $\chi = 0.5, 1.0,$ and $1.5,$ active stresses were calculated for the dog. These stresses were then imported into MatLab to calculate the active material parameter values.

3.5 Results

3.5.1 Material model validation

Equibiaxial tensile test simulations for the passive and total material models for rabbit specimen 4 were performed in ADINA. The resulting stresses for the passive and total material models are plotted in Figs. 3.1 and 3.2, respectively, as functions of stretches, and show very good agreement with the measurements, thus validating our material model implementation and computational procedure. The differences between the computed and measured values that have been plotted in these two figures mostly reproduce existing differences between measured values reported by Lin and Yin (1998) in their Fig. 4 and predictions of their model as reported in their Table 1, and may only to a much lesser degree be caused by approximations introduced by the present procedure.

Although the stresses plotted in Figs. 3.1 and 3.2 could have been calculated directly, it is important for our future work to obtain them through numerical simulations in ADINA. Without using ADINA or a similar finite element code, the issues that led to the implementation of the modifications and constraints to our material model and parameter values would not have been evident, potentially leading to the calculation of material parameter values that would cause numerical simulations of heart operation using this material model to diverge.

3.5.2 Adjustment of material compressibility

An appropriate value of the bulk modulus κ_s was determined by comparing the total stresses for specimen 4 of Lin and Yin calculated in ADINA for various values of κ_s to incompressible ones calculated using MatLab. Simulations were performed for values of κ_s from 1×10^5 to 1×10^9 kPa in multiples of 10. For each κ_s , the value of λ_3 when $\lambda_1 = \lambda_2 = 1.33$ was used to determine $I_3 - 1$, which should approach zero as $\kappa_s \rightarrow \infty$. Additionally, the slightly compressible Cauchy stresses $T_{11,sc}$ and $T_{22,sc}$ taken from the simulation results for the same stretches, were compared to their incompressible values of $T_{11,inc} = 40.679$ kPa and $T_{22,inc} = 32.355$ kPa. Based on the results of these comparisons, presented in Table 3.4, a value of $\kappa_s = 1 \times 10^7$ kPa was chosen, as this is the smallest value of κ_s for which the stresses calculated using the slightly compressible model in ADINA are approximately equal to those calculated using the incompressible model. Any further increase in κ_s increases the stiffness of the solid, which could lead to convergence problems in the simulations, without having any significant impact on the stress calculations. This value of κ_s is the one that has been used to generate all plots presented in this chapter. The fact

Table 3.4: Calculation results to determine appropriate value of material bulk modulus.

κ_s [kPa]	λ_3	I_3-1	T_{11} [kPa]	T_{22} [kPa]	ΔT_{11} [kPa]	ΔT_{22} [kPa]
1×10^5	0.56546	4.9×10^{-4}	40.597	32.284	0.082	0.071
1×10^6	0.56534	4.9×10^{-5}	40.672	32.348	0.008	0.007
1×10^7	0.56532	4.9×10^{-6}	40.679	32.354	0.000	0.001
1×10^8	0.56532	4.9×10^{-7}	40.680	32.355	-0.001	0.000
1×10^9	0.56532	4.9×10^{-8}	40.680	32.355	-0.001	0.000

Table 3.5: Material parameter values for passive canine LV myocardium material model.

Parameter	Lower	Middle	Upper
C_1 (kPa)	2.206	5.399	5.275
C_2	0.490	0.571	0.826
C_3	0.231	0.0373	-0.0554
C_4	0.0323	0.00498	0.0391
C_5	0.0001	0.0001	0.0001
C_6	0	0	0

that stresses using the slightly compressible material model were found to be approximately equal to stresses calculated using the incompressible material model validates our procedure to use incompressible expressions for calculating the model parameters.

3.5.3 Passive material parameter calculations

Passive canine LV myocardium material parameter values (C_i in Eqs. (3.17) and (3.26) have been calculated using MatLab for the three sets of canine stress-stretch values presented in Fig. 3.1, which will be referred to as “lower”, “middle”, and “upper” to denote their relative stress magnitudes. The results of these calculations are presented in Table 3.5. Using these parameter values, equibiaxial tensile test simulations were performed in ADINA. The resulting stress-stretch values have been plotted in Fig. 3.1.

The current computational results are in excellent agreement with the measurements, which demonstrates that the calculations of material parameter values were per-

formed successfully. The three sets of material parameter values in Table 3.5 will be used in our passive LV filling simulations described in Chapter 4 to determine which set leads to results that most closely match previous experimental values.

For the lower set of material parameter values, the difference between the magnitudes of the Cauchy stresses calculated using the incompressible material model with $C_5 = 0$ or $C_5 = 0.0001$ are 0.3%, 0.08%, and 0.02% for T_{11} , and 1.7%, 0.04%, and 0.02% for T_{22} at $\lambda_1 = \lambda_2 = 1.01, 1.06,$ and $1.3,$ respectively. For these same three values of λ_1 and λ_2 , the differences in the magnitudes of the Cauchy stresses for the medium set of material parameter values are 1.5%, 0.2%, and 0.02% for T_{11} , and 4.8%, 0.2%, and 0.02% for T_{22} . Lastly, for the upper set of material parameter values at the same three stretches, the differences in the magnitudes of the Cauchy stresses are 0.4%, 0.1%, and 0.02% for T_{11} , and 12%, 0.2%, and 0.02% for T_{22} . For all three sets of material parameter values, the difference for the two values of C_5 is much less than 1% at $\lambda_1 = \lambda_2 = 1.06$ and decreases for increasing values of λ_1 and λ_2 . The large difference of 12% for T_{22} for the upper material parameter values at $\lambda_1 = \lambda_2 = 1.01$ should not be interpreted as a significant difference in the actual magnitude of the stresses, because, for this case, T_{22} is relatively small and this difference corresponds to a difference in magnitude of 6×10^{-5} kPa.

3.5.4 Active material parameter calculations

Active canine LV myocardium stresses for use with the lower passive canine stresses were approximated from rabbit values from specimen 1 of Lin and Yin (1998) using Eq. (3.44). Specimen 1 was chosen because comparisons of computed passive canine and rabbit stresses show that rabbit specimen 1 is closest to the lower canine case for large values

Table 3.6: Material parameter values for active canine LV myocardium material model.

Parameter	$\chi = 0.5$	$\chi = 1.0$	$\chi = 1.5$
D_1 (kPa)	-0.172	-0.352	-0.518
D_2 (kPa)	1.237	2.476	3.711
D_3 (kPa)	1.327	2.660	3.983
D_4 (kPa)	0.0115	0.0251	0.0356
D_5 (kPa)	0.317	0.632	0.951

of stress. The lower passive canine stresses were chosen to illustrate this method, but the method is equally valid for other cases. Using these approximated active canine LV myocardium stresses, active material parameter values (D_i in Eq. (3.19)) were calculated in MatLab for $\chi = 0.5, 1.0,$ and 1.5 . The results of these calculations are presented in Table 3.6. Using these active canine material parameter values, equibiaxial tensile test simulations were performed in ADINA. The results of these simulations show excellent agreement with the active rabbit stress values, as can be seen in Fig. 3.4. Each set of active stresses can be added to the canine LV myocardium passive stresses representing the lower case in Fig. 3.1 to give total canine LV myocardium stresses. These total stresses are plotted in Fig. 3.5, along with the passive and total stresses for rabbit specimen 1 from Lin and Yin (1998), which were used to calculate the active part of the canine stresses.

Although the active and total stresses for the canine LV myocardium presented in Figs 3.4 and 3.5 are approximations, they are based on realistic assumptions and measurements available in the literature. The optimal value of χ to achieve physiologically sound results will be determined as part of the cardiac cycle simulations, presented in Chapter 5.

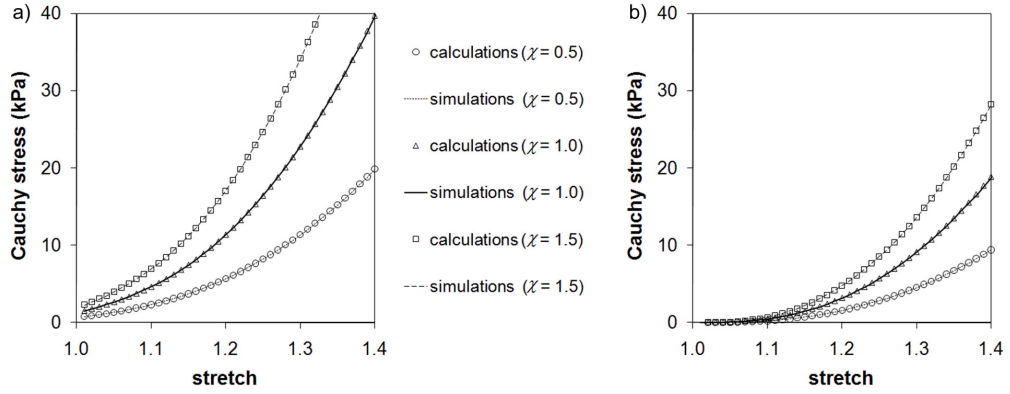


Figure 3.4: Calculated and simulated canine active stresses in the fibre (a) and cross-fibre (b) directions.

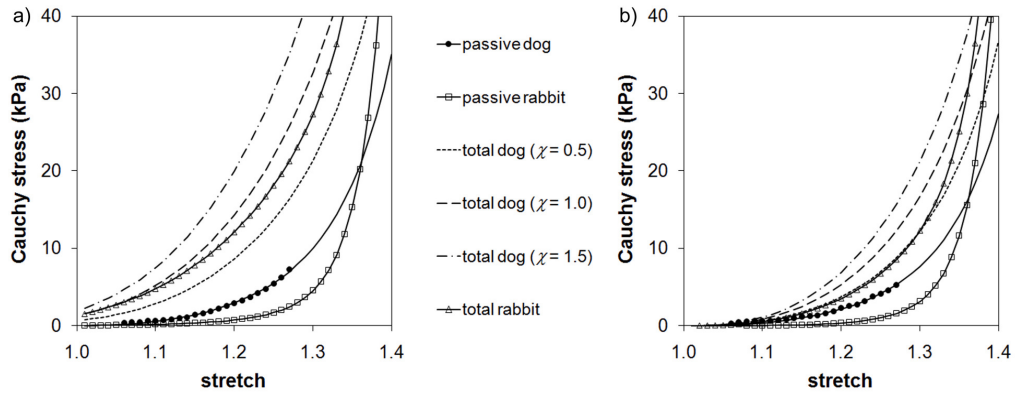


Figure 3.5: Passive and total stresses for the canine and rabbit LV myocardia in the fibre (a) and cross-fibre (b) directions. Canine passive stresses correspond to the lower case in Fig. 3.1, and rabbit passive and total stresses correspond to specimen 1 in Figs. 3.1 and 3.2, respectively. The solid symbols indicate experimental values from Novak et al. (1994), while the hollow symbols were added to distinguish between the passive and total rabbit curves. All lines represent computational results obtained from equibiaxial tensile test simulations performed in ADINA.

3.6 Discussion

The present approach for modeling the passive material behaviour of canine myocardium has been proved valid to the extent that it can be tested versus available experimental results. Reconstructed stresses, using our calculated material parameter values for the passive canine LV myocardium, show excellent agreement with previous measurements. Although some parameter values were constrained to prevent numerical problems, no significant discrepancies were found between the computed and experimental results, which implies that these constraints did not have any adverse effect on the model fit. Because some of these constraints were not enforced when the parameter values were fit to their data by the original authors, some previously published material parameter values are not suitable for numerical simulations, even though they may fit the data well (Sun and Sacks (2005)). In fact, we have confirmed that this is the case for several of the sets of Lin and Yin (1998) passive parameter values.

The present transversely isotropic model only partially represents the LV myocardium material, which is fully orthotropic (LeGrice et al. (1995)). Unfortunately, orthotropy cannot be accounted for in our procedure due to the lack of published measurements of material properties in both non-fibre directions. In the event that fully-orthotropic stress-stretch measurements became available, the present passive transversely isotropic material model could be extended to a fully orthotropic one through the introduction of additional terms in the strain energy density function containing new strain invariants I_6 and I_7 , defined as

$$I_6 = \mathbf{M}^T \mathbf{C} \mathbf{M} \quad (3.45)$$

$$I_7 = \mathbf{M}^T \mathbf{C}^2 \mathbf{M} \quad (3.46)$$

where \mathbf{M} is a unit vector containing the sheet direction (Criscione et al. (2002)). Moreover, a more complete model could also include the invariants I_2 and I_5 which were disregarded in the present model. Additionally, results of shear tests should be utilized along with the results of tensile tests to give a more complete representation of the deformations that would be experienced by the LV. However, a constitutive model that incorporates all of these features would still only represent the stress-stretch behaviour of pieces of an excised LV myocardium and would not necessarily be indicative of the stress-stretch behaviour of an intact *in vivo* LV myocardium.

For the active part of the canine material model, because no measurements of active canine LV myocardium stress-stretch behaviour have been published, we have made use of the only available information, namely stress-stretch measurements for the rabbit LV myocardium. Although this approximation introduces additional uncertainty, it allows us to proceed with our main objective, which is to simulate numerically the operation of the canine LV. The passive material stress-stretch curve for the chosen rabbit specimen matches roughly the corresponding curve for the chosen dog specimen in range of values, but has a steeper slope at large stretches. An attempt to use the rabbit passive-to-total stress ratio for estimating the total canine stress proved unsuccessful, because it resulted in total canine stresses that contradicted the expected stress-stretch behaviour. Instead, we used a different approach, which qualitatively conforms to the expectation that, as the stretch

increases within the physiological range, the active stress would increase. In the rabbit, it was found that, as stretch increases, so too does the contribution of the passive part to the total. Therefore, although there is no experimental basis by which we can validate the estimated active canine material behaviour, the deviation of the estimated total material stress-stretch behaviour from the actual one is expected to decrease with increasing stretch. As an additional attempt to bring our ongoing simulations of the canine LV cardiac cycle closer to the physiological range, we plan to adjust the active material parameter values such as to approximately reproduce measurements of stroke volume for a range of physiological pressures. This could, for example, be achieved by adjusting the value of the parameter χ . As already mentioned in previous sections, in the event that active canine stress-stretch measurements become available in the future, it should be a straightforward exercise to recalculate active material parameters using these more appropriate data.

3.7 Conclusions

A transversely isotropic material model, which was originally proposed for the rabbit LV myocardium, has been adapted for use with a canine LV myocardium. This material model has been modified from a form fitted to measurements to one that is suitable for use in finite element simulations. Additional terms have been added to the model to guarantee convergence at zero stretch and positive tensile stresses for small stretches. Before calculating material parameter values for the passive and active parts of the material model, several constraints on the signs and magnitudes of the parameters were applied. In particular, constraints have been added to ensure that the passive and active parts of the

strain energy density function were strictly convex, which aids in the convergence of our numerical simulations. Material parameter values for the passive canine LV myocardium have been calculated from existing canine stress-stretch measurements. Because no measurements relevant to an active canine LV myocardium are available, parameter values for this case have been estimated from active rabbit myocardium stress-stretch measurements. In both cases, excellent agreement was found between the stresses calculated with the material model and those used to calculate the parameter values.

Chapter 4

Inflation of the passive left ventricle

4.1 Introduction

Numerical simulations of the mechanics of the heart may be classified in three general categories, solid-only, fluid-only, and fluid-structure interaction (FSI). Solid-only simulations compute the deformations of the walls of one or more chambers of the heart by specifying boundary conditions for the pressure fields on their inner surfaces. Fluid-only simulations compute the flow of blood through one or more chambers of the heart by specifying wall motion, which is usually based on magnetic resonance imaging (MRI) data. In contrast, FSI simulations compute both the solid wall motion and the blood flow using coupled models of all related components. All methods used so far rely heavily on drastic simplifications and *ad hoc* assumptions, because much of the required information is

unavailable or of uncertain applicability to each particular approach. Whereas solid-only or fluid-only studies are capable of reproducing realistic details of either the heart wall motion or the blood flow, they fail to simulate the interaction between the two and so are missing an essential aspect of heart mechanics. The ultimate goal of the present study is to develop a complete model of heart mechanics, including physiological models of the heart wall tissue and the blood as well as their interaction. As it is clear that this is an extremely challenging and multi-faceted goal and cannot be accomplished all at once, we address particular elements one at a time. The present chapter is an intermediate step of this process.

A complete model of the heart requires suitable fluid and solid geometries, including muscle fibre orientations, material models for blood and the heart wall, boundary conditions to couple the heart with the rest of the cardiovascular system, and initial conditions. To avoid the complexity of simulating the mechanics of the entire heart, the present study is focused on the left ventricle (LV), which is the chamber that has received the most attention in past literature. Sufficiently accurate patient-specific LV geometries can be extracted from MRI or computed tomography (CT) images, or direct measurements. To be usable in simulations, they would need to be complemented by muscle fibre orientations, myocardium material properties, and inflow and outflow conditions specific to that particular LV, which are difficult or impossible to obtain. In the absence of some or all of this specific information, estimates of the missing properties would have to be devised based on a variety of sources in the literature. Due to the large variability of many parameters from one individual to the next, it is possible that, for a single specimen, values of parameters

obtained from the literature are incompatible with other values specific to the same specimen. For this reason, it seems preferable to use average or typical values of all parameters, rather than mixing values from different individual specimens. In the present study, we have defined our reference geometry such that it is representative of an average excised canine LV. A canine LV was chosen rather than a human LV or one of another mammal, because of the wealth of experimental and computational studies on canine LVs found in the literature.

The LV wall comprises three layers, from its inner to its outer surface: the endocardium, the myocardium, and the epicardium. The inner- and outer-most layers are thin and are generally neglected in defining a material model for the LV wall. The myocardium is relatively thick and contains muscle fibres, which are surrounded by an extracellular matrix. In Chapter 3, we defined a constitutive equation for the myocardium, which models the material as being transversely isotropic with properties that differ in the fibre and cross-fibre directions. The material model consists of a passive part, which represents the behaviour of the tissue when the muscle fibres are fully relaxed, and an active part, which represents the additional stresses added to the passive stresses when the muscle fibres are fully contracted. To model the contraction and relaxation of the muscle fibres in our simulations of the cardiac cycle, we introduce a suitable temporal variation of the active material properties.

Obviously, the LV does not operate in isolation, but is coupled to upstream and downstream components of the cardiovascular system. Simulating the entire cardiovascular system physiologically is beyond our scope. Instead, our objective is to simulate the

effects of this system on LV mechanics by imposing time-dependent pressure waveforms as boundary conditions at the inlet and the outlet of our LV geometry during times when the corresponding valves are open; the prescribed pressure waveforms are derived from *in vivo* measurements. Other authors have used a different type of boundary conditions, by coupling their LV model at the inflow and outflow boundaries to lumped-parameter models representing other components of the cardiovascular system (Watanabe et al. (2004)).

Lastly, because the heart is in continuous operation, in order to start the numerical simulation of the cardiac cycle, one must specify initial conditions, including an appropriate initial geometry and an initial stress distribution. Although MRI or CT images can be used to define the geometry, stresses are extremely difficult to measure, especially *in vivo*, and a complete description of the stress distribution in the entire LV is far beyond current capabilities. It may be argued that, if the numerical approach were well set, the effect of initial conditions would probably disappear following a number of cycles that is sufficient for a periodic state to be attained. This argument is not supported by any evidence for the case of interest; besides, numerical simulations with FSI take an extremely long time, as shown in Appendix A, which makes it impractical to compute a large number of cycles or conduct comparative simulations with different initial conditions. To increase the rate of convergence towards a steady state, one should define initial conditions which are as physiological as possible, and at the least do not contradict known facts about the stress state of the myocardium. If a zero-stress state of the myocardium existed during the cycle, that would have been the best choice; however, the LV is always under stress and even an excised and otherwise unloaded LV contains some residual stresses (Costa et al. (1997)).

The next best choice would be a state at which the muscle fibres are fully relaxed and only passive stresses are present, so that active stresses do not need to be accounted for. The muscle fibres complete their relaxation during the early filling phase of diastole and remain fully relaxed until systole begins. Therefore, any state during the latter part of diastole could be used as an initial state for cardiac cycle simulations. We have chosen end diastole as our starting state because it occurs at a clearly defined instant during the cardiac cycle, which makes it easier to extract useful information from previous publications. The problem now reduces to determining a geometry and a stress distribution at end diastole that are physiologically plausible.

To calculate an end-diastolic geometry and stress distribution, we statically inflated a reference geometry to an end-diastolic pressure following an approach that corresponds to an experimental procedure in which an excised LV is inflated by a static pressure load, applied either directly to the inner walls of the ventricle cavity or to an incoming fluid. Although this process is non-physiological, it is deemed to be representative of the latter part of diastole (McCulloch and Omens (1991)). A number of experimental studies (McCulloch et al. (1987); McCulloch et al. (1989); McCulloch et al. (1992); Omens et al. (1991)) of filling of the passive LV have been conducted on canine LVs. All of these studies used procedures similar to the one described in detail by McCulloch et al. (1987). Briefly, each dog's heart was stopped with drugs at an unspecified time during the cardiac cycle, and excised from the body. The ventricles were then isolated from the great vessels and atria. Cannulae attached to the aortic and mitral valve openings were used to mount the LV as well as provide perfusion for the coronary circulation on the aortic side and incoming

fluid (saline) on the mitral side for pressurization (McCulloch et al. (1987)). The LV was then statically loaded from an unloaded reference state by a gradually increasing pressure from the incoming fluid. These studies (McCulloch et al. (1989); McCulloch et al. (1992); Omens et al. (1991)) contained plots of changes in LV cavity volumes vs. pressure, along with plots of strains vs. volume and transmural distances for selected points (Omens et al. (1991)). Although these results are suitable for comparisons, they do not include the changes in geometry during filling or global stress and strain fields throughout the LV at end diastole, and so they are insufficient to describe fully an end-diastolic state.

In addition to experimental work, two numerical simulations of passive canine LV filling have been published: the studies by Costa et al. (1996) and by Nash and Hunter (2000). Costa et al. (1996) performed solid-only simulations of passive filling of an isolated LV. Their main LV geometry was defined as a truncated prolate ellipsoid, which is an ellipse that is rotated about its major axis, but they also considered a second, non-axisymmetric, LV geometry. These authors assumed that the myocardium was a transversely isotropic material with material properties along the muscle fibre direction that differed from those in transverse directions. The goal of the study of Costa et al. (1996) was to implement a new finite element method capable of calculating the stress-strain behavior in the LV. Nash and Hunter (2000) have simulated solid-only passive filling of both ventricles, but have only presented results for the LV. Their geometry, consisting of both ventricles truncated below their inflow and outflow tracts that contain the valves, was based on measurements of excised canine hearts (Nielsen et al. (1991)), which were arrested during some part of diastole. Nash and Hunter (2000) assumed the myocardium to be fully orthotropic with

material properties that varied in the fibre, sheet, and sheet-normal directions, where the sheet direction is contained in the same surface as the muscle fibres, and the sheet-normal direction is perpendicular to this surface. This work was a review of previous publications and illustrated the importance of anisotropy in a myocardium material model. Costa et al. (1996) plotted transmural and longitudinal variations of strains and stresses at $p = 1$ kPa at a single elevation and wall depth, respectively, whereas Nash and Hunter (2000) reported a pressure-volume plot and a plot of strains vs. volume change. Although the results presented in these studies are suitable for comparisons to the present ones, they are not sufficient for defining an end-diastolic state.

None of these previous studies (McCulloch et al. (1987); McCulloch et al. (1989); McCulloch et al. (1992); Omens et al. (1991); Costa et al. (1996); Nash and Hunter (2000)) provided details on the dimensions of their reference LV geometries. Moreover, the experimental studies did not specify the state during the cardiac cycle at which the LVs were arrested and the numerical studies did not specify the state at which the dimensions used to define the geometries were measured. The only usable information provided by these articles is the reference LV cavity volumes, which ranged from approximately 20 (Omens et al. (1991)) to 40 ml (McCulloch et al. (1989)).

Another difficulty arises when attempting to identify the conditions corresponding to an end-diastolic state in the previous studies. The range of possible canine LV end-diastolic pressures, approximated from measurements made by Ross et al. (1967), is $0.5 \text{ kPa} \leq p \leq 2 \text{ kPa}$. In the present study, we have chosen the value $p = 2$ kPa, because it matches approximately the end-diastolic measurement by Sabbah and Stein (1981), and so

it is consistent with the pressure waveform that we will use in our cardiac cycle simulations. All of the previous studies, with the exception of the one by Costa et al. (1996), inflated their LVs to pressures that exceeded 2 kPa, but none of them fully defined the dimensions and stress distributions at their final states. The only published stresses are those by Costa et al. (1996), evaluated at $p = 1$ kPa; consequently these are the only previous values that our present stress predictions can be compared with.

Following many considerations and preliminary simulations, we concluded that the most suitable reference state from which to start our simulations of the inflation of a passive LV would be one during which the muscle fibres would be fully relaxed and the residual stresses present in the myocardium would be negligible, provided of course that such a state exists approximately, as it is well known that the myocardium is never stress-free (Costa et al. (1997)). It has been suggested (McCulloch and Omens (1991)) that simulations of the inflation of a passive LV are suitable for modeling the behaviour of the myocardium during the latter part of diastole, namely from diastasis to end diastole. Diastasis is the middle phase of diastole, during which the muscle fibres are fully relaxed and both the pressure in the LV and its difference from the pressure in the left atrium are small (Sabbah and Stein (1981)). Based on small changes in wall thickness and diameter measured during diastasis (Sabbah and Stein (1981)), one may also infer that the blood flow velocity within the LV during this phase would be low. Considering these conditions, one may infer that the stresses in the myocardium during diastasis would likely be lower than those at other times during diastole. Therefore, a reference geometry defined at diastasis seems to be the most appropriate choice for a starting condition for simulations of the inflation of the

passive LV.

The primary objective of the present study was to simulate the filling of a representative, idealized, isolated, passive LV as a means of determining a physiologically plausible end-diastolic state under a specified end-diastolic pressure, which could be used as an initial condition for cardiac cycle simulations. Towards meeting this objective, we performed comparative simulations for different values of several parameters of our myocardium model, determined suitable choices of these parameters, and compared the results to those in previous studies. Our predicted end-diastolic dimensions and volume were compared to *in vivo* measurements at end diastole to verify that this state is representative of end diastole. Following this, the LV stretch and stress distributions at our end-diastolic state were determined and discussed.

4.2 Methods

4.2.1 Geometry and mesh

We generated a geometry which was approximately representative of a canine LV during diastasis by rescaling a representative end-systolic geometry (hereafter to be referred to as ESG), which was based on measurements made by Ross et al. (1967) and published by Streeter and Hanna (1973). Ross et al. used a rapid fixation technique to fix canine LVs at end systole and used simultaneous pressure measurements as a means of verifying that the state at which each LV was fixed was indeed end systole. If the state could not be determined or deviated greatly from end systole, the case was excluded from that study. Following excision of the LVs, their volumes were measured by filling the LV

cavities with water. Outer dimensions were measured directly, whereas inner dimensions were measured from a cast made by filling the LV cavities with liquid silicone rubber. Using these measurements, Streeter and Hanna approximated the inner and outer surfaces of the myocardium as truncated prolate ellipsoids whose average dimensions they provided. In the present study, we will also approximate the inner and outer surfaces of ESG as truncated prolate ellipsoids.

Figure 4.1 illustrates the geometric parameters used to define ESG as well as three geometrical landmarks that will be referred to throughout this chapter: the apex, which is the lowest point of the LV; the equatorial plane, which is the horizontal plane passing through the centre of the full ellipsoid; and the basal plane, which is the top plane that truncates the ellipsoid. Note that this truncation deviates from the one used by Streeter and Hanna (1973), who truncated their LV geometry to a curved basal surface. In our case, we truncated the ellipsoid at a height h , defined as the distance between the basal plane and the inner surface of the ellipsoid at the apex, and calculated as

$$h = (1 + f)(a - t_a) \tag{4.1}$$

where the fractional height above the equatorial plane was taken as $f = 0.5$, following the suggestion by Streeter and Hanna.

To define our reference geometry at diastasis (hereafter to be referred to as DG), we modified ESG using a two-step approach. In the first step, we increased the LV cavity volume $V_{f,0}$ at end systole by 25%, such that the new $V_{f,0}$ would be representative of diastasis. This increase was based on a previous two-dimensional simulation of LV filling

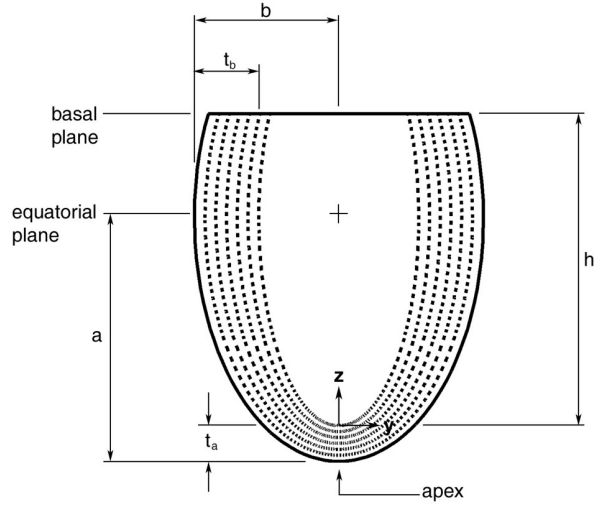


Figure 4.1: Diagram showing an isolated LV geometry; h is the total height; a is the outer semi-major axis; b is the outer semi-minor axis; t_a is the myocardium thickness at the apex; and t_b is the thickness at the equator. Dashed lines separate six layers of the myocardium, each with a distinct fibre orientation.

(Vierendeels et al. (2000)), which showed changes in cavity volume during filling. The resulting cavity volume of DG was 33.7 ml, comparable to 34.5 ml, which is the average of values reported by previous authors (Table 4.1), excluding the one by Omens et al. (1991); the latter value, calculated using information provided in the corresponding article and the one by Nash and Hunter (2000), was much lower than the others and has been treated as an outlier. In the second step, we increased by 16% the myocardium volume V_s calculated from the characteristic dimensions of ESG provided by Streeter and Hanna (1973); this was found to be necessary because there is an apparent discrepancy between the value calculated from these characteristic dimensions and the one calculated from the LV myocardial mass m_s reported by the same authors ($m_s = 99 \pm 4$ g) and the density of myocardial tissue $\rho_s = 1060$ kg/m³ (Holmes (2004)). The former was $V_s = 75.9$ ml, whereas the latter was $V_s = 93 \pm 4$ ml, which is 22.5% larger. The myocardial volume used in the present

Table 4.1: Average volumes of the LV cavity and masses of the LV myocardium.

study	$V_{f,0}$ (ml)	m_s (g)
McCulloch et al. (1989)	40	145
McCulloch et al. (1992)	36	152
Omens et al. (1991)	19.3	97.8
Costa et al. (1996)	30	n/a
Nash and Hunter (2000)	32	n/a
current simulations	33.7	93.6

simulations for DG had the intermediate value 88.3 ml, which corresponds to a myocardium mass $m_s = 93.6$ g. The masses of the myocardia used in the previous experimental studies and the present study are listed in Table 4.1. We note that the m_s values reported by McCulloch et al. (1989) and McCulloch et al. (1992) included sections of the LV inflow and outflow tracts, which are not included in our geometry.

To define DG, we made four assumptions. Firstly, we assumed that DG can be defined as a truncated prolate ellipsoid as shown in Fig. 4.1. Secondly, we assumed that $f = 0.5$, equal approximately to average measurements reported by Streeter and Hanna (1973) for both end diastole and end systole. Thirdly, we assumed that the outer and inner ellipsoids were approximately confocal, in conformity with previous observations reported by Streeter and Hanna. Lastly, to close the system of equations necessary for calculating all dimensions of DG, we assumed a value for the mid-wall eccentricity e , which is a measure of the deviation of an ellipsoidal geometry from a sphere. A mid-wall eccentricity, based on the one proposed by Rankin (1980), may be defined as

$$e = \sqrt{\frac{(2a - t_a)^2 - (2b - t_b)^2}{(2a - t_a)^2}} \quad (4.2)$$

The range of this eccentricity is between 0 (which corresponds to a sphere) and

1. Rankin (1980) measured the dimensions of several *in vivo* canine LVs and plotted the eccentricity as a function of LV cavity volume. He found a linear decrease in eccentricity during filling and a linear increase in eccentricity during ejection, with abrupt changes during the two isovolumetric phases. This implies that the LV tends toward a spherical shape during filling and towards an elongated one during ejection. For DG, we assumed $e = 0.88$ based on calculations made using results obtained from our previous simulations (Doyle et al. (2010b)) and assuming a linear variation in eccentricity between end systole and end diastole.

Using these four assumptions, we calculated the characteristic dimensions for DG to be $a = 46.92$ mm, $t_a = 6.83$ mm, $b = 27.84$ mm, $t_b = 12.42$ mm, and $h = 60.14$ mm.

Although the fibre orientation varies continuously across the myocardium wall, for the finite element analysis it is necessary to divide the wall into layers within each of which the fibre orientation is initially constant. As discussed in Section 4.3.6, a three-layer model was found to be insufficient to properly resolve the stresses through the myocardium. Therefore, we adopted a six-layer model, shown in Fig. 4.1. Each layer had a distinct fibre orientation, spanning the fibre angle range from -60° in the outer layer to $+60^\circ$ in the inner layer, with these angles defined with respect to the local circumferential direction. This range was chosen as representative of the average range found in canine LVs, as determined from plots in articles by both Streeter et al. (1969) and Nielsen et al. (1991), but different from the one measured by Omens et al. (1991) (-37° to $+98^\circ$) and used by Costa et al. (1996); as will be shown in Section 4.3.7, differences between results obtained using the two different fibre angle ranges are not significant.

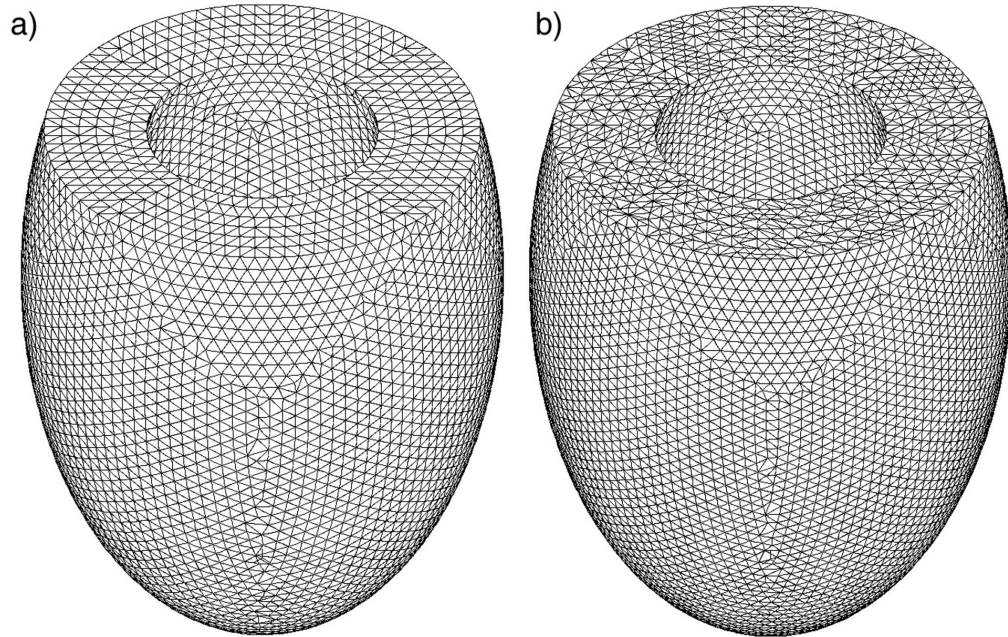


Figure 4.2: Coarse (a) and fine (b) finite element meshes.

DG was meshed on an unstructured grid using 10-node tetrahedral elements, having nodes on each vertex and at the midpoint of each edge. We have considered two meshes for DG, consisting of 130,515 elements (186,292 nodes; to be referred to as the coarse mesh) and 182,150 elements (258,880 nodes; to be referred to as the fine mesh), respectively; the two meshes are shown in Fig. 4.2.

4.2.2 Governing equations

Simulations in this study were performed using the commercial finite element software ADINA v. 8.5.2 (ADINA R & D, Inc., Watertown, MA, USA) coupled with a user-defined material model for the myocardium described in Chapter 3. These simulations were carried out on computer clusters of the High Performance Computing Virtual Laboratory

(HPCVL), which are located at Queen’s University, Kingston, ON, Canada, and are shared resources for several universities and colleges in Eastern Ontario, Canada. More details about the specific clusters used for our simulations can be found in Appendix A, along with details on RAM and CPU requirements as well as the results of a parallelization study.

The LV myocardium undergoes large displacements and large strains and has highly non-linear material behaviour, which are best simulated with the use of the Total Lagrangian form of the governing equations. Simulations were performed statically with the external load being applied over several load steps, denoted as Δs , with the solution being calculated at each load step in a manner similar to the one used in dynamic simulations with time stepping. Nodal displacements \mathbf{U} at the current load step $s + \Delta s$ were calculated using the following equation

$$\mathbf{K}(s) [\mathbf{U}(s + \Delta s) - \mathbf{U}(s)] = \mathbf{R}(s + \Delta s) - \mathbf{F}(s) \quad (4.3)$$

where \mathbf{K} is the stiffness matrix, \mathbf{R} is the external load vector, \mathbf{F} is the force vector equivalent to the element stresses, and $s = n\Delta s$, where n is the number of load steps (ADINA R & D, Inc. (2008a)). Note that in Eq. (4.3) \mathbf{R} is independent of deformation, but $\mathbf{F}(s)$ is a function of $\mathbf{U}(s)$. Further details on the derivation of Eq. (4.3) are given in Appendix B.1. Once a suitable stiffness matrix is defined, this system of equations can be solved for using full Newton iterations and the ADINA direct sparse solver (ADINA R & D, Inc. (2008a)).

To calculate $\mathbf{K}(s)$ and $\mathbf{F}(s)$, a constitutive equation for the myocardium material is required. For this study, the myocardium is modeled as a slightly compressible transversely isotropic hyperelastic material, with properties that differ in the fibre and cross-fibre

directions. It is defined by the following strain energy density function

$$W_p = C_1 (e^Q - 1) + \frac{1}{2} \kappa_s (J_3 - 1)^2 \quad (4.4)$$

where

$$Q = C_2 (J_1 - 3)^2 + C_3 (J_1 - 3) (J_4 - 1) + C_4 (J_4 - 1)^2 + C_5 (J_1 - 3) + C_6 (J_4 - 1) \quad (4.5)$$

In Eqs. (4.4) and (4.5), C_i are material parameter values, κ_s is the bulk modulus, which governs the material compressibility, and J_i are reduced invariants of Green's strain tensor \mathbf{E} . Details of this material model have been presented in Chapter 3.

From this constitutive equation, the components of the second Piola-Kirchhoff stress tensor \mathbf{S} can be calculated as follows

$$S_{ij} = \frac{\partial W}{\partial E_{ij}}, \quad i, j = 1, 2, 3 \quad (4.6)$$

For the Total Lagrangian formulation, \mathbf{K} is the sum of linear (\mathbf{K}_L) and non-linear (\mathbf{K}_{NL}) parts, which are defined as

$$\mathbf{K}_L = \int_V \mathbf{B}_L^T \mathbf{C} \mathbf{B}_L dV \quad (4.7a)$$

$$\mathbf{K}_{NL} = \int_V \mathbf{B}_{NL}^T \mathbf{S} \mathbf{B}_{NL} dV \quad (4.7b)$$

where \mathbf{B}_L and \mathbf{B}_{NL} are strain-displacement matrices and \mathbf{C} is the stress-strain material property matrix (Bathe (1996)).

For the passive material model defined by Eqs. (4.4) and (4.5), three sets of material parameter values have been calculated using the procedure described in Chapter 3. These three sets of material parameter values are given in Table 4.2, where they are referred to as lower, middle, and upper, depending on the relative positions of the corresponding stress-strain curves. Simulations were performed using each of these sets of material parameters to determine which set leads to results that most closely match those in previous studies. The values of the three sets of passive material parameters are slightly different from those presented in Chapter 3, as a result of small differences in the constraints imposed on C_5 and C_6 , which were required to ensure convergence of the simulations using the defined model conditions and a LV geometry. Specifically, C_5 was increased from 0.0001 in the previous calculations to 0.01, and C_6 , which was set to zero in the previous calculations, was bounded in the interval $0 < C_6 \leq 0.0005$. Although simulations performed with the material parameters from Chapter 3 converged for a cubic geometry, they diverged when a LV geometry was considered. By adjusting the constraints imposed on C_5 and C_6 and recalculating the material parameters using the procedure described in Chapter 3, numerical convergence was achieved for simulations with a LV geometry, while maintaining excellent agreement (not shown presently) with previous measurements for simulations performed on a cubic geometry.

The material model has been chosen to be slightly compressible to allow for numerical convergence. Assuming that the myocardium can be modeled as an incompressible material, the bulk modulus can be chosen sufficiently large for stresses calculated using our slightly compressible material model to be essentially the same as stresses calculated using

Table 4.2: Material parameter values for passive canine LV myocardium material model.

parameter	lower	middle	upper
C_1 (kPa)	2.117	5.062	5.021
C_2	0.498	0.593	0.851
C_3	0.237	0.0383	-0.0613
C_4	0.0332	0.00483	0.0413
C_5	0.01	0.01	0.01
C_6	0.0005	0.0005	0.000278

an incompressible version of the same material model for the same stretches. In Chapter 3, we have demonstrated that the value $\kappa_s = 1 \times 10^7$ kPa is an appropriate choice and this value was used in the present study.

4.2.3 Boundary and initial conditions

Considering that the heart is nearly neutrally buoyant in the body, we have neglected gravitational forces in this work. The deformation of the LV was driven by a linearly increasing pressure function applied uniformly to the inner wall of the LV cavity. Based on our objective to inflate the LV to an end-diastolic state, we have chosen the maximum pressure applied to the wall to be 2 kPa, which is approximately equal to the end-diastolic pressure measured by Sabbah and Stein (1981). During the experiments described by McCulloch et al. (1987), the right ventricle (RV) remained attached to the LV, but it is unclear whether the RV was pressurized. In the absence of definitive information, we assumed that the RV was not pressurized in these experiments. Stress-free boundary conditions were applied to the outer walls of the myocardium. Lastly, for the finite element simulations to converge, the geometry must be fixed at some location. In the experimental set-up from McCulloch et al. (1987), the inflow and outflow tracts of their excised LV were attached to

rigid cannulae. Because the present geometry was truncated below the inflow and outflow tracts, we have instead chosen to fix the basal plane in the z -direction. In anticipation of future FSI simulations for which we will couple the present solid geometry to a fluid geometry that will be rigid above the basal plane, the inner edge of the basal plane was fixed in all three directions.

As the initial condition for the simulations, we assumed zero stresses in the entire myocardium. This condition is only approximately valid, because it is known that the myocardium has residual stresses even in an excised condition (Costa et al. (1997)). This issue will be further discussed in Section 4.4.2.

4.2.4 Procedure for principal stretch and stress calculations

The principal stretches are defined as the ratios of corresponding deformed and undeformed lengths and are denoted as λ_i , $i = 1, 2, 3$. The principal stresses presented in this work are Cauchy stresses T_i , $i = 1, 2, 3$, which can be computed from the second Piola-Kirchhoff stresses calculated from Eq. (4.6) using a push-forward operator as described in Chapter 3. The only available measurements of principal stretches have been reported by Omens et al. (1991) at a location halfway through the LV free wall, which is the part of the LV that does not share a common boundary with the RV. In consideration of the orientations of the LV inflow and outflow tracts in our fluid geometries (not presented in this chapter), which will be coupled with the present solid geometries for FSI simulations, we have inferred that the section of the geometry that would likely be the LV free wall would be the quadrant that is bounded by the positive x - and y -axes. As the best choice for comparisons with the measurements, we will present values of the principal stretches

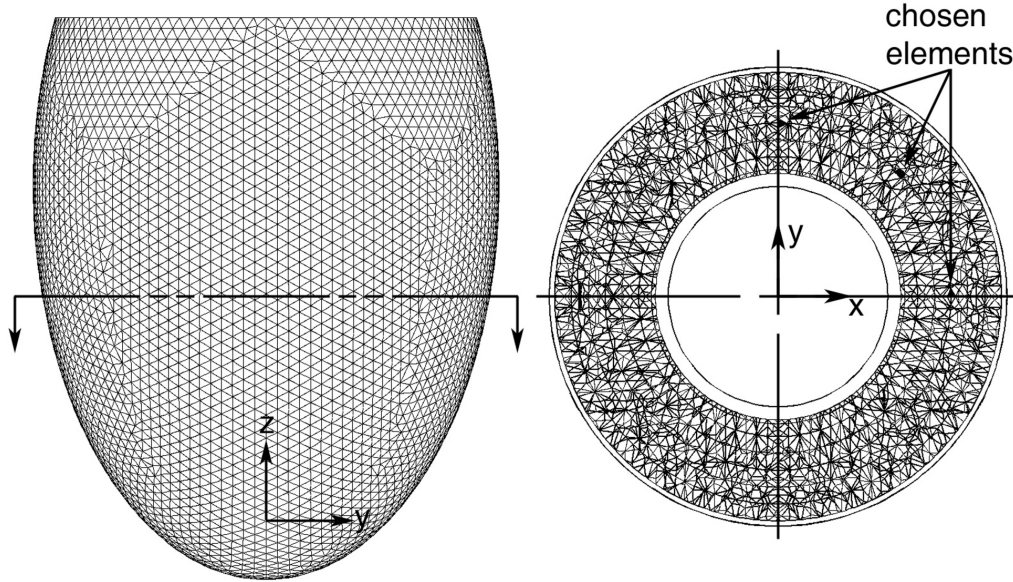


Figure 4.3: Location of elements used for principal stretch and stress calculations. These elements are located at a relative elevation from the apex of $z/h = 0.5$.

which were the averages of values in six elements in the mesh, shown in black in Fig. 4.3 for the finer of our two meshes; these elements were located approximately halfway through the wall (on either side of the centreline), at three circumferential positions, one near the positive x -axis, another near the positive y -axis, and a third one near the bisector of the angle between these axes, and at a relative elevation of $z/h = 0.5$ in DG. This elevation was chosen as a representative height; unfortunately, Omens et al. (1991) did not specify the elevation of their measurements.

Transmural variations of principal stretches and stresses were calculated along the positive x - and y -axes in the equatorial plane, which was at a relative elevation of $z/h = 0.67$ in DG. The relative depth at which a stretch or stress is reported is the distance t from the exterior wall normalized by the local deformed wall thickness t_{\max} . For each relative depth

t/t_{\max} , average stretches and average stresses were calculated by averaging values obtained on the x - and y -axes. The equatorial plane was chosen because it is only at this elevation that the horizontal plane contains the third material axis x_3 , which is perpendicular to the local circumferential direction. At any other elevation, the x_3 directions in each layer would differ on the horizontal plane, requiring that each plane be oriented perpendicular to the local circumferential direction. Costa et al. (1996) presented principal stretches and stresses at $p = 1 \text{ kPa}$ at a relative elevation of $z/h = 0.56$; although this elevation is somewhat different from the present one, this issue is not of serious concern, because, as will be shown in the following, the values of principal stretches and stresses are fairly insensitive to elevation except close to the apex or the base. Omens et al. (1991) presented principal stretches at $p = 1.07 \text{ kPa}$, but did not specify the elevation of the plane in which they took their measurements.

Longitudinal variations of principal stretches and stresses were calculated from the apex to the base halfway through the wall at circumferential locations corresponding to the positive x - and y -axes. The relative distances from the apex c/c_{\max} were calculated using the deformed length of each edge and for each c/c_{\max} average stretches and average stresses were calculated by averaging values obtained at the two circumferential locations.

4.3 Results

4.3.1 Material parameter selection

The first step in our simulations of filling of the passive LV was to determine which of the three sets of passive material parameters that were described in Section 4.2 resulted

in cavity volume changes that were closest to values reported by authors of previous experimental and computational studies. To compare our results with those in the literature, we need to normalize the volume changes. Two types of normalized volume changes have been introduced by previous authors: Nash and Hunter (2000) introduced the parameter $\Delta V_f/V_{f,0}$ and Omens et al. (1991) introduced the parameter $\Delta V_f/m_s$. Figure 4.4 plots these two types of normalized volume changes vs. pressure for the three presently considered cases, along with results from the literature. It should be noted that for the present simulations, because the LV cavity itself is not meshed, V_f cannot be calculated directly. Details on how V_f was calculated are given in Appendix B.2. The present results were obtained using the fine mesh. The previous experimental results are presented as mean values of 6 (McCulloch et al. (1989)), 5 (McCulloch et al. (1992)), and 7 (Omens et al. (1991)) samples; each uncertainty bar is equal to two standard deviations of corresponding measurements. The computational results from Nash and Hunter (2000) are only presented in Fig. 4.4a, because the authors did not provide the mass (or volume) of the myocardium in their study, which prevented us from calculating $\Delta V_f/m_s$ for their results.

Normalizing the LV volume changes as $\Delta V_f/V_{f,0}$ takes into account differences in cavity volume for different LVs but not differences in wall thickness. Even when considering the significant experimental uncertainty, Fig. 4.4a shows that this parameter does not lead to a collapse of the three available sets of measurements. However, when volume changes are normalized by the myocardium mass, the three sets of experimental results nearly collapse, as seen in Fig. 4.4b. This shows the importance of accounting for the mass (or volume) of the myocardium when choosing a suitable LV geometry. In conclusion, the parameter

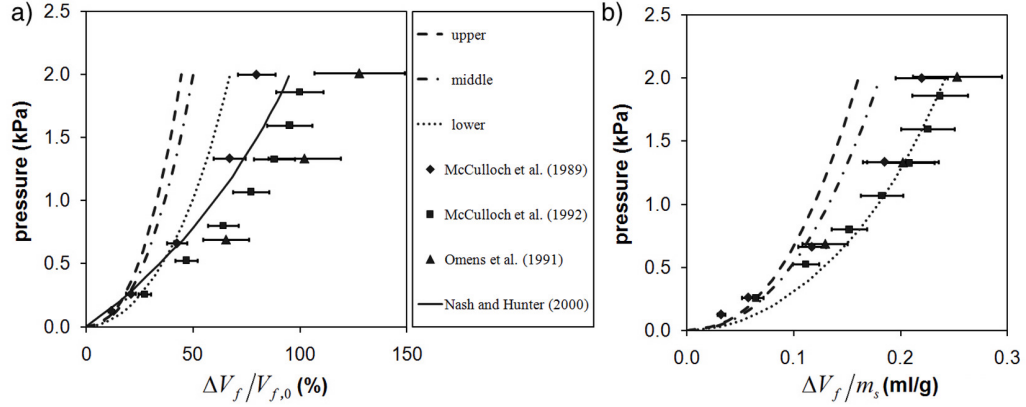


Figure 4.4: Normalized volume changes vs. pressure for three sets of material parameter values, along with three previous experimental studies (points), and one previous computational study (solid line) for (a) only.

$\Delta V_f/m_s$ seems to be more appropriate than $\Delta V_f/V_{f,0}$ for comparing results of studies using different LVs.

The calculated values of $\Delta V_f/m_s$ for the three sets of material parameter values have comparable trends but significantly different magnitudes, with the lower set of results being generally the one closest to the experimental values. Although the calculated values are higher than the measurements for pressures lower than about 0.7 kPa, the agreement between predictions and measurements is very good for the range of higher pressures, which is of interest in this study. Based on these observations, the lower set of material parameters were chosen for use in the remainder of the present simulations.

4.3.2 Mesh dependence

To determine the dependence of the results on the mesh, simulations were performed using the two meshes defined in Section 4.2.1. For each mesh, we calculated $\Delta V_f/m_s$ and the transmural and longitudinal variations of the principal stretches and

stresses at $p = 2$ kPa. These principal stretches and stresses were calculated at the locations described in Section 4.2.4, and, through interpolation, values were obtained for the same transmural and longitudinal positions for each mesh to allow for a quantitative comparison. The values of $\Delta V_f/m_s$ for the two meshes were nearly identical, with differences being lower than 0.1%. The transmural and longitudinal variations of the principal stretches and stresses also showed excellent agreement for the two meshes with average differences in both directions being less than 1% for the stretches and less than 7% for the stresses. These small percentage differences suggest that the results are nearly mesh independent. It is also clear that the stresses are more sensitive to mesh density than the stretches and volume changes. This conclusion is reinforced by the fact that, at certain isolated locations, the percentage differences for the stresses were significantly larger than the corresponding averages. For the remainder of the simulations presented in this study, we will use the fine mesh to keep mesh dependence as low as possible.

4.3.3 Verification of end-diastolic state

As mentioned in the introduction, we assumed that the end-diastolic state of the LV was reached at a pressure of $p = 2$ kPa. Although DG was ellipsoidal, our calculated end-diastolic geometry was not, because the LV deformed in a three-dimensional manner. Even so, it was possible to roughly fit an ellipsoid to the end-diastolic LV and to determine its characteristic dimensions so that they can be compared to previous measurements. As the LV deformed during the simulations, the original equatorial plane shifted away from the basal plane, which was fixed in the vertical direction. For our end-diastolic geometry, we calculated an average outer radius b , an average equatorial thickness t_b , and a rough

location of the equatorial plane, by calculating the maximum outer and inner radii along the $+x$, $+y$, $-x$, and $-y$ axes along with their vertical positions. These radii were calculated at nodes within the deformed mesh, which were not necessarily located at the same vertical positions. In fact, we observed that the average vertical position of the outer radii was higher than the average vertical position of the inner radii. We then calculated each outer radius at the node below the one at which the maximum value was obtained, and each inner radius at the node above the one at which the maximum value was obtained. We then chose the height of the equatorial plane to be the average vertical position of these sixteen nodes (eight on the outer surface and eight on the inner surface). Through interpolation, we found the outer and inner radii in this equatorial plane. Then b was determined by averaging the four outer radii in the equatorial plane and t_b was determined by averaging the thicknesses in the equatorial plane. The semi-major axis a was calculated as the vertical distance of the outer edge of the apex from the equatorial plane, and the wall thickness at the apex t_a was calculated as the distance between the inner and outer edges at the apex. Lastly, the end-diastolic h was calculated as the distance from the basal plane to the inner edge of the myocardium at the apex. The calculated end-diastolic dimensions were $a = 47.4$ mm, $t_a = 5.1$ mm, $b = 31.8$ mm, $t_b = 8.5$ mm, and $h = 67.6$ mm, and the calculated end-diastolic volume was $V_f = 56.3$ ml. The corresponding measurements by Streeter and Hanna (1973), were $a = 47 \pm 2$ mm, $t_a = 6 \pm 1$ mm, $b = 28 \pm 1$ mm, $t_b = 9 \pm 1$ mm, and $V_f = 52 \pm 5$ ml. These measurements are presented as an average of five samples plus or minus their standard deviation and the reported values were rounded-off from the original measurements for consistency with their estimated uncertainty (Tavoularis (2005)). For

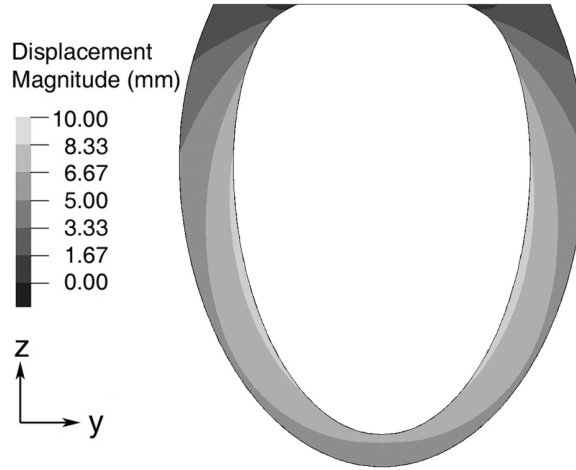


Figure 4.5: End-diastolic displacement magnitudes at the centre of the left ventricle geometry in the y - z plane, calculated at $p = 2$ kPa.

the most part, the calculated dimensions and cavity volume were either within or fairly close to the measurement ranges. This verifies that at $p = 2$ kPa the present LV geometry is representative of a LV at end diastole.

Using the previously presented dimensions and Eq. (4.2), we calculated an end-diastolic eccentricity of $e = 0.79$, which is 10% lower than the value of $e = 0.88$ calculated at diastasis. This decrease in eccentricity is in agreement with the trend observed by Rankin (1980).

4.3.4 Deformations

Figure 4.5 shows contours of displacement magnitudes on the centre-plane of the end-diastolic geometry ($p = 2$ kPa). Changes in the dimensions of DG during inflation are visible in this figure. Near the basal plane, the displacement was small, which is to be expected if one considers that this boundary was kept fixed.

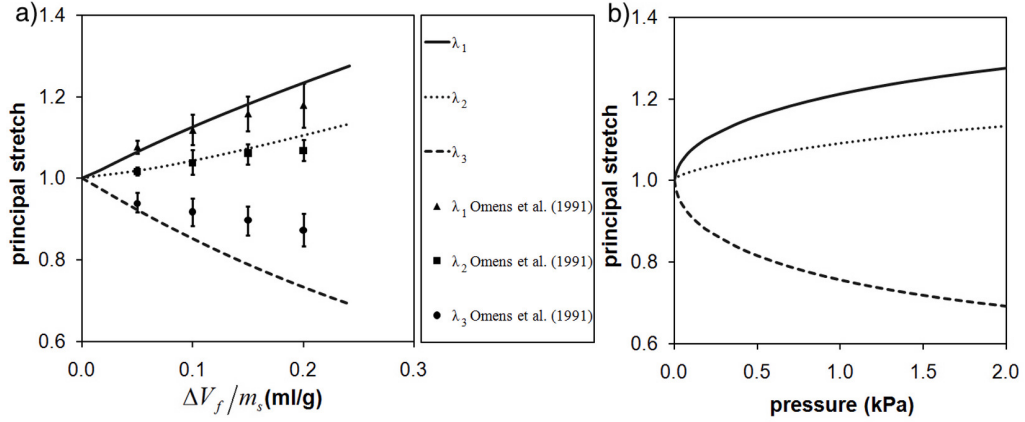


Figure 4.6: Representative principal stretches versus normalized volume change (a) and pressure (b), calculated as described in Section 4.2.4.

Average principal stretches halfway through the myocardium, calculated as described in Section 4.2.4, have been plotted in Figs. 4.6a and b, versus the normalized volume change and pressure, respectively. The principal stretches in the study of Omens et al. (1991), also shown in Fig. 4.6a, were computed from the principal strains presented in their Fig. 4. Each uncertainty bar is equal to two standard deviations of 7 samples, as reported by these authors. As we could not determine an exact correspondence between volume and pressure in the Omens et al. results, we have not plotted these in Fig. 4.6b.

The trends of the presently found principal stretches in Fig. 4.6a are consistent with the trends in the results of Omens et al. (1991), in the sense that they indicate tension for λ_1 and λ_2 and compression for λ_3 and also that deformations in all directions increase with increasing volume change. The present λ_1 and λ_2 are comparable to λ_1 and λ_2 found by Omens et al. (1991), whereas the present λ_3 indicates larger deformations than the deformations in the previous study. To investigate a possible cause for the large differences in λ_3 , values of the third invariant of Green's strain tensor $I_3 = \lambda_1^2 \lambda_2^2 \lambda_3^2$ were calculated for

the present study and the experiments of Omens et al. (1991) for $\Delta V_f/m_s = 0.05 \text{ ml/g}$ and 0.20 ml/g . This parameter is an indicator of the compressibility of a material, being equal to 1 for an incompressible material. For DG, I_3 changed very slightly ($I_3 = 1.0001$ for $\Delta V_f/m_s = 0.05 \text{ ml/g}$ and $I_3 = 1.0006$ for $\Delta V_f/m_s = 0.20 \text{ ml/g}$), whereas for the measurements of Omens et al. (1991), I_3 increased significantly with increasing volume change ($I_3 = 1.06$ for $\Delta V_f/m_s = 0.05 \text{ ml/g}$ and $I_3 = 1.21$ for $\Delta V_f/m_s = 0.20 \text{ ml/g}$). The increase in I_3 found for the measurements of Omens et al. (1991) is consistent with their observation that the volume of the myocardium increased as the LV was pressurized. They suggest that this increase in myocardium volume could be caused by fluid entering the myocardium from the LV cavity or possibly due to errors associated with their strain calculations. They mention that, because during their measurements the wall was not being perfused, this volume change was not caused by a transfer of fluid in the vasculature of the LV wall. In contrast to this finding of Omens et al. (1991), Yin et al. (1996), who measured the change in volume of a perfused section of the septum of a passive canine LV myocardium, found that the volume of the myocardium decreased with increasing pressure. In view of this contradiction, we made no effort to match the wall volume changes found by Omens et al. (1991).

A comparison of Figs. 4.6a and b shows that in the pressure range of present interest ($1 \text{ kPa} \leq p \leq 2 \text{ kPa}$) the rates of variation of stretches with respect to pressure were much lower than their corresponding rates with respect to volume change.

Transmural and longitudinal variations of principal stretches (and stresses, which will be discussed in the following section) will be presented for two values of pressure: at

$p = 1$ kPa, which allows comparisons with previous results, and at $p = 2$ kPa, which is deemed to be the end-diastolic pressure.

Figures 4.7a and b are plots of the transmural (from the exterior to the interior of the myocardium) and longitudinal (from the apex to the base) variations of the principal stretches, respectively, for $p = 1$ kPa; Figures 4.7c and d are plots of the same stretch variations at $p = 2$ kPa. The curves are polynomial fits through average values at locations described in Section 4.2.4. These figures also show transmural variations of the principal stretches in the experiments of Omens et al. (1991), which were calculated from the normal and shear strains presented in their Fig. 6 as the eigenvalues of the right Cauchy-Green deformation tensor \mathbf{C} , and corresponding variations in the simulations of Costa et al. (1996), which were curve fits through their point data in their Fig. 5.

The present transmural stretches at $p = 1$ kPa are in fair qualitative agreement with the previous work. The values of λ_2 in the present and previous studies are comparable. For λ_1 and λ_3 , the deformations in all three cases increase with increasing distance from the exterior wall, however, the deformations in the present study are larger than the deformations found in the previous ones. Because the longitudinal variations of stretches at $p = 1$ kPa indicate only small changes in all stretches except near the apex and near the base, differences in transmural stretches between the present and the previous cases cannot be attributed to differences in elevations. The differences in the trends of the stretches near the apex for the present and the previous simulations are caused by differences in the boundary conditions that were used in the two studies. Costa et al. (1996) resolved the singularity that would occur if the mesh were reduced to a single point at the apex by

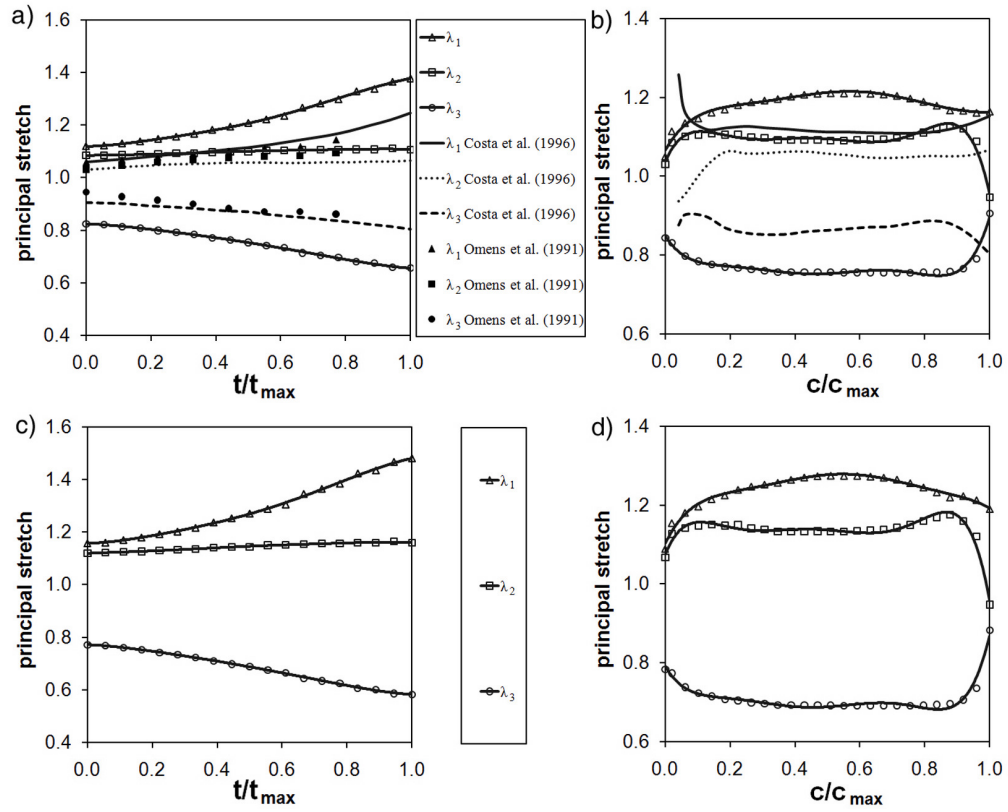


Figure 4.7: Representative transmural (a,c) and longitudinal (b,d) variations of the principal stretches at $p = 1$ kPa (a,b) and $p = 2$ kPa (c,d), calculated as described in Section 4.2.4.

adding a small hole. In the present study, this singularity was resolved by subdividing the geometry into quarters. At the basal plane, the present and previous models were both constrained in the z -direction, resulting in comparable principal stretches at this location ($\lambda_1 = 1.16$, $\lambda_2 = 0.95$, $\lambda_3 = 0.91$ compared to $\lambda_1 = 1.15$, $\lambda_2 = 1.07$, $\lambda_3 = 0.81$ in the work of Costa et al. (1996)). All three principal stretches in the present and previous studies were fairly uniform away from the apex and the basal plane; however, for λ_1 and λ_3 , deformations were larger in the present study than in the previous one. These differences in deformations away from the basal plane resulted in differences between trends in the present and previous stretches as they approached nearly identical values at the basal plane.

The transmural and longitudinal variations of principal stretches at $p = 2$ kPa are very similar to those at $p = 1$ kPa, although they correspond to deformations which increased by an average factor of 1.06. This shows that the overall sensitivity of deformations to pressures within the range bounded by these two values is relatively low.

4.3.5 Principal stresses

Figures 4.8a and b are plots of average principal Cauchy stresses halfway through the myocardium versus the normalized volume change and pressure, respectively, at the same locations as the principal stretches presented in Figs. 4.6a and b. Consistent with the principal stretches, T_1 and T_2 are tensile and T_3 is compressive. All stresses grow in a non-linear manner with increasing volume change, which is consistent with the non-linear form of the myocardium material model. In the middle of the myocardium, where the stresses are shown, they were nearly proportional to the pressure. As the pressure doubled from 1 to 2 kPa, the stresses increased by an average factor of 2.1; this demonstrates that the

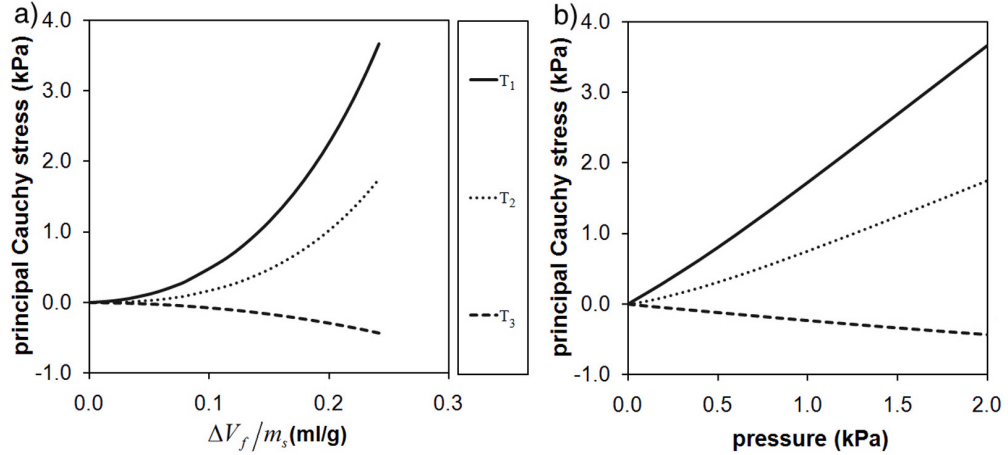


Figure 4.8: Representative principal Cauchy stresses versus normalized volume change (a) and pressure (b), calculated as described in Section 4.2.4.

stresses in the myocardium at end diastole are very sensitive to the choice of end-diastolic pressure. One may recall that the deformations were not very sensitive to pressure in the range between 1 and 2 kPa; even so, because of the exponential form of the myocardium material model and the relatively large deformations for $p \geq 1$ kPa, small increases in deformation correspond to large increases in stress.

Figures 4.9a and b are plots of the transmural (from the exterior to the interior of the myocardium) and longitudinal (from the apex to the base) variations of the principal Cauchy stresses, respectively, for $p = 1$ kPa, whereas Figs. 4.9c and d are plots of the same stress variations at $p = 2$ kPa. These stresses are presented at the same locations as the stretches presented in Fig. 4.7. It should be noted that, in Fig. 4.9, different scales are used for the transmural and longitudinal variations of the stresses, and that due to the large increase in the magnitudes of the transmural stresses from $p = 1$ kPa to 2 kPa, the scale used in Fig. 4.9c is twice as large as the scale used in Fig. 4.9a.

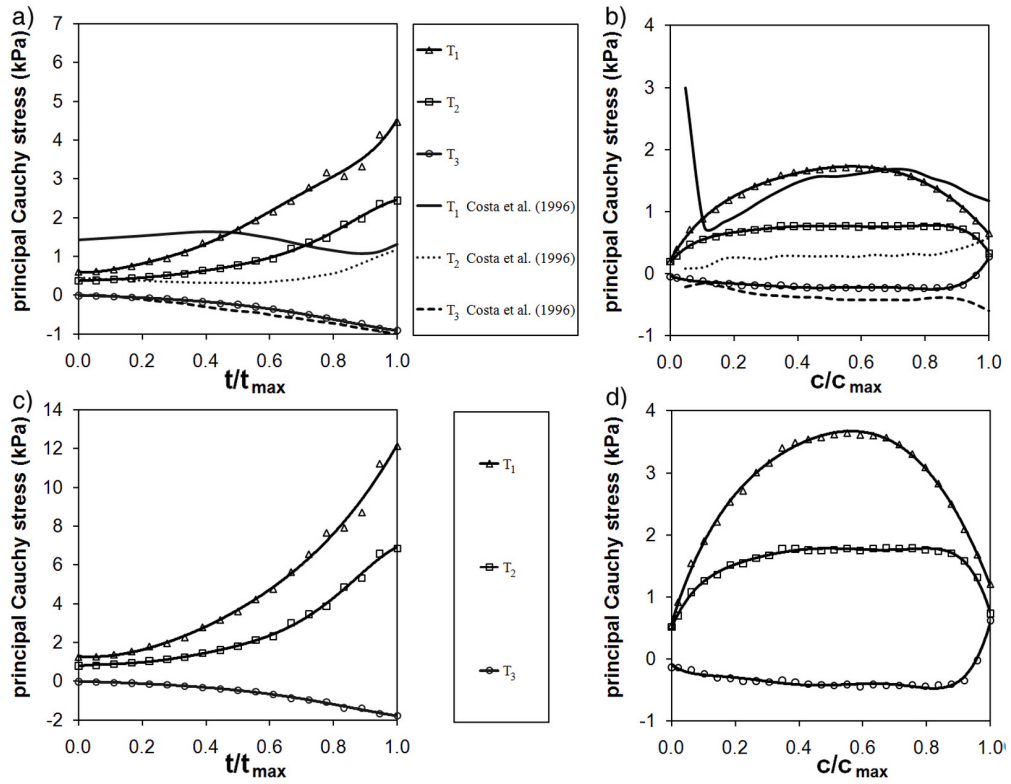


Figure 4.9: Representative transmural (a,c) and longitudinal (b,d) variations of the principal Cauchy stresses at $p = 1$ kPa (a,b) and $p = 2$ kPa (c,d), calculated as described in Section 4.2.4.

Principal stresses through the wall at $p = 1$ kPa show good agreement for T_3 in both slopes and magnitudes between the current and previous computational results. The T_2 results in the outer half of the wall are comparable to the previous computational results. In the inner half, the two sets diverge gradually, such that the present prediction at the inner surface is much larger than the one by Costa et al. (1996). Lastly, the results for T_1 differ substantially in both slopes and magnitudes. The current results exhibit high stress concentrations in both T_1 and T_2 at the inner surface of the wall, where the pressure boundary condition was applied.

The longitudinal principal stress variations at $p = 1$ kPa exhibit end effects at the apex, similar to those observed for the principal stretches. In the middle section, the values of T_3 for the current and previous studies were comparable in slopes and magnitudes. With the exception of the region near the basal plane, the values of T_2 for the current and previous studies show comparable slopes with the magnitudes in the present study being larger than the magnitudes in the previous one. For T_1 , both the trends and the magnitudes differ in the two cases; however, with the exception of the spike at the apex for the stresses by Costa et al., both stresses increase to a maximum part-way between the apex and the base, before decreasing towards the basal plane. Further, the averages of each T_1 from the apex to the base are nearly equal ($\bar{T}_1 = 1.34$ for the current study and $\bar{T}_1 = 1.46$ for the Costa et al. study). One may partially attribute these differences to differences in geometry: the geometry of Costa et al. contains a hole at the apex, which produces large local values of T_1 and significantly influences the longitudinal variation of this variable. End effects seem to have a much larger influence on the stresses than on the stretches, making

it difficult to identify other effects. Overall, in view of the differences in the forms of and the parameter values used in the transversely isotropic material models employed by the present and previous computational studies, it is not surprising that the stress distributions in these studies are different.

At $p = 2$ kPa, the trends of the transmural and longitudinal variations of the principal stresses were comparable to the trends found at $p = 1$ kPa but the magnitudes of these stresses were larger. We investigated whether the stresses increased proportionately to the increasing pressure in the range from $p = 1$ to 2 kPa, and found that the stress magnitudes, for the most part, increased by a factor greater than 2 in this pressure range. Moreover, the stress to pressure ratio was found to vary non-uniformly in space: transmurally, the stresses increased by an average factor of 2.09 at the exterior wall and 2.86 at the interior wall, whereas, longitudinally, the stresses increased by an average factor of 2.69 at the apex, 2.04 at the base, and 2.22 halfway in-between. These observations make it clear that stresses in the myocardium must be calculated at the desired end-diastolic pressure and cannot be obtained by proportional scaling of stresses calculated at a lower pressure.

The local principal stress axes y_1 , y_2 , and y_3 are distinct from the local material axes x_1 (fibre), x_2 (sheet), and x_3 (sheet-normal). To illustrate the differences between these two sets of axes, we determined the principal directions along the x - and y -axes in the equatorial plane, in which x_3 is radial. The local material axes x_1 and x_2 depend on the orientation of the muscle fibres, which changes from layer to layer through the wall. Let φ_1 be the angle between y_1 and the local circumferential direction, φ_2 be the angle between y_2 and the local circumferential direction, and φ_3 be the angle between y_3 and the local radial

direction. All three angles were calculated as the average of values obtained along the x - and y -axes in the equatorial plane.

As shown in Fig. 4.10, the angles φ_1 and φ_2 varied non-linearly through the wall and the difference between them was approximately 90° throughout. The variations of these angles through the wall were non-linear, with general shapes comparable to those found by Omens et al. (1991) for the principal stretch directions at $p = 1.07$ kPa. Nevertheless, the magnitudes of these angles were different from those in the previous study, as anticipated in view of differences in muscle fibre angles between the two cases and differences between principal stretch and principal stress directions. The average values of φ_1 and φ_2 through the wall were 19.7° and -70.3° , respectively, which represent a difference of approximately 20° between the local principal stress directions and the local material axes within the plane containing the muscle fibres. The angle φ_3 was nearly constant through the wall with an average value of $\varphi_3 = 4.9^\circ$, which implies that, in the equatorial plane, the principal axis y_3 is nearly radial.

4.3.6 Effect of the number of myocardial layers

The sensitivity of the results to the number of wall layers used in our model was investigated by comparing our main results obtained using the six-layer model and results obtained using a three-layer model. All comparisons were made for the assumed end-diastolic pressure of $p = 2$ kPa. This is the first study of its kind, although a previous FSI study (Watanabe et al. (2003)), performed over the cardiac cycle, has examined the effects of the number of wall layers on global parameters, such as volume change. Average percentage differences in the transmural variations of the principal stretches and principal

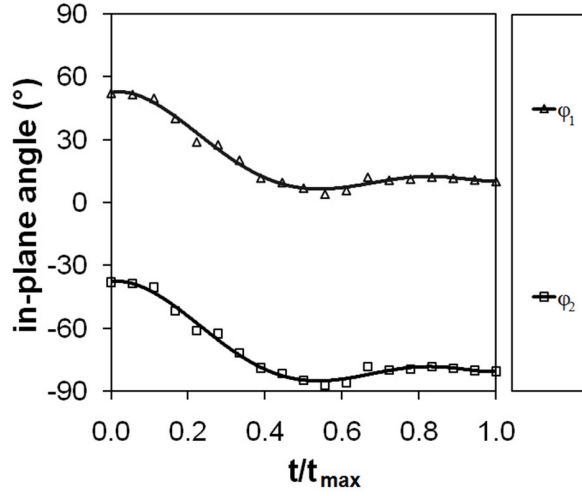


Figure 4.10: Representative transmural variations of the in-plane angles at $p = 2$ kPa, corresponding to the average stresses shown in Fig. 4.9c.

stresses were found to be 1% and 8%, respectively. However, larger differences in principal stresses were found locally, as illustrated in Fig. 4.11a. Specifically, in the region between $t/t_{\max} = 0.67$ and $t/t_{\max} = 0.83$, which corresponds to the outer half of the inner layer in the three-layer model and layer 5 in the six-layer model, the average percentage difference between the principal stresses in the two cases increased to 17%. In this region, there was a noticeable shift in T_1 for the three-layer case, whereas there was no apparent discontinuity in the six-layer case. The most compelling evidence that a three-layer wall was insufficient to resolve the transmural variations of the stresses can be seen in Fig. 4.11b, which is a plot of the variations of φ_1 and φ_2 for the two cases. In Fig. 4.11b, large sudden jumps in φ_1 and φ_2 are visible for the three-layer model at the boundaries between the layers, whereas no such jumps are visible for the six-layer model. In summary, our study has shown for the first time that a model containing three wall layers would be insufficient to resolve the transmural variations of the stresses in the myocardium, whereas a model containing

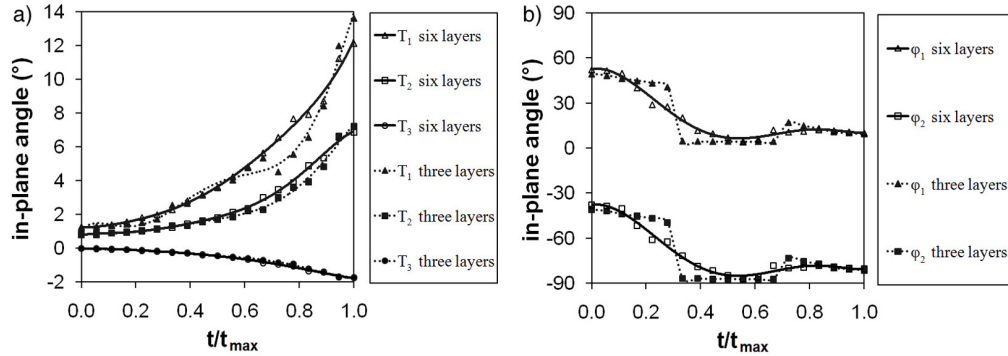


Figure 4.11: Representative transmural variations of the principal stresses (a) and the in-plane angles (b) at $p = 2$ kPa for two models with different numbers of wall layers.

six layers provided stress variations that were nearly free of apparent discontinuities across layers. In conclusion, the use of six layers is deemed to be sufficient for the present simulations.

4.3.7 Effect of muscle fibre orientation

The sensitivity of the analysis to muscle fibre orientation was investigated at $p = 1$ kPa, by comparing results obtained for our reference case to those calculated with a fibre angle range from -37° to $+98^\circ$, as measured by Omens et al. (1991) and used by Costa et al. (1996). Differences in the transmural variations of the principal stretches, calculated for each case as described in Section 4.2.4, were found to be small, with the average percentage difference being approximately 1%. These differences were found to be much smaller than the differences between the current results and those from previous studies presented in Fig. 4.7a. The average difference between the principal stretches from our reference case and the measurements of Omens et al. (1991) was 8%. From this we can conclude that differences in fibre orientation between the current and previous studies cannot account for

the observed differences in the principal stretches. Larger percentage differences were found between the transmural variations of the principal stresses calculated in the two cases, with the average difference being approximately equal to 10%. Differences in the angles φ_1 and φ_2 were much larger near the exterior surface (23°) than near the interior surface (4°). The difference in these angles at the exterior surface between the two cases was equal to the difference in fibre angles in the outermost layer. In contrast, the difference in these angles near the interior surface was much smaller than the corresponding difference in fibre angles in the innermost layer; this can be attributed to the pressure boundary condition that was applied on this surface.

4.4 Discussion

This section re-evaluates the rationale for the several simplifications that have been made in defining the numerical model in this study and the potential impact that these simplifications may have on the observed or conjectured differences between the present results and their physiological counterparts.

4.4.1 Assessment of the geometry, material model, and boundary conditions

The LV geometry used in the present study is idealized, and is considered to represent an average isolated canine LV. The wall is axisymmetric, whereas the actual LV wall consists of two distinct sections: the septum, which separates it from the RV, and the free wall. Thus, the wall thickness and muscle fibre orientation in actual LV would be non-

axisymmetric. LV non-axisymmetry and the coupling of the LV and RV mechanics would undoubtedly play some role in the deformation of the myocardium during filling. Even so, the fair agreement of the calculated volume changes and other bulk properties with previous experimental values suggests that the present model is adequate for the intended purposes. Appendix C briefly describe the extension of this work to an anatomical LV-RV geometry and the limitations of such an extension.

In the present work, we have modeled the LV myocardium as a transversely isotropic material, in full knowledge of the fact that a fully orthotropic material model (Nash and Hunter (2000); LeGrice et al. (1995)) would be more appropriate. The reason for our choice was that the available stress-stretch measurements (Novak et al. (1994)) were adequate for the calculation of transversely isotropic material parameter values but not orthotropic ones. Comparative simulations of the mechanics of the myocardium over the cardiac cycle using a transversely isotropic material model and an orthotropic one have been performed by Usyk et al. (2000). These authors calculated the orthotropic material parameter values by adjusting transversely isotropic values to improve the fit to experimental strains at end diastole; predictably, they found that the use of this orthotropic model resulted in a better agreement between the computed transmural strains and previous measurements at end diastole. The orthotropic material parameter values used by Usyk et al. cannot be of general use, because they were not determined from independent material tests, but fitted to specific data at end diastole, which are subject to many other influences. Moreover, Usyk et al. found that, at end systole, the transmural strains computed using the transversely isotropic and orthotropic material models were not very different. In conclu-

sion, although it may be plausibly expected that the use of an orthotropic material model would change the results of the present simulations, it is unclear in what direction such changes would be. In the absence of suitable experimental results of biaxial stress-stretch tests in the two cross-fibre directions, we are unable to validate an orthotropic model; if such results become available, it would be a straightforward exercise to repeat the present simulations using an orthotropic model instead of a transversely isotropic one.

In the present study, a slightly compressible model was used for the myocardium, but the material bulk modulus was sufficiently high for compressibility effects to be negligible. This assumption appears to contradict the finding of Yin et al. (1996) that the volume of the myocardium changes during filling, which is equivalent to a compressible material. Further insight on possible effects of compressibility on the presently computed stretches can be gained by a re-examination of the results shown in Fig. 4.6a. The computed stretches λ_1 and λ_2 are compatible with the experimental results of Omens et al. (1991), whereas the computed stretch λ_3 is significantly lower (i.e., the deformation is larger). Assuming that compressibility only affects λ_3 and using the I_3 values calculated from the stretches of Omens et al. (1991), one may recalculate λ_3 ; the resulting values are much closer to the experimental ones than the values shown in Fig. 4.6a. This observation shows that compressibility may play a significant role in the deformation of the LV myocardium during passive filling. To examine the validity of this hypothesis, we would need to employ a more complex material model, such as the poroelastic and viscoelastic material models proposed by Huyghe et al. (1991) and Yang and Taber (1991). This is delegated to future research.

Another issue that deserves attention is the difference between the fixed boundary

conditions that were imposed on the present simulations and the physical conditions in the experiments that we used for validation of our results. In the experiments, the LV inflow and outflow tracts were attached to rigid cannulae, which constrained their motion and anchored the LV. In the simulations, we truncated the geometry below the LV inflow and outflow tracts, and fixed the basal plane in the vertical direction and its inner edge in all three directions. It would have been preferable to allow the inner edge of the base to deform in the horizontal plane, but this would result in global translational motion. Alternatively, extending the LV geometry to include the inflow and outflow tracts would have allowed us to represent more accurately the experimental boundary conditions. This can be done in the future, provided that the dimensions of the LV inflow and outflow tracts become available to us, which was not the case at present.

It is clear from this discussion that both the LV geometry and the material properties used in the present simulations differ to some extent from those of actual canine LV. We opted to use representative properties, rather than “actual” ones. This is deemed to be justified in view of the large variability in the anatomy and the physiology of individual canine LV, which also introduces a large variability in material behaviour. Moreover, because the longitudinal and transmural variations of *in vivo* stresses in the myocardium have not been measured, it is presently impossible to validate the calculated stresses in a convincing manner. We believe, however, that the longitudinal stress variations in the present study are an improvement over those calculated by Costa et al. (1996), because we resolved the singularity at the LV apex by alternative means, rather than introducing a hole, as Costa et al. did.

4.4.2 Residual stresses

We started the present simulations from a reference state which was subjected to uniform pressure and free from any stresses. It is known, however, that even the unloaded (i.e., subjected to uniform pressure) excised LV has residual stresses. Although direct measurements of any stresses in the myocardium, including residual ones, are not yet available, previous authors have measured residual strains by cutting pieces of rat (Omens and Fung (1990)) and canine (Costa et al. (1997)) LV myocardia. In these experiments, the authors started from an unloaded, isolated heart (which presumably had residual stresses). Omens and Fung (1990) removed a thin equatorial slice of the LV and then made a radial cut to it, which caused the two sides to separate, thus relieving the circumferential residual stresses and bringing the slice to a state that was defined as stress-free. Then, they calculated the residual circumferential and radial strains by comparing the undeformed and deformed geometries of the slice. They found that the circumferential residual strains were negative near the inner surface of the myocardium and positive near the outer surface. Omens and Fung suggested that circumferential stresses predicted by numerical simulations may be too large near the inner edge of the myocardium and that the inclusion of residual stresses with corresponding signs to the measured residual strains, would serve to correct this overprediction. Costa et al. (1997) embedded markers in the LV myocardium wall and then excised a square piece of it, which allowed them to determine residual strains from the deformation of this piece following its removal. Their findings were consistent with the ones presented by Omens and Fung. Moreover, Guccione et al. (1991), using an approach to be discussed in the next paragraph, found that an increase in the circumferential residual

stress in their numerical simulations acted as to decrease the transmural variation of the overall circumferential stress. Portions of the first and second principal stresses are in the circumferential direction in the present model, so the presence of a residual circumferential stress could potentially reduce the slope of the transmural variation of T_1 and T_2 shown in Figs. 4.9a and c.

Residual stresses may be introduced in the present analysis by following one of two possible approaches. The first approach is based on the work of Guccione et al. (1991), who used a cylindrical LV with an isotropic myocardium material model and defined as a stress-free state the condition at which the cylinder was split open lengthwise to form a gap between two opposing free edges; the gap was then characterized by an opening angle. Then, they applied flexion to this object until the free edges met to form a closed cylinder, and defined this as the unloaded geometry, which, however, was subject to known non-zero residual stresses. This approach is fairly straightforward to implement for a cylindrical geometry, but quite cumbersome for a prolate ellipsoidal geometry for which an appropriate stress-free state would be difficult to conceive. We found no simple way to implement such an approach and delegated it to future research.

The second approach would be to define a suitable non-zero residual stress field that could be imposed as an initial condition on the existing geometry. Although ADINA permits the definition of initial stresses, we could not pursue this option because it is incompatible with our user-supplied material model. ADINA also permits the definition of initial strains, which are used to calculate initial stresses with the use of the chosen material model. Our attempts to implement such initial strains were unsuccessful. Another

option would be to modify our material model so that it would incorporate residual stresses. However, such a material model would require the inclusion of additional invariants, which would be functions of the residual stresses, as described by Hoger (1993). The introduction of these invariants would require the formulation of a completely new material model, which would require additional stress-stretch data for the calculation of its parameters. Because residual stresses have not yet been measured, such data are not available, and so it is not possible to put together such a material model.

The residual strains measured by Costa et al. (1997) were smaller than the strains calculated in the present simulations. This likely implies that the residual stresses corresponding to the measurements would also be smaller than the calculated ones. The effect of omission of residual stresses in the simulations cannot be estimated with any certainty because of the lack of relevant measurements. Nevertheless, because the overall stresses in the myocardium increase with increasing pressure, the relative contribution of residual stresses would most likely diminish with increasing deformation. This speculation is consistent with the improvement of the fit between our results and the measurements (Fig. 4.4b) as pressure increases. In summary, we cannot be entirely confident that by neglecting residual stresses we have not missed a significant effect on the prediction of LV deformation. Taking residual stresses into account would require a very significant additional effort and, even if it were accomplished numerically, it would not lead to conclusive statements, unless the stresses were validated against measurements which are not presently available.

4.5 Conclusions

Simulations of filling of the passive LV were performed successfully by inflating an unloaded, stress-free geometry to end diastole. For this geometry, the optimal choice among three sets of material parameters was determined as the one resulting in best agreement between normalized volume changes in the simulations and values obtained from previous experimental studies. By comparing transmural and longitudinal stresses calculated using two different mesh densities, we were able to show that our results are nearly mesh independent.

Through comparison to measurements made at end diastole, we verified that our chosen end-diastolic pressure leads to a state that is representative of end diastole. We have described the stresses at this state, found them to have complex non-zero spatial variations, which justifies the present approach of generating end-diastolic LVs by the application of a static pressure load, rather than adopting a stress-free, end-diastolic geometry in an *ad hoc* manner. Further, by comparison of our calculated stresses at our end-diastolic pressure to those at an intermediate pressure, we have illustrated that it is inappropriate to scale stresses obtained at an intermediate pressure by a constant factor to obtain stresses at end diastole.

Trends in the volumetric changes of principal stretches were found to be consistent with previous measurements. However, significant differences between the corresponding values in one direction were observed and attributed to the insufficient capacity of our model to account for wall compressibility. Trends in the volumetric changes of principal stresses were consistent with the form of our material model, but could not be validated due to a

lack of measurements of stresses in the myocardium.

Transmural variations of principal stretches showed fair qualitative agreement with previous measurements at an intermediate pressure. Differences between the longitudinal variations of principal stretches and principal stresses in this work and those in a previous computational study are attributed to the difference in the boundary conditions at the apex.

The sensitivity of the results of our simulations to the range of muscle fibre orientations and the number of wall layers was examined. Differences between principal stretch variations for two ranges of fibre orientations in the present study were very small and could not account for differences between principal stretches found in the current and previous studies. Moreover, it was found that the transmural variations of the principal stresses could not be resolved accurately with the use of a three-layer myocardium model, but the use of a six-layer model had sufficient resolution for the present purposes.

Lastly, we evaluated the various assumptions made in defining our numerical model and the potential impact that possible deviation from these assumptions may have had on our results. We speculated on the potential effects of residual stresses, and concluded that, although such effects might play some role, taking them into consideration properly would require validation against measurements which are not available at present.

In summary, the present simulation of static inflation of the LV to a pressure and volume that are typical of end diastole has provided us with a geometry and a stress distribution that are suitable as starting conditions for our ongoing cardiac cycle simulations with fluid-structure interaction. We found this to be necessary after considering that there are no available measurements of stresses in the myocardium and that the only previously

published calculations of stresses (Costa et al. (1996)) were not suitable for our use, because they were reported for a pressure that was much lower than our specified end-diastolic pressure and also because of distortion caused by the inclusion of a hole at the LV apex. The present article further enriches the related literature with some new results. Transmural and longitudinal variations of stresses through the myocardium at an internal pressure of 2 kPa have been presented for the first time. Moreover, we have shown that these stresses are extremely sensitive to pressure and that estimates of end-diastolic stress variations by scaling stresses obtained at a lower pressure would be inaccurate. Finally, we have demonstrated that the use of a three-layer myocardium model has inadequate resolution for stress calculations.

Chapter 5

Cardiac cycle simulations

5.1 Introduction

A complete numerical model of the mechanics of the heart requires both fluid and solid components, including geometries, material models, and boundary and initial conditions for each, which must be coupled together through fluid-structure interaction (FSI) effects. The numerical simulation of the mechanics of the entire heart including four deformable chambers and four moving valves is beyond current capabilities. Instead, researchers have generally focused their simulations on the left ventricle (LV), which is the main pumping chamber of the heart and is responsible for pumping blood through the body. The LV contains a single inlet and a single outlet; flow through the inlet is controlled by the mitral valve (MV), which separates the LV from the left atrium (LA), and flow through the outlet is controlled by the aortic valve (AV), which separates the LV from the aorta (Ao). The work presented in this chapter focuses on the mechanics of the LV over the cardiac cycle and builds upon the work presented in the previous two chapters, which described

the development of the myocardium material model and the calculation of an end-diastolic state to be used as an initial state for the present cardiac cycle simulations.

Following consideration that more information is available in the literature for canine hearts than any other mammal heart, including the human heart, it was decided to conduct this study for a canine heart model. An average LV was considered rather than a specific one because not all required model inputs from a single specimen were available and also because there is a large variability in many of these inputs from one specimen to the next. The choice of an average LV allowed the determination of values for all necessary model inputs by averaging data from the literature.

In Chapter 3, a material model for the canine LV myocardium was defined. The myocardium is the thick middle layer of the heart wall and contains the muscle fibres surrounded by an extracellular matrix; the other two layers, the epicardium and the endocardium, are relatively thin and will be neglected in the wall model for the present simulations. A material model for the myocardium is generally defined in terms of a strain energy density function with material properties that vary in two or three directions. Material models of the former are referred to as transversely-isotropic, and of the latter are referred to as fully orthotropic. Material directions in transversely-isotropic models are defined as fibre and cross-fibre, while material directions in orthotropic models are defined as fibre, sheet, and sheet-normal, for which the sheet direction is defined perpendicular to the muscle fibre direction in the surface that contains the fibres, and the sheet-normal direction is defined perpendicular to this surface. The definition of the material model for the myocardium is further complicated by the need to account for not only the stresses

caused by the deformation of the myocardium, which are referred to as passive stresses, but also the additional stresses caused by the contraction and relaxation of the muscle fibres, which are referred to as active stresses. The total stresses are calculated as the sum of the passive and active stresses. By varying the application of the active stresses as a function of time, the contraction and relaxation of the muscle fibres can be modeled.

In Chapter 4, solid-only simulations of the inflation of the passive LV to an end-diastolic state were described; the objective of these simulations was to produce results that are usable as an initial state for cardiac cycle simulations. These simulations began from diastasis, which is the middle phase of filling, and is characterized by both a small magnitude of pressure inside the LV cavity and a small pressure difference between the LA and the LV (Sabbah and Stein (1981)). Further, one can infer that the blood flow velocities and myocardium stresses during diastasis are at their lowest values during the cardiac cycle. Under the assumptions of zero wall stress, zero pressure, and fully relaxed muscle fibres, the reference geometry at diastasis was inflated to an end-diastolic pressure. In the present study, the procedure described in Chapter 4 was replicated and quasi-static FSI simulations of the inflation of the passive LV were performed to generate initial conditions for the cardiac cycle simulations.

The primary objective of the present study is to perform FSI simulations of the mechanics of a canine LV over the cardiac cycle. These simulations make use of the myocardium material model from Chapter 3, which was adapted and validated for the canine LV and featured both passive and active components, and the methodology for generating initial conditions at end diastole, as described in Chapter 4. While the simulations are

not specimen-specific due to the use of an idealized average canine LV geometry, wherever possible, each phase has been rigorously validated with the goal of obtaining results that are representative of an average canine LV and are both physiologically plausible and comparable to previous studies. In this chapter, the details of the numerical model have been explicitly specified to illuminate issues relating to the performance of such simulations. The simulations have also been designed in a modular way such that pieces of the model, such as the geometry, could be modified at a later time, if more appropriate choices become available in the literature.

5.2 Literature review

Previous numerical studies of the mechanics of the heart are divided into three groups, solid-only, which specify the pressure from the flowing blood as boundary conditions; fluid-only, which specify the motion of the heart wall through boundary conditions; and FSI, which solve the motions of the fluid and solid phases and couple them together on the fluid-solid boundaries.

5.2.1 Solid-only simulations

Solid-only simulations of myocardium mechanics are generally performed to validate or modify previously-defined material models to increase understanding of the mechanical behaviour of the myocardium. Guccione et al. (1995) performed solid-only simulations over the cardiac cycle using an axisymmetric canine LV geometry, and a transversely-isotropic material model with time-varying active stresses in the fibre-direction only. From

their results at end diastole, the authors suggested that it may be necessary to vary the passive material properties through the myocardium to capture better the variation of end-diastolic strains found experimentally. They also found that at end systole, some of their strain components were in good agreement with previous experiments, but others deviated substantially, suggesting the need for further work to model more accurately the active behaviour of the myocardium.

Nash and Hunter (2000) performed quasi-static simulations of the systolic phase of the cardiac cycle. These simulations started from an end-diastolic canine LV/RV geometry, which was calculated from anatomical measurements (Nielsen et al. (1991)) of excised canine ventricles arrested during diastole. Their material model consisted of two parts, an orthotropic passive model, referred to as the “pole-zero” equation, and a uniaxial (in the fibre direction only) active model. Limited comparisons were made between the results of this study and previous experiments. Stevens and Hunter (2003) extended this work to the simulation of the mechanics of porcine ventricles over the cardiac cycle through the use of a more complex active material model.

Usyk et al. (2000) performed their simulations to determine the influence of passive material orthotropy during filling and transverse active stresses during ejection. The passive myocardium was modeled as a slightly compressible orthotropic material, while either a uniaxial or transversely isotropic active model. The orthotropic passive material parameters were adapted from a transversely isotropic material model to improve their agreement with average strain measurements made in intact canine LVs. The compressibility was also modified to match myocardium volume changes. While the incorporation of orthotropy

improved end-diastolic results, end-systolic strains calculated using transversely isotropic and orthotropic passive material models showed only minor differences. At end systole, strains calculated for the biaxial case showed better agreement with the experiments than the uniaxial case, but the biaxial active model was still not sufficient to correctly predict the trends for all strain components suggesting that an orthotropic active material model may be required.

Kerckhoffs et al. (2007) performed simulations of the mechanics of a canine LV/RV geometry, coupled with lumped parameter models of the systemic and pulmonary circulations. They used optimized passive material parameter values (Usyk et al. (2000)), with additional active stresses in the fibre direction. They performed multiple periods of their simulations to achieve a “steady-state” solution for healthy and diseased ventricles.

Kroon et al. (2009) performed simulations of the deformation of a canine LV myocardium, for which they allowed the local muscle fibre orientations to adapt to minimize shear strain, under the hypothesis that this adaptation would account for discrepancies in the material behaviour found with previous models. Their geometry was defined as a truncated prolate ellipsoid (which is an ellipse that has been rotated about its major axis) and was coupled to a lumped parameter model of the circulatory system to form a closed loop. They assumed the myocardium to be a transversely isotropic material with separate passive and active material properties. During systole, Kroon et al. allowed the muscle fibre orientations to adapt such that over multiple cycles the shear strain was minimized. The muscle fibre orientations were defined by two angles, a helical angle and a transverse angle. Through their adaptation, they found that although their initial helical angles, taken

from a previous study, were nearly equal to their final values, their initial transverse angles, which were chosen to be 0° throughout the wall were adapted substantially, resulting in non-zero transverse angles, which varied through the wall and from the apex to the base. The resulting angles showed very good agreement with previous measurements.

These solid-only simulations show the need for additional research into the complex material behaviour of the canine LV myocardium. Observations made by Guccione et al. (1995) as well as adaptations of material parameter values (Usyk et al. (2000)) and material direction orientations (Kroon et al. (2009)) suggest that it is insufficient to study the material behaviour of pieces of the myocardium, and that the material behaviour of the entire LV wall should be considered. Additionally, although adaptations of material parameters (Usyk et al. (2000); Kroon et al. (2009)) improved the agreement between simulated and measured strains, stresses in the LV myocardium have not yet been measured *in vivo* and additional insight into the material behaviour may be gained through the measurement of these stresses. Further insight into the behaviour of the myocardium could also be gained through the coupling of these solid models with fluid models of the incoming and outgoing blood flow. In most solid-only simulations, uniform time-varying LV cavity pressures were specified. As will be shown in the present study, the inclusion of flowing blood introduces non-uniform LV cavity pressures, which causes changes in the deformation of the myocardium that would differ from the changes calculated with a uniform pressure field.

5.2.2 Fluid-only simulations

Computational fluid dynamic (CFD) simulations of the LV examine the flow of blood into and out this chamber. These simulations rely on the specification of myocardium motion, either through simplifying assumptions or through the definitions of multiple fluid meshes throughout the cardiac cycle based on magnetic resonance imaging (MRI) techniques. Several CFD-MRI studies (Saber et al. (2001); Saber et al. (2003); Long et al. (2003); Long et al. (2008)) have been performed for the LV. Saber et al. (2001) approximated the valves as instantly opening and closing as their MRI data could not sufficiently resolve the valve leaflets or their motion. They initially (Saber et al. (2001)) considered uniform pressure boundary conditions to drive the flow during diastole, but improved MRI techniques improve their inflow and outflow conditions by including the ascending aorta and part of the LA (Saber et al. (2003)). The goal of the study of Long et al. (2003) was to determine the effects of inflow boundary conditions on the flow during diastole. They found a large variability in results with changes in inflow boundary conditions, indicating the importance of proper inflow boundary conditions. However, additional work is still required, because the authors believe that the motion of the MV annulus also influences the flow and this motion was neglected in their study. Long et al. (2008) recently used improved MRI techniques to extend their work.

Nakamura et al. performed two-dimensional (Nakamura et al. (2001)) and three-dimensional (Nakamura et al. (2002); Nakamura et al. (2003); Nakamura et al. (2006b)) CFD simulations of blood flow in the LV during diastole. They assumed that intraventricular pressure was insufficient to drive wall motion during diastole, so they neglected FSI

effects and calculated the wall motion independently from the flow. These studies focused on the opening of the MV and its effect on the flow in the LV. Nakamura et al. (2002) and Nakamura et al. (2006b) found noticeable differences in the blood flow depending on how the valve was opened, suggesting the importance of including MV motion in a study of LV filling. Lastly, Nakamura et al. (2006a) added a model of the aorta to their previous LV geometry (Nakamura et al. (2003)) to investigate flow in the LV and the aorta during systole with prescribed wall motions.

Baccani et al. (2002), Baccani et al. (2002), and Baccani et al. (2003) modeled the LV as a two-dimensional axisymmetric ellipse truncated at its maximum diameter. They used the change in LV cavity volume due to the incoming fluid to explicitly calculate the change in diameter and height of their ellipse. In their first two studies (Baccani et al. (2002); Baccani et al. (2002)), the authors assumed the MV to be stationary, while in the third study (Baccani et al. (2003)), they modified their model to account for MV motion. This work was extended to three-dimensions (Domenichini et al. (2005)) by rotating their axisymmetric geometry; however, the 3-D simulations did not account for MV motion. Lastly, Domenichini et al. (2007) performed numerical simulations, based on their previous works, and experiments, using an idealized rubber LV model. Although small differences existed between their numerical and experimental models, they found very good agreement between the velocities in the two cases.

Doenst et al. (2009) and Schenkel et al. (2009) performed patient-specific combined CFD/MRI simulations of the human heart, which they refer to as the Karlsruhe Heart Model. Their heart model consisted of the whole heart and the greater vessels (aorta, pul-

monary artery, and vena cava). The motions of the ventricles and atria were driven by MRI data, whereas the greater vessels were rigid (Doenst et al. (2009)). The valves were modeled as planes and the opening and closing of the valves was controlled by baffle boundary conditions in which the pressure drop across each valve varied from infinity for a closed valve to zero for an open valve. Pressure boundary conditions at the distal ends of the greater vessels were calculated from electric circuit models of the cardiovascular system. Simulation results were presented for the LV only. Velocity vectors and streamlines during diastole showed qualitative agreements with *in vivo* data (Schenkel et al. (2009)). Doenst et al. examined LV blood flow of a healthy volunteer as well as a patient before and after surgery to determine the effect of the surgery on the flow.

Fluid-only simulations can be divided into two general categories, namely those in which the wall motion is assumed and those in which the wall motion is defined based on medical images. Studies in which the wall motion is assumed are unable to resolve the complex non-uniform deformations of the myocardium over the cardiac cycle. Assuming sufficient spatial and temporal resolutions, studies in which the wall motions are specified capture the deformation of the myocardium for a specific period for a specific LV geometry. In either case, the influence of the blood flow on the wall deformation is not included in the numerical models. Further, in the case of CFD-MRI studies, what-if scenarios cannot be considered because there is no feedback mechanism to adjust the deformation of the myocardium for different flow conditions. To truly capture the complex interactions between the blood flow and the motion of the myocardium, fully coupled FSI models are required.

5.2.3 Fluid-structure interaction simulations

FSI simulations of the heart can be divided into two general groups, those that use finite element or finite volume techniques, which generally consider a single heart chamber, and those that use the immersed boundary method (IBM), which can be used for the entire heart. IBM models are capable of including multiple heart chambers and moving valves, but not of calculating stress-strain results for the myocardium.

Watanabe et al. (2002), Watanabe et al. (2003), Watanabe et al. (2004), and Watanabe et al. (2004) performed FSI simulations of LV mechanics over the cardiac cycle using an idealized human LV geometry based on MRI data. Their myocardium material model consisted of passive and active components and was adapted from the one proposed by Lin and Yin (1998) based on measurements of pieces of rabbit LV myocardia. Passive material parameters were calculated as fractions of the values given by Lin and Yin and active parameters were determined to satisfy model criteria. To account for the variation in active material properties during the contraction and relaxation of the muscle fibres, the authors defined the active material parameters as the products of their maximum values and a forcing function, calculated by an electrophysiological model, which varied from 0 when the muscle fibres were fully relaxed to 1 when they were fully contracted. They defined electric circuit models to account for the preload and afterload of the LV and coupled these models to their finite element simulations as boundary conditions at the LV inflow and outflow tracts. Both fully coupled FSI and solid-only simulations were performed. In the “solid-only” cases, which were performed statically, the fluid inertia was neglected, and the pressure on the FSI boundary was calculated through coupling between the solid model and

the electric circuit models. The results from these studies demonstrate the feasibility of performing FSI simulations of the mechanics of the LV over the cardiac cycle. However, these simulation results have not been validated against experiments.

Three previous research groups (Deserranno et al. (2003); Cheng et al. (2005); Yang et al. (2007)) have used ADINA (ADINA R & D, Inc., Watertown, MA, USA), which is the chosen software for the present study, to perform FSI simulations of the mechanics of the LV or RV. Deserranno et al. (2003) simulated axisymmetric filling of an ellipsoidal LV geometry with a flexible valve leaflet. To model the temporal variation of the wall stiffness, the authors wrote a user-defined FORTRAN function for a time-varying Young's modulus.

Cheng et al. (2005) simulated the filling of a thin-walled ellipsoidal LV with time-varying solid wall properties. Their geometry was three-dimensional, with separate LV outflow and inflow tracts and a symmetry plane allowing for the simulation of only the posterior half. To model a time-varying Young's modulus for the LV wall, the authors assumed multiple constant Young's moduli and for each one, applied several time-varying intraventricular pressures. They interpolated between the resulting pressure-volume curves to define a curve that would lead to the correct form of the input pressure wave. They adjusted this curve until their desired input pressure wave was reproduced. Their results, which consist of plots of pressure contours and velocity vectors at several times during filling, were qualitatively comparable to other works, both experimental and computational.

Yang et al. (2007), Tang et al. (2008), and Tang et al. (2010) performed FSI simulations of a human RV/LV geometry based on MRI data. The objective of these studies was to model the mechanics of the RV. The LV was included to account for the

interaction between the LV and RV; to reduce computational time, flow in the LV was not considered but rather the shape of the LV was controlled by a uniform pressure boundary condition applied to the wall. They assumed the RV wall to be a nearly-incompressible material, which they modeled using either an isotropic or an anisotropic version of the Mooney-Rivlin material model (Tang et al. (2010)). To account for the active contraction of the muscle fibres, time-varying material stiffnesses were specified, but no further details were provided in their articles on how this was implemented. In their most recent model (Tang et al. (2010)), to account for the variation of muscle fibre angles in the myocardium, they defined wall layers with different fibre angles. Flow in the RV was driven by pressure boundary conditions applied at the ends of the inflow and outflow tracts. Valves were modeled as instantly opening and closing, with a closed valve modeled by a zero velocity boundary condition. These authors neglected the isovolumetric phases of the cardiac cycle, such that one valve was open throughout the simulations.

Krittian et al. (2010) and Oertel et al. (2009) performed FSI simulations of blood flow in the LV of their Karlsruhe Heart Model. These studies were motivated by their inability to “capture the effects of out of plane movement or torsion” with a CFD/MRI study (Krittian et al. (2010)). Their simulations were performed using the commercial software packages Abaqus (SIMULIA, Providence, RI, USA) for the solid and FLUENT (ANSYS, Inc., Canonsburg, PA, USA) for the fluid, which were coupled together using MpCCI (Fraunhofer SCAI, Germany). The authors assumed that the myocardium was incompressible and comprised an isotropic matrix containing muscle fibres. Their solid material model consisted of passive and active components. The passive component was

defined as a transversely-isotropic material with parameter values calculated for pig LVs (Schmid et al. (2009)). The active component appears to apply stresses in the fibre direction only but details of this model are not clear. Their simulations began from atrial contraction, for which the initial state of the myocardium was assumed to be stress-free. Four different valve opening percentages were specified, but details on how the valve opening was implemented were not provided. The authors also did not provide details on any fixed boundary conditions or on how they dealt with issues relating to the isovolumetric phases of the cycle, during which they presumably had both valve closed creating an enclosed fluid region with deformable boundaries. The results of the fluid phase for this study resembled the blood flow results obtained for their previous CFD/MRI studies and represent a substantial step in FSI simulations of blood flow in the LV. The results presented by these authors were limited to the fluid domain only, and did not address the myocardium.

To date, the only complete FSI models of the heart containing all four chambers and moving valves were simulated using the IBM, which was developed by Peskin in the 1970s (Peskin (1977)). The IBM is a technique for FSI in which a viscous incompressible fluid is solved on a regular grid and the solid is defined as a group of infinitesimal fibres, containing no mass or volume, which surround the fluid (Peskin and McQueen (1996)). The solid fibres are “immersed” in the fluid domain and can move freely without deforming the fluid mesh. Peskin’s IBM heart model was three-dimensional and included all four heart chambers, all four moving valves, the ascending aorta, the pulmonary artery, the inferior and superior vena cavae, and four pulmonary veins (McQueen and Peskin (1997); McQueen and Peskin (2000); McQueen et al. (2001)). The great vessels that surround the heart act

as sources or sinks for the blood flow. Although based on anatomical observations, the heart geometry and muscle fibres were defined mathematically. Time-varying stiffness and resting lengths were defined for the fibres to account for their changing properties during the cardiac cycle. Using this model, the complete cardiac cycle was simulated. Although the IBM is able to provide detailed results for the blood flow in the heart, it cannot perform quantitative solid mechanics due to the lack of volume and mass present in the solid fibres.

Vigmond et al. (2008) recently performed simulations which coupled Peskin's IBM heart model with their interconnected cable method for modeling the electrical activity in the heart. This coupled model therefore contains blood flow and the mechanical and electrical behaviour of the heart wall; however, the coupling between the electrical and mechanical models is currently unidirectional from the electrical to the mechanical.

FSI models that make use of the IBM fail to capture the complex mechanics of the LV myocardium during the cardiac cycle. Previous finite element or finite volume models have made simplifying assumptions about the geometry, boundary conditions, and/or myocardium material models that prevent them from accurately capturing the complete mechanical behaviour of the LV. In particular, FSI studies that show detailed blood flow results have in general not included detailed results of myocardium mechanics.

5.3 Methods

5.3.1 Cardiac cycle definitions

This section presents a brief description of the cardiac cycle. Further details can be found in Chapter 2. The period for the cardiac cycle simulations has been chosen to

Table 5.1: Durations of the phases of the cardiac cycle for a heart rate of 100 beats/min.

phase	τ
IVC	0.055
ejection	0.257
IVR	0.073
filling	0.615

be 600 ms/heartbeat, which corresponds to a heart rate of 100 beats/min. Simulations in the present study start at end diastole and proceed through the four phases of the cardiac cycle, isovolumetric contraction (IVC), ejection, isovolumetric relaxation (IVR), and filling, with the duration of each phase given in Table 5.1 in non-dimensional form, where τ is the time normalized by the period.

5.3.2 Geometry

The reference geometry used in this study, hereafter referred to as DG, was defined at diastasis. It is from this reference geometry that the LV was inflated to an end-diastolic state prior to the start of the cardiac cycle simulations. The reference solid geometry was defined as a truncated prolate ellipsoid with an outer semi-major axis of $a = 46.92$ mm, an outer semi-minor axis of $b = 27.84$ mm, an apical thickness of $t_a = 6.83$ mm, an equatorial thickness of $t_b = 12.42$ mm, and a total height of $h = 60.14$ mm, as shown in Fig. 5.1a. This geometry consisted of six wall layers, each with their own unique muscle fibre orientation, ranging from -60° in the outer layer to $+60^\circ$ in the inner layer, with the angles defined with respect to the local circumferential direction. This range of fibre angles was chosen as it is representative of the average ranges found in canine LVs, based on measurements obtained from two independent studies (Streeter et al. (1969); Nielsen et al. (1991)).

The parts of the LV geometry that contain fluid are shown in Fig. 5.1b. This figure also illustrates three geometrical landmarks that will be referred to throughout this article: the basal plane, which is the top plane that truncates the ellipsoid, the equatorial plane, which is the horizontal plane passing through the centre of the full ellipsoid; and the apex, which is the lowest point of the LV. The fluid geometry was divided into two sections by the basal plane; the section above this plane was taken to be rigid and the section below the plane was taken to be deformable. The boundary of the lower section matched the inner boundary of the corresponding solid geometry allowing for matching FSI boundary conditions to be applied to the fluid and solid models. The upper section included two cylindrical tubes of equal lengths L_1 , which represented the inflow and outflow tracts of the LV and contained idealized zero-thickness mitral and aortic valves, respectively, at a distance L_2 from the distal end of the cylinders. The reason for not defining the valve planes at the proximal ends of the LV inflow and outflow tracts was that, in that case, the two valves would have a common point, at which flow erroneously passes through a valve when it is closed. To complete the fluid geometry, a section of a sphere was added to the top of the lower section of the geometry, whose radius R and centre were chosen such that the sphere passes through all three points of the triangle that makes up the lower edges of the LV inflow and outflow tracts, as shown in Fig. 5.1b. Figure 5.2 depicts this sphere as a semi-circle and also includes the triangle from Fig. 5.1b and the dimensions needed to determine suitable values of R , and the height of the centre of the sphere z_c , where z_c is measured from the apex of the fluid geometry. The dimensions for the fluid geometry were $D_{AV} = 9.78$ mm, $D_{MV} = 18.88$ mm, $L_1 = 9.78$ mm, $L_2 = 7.78$ mm, $w_1 = 26.71$ mm,

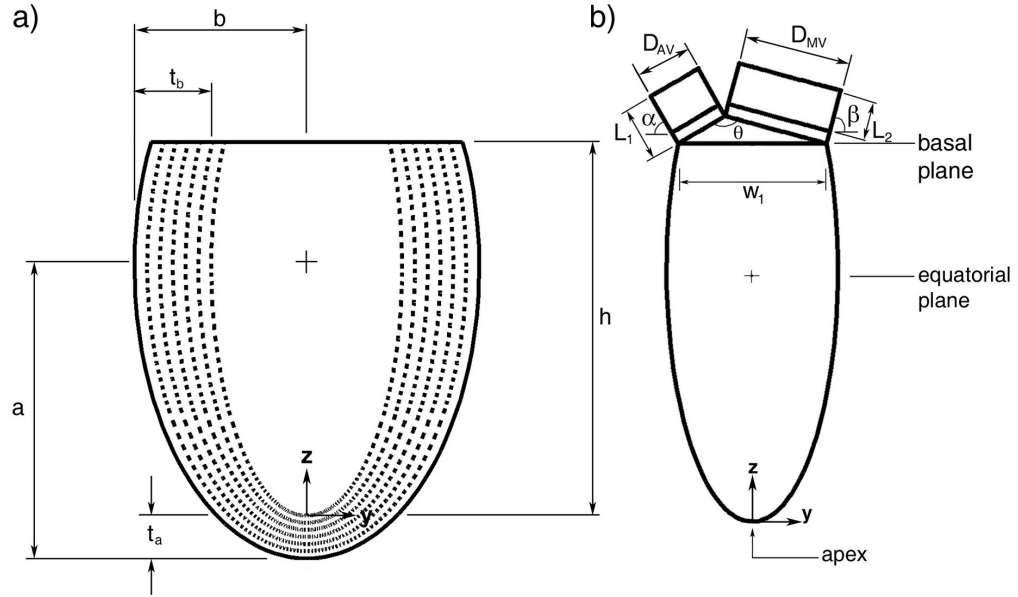


Figure 5.1: Diagram showing the solid (a) and fluid (b) geometries along with key dimensions and geometric landmarks.

$\alpha = 60^\circ$, $\beta = 75^\circ$, and $\theta = 135^\circ$. Using the Pythagorean theorem with $w_1 = 26.71$ mm, $w_2 = 9.78$ mm, and $h_3 = 4.89$ mm, the radius of the sphere and the height of its centre were calculated to be $R = 18.88$ mm and $z_c = 46.78$ mm. Once the sphere was defined, it was truncated at the height h , to leave only the section above the basal plane. The cylinders were then subtracted from the remaining piece of the sphere, leaving circular surfaces at each interface. Additional details on the definition of the upper section of the fluid geometry are provided in Appendix D.1.

5.3.3 Mesh

The solid geometry was meshed using ten-node tetrahedral elements on an unstructured grid, which consisted of 53,920 elements (78,252 nodes). While this mesh is undoubtedly fine enough to describe accurately the LV cavity volume changes and stretches,

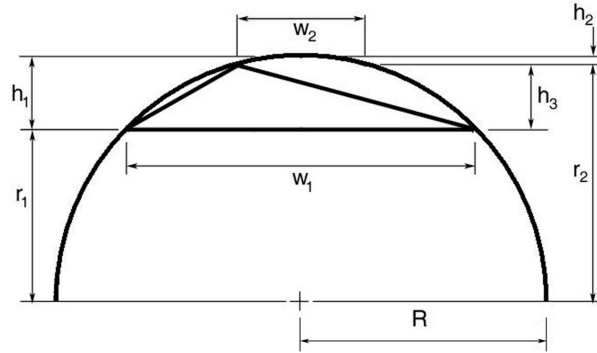


Figure 5.2: Diagram showing the dimensions used to define the section of a sphere used to cap the fluid geometry

it was shown in Chapter 4 for solid-only simulations, that a finer mesh would be required to fully resolve the stresses. Attempts to use a refined solid mesh were unsuccessful, as this caused the FSI simulations to diverge. Further investigation into this issue is required and is delegated to future work.

The fluid geometry was meshed using 4-node tetrahedral elements on an unstructured grid. These elements have nodes at each corner to calculate velocity and pressure. For stability, they use an additional node in the centre to calculate velocity. These elements are generally referred to as MINI elements and the additional velocity degree of freedom at the element centre is called the bubble velocity (Gresho and Sani (1998)). Two mesh densities were considered for the fluid, 132,667 elements (24,023 nodes) and 233,811 elements (41,733 nodes), which will be referred to as mesh 1 and mesh 2, respectively. Figure 5.3a shows the mesh for the solid and Fig. 5.3b shows mesh 1 for the fluid.

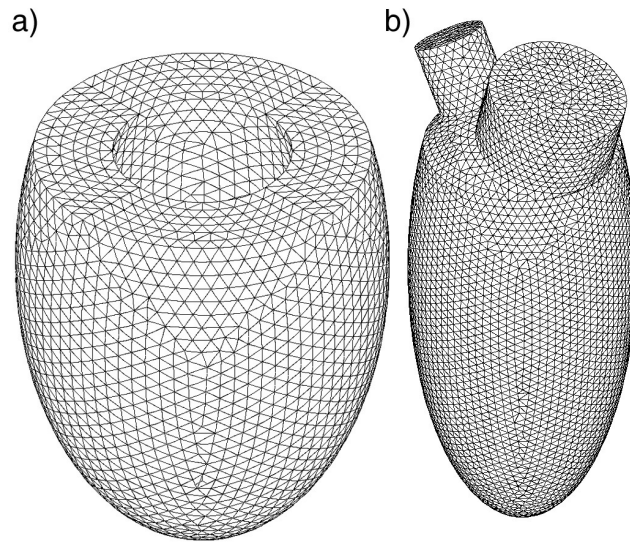


Figure 5.3: Mesh for the solid geometry (a) and mesh 1 for the fluid geometry (b).

5.3.4 Numerical methods

Simulations in this study were performed using the commercial finite element software ADINA v. 8.5.2 (ADINA R & D, Inc., Watertown, MA, USA), for which separate solid and fluid models are defined and linked through coincident FSI boundary conditions. Further details on the ADINA software can be found in ADINA R & D, Inc. (2008a), ADINA R & D, Inc. (2008b), and Bathe (1996). Simulations were performed on the clusters of the High Performance Computing Virtual Laboratory (HPCVL), which are available to researchers at several universities and colleges in Eastern Ontario, Canada. Details on the specific clusters used for these simulations, as well as the results of parallelization studies performed on one of these clusters are provided in Appendix A.

Governing equations for the myocardium

The LV myocardium undergoes large displacements for large strains and has highly non-linear material behaviour, which are best simulated with the use of the Total Lagrangian form of the governing equations. Simulations in this work were performed dynamically, that is, with respect to time. The appropriate form of the governing equation for the solid model is therefore

$$\mathbf{M}\ddot{\mathbf{U}}(t + \Delta t) + \mathbf{C}\dot{\mathbf{U}}(t + \Delta t) + \mathbf{K}(t)[\mathbf{U}(t + \Delta t) - \mathbf{U}(t)] = \mathbf{R}(t + \Delta t) - \mathbf{F}(t) \quad (5.1)$$

where \mathbf{U} , $\dot{\mathbf{U}}$, and $\ddot{\mathbf{U}}$ are the nodal displacement, velocity and acceleration vectors, respectively, \mathbf{M} is the mass matrix, \mathbf{C} is the damping matrix, \mathbf{K} is the stiffness matrix, \mathbf{R} is the external load vector, \mathbf{F} is the force vector equivalent to the element stresses, and t is time (ADINA R & D, Inc. (2008a)). It should be noted that in Eq. (5.1), \mathbf{R} is independent of deformation, but $\mathbf{F}(t)$ is a function of $\mathbf{U}(t)$. Following the definition of a suitable stiffness matrix, the solid equations are solved using the implicit Newmark method, described in detail by Bathe (1996).

To calculate $\mathbf{K}(t)$ and $\mathbf{F}(t)$, a constitutive equation for the myocardium material is required. For this study, the myocardium was modeled as a slightly compressible transversely isotropic hyperelastic material, with properties that differed in the fibre and cross-fibre directions. It was defined by a strain energy density function W , which consisted of passive (p) and active (a) parts. By varying the application of the active stresses in time, the contraction and relaxation of the muscle fibres was modeled. The strain energy density function used in this study has been described in detail in Chapter 3 and is defined as

$$W = W_p + W_a \quad (5.2)$$

where

$$W_p = C_1 (e^Q - 1) + \frac{1}{2} \kappa_s (J_3 - 1)^2 \quad (5.3)$$

$$Q = C_2 (J_1 - 3)^2 + C_3 (J_1 - 3) (J_4 - 1) + C_4 (J_4 - 1)^2 \quad (5.4)$$

$$W_a = D_0 + D_1 (J_1 - 3) (J_4 - 1) + D_2 (J_1 - 3)^2 \\ + D_3 (J_4 - 1)^2 + D_4 (J_1 - 3) + D_5 (J_4 - 1) \quad (5.5)$$

In Eqs. (5.3-5.5), C_i and D_i are passive and active material parameter values, respectively, κ_s is the bulk modulus, which governs the material compressibility, and J_i are reduced invariants of Green's strain tensor \mathbf{E} .

From this constitutive equation, the components of the second Piola-Kirchhoff stress tensor \mathbf{S} can be calculated as follows

$$S_{ij} = \frac{\partial W}{\partial E_{ij}}, i, j = 1, 2, 3 \quad (5.6)$$

Based on the analysis presented in Chapter 4, $C_1 = 2.117$ kPa, $C_2 = 0.498$, $C_3 = 0.237$, $C_4 = 0.0332$, $C_5 = 0.01$, $C_6 = 0.0005$, and $\kappa_s = 1 \times 10^7$ kPa. For the active material model, to account for the contraction and relaxation of the muscle fibres, the material parameters D_i are defined as

$$D_i = F D_{i,\max} \quad (5.7)$$

where F is a forcing function, which varies between 0 when the muscle fibres are fully relaxed and 1 when the muscle fibres are fully contracted, and $D_{i,\max}$ are the values of the active material parameters when the muscle fibres are fully contracted (Watanabe et al. (2004)). By varying the value of F over the interval $0 \leq F \leq 1$, the contraction and relaxation of the muscle fibres were modeled. Using the relationship between the forcing function proposed by Watanabe et al. (2004) and their simulated LV pressure function as a guide, along with a chosen cardiac cycle period of 600 ms/heartbeat and the durations of the phases of the cardiac cycle given in Table 5.1, a forcing function was defined, such that the muscle fibres contract during IVC and rapid ejection, and relax during reduced ejection, IVR, and early filling. This forcing function was defined by four sigmoid functions (two increasing and two decreasing) as

$$F = \left\{ \begin{array}{l} 1 / (1 + e^{-a_1(\tau - b_1)}), \quad 0 \leq \tau < 0.052 \\ 1 / (1 + e^{-a_2(\tau - b_2)}), \quad 0.052 \leq \tau < 0.170 \\ 1 / (1 + e^{-a_3(\tau - b_3)}), \quad 0.170 \leq \tau < 0.330 \\ 1 / (1 + e^{-a_4(\tau - b_4)}), \quad 0.330 \leq \tau \leq 1.000 \end{array} \right\} \quad (5.8)$$

where a_i control the slopes of the sigmoid functions and b_i control the locations of their centres. Through multiple simulations, the parameters for the sigmoid functions were adjusted such that the resulting LV pressure waveform resembles previous measurements (Sabbah and Stein (1981)) over the majority of the cardiac cycle; the values of these parameters are summarized in Table 5.2 and the resulting sigmoid functions are plotted in Fig. 5.4.

The values of the active material parameters $D_{i,\max}$ are defined in terms of a multiplier χ , which multiplies the active stresses from measurements of rabbit active stresses

Table 5.2: Parameter values for sigmoid forcing functions.

function	a_i	b_i
1	100.00	3.06
2	100.00	3.06
3	60.61	10.61
4	60.61	10.61

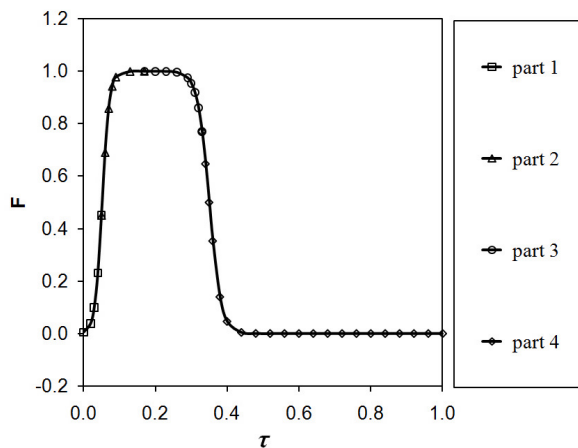


Figure 5.4: Forcing function.

from Lin and Yin (1998) to approximate the active stresses in a canine LV, as described in Chapter 3. The values of $D_{i,\max}$ as functions of χ are given in Table 5.3. Note that because only the derivative of W is required to calculate stresses, the value of D_0 in Eq. (5.5) is not needed and has been set to be zero. In parallel with modifications of the sigmoid function parameters, χ was also modified to match, as much as possible, the LV pressure waveform measured by Sabbah and Stein (1981). Simulations were performed for several values of χ , as discussed in Section 5.4.3, following which the value $\chi = 4.5$ was selected.

Table 5.3: Active material parameter values.

parameter	value (kPa)
$D_{1,\max}$	-0.352χ
$D_{2,\max}$	2.476χ
$D_{3,\max}$	2.660χ
$D_{4,\max}$	0.0251χ
$D_{5,\max}$	0.632χ

Governing equations for the fluid

Blood consists of 55% (by volume) plasma, which is a liquid, and three types of solid formed elements, which are red blood cells, white blood cells, and platelets. Plasma, which is 90-92% water and 8-10% solutes, behaves like a Newtonian fluid. However, with the addition of the formed elements, whole blood behaves like a non-Newtonian fluid. The non-Newtonian effects of blood become more significant with decreasing blood vessel size (Pedley (1980)), but it is generally accepted that blood can be assumed to be a Newtonian fluid when modeling flow in the heart, the aorta and other large vessels. In the present study, blood is assumed to be a Newtonian fluid with a density $\rho_f = 1050 \text{ kg/m}^3$ (defined at zero pressure) and a viscosity $\mu = 0.00316 \text{ kg/m} \cdot \text{s}$ (Cheng et al. (2005)).

To ensure solution convergence during the isovolumetric phases of the cardiac cycle, during which both valves are closed and the LV cavity is deforming, blood was set to be a slightly compressible fluid with a bulk modulus $\kappa_f = 1 \times 10^7 \text{ kPa}$, which matches the value for the myocardium. It was necessary to set equal values for the bulk moduli of the fluid and the solid in order to prevent compression of the material that would have the smaller bulk modulus.

During FSI computations, the fluid domain changes with time, causing the fluid

mesh to deform. Typically, fluid simulations are performed using an Eulerian approach, in which the mesh remains stationary and the fluid moves through it. A contrasting approach, referred to as Lagrangian, is typically used in solid simulations, where the mesh moves with the deforming material. For FSI simulations, a hybrid approach, referred to as arbitrary-Lagrangian-Eulerian (ALE), is used. The ALE method allows fluid flow to be tracked through a moving mesh. Moving boundaries are tracked using the Lagrangian approach, while stationary boundaries make use of the Eulerian approach, with the ALE method used at all points in between (Bathe (1996)). The ALE form of the continuity and momentum equations for slightly compressible fluids are defined as

$$\frac{\rho_f}{\kappa_f} \left(\frac{\partial p}{\partial t} + (\mathbf{v} - \mathbf{w}) \cdot \nabla p \right) + \rho_m \nabla \cdot \mathbf{v} = 0 \quad (5.9)$$

$$\rho_f \frac{\partial \mathbf{v}}{\partial t} + \rho_f (\mathbf{v} - \mathbf{w}) \cdot \nabla \mathbf{v} - \nabla \cdot \boldsymbol{\sigma}_f = \mathbf{f}^B \quad (5.10)$$

where p is pressure, \mathbf{v} is the velocity vector, \mathbf{w} is the mesh velocity vector, ρ_m is the density of the compressible fluid, $\boldsymbol{\sigma}_f$ is the stress tensor, and \mathbf{f}^B is the body force per unit volume (ADINA R & D, Inc. (2008b)).

The density ρ_m is defined as

$$\rho_m = \rho_f \left(1 + \frac{p}{\kappa_f} \right) \quad (5.11)$$

Note that in the limit as $\kappa_f \rightarrow \infty$, $\rho_m \rightarrow \rho_f$ and Eq. (5.9) reduces to its incompressible form.

Based on the Newtonian fluid assumption, $\boldsymbol{\sigma}_f$ can be defined as

$$\boldsymbol{\sigma}_f = -p\mathbf{I} + \mu(\nabla\mathbf{v} + \nabla\mathbf{v}^T) \quad (5.12)$$

where \mathbf{I} is the identity matrix.

Because the governing equations for the fluid are non-linear, the solution of the fluid system of equations requires two steps, outer iterations, which are used to generate a system of linear equations, and the solving of this linearized system. For the outer iterations, the Newton-Raphson method was used, and for the linearized system of equations, a direct sparse solver was used (ADINA R & D, Inc. (2008b)).

Time steps

Time integration for the FSI simulations is controlled by the fluid model. In the present study, the second-order ADINA composite method was used for time integration. This is an implicit time-stepping method; details of this method can be found in Appendix D.2.

Two time step durations were considered in the present study, 600 time steps of 1 ms and 303 time steps, which consisted of 297 time steps of 2 ms and 6 time steps of 1 ms. The additional 1 ms time steps were included for the times when the valves opened or closed so that these times matched for both time step durations. The times at which the valves opened or closed were chosen based on the pressure boundary conditions from Sabbah and Stein (1981) and three of these four times were most closely approximated by odd integers, which is the reason for using these additional time steps.

The automatic time stepping option in ADINA was used as a means to facilitate convergence of the numerical simulations. In the event that the simulations start to diverge

because the time step is too large, this option automatically subdivides the time step, up to a specified maximum number of times, which promotes convergence (ADINA R & D, Inc. (2008b)).

Fluid-structure interaction

Simulations in this work were performed using a direct FSI coupling method, in which the equations for the fluid, solid, and fluid-solid interface are solved simultaneously. This contrasts with the partitioned method, in which fluid and solid systems of equations are solved sequentially. The direct method is faster and more stable than the partitioned method, but it requires more RAM, because both fluid and solid models need to reside in memory at the same time. From experience, the direct method has been found to be more stable than the partitioned method. Attempts to perform simulations in the present study using the partitioned method resulted in the simulations diverging during the first time step. Further details on these methods along with the FSI boundary conditions enforced in ADINA are provided in Appendix D.3.

Initial conditions

Prior to beginning cardiac cycle simulations, initial conditions at end diastole were generated by inflating DG to an end-diastolic pressure of $p_{LV} = 2$ kPa using a procedure described in Chapter 4. In the previous study, only the solid geometry was considered and the simulations were performed statically. In the present study, both the fluid and the solid were considered, and the simulations were performed quasi-statically, that is with a sufficiently large time step as to minimize the velocity of the incoming blood flow, such

that its effect on the deformation of the myocardium was negligible. To do so, the time interval over which the simulations were performed had to be sufficiently long but not so long as to prevent the simulations from being completed within an acceptable amount of computational time. The resulting simulations consisted of 250 time steps, each with a duration of 80 ms.

To verify that the results from the quasi-static FSI simulations were comparable to the previous solid-only simulations, the calculated LV cavity volumes V_f at end diastole for the two cases were compared. For the solid-only simulations, $V_f = 56.3$ ml and for the FSI simulations, $V_f = 56.2$ ml. Considering the small difference between these two values and the analysis of the results of the solid-only simulations presented in Chapter 4, the end-diastolic state calculated from the FSI simulations was deemed suitable for use as an initial state for the present cardiac cycle simulations.

Boundary conditions

Coincident FSI boundary conditions were applied to the inner surfaces of the solid geometry and the outer surfaces of the ellipsoidal part of the fluid geometry. The basal plane of the solid geometry was fixed in the vertical direction, while its inner edge was fixed in all three directions. For the upper part of the fluid geometry, no-slip wall boundary conditions were applied to all outer walls. As mentioned in Chapter 4, because the heart is nearly neutrally buoyant in the body, gravity has been neglected in the present study.

Because the LV does not operate in isolation, but is coupled to upstream and downstream components of the cardiovascular system, appropriate inflow and outflow boundary conditions must be defined. In the present study, values of pressures at the distal ends of

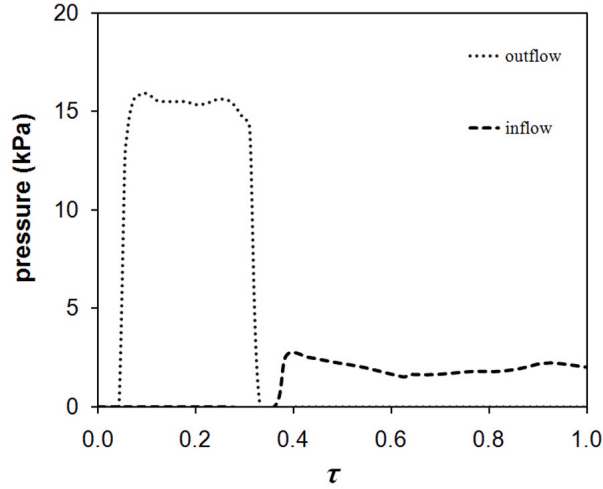


Figure 5.5: Outflow and inflow pressure boundary conditions based on measurements from Sabbah and Stein (1981).

the LV inflow and outflow tracts were specified based on previous measurements (Sabbah and Stein (1981)); these pressure boundary conditions are plotted in Fig. 5.5. An alternative approach would be to couple the LV model to lumped-parameter models representing the upstream and downstream components of the cardiovascular system (Watanabe et al. (2004)), but this was beyond the scope of the present study.

To control the flow direction, idealized mitral and aortic valves were modeled as instantly opening and closing planar boundaries at a distance L_2 from the distal ends of the LV inflow and outflow tracts, as shown in Fig. 5.1b. The choice of instantly opening and closing valves was made to reduce computational time and complexity in the numerical model, as accurately modeling the opening and closing of realistic valve geometries is beyond the scope of the present study. The opening and closing of the valves were controlled by “gap” boundary conditions, which remove or add wall boundary conditions using time functions. The times at which the valves opened or closed were chosen to coincide with the

start of each phase of the cardiac cycle and the application of inflow and outflow pressure boundary conditions. More specifically, the AV opens at the start of ejection ($\tau = 0.055$) and closes at the end of ejection ($\tau = 0.312$), and the outflow pressure boundary condition is applied while the AV is open. The MV opens at the start of filling ($\tau = 0.385$) and closes at the end of filling ($\tau = 1.0$), and the inflow pressure boundary condition is applied while the MV is open.

5.4 Preliminary tests

Preliminary tests were performed to determine the best choices of several model inputs, and the results of these tests are described briefly in this section. Because simulations in this section were of a preliminary nature, some of the model inputs in each test may have differed from their final chosen values, however, comparisons were made between results for which only the model input of interest was varied.

5.4.1 Time step dependence

To determine the influence of the time step duration on the simulations results, simulations were performed using 303 and 600 time steps. Recall that the 303 time step case consisted of 297 steps of 2 ms and 6 steps of 1 ms, while the 600 time steps were all 1 ms. To reduce the computational time for these simulations, only IVC and ejection were simulated, that is simulations were performed over the interval $0 \leq \tau \leq 0.312$. The differences in the resulting LV pressure and cavity volumes calculated for the two time step durations were lower than 1%, which are deemed to be insignificant. Therefore, it was determined that

303 time steps was sufficient to give results that were nearly independent of the time step duration and it is this number of time steps that was used for all subsequent simulations presented in this article.

5.4.2 Fluid mesh dependence

Simulations were performed over the interval $0 \leq \tau \leq 0.312$ for the two fluid meshes described in Section 5.3.3. Differences in p_{LV} , calculated at the centre of the basal plane, and V_f calculated for the two fluid meshes were found to be lower than 1%. Therefore, mesh 1, which is coarser than mesh 2, was deemed to be sufficient for use for the remainder of the simulations presented in this chapter. The use of an even more refined mesh would be required for a more complete assessment of the mesh dependence of the solution, but this would also require a substantial increase of the computational cost. Simulations with additional mesh refinement are delegated to future research.

5.4.3 Variation of multiplier for active material parameter values

Simulations were performed for several values of χ to determine the influence of χ on the results. For $\chi = 4$, the increase in p_{LV} during IVC was insufficient to cause blood to exit the LV when the AV opened and ejection began; therefore, it was determined that χ must be greater than 4. For $\chi > 4$, the maximum value of p_{LV} increases with increasing χ , such that χ reaches a value for which the simulations diverge during the filling phase due to an insufficient decrease in p_{LV} during IVR. It was determined that χ must be less than 6 in order for the simulations to converge over a single period. Therefore, χ must be in the range of $4 < \chi < 6$. Because an increase in χ increases the maximum value of p_{LV} more

significantly than it decreases V_f during ejection, a value of $\chi = 4.5$ was chosen for use in the remainder of the simulations presented in this chapter.

5.4.4 Periodicity

Simulations were performed for four periods using an earlier version of the myocardium geometry with a three-layer wall, and coarser fluid and solid meshes than those considered in the present study. A few observations can be made about the results from these four periods. First, the smoothness found in the temporal variations of p_{LV} and V_f present during the first period gave way to fluctuations in subsequent periods. Second, as a result of the closing of the AV at the end of each period, p_{LV} decreased shortly after the start of a new period; in fact, at $\tau = 5.6 \times 10^{-6}$, p_{LV} became negative for periods 2 and 3 and $p_{LV} \approx 0.99$ kPa for period 4. Third, after four periods, there is no indication that the results would converge towards a periodic solution. Additional periods would be required to make a more accurate assessment of the degree of periodicity of the solution.

5.5 Results

Results in this section were obtained during the first two periods of the cardiac cycle simulations, for the chosen geometry and mesh density, and for $\chi = 4.5$.

5.5.1 Left ventricle cavity volume and pressure changes

Figure 5.6a is a plot of p_{LV} as a function of τ over the first two periods of the cardiac cycle simulations, for which p_{LV} was calculated at a node in the fluid mesh located

at the centre of the basal plane. This figure also contains measured values of p_{LV} , p_{LA} , and p_{Ao} obtained from Sabbah and Stein (1981), the latter two of which were used as boundary conditions for the present simulations. The calculated temporal variations of p_{LV} show fairly good agreement with previous measurements, especially during the first three phases of the cardiac cycle, IVC, ejection, and IVR, but differ from the measurements during the early part of filling. During IVC, p_{LV} increased in both the present simulations and the previous measurements. Trends of p_{LV} for the present simulations were comparable for most of the two periods, however, at the start of IVC for the second period, $p_{LV} < 0$ for a single time step, as a result of the sudden closure of the MV. At $\tau = 0.055$, which signifies the opening of the AV and the end the IVC phase, p_{LV} was calculated to be $p_{LV} = 13.5$ kPa for both periods, which is slightly higher than the measured value $p_{LV} = 12.7$ kPa. During rapid ejection, p_{LV} increased to a maximum in both studies, before decreasing throughout the rest of ejection. The maximum value of p_{LV} in the present study exceeded the measured value by approximately 5 kPa, but at the end of ejection during period 1, pressures in both studies were nearly equal. During period 2, p_{LV} spiked upward at the end of ejection due to the sudden closure of the AV. Another noticeable difference between the trends of p_{LV} for the two periods was that, whereas for period 1 p_{LV} decreased after reaching its maximum during rapid ejection, during period 2 p_{LV} decreased, then increased, and decreased again, before finally increasing at the end of ejection. During IVR, p_{LV} decreased in both studies. At $\tau = 0.385$, which signifies the opening of the MV and the end of IVR, p_{LV} in the present study was 2.6 kPa for period 1 and 2.9 kPa for period 2, both of which are close to the measured value of $p_{LV} = 2.6$ kPa. Despite starting IVR from very different pressures, the

trends and value of p_{LV} at the end of IVR were comparable. Lastly, the calculated trends in p_{LV} differed from the measurements during rapid filling. Rather than continuing to decrease towards a minimum pressure near $\tau = 0.5$, the calculated p_{LV} increased shortly after the start of filling until it exceeded p_{LA} . This difference between the simulations and measurements led to a non-physiological backflow into the LV during the filling phase. After this backflow occurred, p_{LV} decreased such that, during the latter two phases of filling, diastasis and atrial contraction, the calculated trend in p_{LV} was comparable to the measurements with the magnitude of p_{LV} being approximately equal to the measured p_{LA} during these phases. For the second period, the maximum value of p_{LV} decreased and its location shifted to a later time; however, backflow was still present. Based on the periodicity study described in Section 5.4.4, there is no evidence to suggest that this decrease in the maximum value of p_{LV} from period 1 to period 2 would lead to removal of the non-physiological backflow from the present simulations, but additional periods would be required to determine the validity of this claim. Due to the high computational cost of running each period, at present, a sufficient number of periods could not be run with the current mesh density to further study this issue.

Changes in LV cavity volume V_f normalized by the end-diastolic LV cavity volume $V_{f,ED}$, calculated at $\tau = 0$, are plotted vs. τ in Fig. 5.6b for two periods of the cardiac cycle simulations. During IVC, $V_f/V_{f,ED}$ increased by 0.01 for period 1 and by 0.08 for period 2, before decreasing during ejection. Although no fluid enters or exits the LV cavity during IVC, these volume changes are consistent with the slightly compressible form of the material model for blood, which was required to ensure model convergence during the

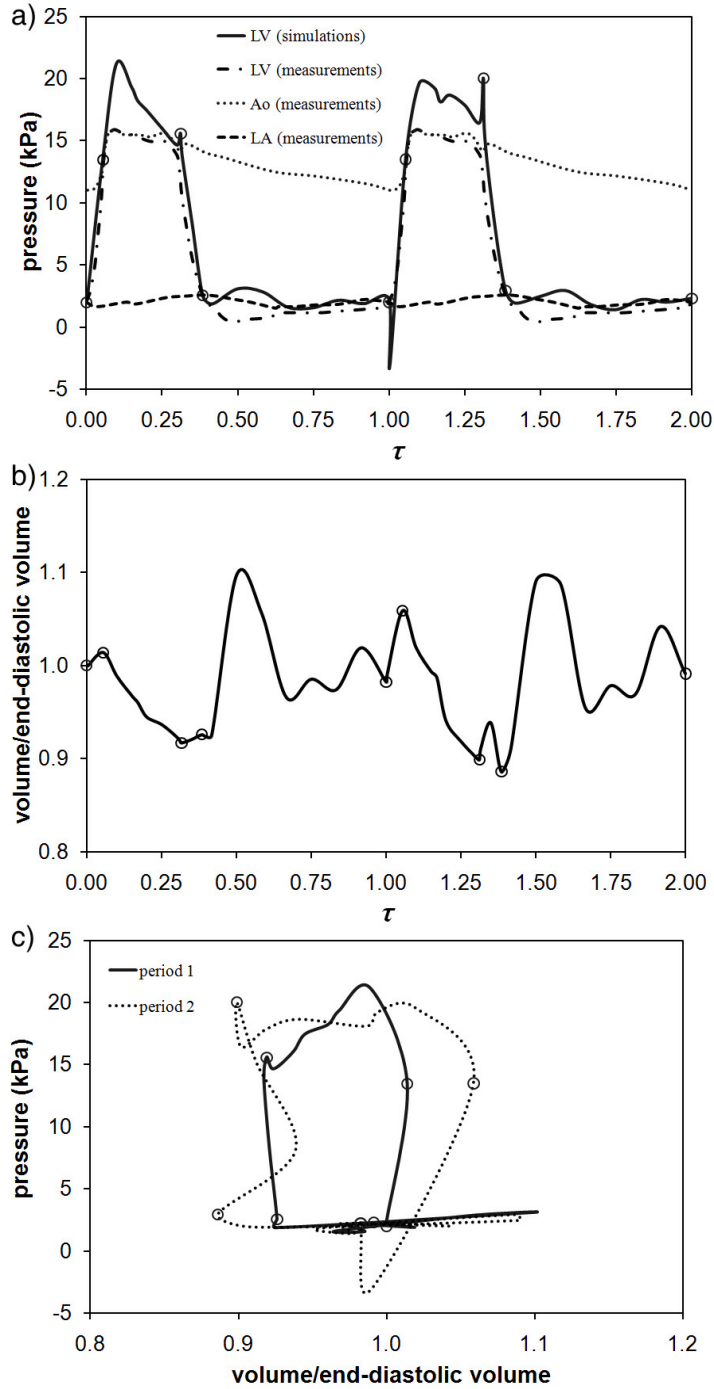


Figure 5.6: a) Temporal variation of LV cavity pressure from present simulations along with measured values of p_{LV} , p_{LA} , and p_{Ao} from Sabbah and Stein (1981); b) temporal variation of LV cavity volume; c) variation of LV cavity pressure with LV cavity volume. In these figures, volumes have been normalized by the end-diastolic volume at $\tau = 0$. Circles denote the start of a phase of the cardiac cycle and the opening or closing of a valve.

isovolumetric phases. The change in V_f during ejection can be characterized by two terms, stroke volume SV or ejection fraction EF . Stroke volume is defined as the difference between $V_{f,ED}$ and the end-systolic volume $V_{f,ES}$, i.e. $SV = V_{f,ED} - V_{f,ES}$. Ejection fraction is defined as the ratio of SV to $V_{f,ED}$, i.e. $EF = SV/V_{f,ED}$. The term EF is preferred to SV when comparing results from different studies because SV is dependent on the initial value of V_f . As described in Chapter 2, a physiological EF for a canine LV is approximately $EF = 0.44$. In the present study, an insufficient volume of blood exited the LV during ejection, resulting in $EF = 0.081$ for period 1 and 0.084 for period 2. For period 1, $V_f/V_{f,ED}$ increased by 0.01 during IVR, while for period 2, $V_f/V_{f,ED}$ increased and then decreased resulting in a net decrease in $V_f/V_{f,ED}$ of 0.01. At the start of filling phase, $V_f/V_{f,ED}$ increased rapidly for both periods to a maximum volume that was significantly larger than the original value of $V_{f,ED}$. The period of time over which this rapid increase in $V_f/V_{f,ED}$ occurred corresponded to the range of times over which p_{LV} increase above p_{LA} . Near $\tau = 0.5$, $V_f/V_{f,ED}$ reached a maximum, before the observed non-physiological backflow led to a decrease in $V_f/V_{f,ED}$. During the remainder of filling, $V_f/V_{f,ED}$ increased and decreased two more times before reaching an end-diastolic value that was approximately 98% of the end diastolic $V_f/V_{f,ED}$ at $\tau = 0$ for period 1 and 99% for period 2.

Figure 5.6c, combines the results from Fig. 5.6a and b into plots of pressure versus $V_f/V_{f,ED}$ for the two periods. For period 1, the pressure-volume trends during the first three phases of the cardiac cycle were consistent with physiological expectations, but the trend during filling was inconsistent with expectations due to the backflow present during

this phase. For period 2, the overall trends differed slightly from the trends found for period 1, primarily during the isovolumetric phases, which showed larger volume changes during period 2 than during period 1.

5.5.2 Myocardium deformations

Figures 5.7 to 5.10 are contour plots of displacement magnitudes in the myocardium in the y - z centre-plane over two periods of the cardiac cycle; Figures 5.7 and 5.9 contain displacements for selected times during IVC, ejection, and IVR for periods 1 and 2, respectively, while Figs. 5.8 and 5.10 contain displacements for selected times during filling for periods 1 and 2, respectively. These displacement magnitudes have been calculated with respect to the reference geometry DG. To illustrate the displacements with respect to end diastole, outlines of the end-diastolic geometries at $\tau = 0$ and $\tau = 1.0$ have been included for periods 1 and 2, respectively.

For period 1, as shown in Fig. 5.7, small differences in displacement magnitude are visible from one time to the next for the first three phases of the cardiac cycle. These small changes in displacement were due to the relatively small value of EF . Displacement magnitudes are largest at the apex, and lowest near the basal plane whose inner edge is fixed in space. For period 2, larger displacement magnitudes are visible in Fig. 5.9 than for the corresponding times during period 1, shown in Fig. 5.7. Additionally, a stronger asymmetry is visible during the second period as shown by the horizontal motion of the apex. Despite that fact that the LV cavity volume did not vary much from period 1 to period 2, it is clear that the shape of the LV geometry differed substantially for the two periods.

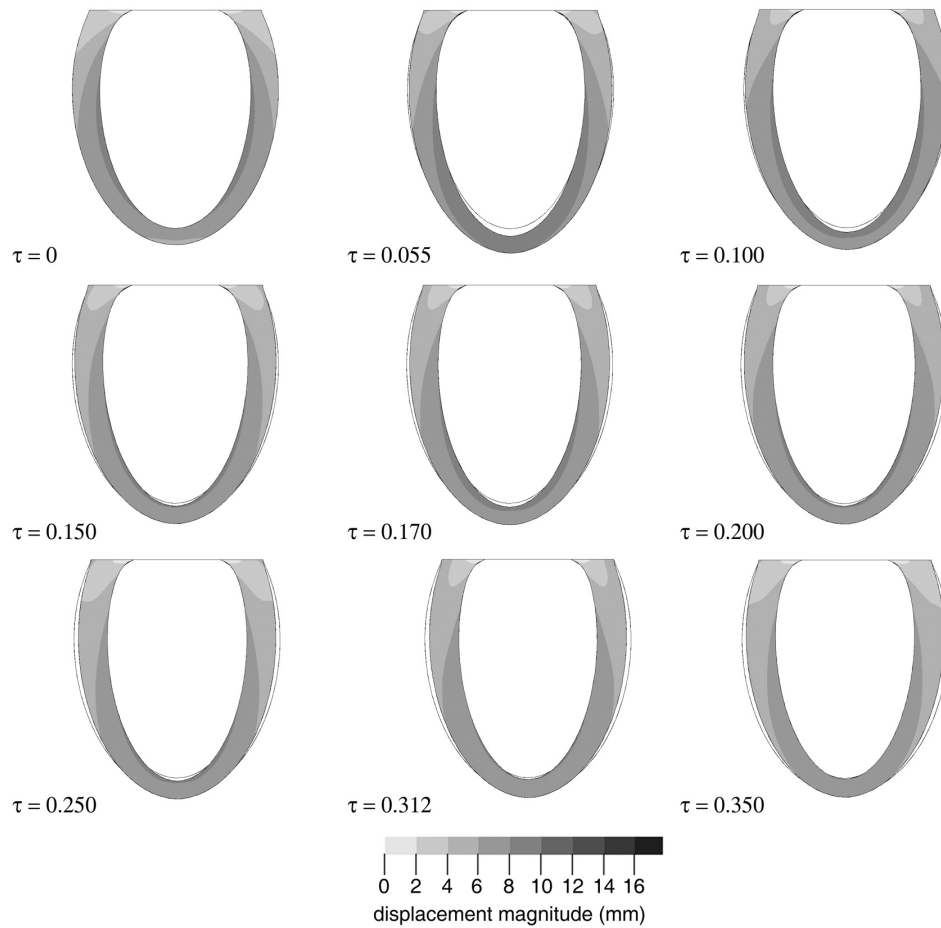


Figure 5.7: Displacement magnitudes in the myocardium in the y - z centre-plane at selected times during IVC, ejection, and IVR for period 1. Outline represents end-diastolic geometry at $\tau = 0$.

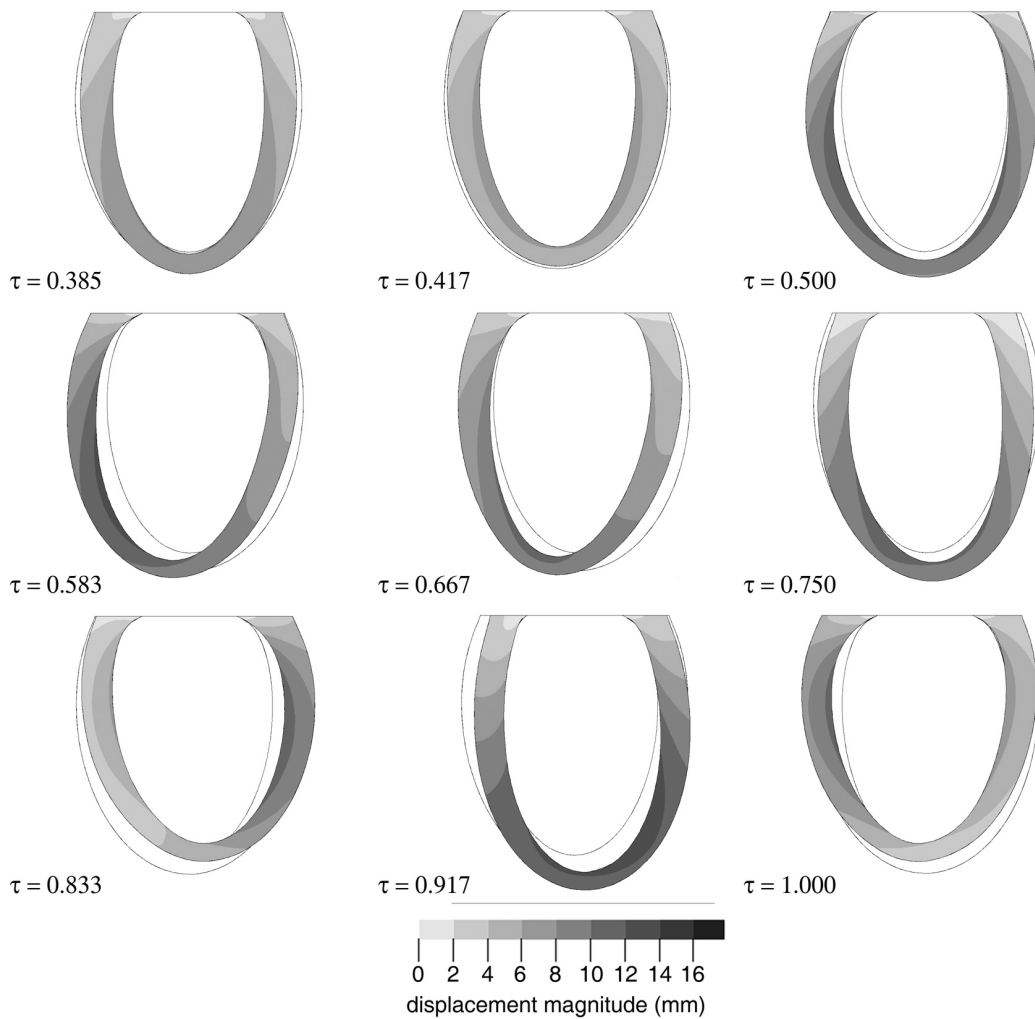


Figure 5.8: Displacement magnitudes in the myocardium in the y - z centre-plane at selected times during filling for period 1. Outline represents end-diastolic geometry at $\tau = 0$.

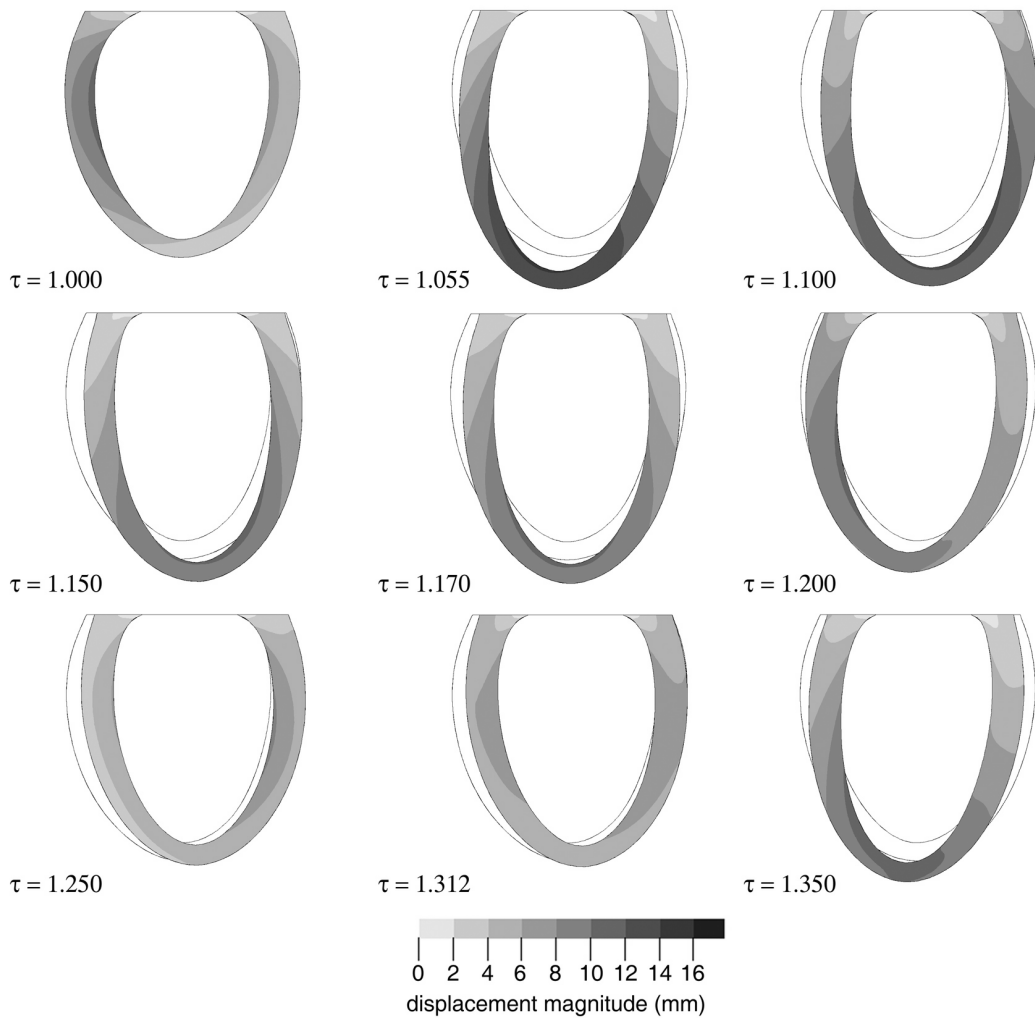


Figure 5.9: Displacement magnitudes in the myocardium in the y - z centre-plane at selected times during IVC, ejection, and IVR for period 2. Outline represents end-diastolic geometry at $\tau = 1.000$.

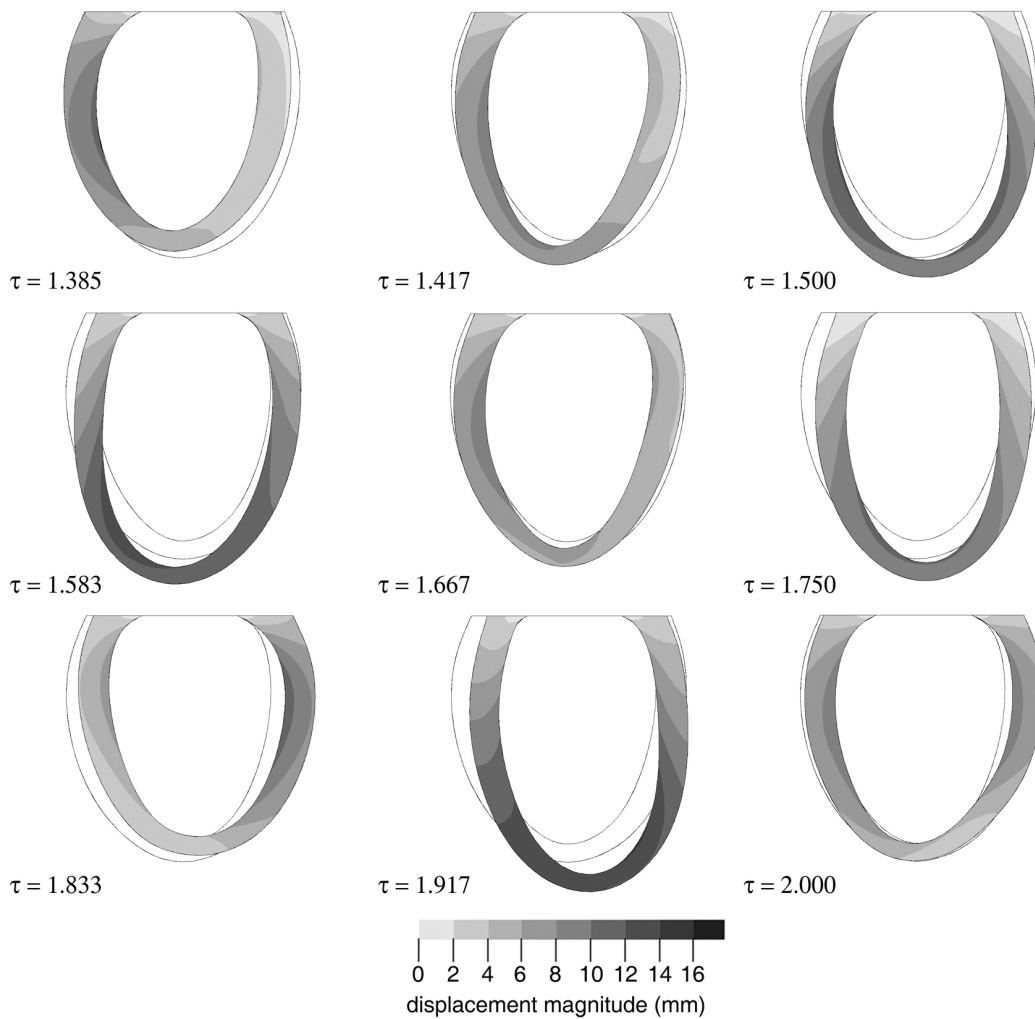


Figure 5.10: Displacement magnitudes in the myocardium in the y - z centre-plane at selected times during filling for period 2. Outline represents end-diastolic geometry at $\tau = 1.000$.

Larger displacement magnitudes and a more prevalent horizontal motion of the apex were observed to occur during filling (Fig. 5.8) than during ejection (Fig. 5.7) for period 1. For period 2, displacement magnitudes during filling, shown in Fig. 5.10, were of the same order as the displacement magnitudes found for the previous three phases. Differences in displacement magnitudes during filling between periods 1 and 2 were less apparent than the differences found during the previous three phases.

One of the criteria for determining whether the simulations would tend to reach a periodic state is a comparison of the LV geometries calculated at the end of a period to the geometries at the start of the period, as, for a periodic solution, these geometries should be identical. For period 1, although V_f at $\tau = 1.0$ was nearly equal to V_f at $\tau = 0$, noticeable differences are visible between the geometries at the two times, as shown in the last image in Fig. 5.8. These differences appear to have decreased for the second period, as shown in the last image in Fig. 5.10; however, additional periods would be required to determine if the calculated LV geometry at the end of a period would converge to match the results at the start of the period, that is, if the results would converge to a periodic state.

Principal stretches are defined as the ratios of deformed and undeformed lengths and are denoted as λ_i , $i = 1, 2, 3$. In the present study, these stretches were calculated with respect to the reference geometry DG. The temporal variations of the principal stretches during the cardiac cycle are presented in Fig. 5.11 for the first two periods of the cardiac cycle; these values (and the corresponding principal Cauchy stresses to be discussed in the next section) were calculated as the average of values obtained at eight nodes, located at a relative elevation of $z/h = 0.5$ in DG, and on either side of the centreline through the

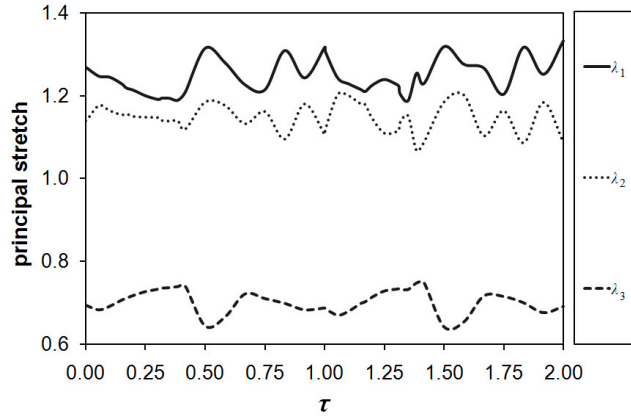


Figure 5.11: Representative temporal variations of principal stretches for two periods of the cardiac cycle.

thickness of the myocardium at circumferential locations corresponding to the positive and negative x - and y -axes. The stretches calculated at these eight nodes were nearly equal, with standard deviations for λ_1 , λ_2 , and λ_3 , respectively, of 0.025, 0.013, and 0.017, averaged over period 1 and 0.025, 0.015, and 0.018, averaged over period 2. These standard deviations are small compared to the average and, therefore, do not represent significant differences between the stretches calculated at each of the eight nodes. The trends in λ_1 , λ_2 , and λ_3 in Fig. 5.11 were consistent with the trends in $V_f/V_{f,ED}$ shown in Fig. 5.6b in the sense that as $V_f/V_{f,ED}$ decreased, so too did the deformations in the myocardium. The trends in λ_3 were comparable for both periods, while the trends in λ_1 and λ_2 showed stronger variations in period 2 than in period 1. The differences in λ_1 and λ_2 between periods were consistent with the differences observed in the plots of displacement magnitudes.

5.5.3 Myocardium stresses

Figures 5.12 to 5.15 show contour plots of effective stresses in the myocardium in the y - z centre-plane over two periods of the cardiac cycle. The effective stress T_e is a scalar stress calculated as

$$T_e = \sqrt{\frac{1}{2} \left[(T_{xx} - T_{yy})^2 + (T_{xx} - T_{zz})^2 + (T_{yy} - T_{zz})^2 + 6(T_{xy}^2 + T_{xz}^2 + T_{yz}^2) \right]} \quad (5.13)$$

where T_{ij} are the components of the Cauchy stress tensor.

Figures 5.12 and 5.14 show effective stresses for selected times during IVC, ejection, and IVR for periods 1 and 2, respectively, while Figs. 5.13 and 5.15 show the corresponding stresses for selected times during filling. These stress contours have been smoothed and the magnitudes have been truncated to a maximum value of 48 kPa for IVC, ejection, and IVR and 24 kPa for filling to improve visualization of lower magnitude stresses. Because of the fixed boundary condition applied to the inner edge of the basal plane, the stresses along this edge are much larger than the values found throughout the myocardium.

For IVC, ejection, and IVR, the stresses shown in Fig. 5.14 for period 2 are comparable to the stresses shown in Fig. 5.12 for period 1. In both cases, the stresses are low at the start of IVC, increase during IVC and into ejection due to the contraction of the muscle fibres, and then decrease during the latter part of ejection and the early part of IVR due to the relaxation of the muscle fibres. Larger stresses were found near the inner surface of the myocardium than near the outer surface, which is expected, because the LV cavity pressure acts on the inner surface. For the filling phase, the effective stresses were comparable during period 1 (Fig. 5.13) and period 2 (Fig. 5.15), and of a much lower

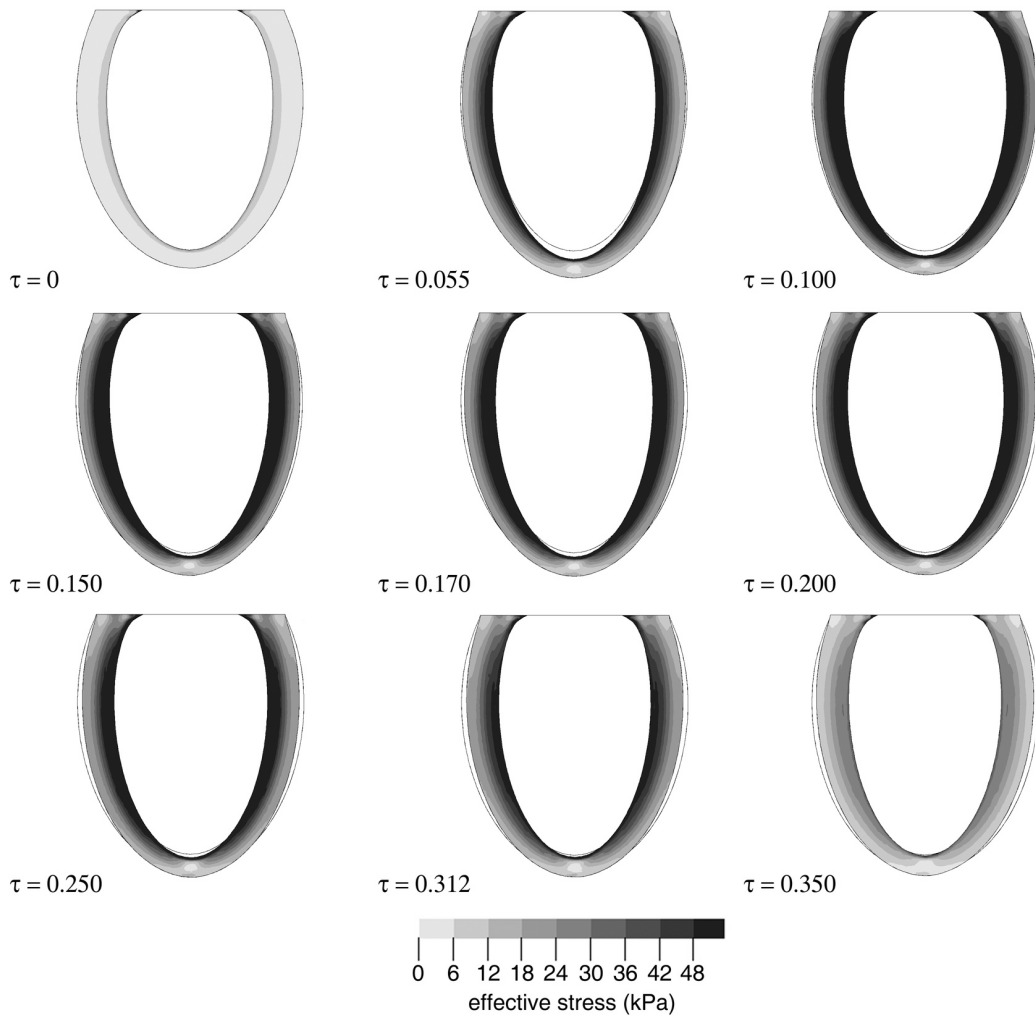


Figure 5.12: Effective stresses in the myocardium in the $y-z$ centre-plane at selected times during IVC, ejection, and IVR for period 1. Outline represents end-diastolic geometry at $\tau = 0$.

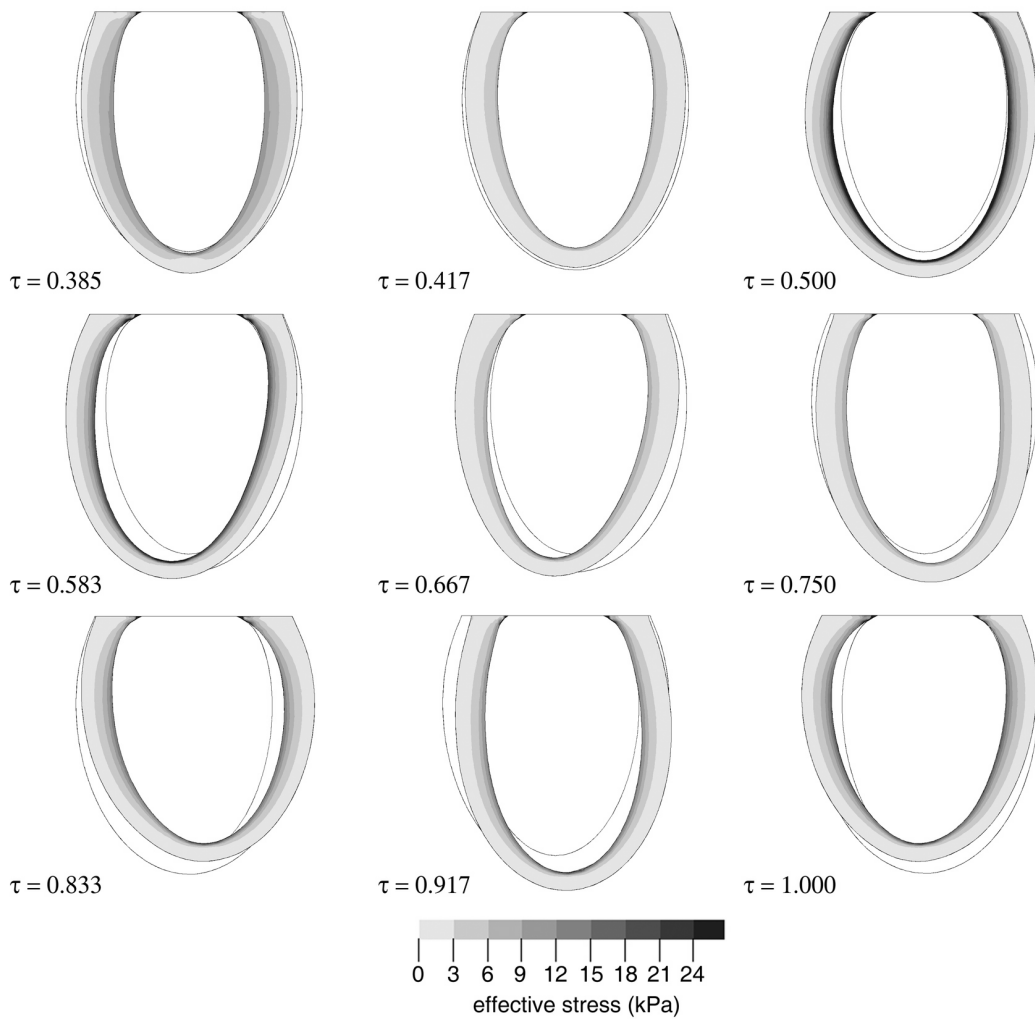


Figure 5.13: Effective stresses in the myocardium in the y - z centre-plane at selected times during filling for period 1. Outline represents end-diastolic geometry at $\tau = 0$.

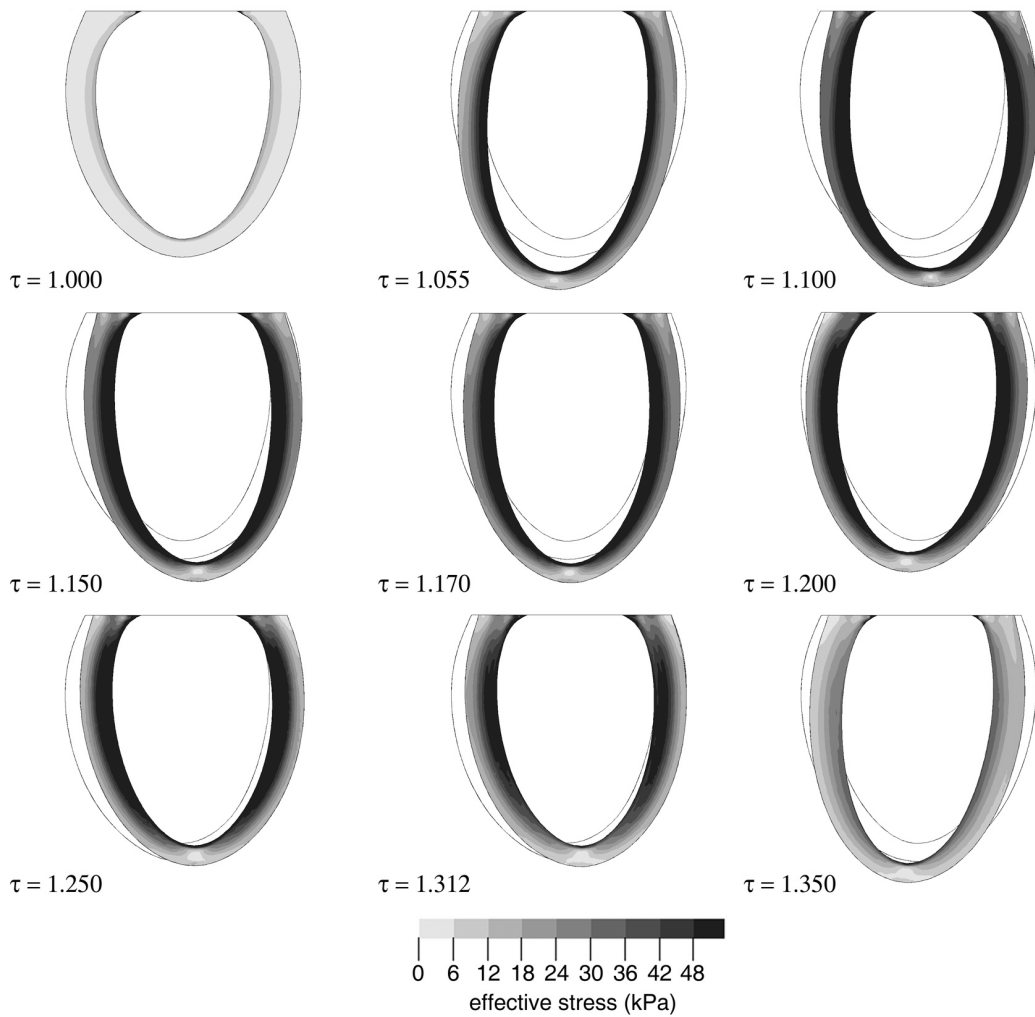


Figure 5.14: Effective stresses in the myocardium in the y - z centre-plane at selected times during IVC, ejection, and IVR for period 2. Outline represents end-diastolic geometry at $\tau = 1.000$.

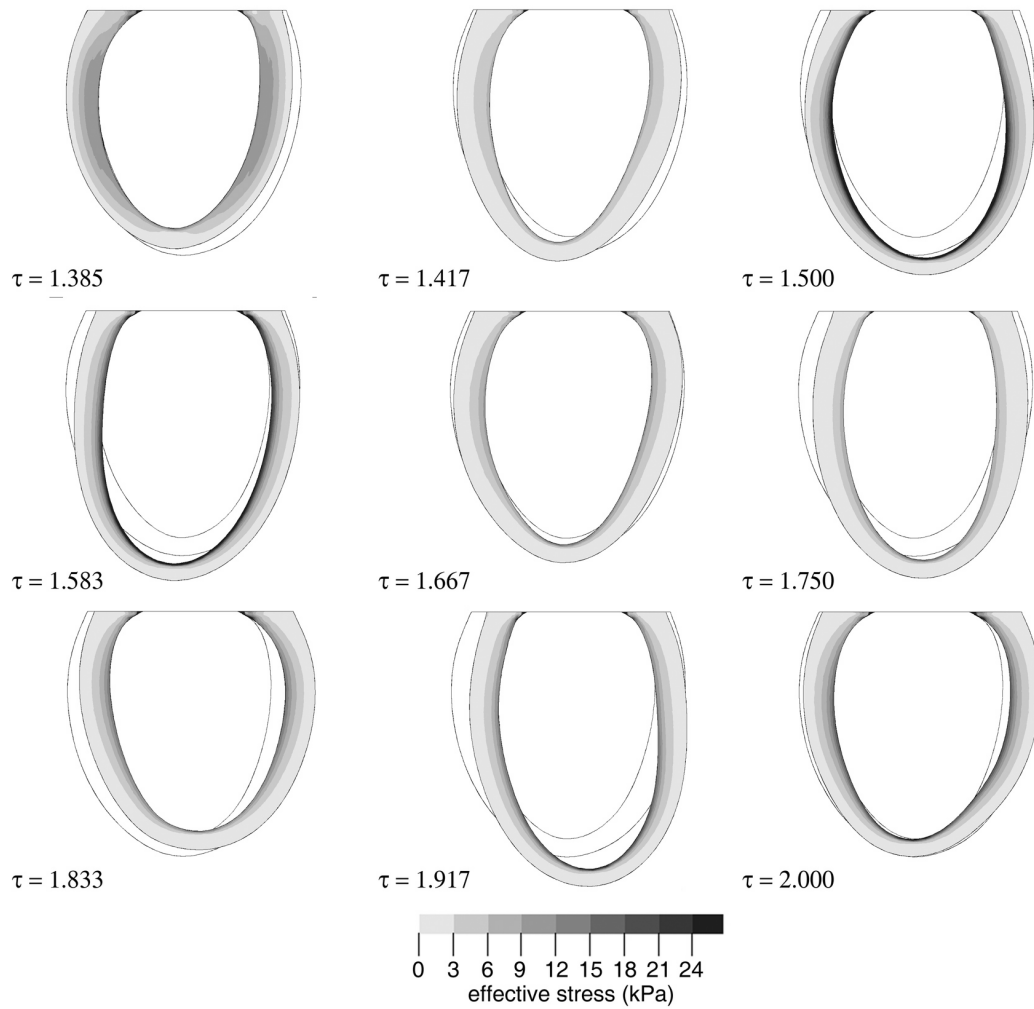


Figure 5.15: Effective stresses in the myocardium in the y - z centre-plane at selected times during filling for period 2. Outline represents end-diastolic geometry at $\tau = 1.000$.

magnitude than the stresses observed during the other three phases of the cycle. Stresses during filling are largest at $\tau = 0.500$ ($\tau = 1.500$), which corresponds to the time for which the LV cavity volume is largest.

Figure 5.16 is a plot of the temporal variations of the principal Cauchy stresses, denoted as T_i , $i = 1, 2, 3$, for two periods of the cardiac cycle, calculated as described in Section 5.5.2. The local principal stress directions will be discussed in Section 5.5.6. The trends in T_1 and T_2 were consistent with the trend in p_{LV} shown in Fig. 5.6a, that is, the stresses and pressure increased to maxima during rapid ejection, decreased gradually during the remainder of ejection, decreased more significantly during IVR and then fluctuated during filling. The magnitude of T_1 during ejection was found to be substantially larger than T_2 , which is as expected due to the application of the majority of the active stresses from the muscle fibre contract in the fibre direction. Differences in the stresses between periods are most apparent in T_1 during ejection; whereas T_1 decreases from its maximum at early ejection during period 1, for period 2, T_1 decreases and then increases during ejection, before decreasing from the latter part of ejection through IVR. Larger variations were found for the stresses than for the stretches; the standard deviations for T_1 , T_2 , and T_3 were, respectively, 3.5, 0.70, and 0.82 when averaged over period 1, and 3.7, 0.82, and 0.87 when averaged over period 2.

Stresses in the myocardium have not been measured *in vivo*. However, they have been estimated by DeAnda et al. (1998) using Laplace's Law for canine LVs with an ejection fraction of $EF \simeq 0.21$. The trend of the temporal variation of the average wall stress calculated by DeAnda et al. (1998) is comparable to the trend of T_1 found

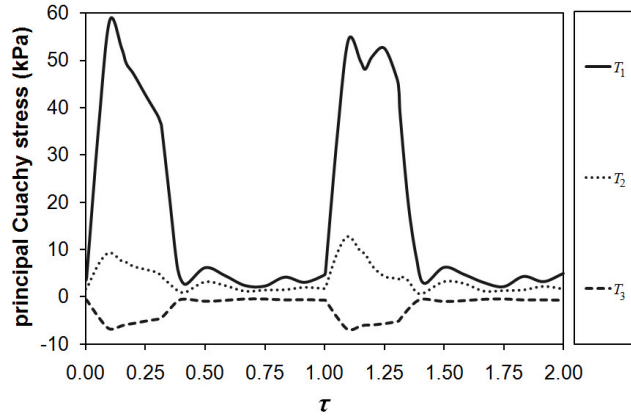


Figure 5.16: Representative temporal variations of principal Cauchy stresses for two periods of the cardiac cycle, calculated as described in Section 5.5.2.

in the present study. This is to be expected because both the average wall stress and the maximum principal stress T_1 increase and decrease with corresponding increases and decreases in pressure.

5.5.4 Left ventricle cavity pressure variations

Figures 5.17 to 5.20 show contour plots of p_{LV} in the y - z centre-plane over two periods of the cardiac cycle; Figures 5.17 and 5.19 show p_{LV} for selected times during IVC, ejection, and IVR for periods 1 and 2, respectively, whereas Figs. 5.18 and 5.20 show p_{LV} during filling for periods 1 and 2, respectively. These pressure contours have been truncated at a maximum value of $p_{LV} = 20$ kPa for IVC, ejection, and IVR and 4 kPa for filling to improve visualization of lower pressures.

Consistent with the temporal variation of p_{LV} shown in Fig. 5.6a, the pressure contours in Figs. 5.17 to 5.20 show an increase in p_{LV} during IVC and rapid ejection, a decrease during the remainder of ejection and through IVR, and relatively low values of

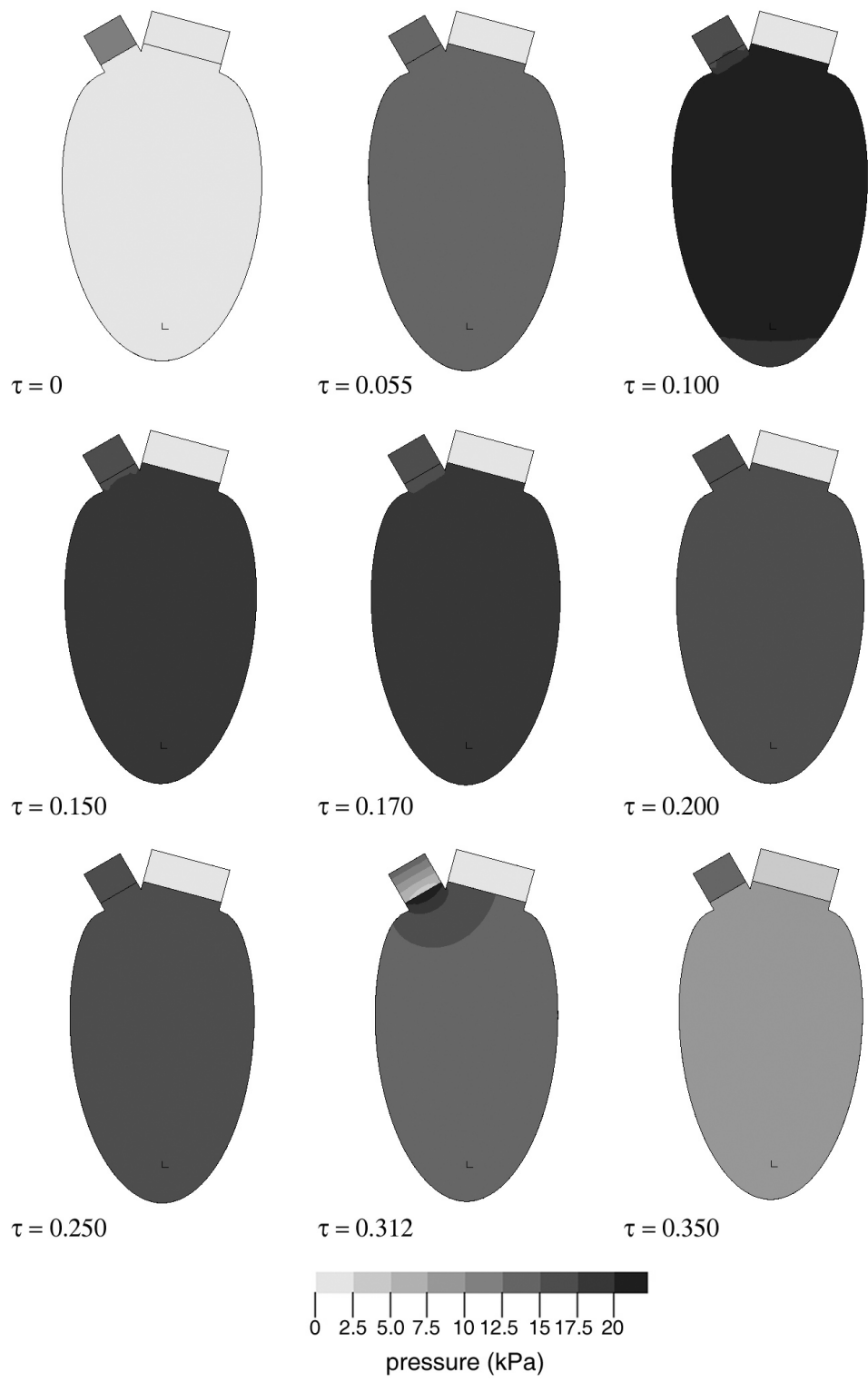


Figure 5.17: Pressures in the LV cavity in the y - z centre-plane at selected times during IVC, ejection, and IVR for period 1.

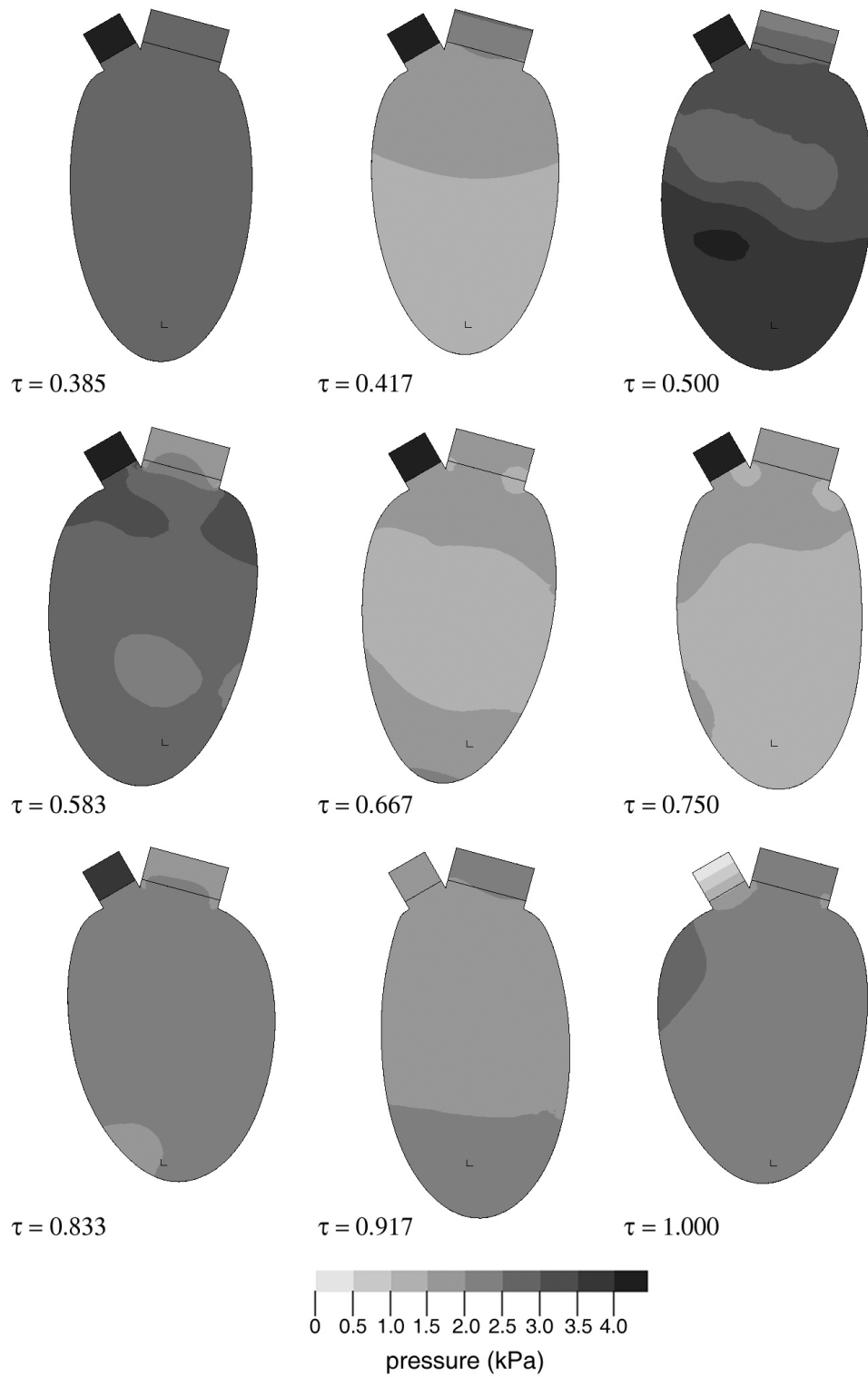


Figure 5.18: Pressures in the LV cavity in the y - z centre-plane at selected times during filling for period 1.

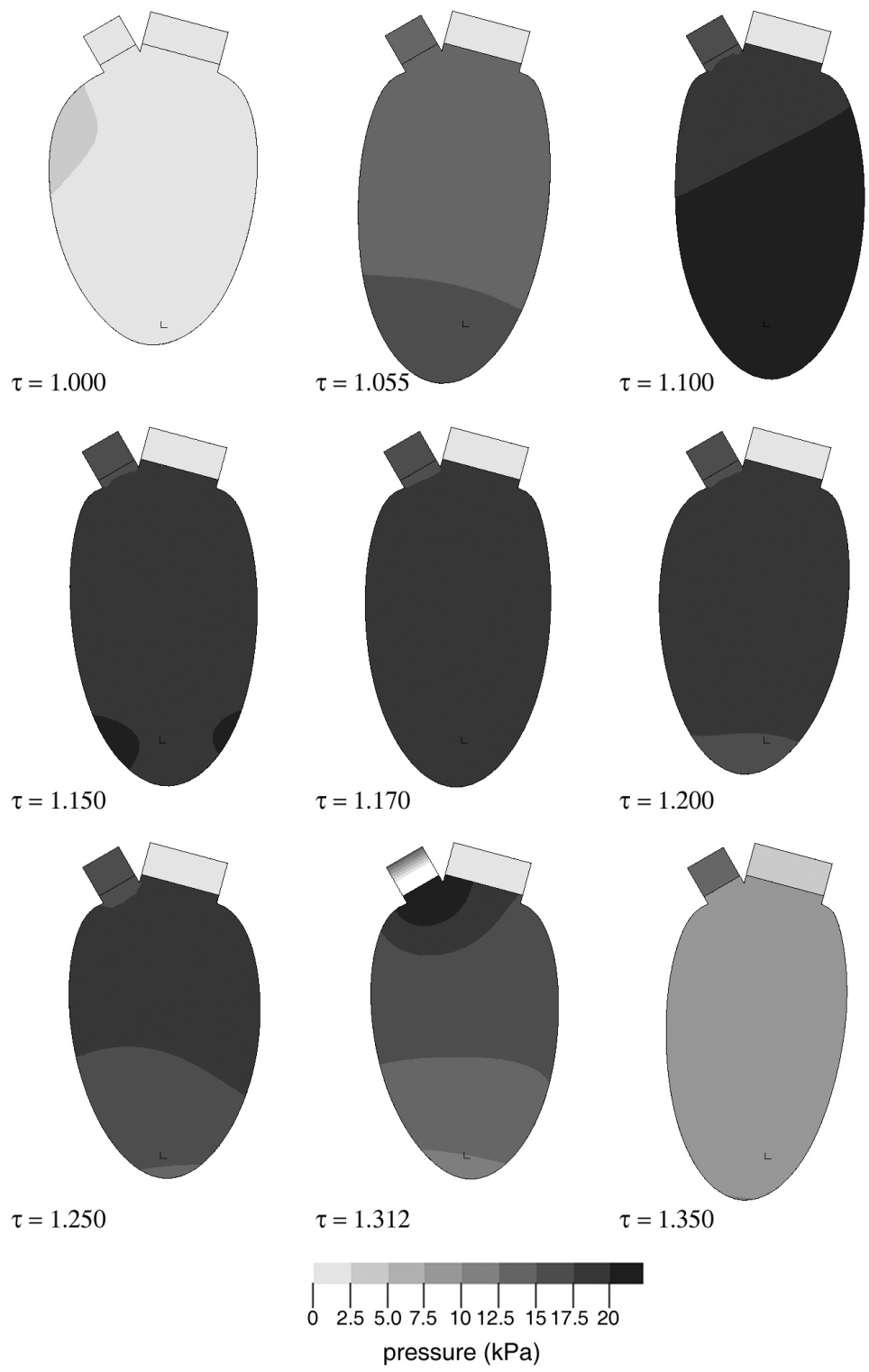


Figure 5.19: Pressures in the LV cavity in the y - z centre-plane at selected times during IVC, ejection, and IVR for period 2.

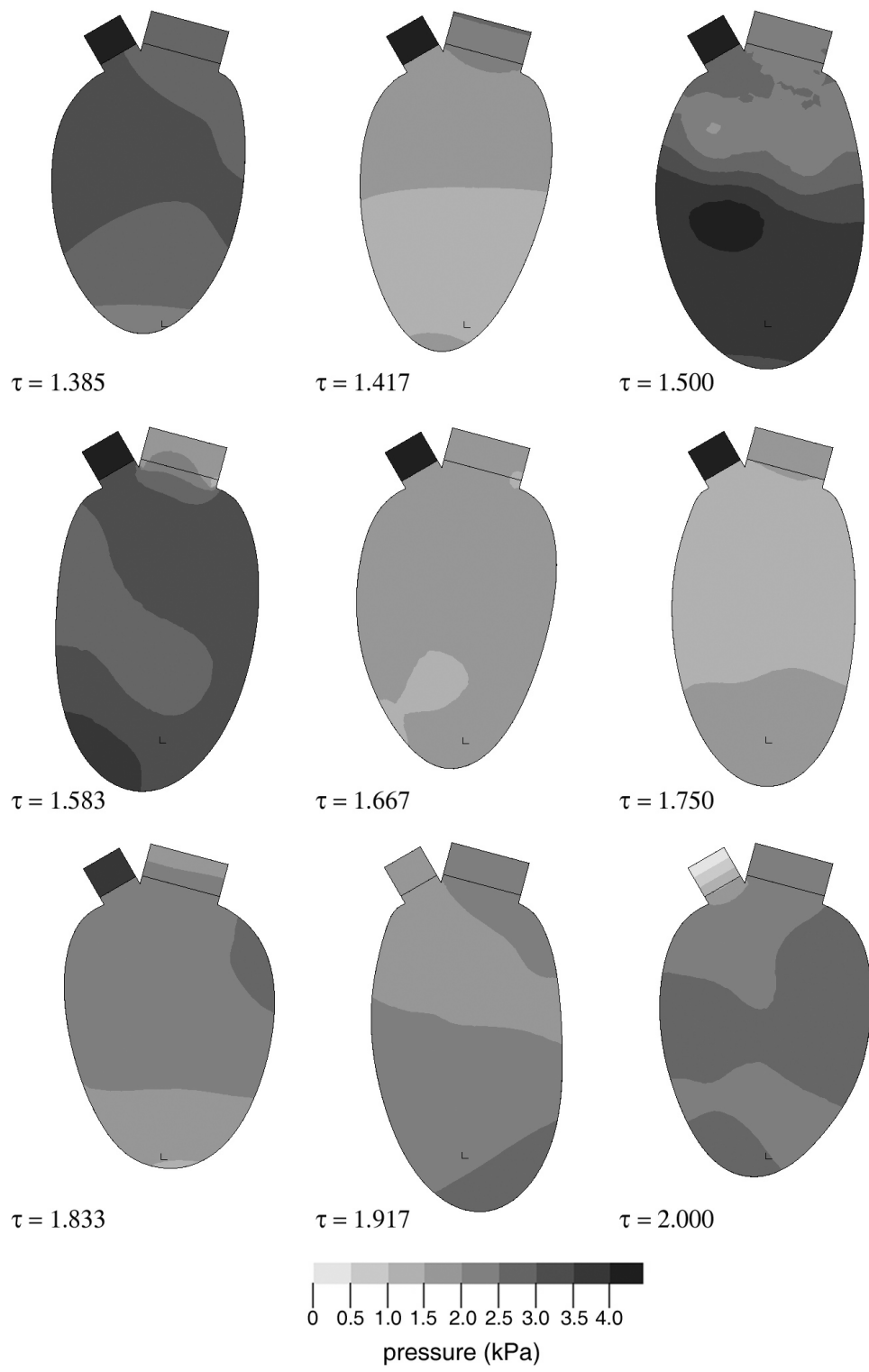


Figure 5.20: Pressures in the LV cavity in the y - z centre-plane at selected times during filling for period 2.

p_{LV} during filling. For period 1, differences in the pressure inside the LV cavity during IVC, ejection, and filling, shown in Fig. 5.17, are lower than the contour plot resolution of 2.5 kPa, making it appear as though the pressure in the LV cavity for a given time was uniform. However, as will be shown in Section 5.5.6, small differences in p_{LV} are present both vertically and horizontally within the LV cavity. For period 2, non-uniformities in p_{LV} are visible during IVC, ejection, and filling, as shown in Fig. 5.19. Larger non-uniformities in the pressure contours are also visible during filling for the second period, shown in Fig. 5.20, compared to those in the first period, shown in Fig. 5.18. For filling, the range of pressure contours shown is smaller than the range shown for the other three phases, which improved the contour plot resolution to 0.5 kPa in order to illustrate more effectively small differences in the pressures throughout the LV cavity. In particular, both vertical and horizontal variations of p_{LV} are visible for $\tau = 0.500$ and 0.583 in Fig. 5.18, and for $\tau = 1.500$ and 1.583 in Fig. 5.20. These complex spatial variations of p_{LV} show the importance of coupling simulations of blood flow with simulations of myocardium deformation, rather than performing solid-only simulations, for which a uniform pressure is imposed as a boundary condition on the inner surface of the myocardium model.

5.5.5 Blood velocities

Figures 5.21 to 5.24 are plots of blood velocity vectors in the LV cavity in the y - z centre-plane for two periods of the cardiac cycle; Figures 5.21 and 5.23 show velocity vectors at selected times during IVC, ejection, and IVR, for periods 1 and 2, respectively, whereas Figs. 5.22 and 5.24 show velocity vectors during filling for periods 1 and 2, respectively. These velocity vectors are truncated to a maximum value of 1.5 m/s to show as clearly as

possible the lower velocities within the LV cavity.

The blood velocities in the LV cavity are nearly zero at the start of period 1, because the initial inflation of the LV geometry to an end-diastolic state was performed quasi-statically as to minimize the blood velocities. As shown in Fig. 5.21, the velocities inside the LV cavity remain relatively small during IVC, ejection, and filling, while the velocities of the fluid exiting through the LV outflow tract are large. Such difference is expected in view of the fact that the diameter of the LV outflow tract is much smaller than the width of the LV cavity. During filling, blood enters rapidly the LV cavity at $\tau = 0.500$, as shown in Fig. 5.22, and then exits as non-physiological backflow at $\tau = 0.583$. Alternating entering and exiting of blood is visible in the velocity vectors throughout the remainder of the first period. For IVC, ejection, and IVR, the velocity vectors within the LV cavity for the second period, shown in Fig. 5.23, are larger in magnitude than the corresponding vectors for period 1. During filling, the velocity vectors for period 2, shown in Fig. 5.24, are comparable to the corresponding vectors found for period 1, with slightly lower magnitudes in period 2, particularly near end-diastole.

5.5.6 Representative times during the cardiac cycle

In this section, detailed descriptions of the solid and fluid mechanics are presented for selected time during the cardiac cycles. Specifically, results are presented for mid-ejection ($\tau = 0.150$ and $\tau = 1.150$), end systole ($\tau = 0.312$ and $\tau = 1.312$), and end diastole ($\tau = 1.00$ and $\tau = 2.00$). Due the non-physiological backflow that presently occurs during filling, results have not been presented for a selected time during mid-filling. For each selected time, contour plots of solid displacements and stresses are presented along with a

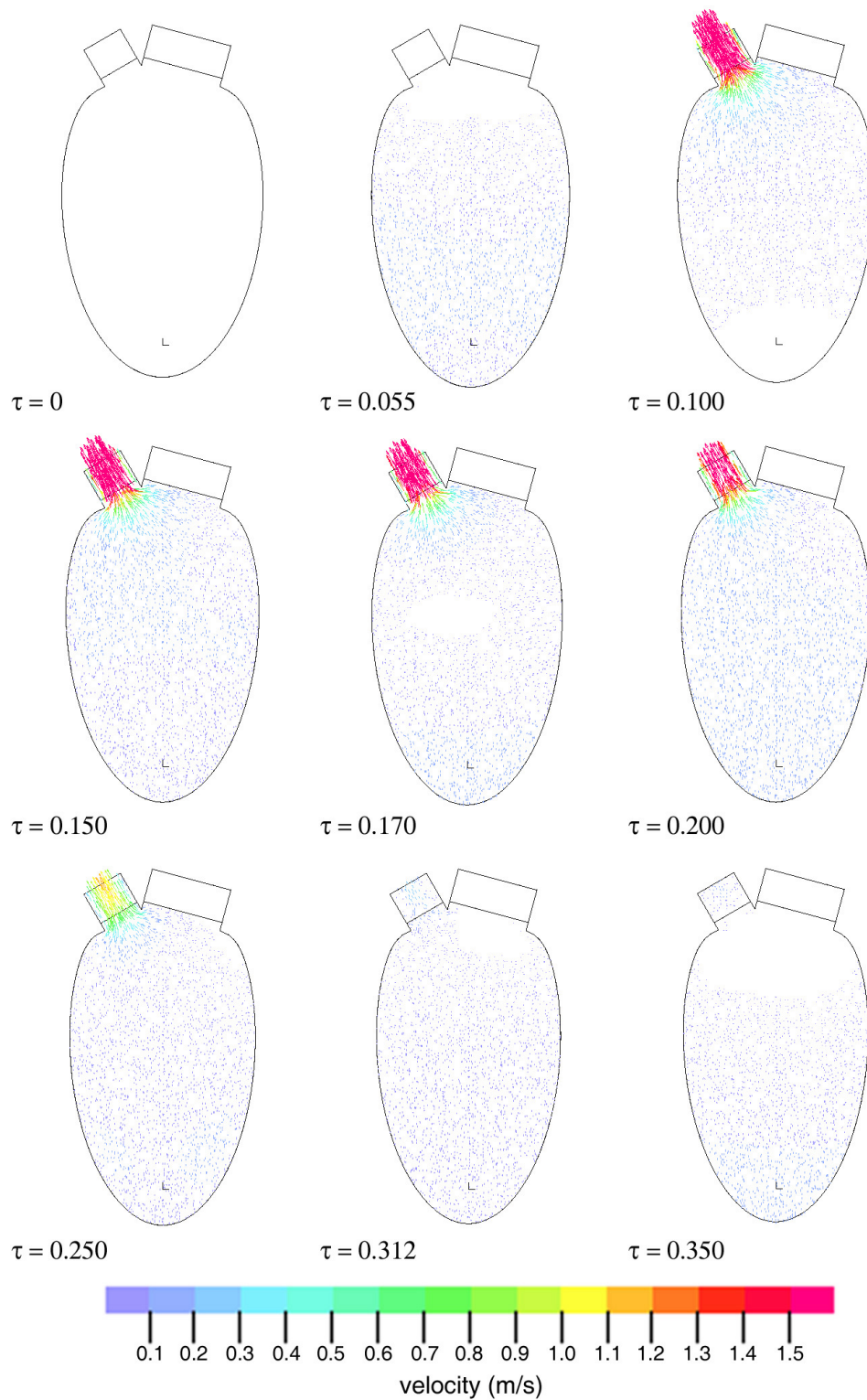


Figure 5.21: Blood velocities in LV cavity in the y - z centre-plane at selected times during IVC, ejection, and IVR for period 1.

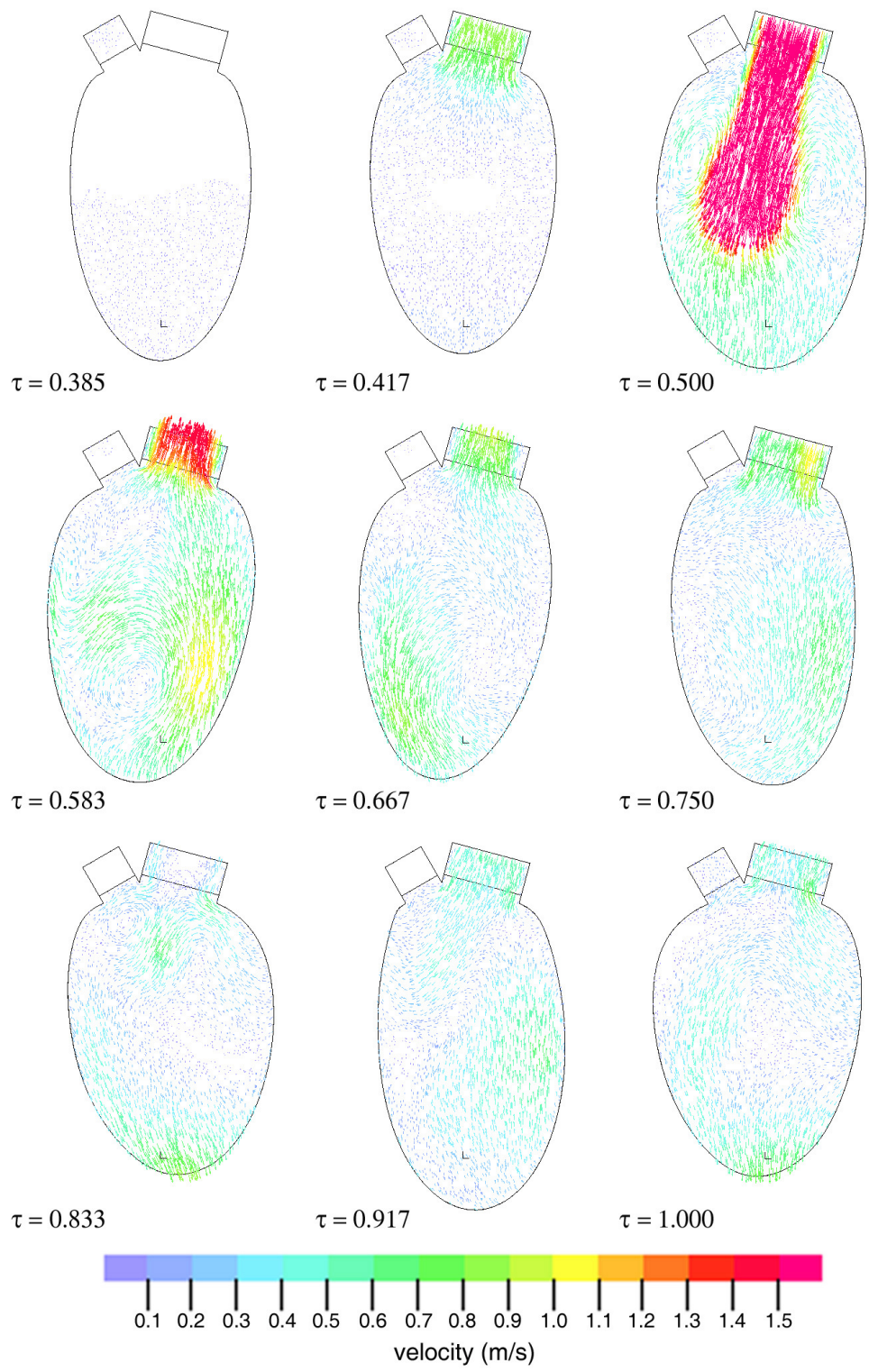


Figure 5.22: Blood velocities in the LV cavity in the y - z centre-plane at selected times during filling for period 1.

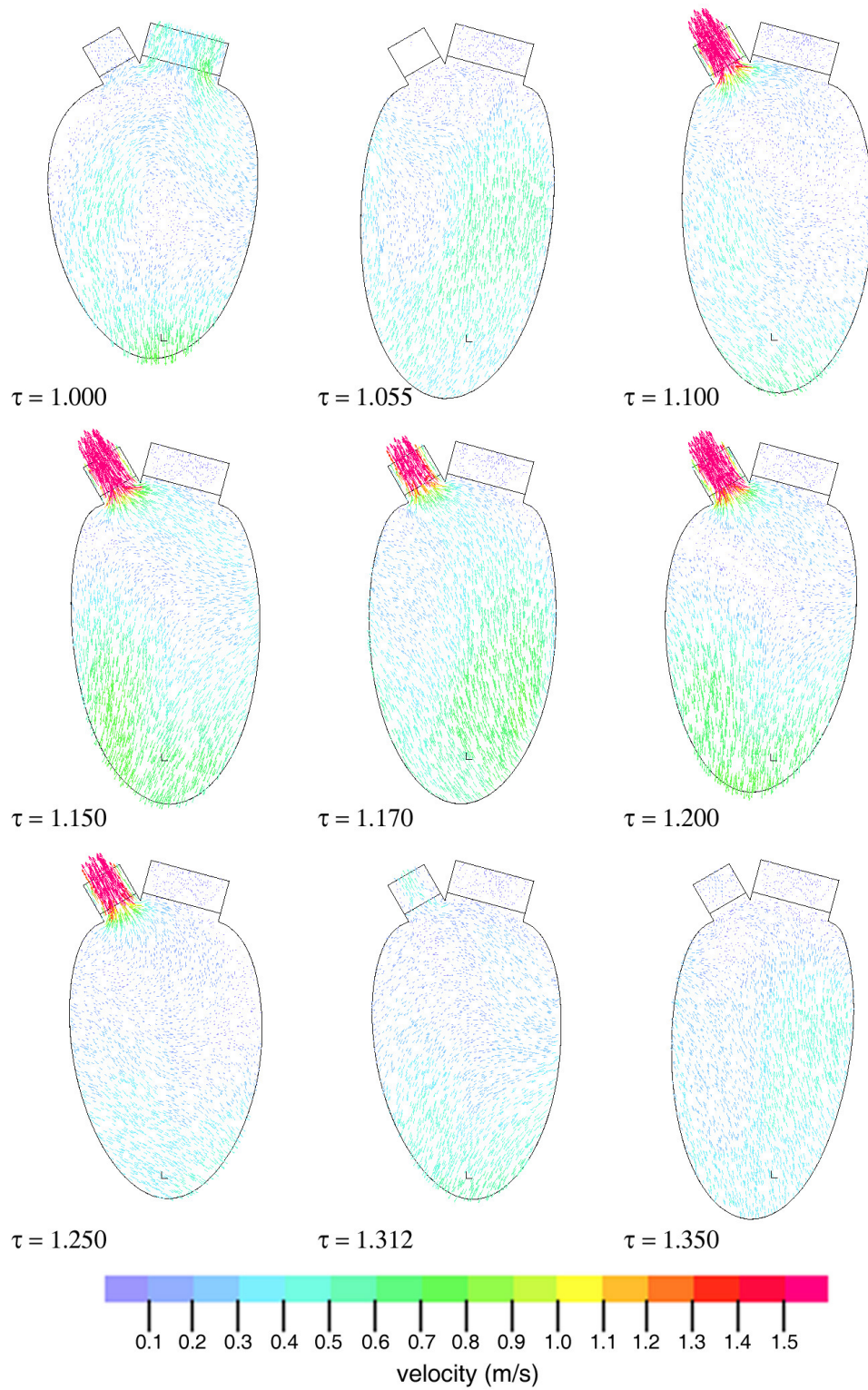


Figure 5.23: Blood velocities in the LV cavity in the y - z centre-plane at selected times during IVC, ejection, and IVR for period 2.

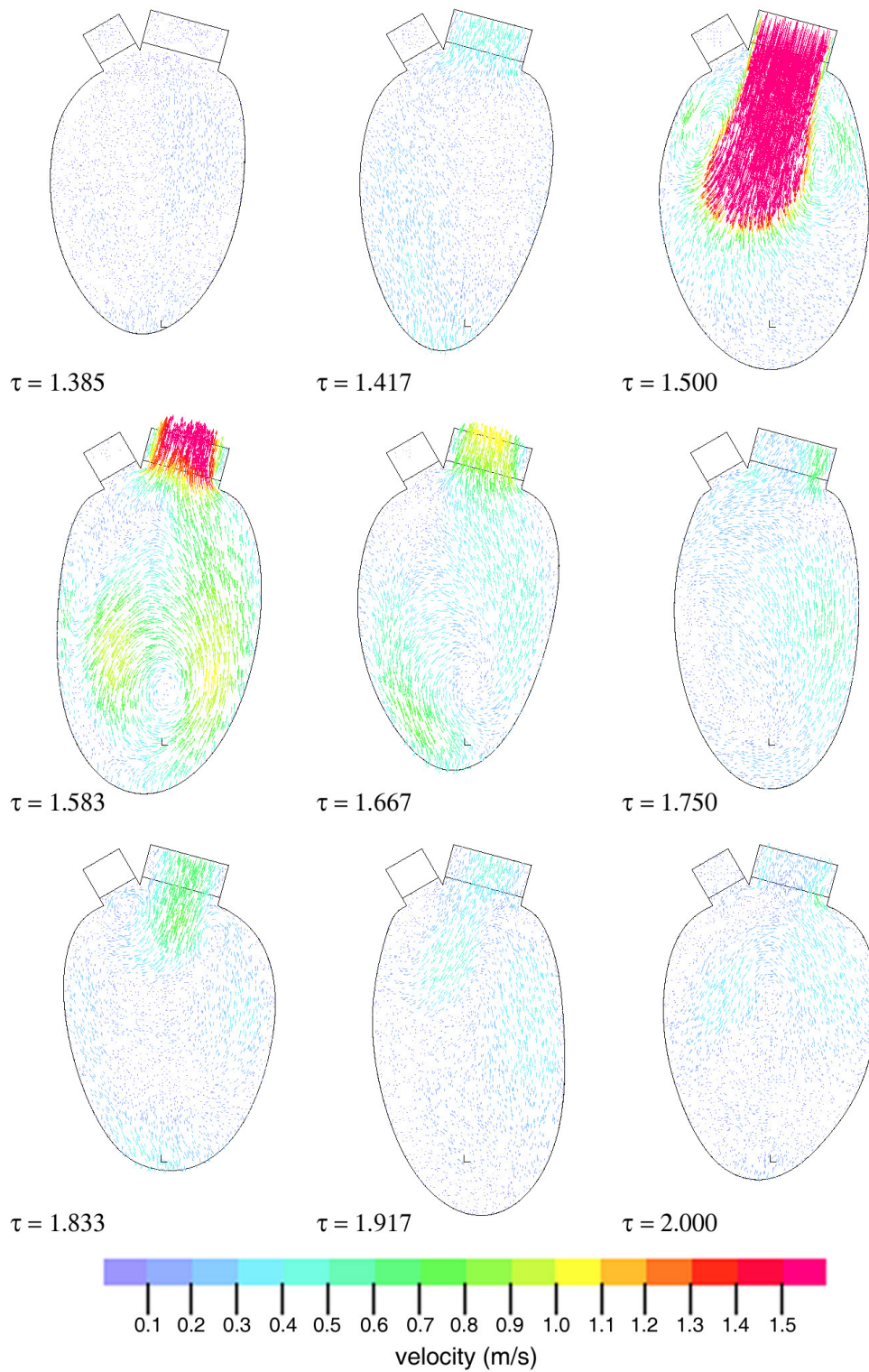


Figure 5.24: Blood velocities in the LV cavity in the y - z centre-plane at selected times during filling for period 2.

contour plot of LV cavity pressures and a vector plot of blood velocities.

Calculation methodology

For the myocardium, detailed spatial variations of the principal stretches and principal stresses in the myocardium are also presented and are calculated as described in the following. Representative transmural (from the exterior to the interior) variations of the principal stretches and stresses were calculated in the equatorial plane, which is located at a relative elevation of $z/h = 0.67$ in DG. At each relative depth from the exterior surface in the deformed geometry, denoted as t/t_{\max} , the average principal stretches and stresses were calculated as the averages of corresponding values obtained along the positive and negative x - and y -axes. Longitudinal variations (from the apex to the base) of the stretches and stresses were calculated at a location halfway through the myocardium. At each relative height c/c_{\max} from the apex in the deformed geometry, average principal stretches and stresses were calculated as the averages of values obtained at circumferential locations corresponding to the positive and negative x - and y -axes.

The local principal stress directions y_1 , y_2 , and y_3 in the myocardium differ from the local material directions x_1 (fibre), x_2 (sheet), and x_3 (sheet-normal). Differences between these two sets of directions were characterized in the equatorial plane, in which x_3 is radial. To examine these differences, three angles were defined, φ_1 , which is the angle between y_1 and the local circumferential direction, φ_2 , which is the angle between y_2 and the local circumferential direction and φ_3 , which is the angle between y_3 and the local radial direction, which coincides with x_3 in the equatorial plane. Average transmural variations of these angles were calculated using the same method as the average principal stretches

and stresses described in the previous paragraph.

For the LV cavity, average transmural variations of the pressure and velocities were calculated in the equatorial plane as the average of values obtained at four radial locations r/r_{\max} corresponding to the positive and negative x - and y -axes. Average longitudinal variations of the pressures and velocities were also calculated from the apex to the base in the centre of the LV cavity. Lastly, average Reynolds numbers were calculated for systole and diastole based on the definitions proposed by Krittian et al. (2010); the Reynolds number is defined as $Re = \rho_f v D / \mu$, where v is the characteristic velocity and D is the characteristic diameter. For systole, $D = D_{AV}$ and $\bar{v} = \Delta V_{f,eject} / \left[(0.6 \Delta \tau_{eject}) \pi (D_{AV}/2)^2 \right]$ and for diastole, $D = D_{MV}$ and $\bar{v} = \Delta V_{f,fill} / \left[(0.6 \Delta \tau_{fill}) \pi (D_{MV}/2)^2 \right]$.

Mid-ejection

Figure 5.25 shows displacement magnitude and effective stress contours for the myocardium, while Fig. 5.26 shows pressure contours and velocity vectors for the LV cavity, all of which are presented in the y - z centre-plane at mid-ejection ($\tau = 0.150$ and 1.150). The scales for these plots have been chosen to more accurately reflect the range of values observed for each pair of plots representing periods 1 and 2, rather than being representative of the range over IVC, ejection, and IVR as was shown in previous sections. At mid-ejection, flow is rapidly exiting the LV cavity, both the pressures and effective stresses are large, and large displacements of the myocardium are visible, particularly near the apex.

Figure 5.27 contains several plots at mid-ejection ($\tau = 0.150$ and 1.150), which show the transmural and longitudinal variations of the principal stretches and stresses, as well as the transmural variations of the in-plane angles, which characterize the principal

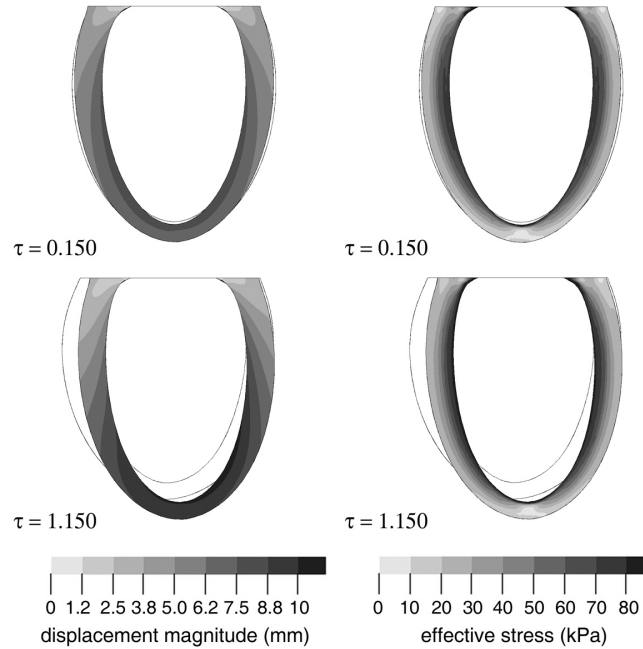


Figure 5.25: Displacement and effective stress contours for the myocardium in the y - z centre-plane at mid-ejection for two periods ($\tau = 0.150$ and $\tau = 1.150$).

stress directions. Figure 5.27a shows the deformations of the myocardium increasing from the exterior to the interior surface in a nearly-linear fashion. The corresponding principal stresses (Fig. 5.27c) also show an increase in magnitude from the exterior to the interior surfaces, with non-linear variations consistent with the form of the myocardium material model. Visible shifts in the stresses near $t/t_{\max} = 0.83$ are a consequence of insufficient mesh resolution in this region, which would likely be removed by mesh refinement.

Longitudinally, the principal stretches are nearly constant away from the apex or the base; changes in λ_1 , λ_2 , and λ_3 near the basal plane are a consequence of the imposed fixed boundary conditions along this plane and its inner edge. Trends of the longitudinal variations of T_2 and T_3 , shown in Fig. 5.27d, are consistent with trends of the corresponding stretches. T_1 , which contains a significant amount of the active stresses representing the

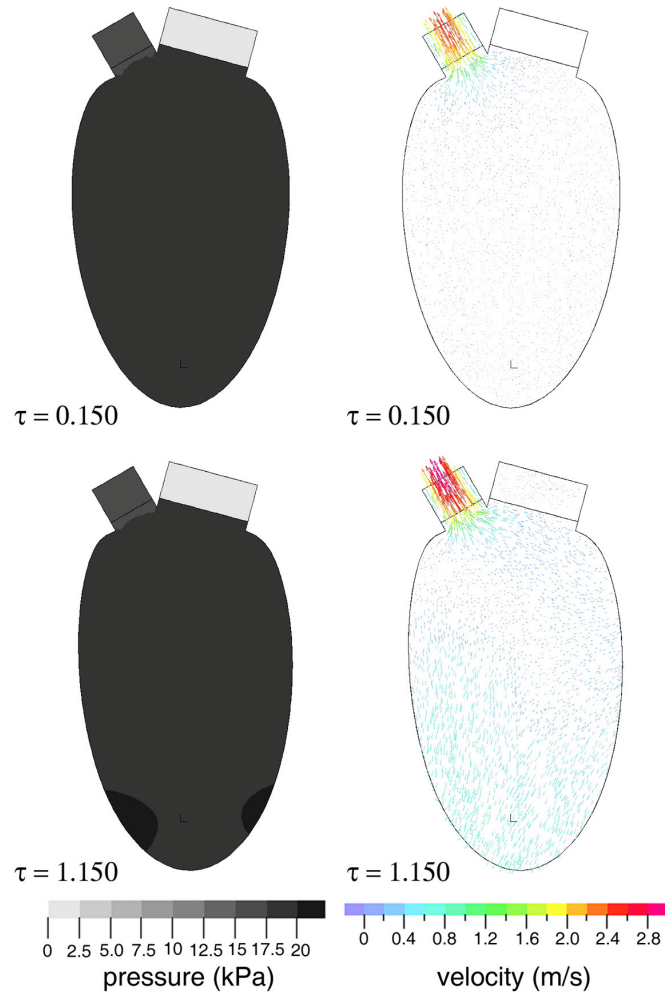


Figure 5.26: Pressure contours and velocity vectors for the LV cavity in the y - z centre-plane at mid-ejection for two periods ($\tau = 0.150$ and $\tau = 1.150$).

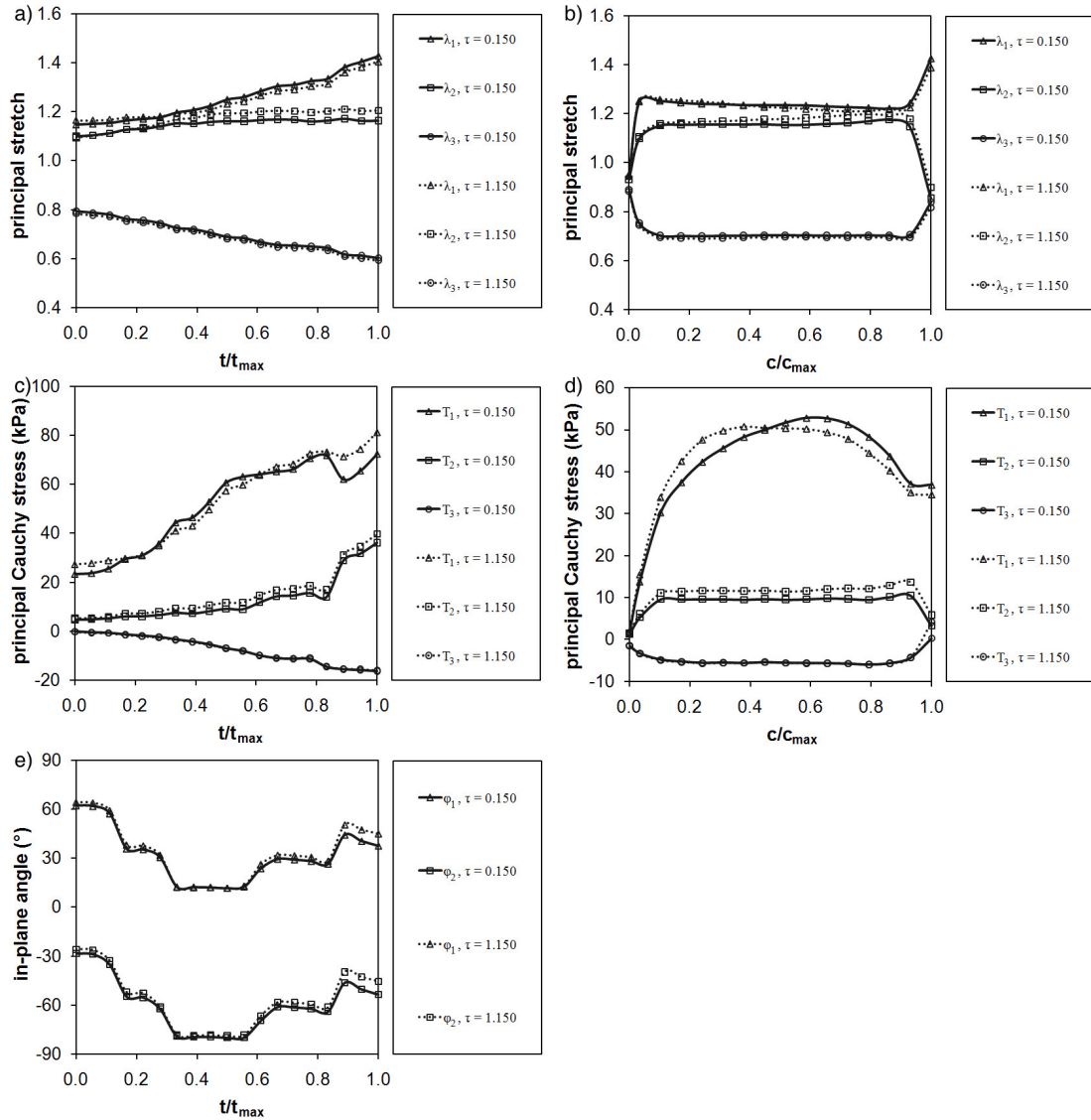


Figure 5.27: Representative transmural (a,c,e) and longitudinal (b,d) variations of the principal stretches (a,b), principal stresses (c,d), and in-plane angles (e) in the myocardium during mid-ejection for two periods ($\tau = 0.150$ and $\tau = 1.150$), calculated as described in Section 5.5.6.

contraction of the muscle fibres, increases dramatically from the apex until a maximum is reached near $c/c_{\max} = 0.67$ for period 1 and $c/c_{\max} = 0.40$ for period 2. In both cases, T_1 decreases from its maximum with increasing distance from the apex, until it reaches a plateau at the basal plane.

The transmural variations of φ_1 and φ_2 , shown in Fig. 5.27e, have five distinct regions, separated by apparent discontinuities and the values of φ_1 and φ_2 are approximately 90° out of phase. These discontinuities illustrate the influence of the muscle fibre orientation on φ_1 and φ_2 during systole, particularly the influence of the active stresses, which are primarily directed in the fibre direction. In the actual LV wall, the muscle fibre angle varies linearly through the wall. The apparent discontinuities found in Fig. 5.27e can be partially attributed to the manner in which the muscle fibre angles are described in the present study, for which the LV wall is divided into six layers, each with their own muscle fibre angle that varies in a step-wise manner from one layer to the next. One can speculate that increasing the number of wall layers would likely reduce the magnitudes of the apparent discontinuities, but potentially increase their number. It seems possible that for a sufficiently large number of wall layers, or with the use of an alternative methodology that allows for the definition of a continuous linear variation of the muscle fibre angle through the wall, these apparent discontinuities may be removed resulting in a smooth variation of φ_1 and φ_2 through the wall. It should be mentioned that, in Chapter 4, the transmural variations of φ_1 and φ_2 for the passive LV myocardium undergoing static loading were found to be smooth and without the apparent discontinuities present in Fig. 5.27e. The primary reason for the differences between the two cases is that the presence of the active stresses

during systole makes the myocardium much more anisotropic than during diastole.

Lastly, φ_3 was found to be nearly constant through the myocardium with an average value of 6.5° for $\tau = 0.150$ and 4.2° for $\tau = 1.150$. This implies that, in the equatorial plane, y_3 is nearly radial.

Plots of the radial and longitudinal variations of p_{LV} and the x -, y - and z -components of the blood velocity are presented in Fig. 5.28 at mid-ejection ($\tau = 0.150$ and 1.150). Although the resolution of the contours of p_{LV} shown in Fig. 5.26 was insufficient to show variations of p_{LV} in the LV except near the apex at $\tau = 1.150$, the plots in Figs. 5.28a and b show small variations in both the radial and longitudinal directions. For the most parts, the selected average velocity components plotted in Figs. 5.28c and d were fairly small and constant both radially and longitudinally. Noticeable differences were found between the first and second periods, with v_z for period 2 showing the largest magnitudes and strongest variability.

End systole

Figure 5.29 is a plot at end systole of the myocardium displacement and effective stress contours, while Fig. 5.30 is a plot of pressure contours and velocity vectors for the LV cavity. For period 1, displacement magnitudes were comparable at end systole and mid ejection, while for period 2, displacement magnitude at end systole were smaller than at mid-ejection. The effective stresses were lower at end systole than at mid-ejection, because the muscle fibres were contracting at mid-ejection and relaxing at end systole. Pressures in the majority of the LV cavity were also lower at end systole than at mid-ejection, however, due to the closing of the aortic valve, p_{LV} was large near the start of the LV outflow

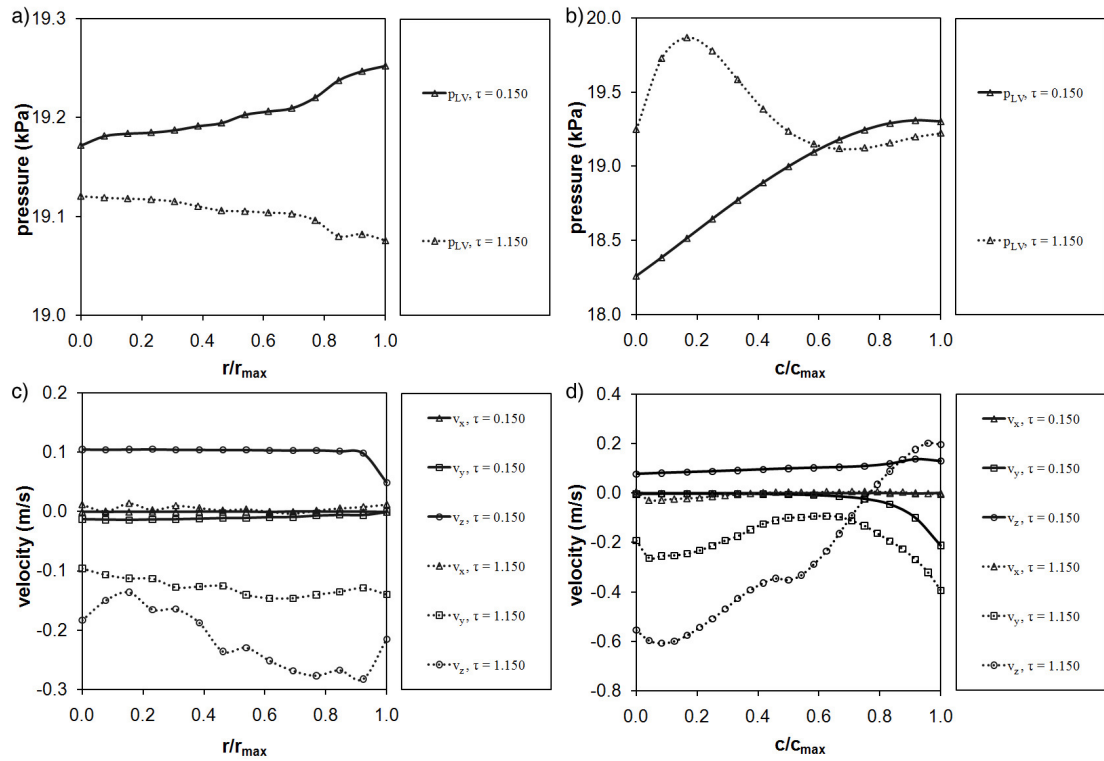


Figure 5.28: Representative radial (a,c) and longitudinal (b,d) variations of the LV cavity pressure (a,b) and blood velocities (c,d) during mid-ejection for two periods ($\tau = 0.150$ and $\tau = 1.150$), calculated as described in Section 5.5.6.

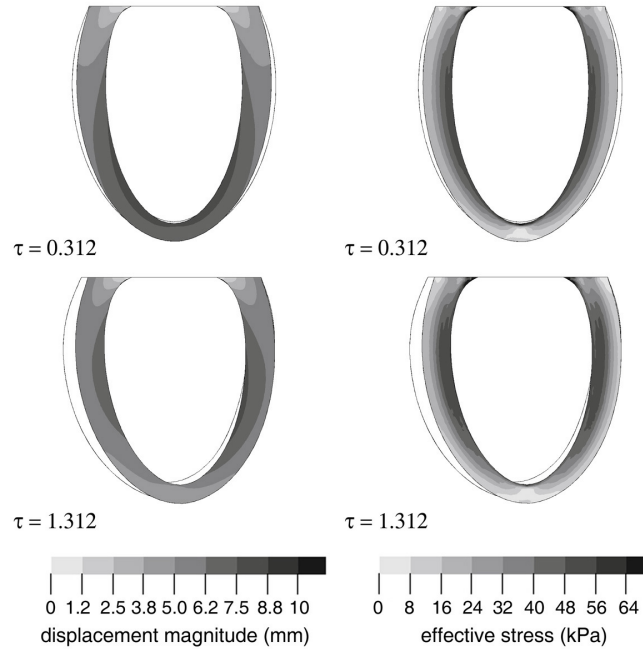


Figure 5.29: Displacement and effective stress contours for the myocardium in the y - z centre-plane at end systole for two periods ($\tau = 0.312$ and $\tau = 1.312$).

tract. The velocity vectors at end systole show noticeable differences between periods. For period 1, the velocities throughout the LV cavity were relatively small, while for period 2, velocities of the order of 0.5 m/s were observed near the apex, suggesting that the LV cavity is deforming downward in this region. This difference between periods is most likely related to the much larger pressure at the start of the LV outflow tract found for period 2.

Figure 5.31 shows plots of the transmural and longitudinal variations of the principal stretches and stresses at end systole, along with plots of the transmural variations of the corresponding in-plane angles, which characterize the principal stress directions. Trends for the transmural and longitudinal variations of the principal stretches and stresses, shown in Figs. 5.31a-d, are comparable to the trends found in Figs. 5.27a-d at mid-ejection. The principal stresses have smaller magnitudes at end systole than at mid-ejection, because the

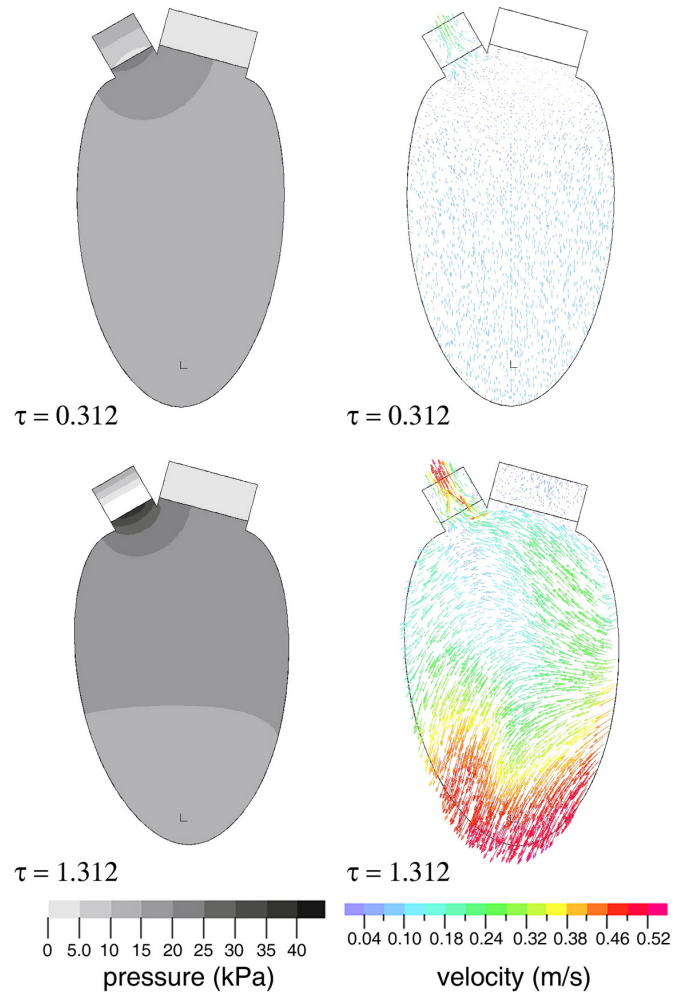


Figure 5.30: Pressure contours and velocity vectors for the LV cavity in the y - z centre-plane at end systole for two periods ($\tau = 0.312$ and $\tau = 1.312$).

muscle fibres are more relaxed at end systole than at mid-ejection. The variations of φ_1 and φ_2 are also comparable between mid-ejection and end systole. The average value of φ_3 at end systole was 8.2° for period 1 and 10.5° for period 2.

Plots of the radial and longitudinal variations of p_{LV} and the x -, y - and z -components of the blood velocity are presented in Fig. 5.32 at end systole ($\tau = 0.312$ and 1.312). In Fig. 5.32a, p_{LV} decreases slightly from the centre to the outer edge of the LV cavity, which contrasts with the corresponding mid-ejection plot, for which p_{LV} increased toward the exterior surface. Further, at end systole, p_{LV} was on average 1.75 kPa larger during period 2 than during period 1, while during mid-ejection p_{LV} was nearly the same for both periods. Longitudinally, as shown in Fig. 5.32b, p_{LV} increased significantly from the apex to the base during period 2, while it remained nearly constant during period 1. The velocities at end systole, shown in Fig. 5.32c and d, were fairly small and, for the most part, were nearly constant, with the exception of v_z during period 2. This behaviour is comparable to that observed at mid-ejection.

For systole, average Reynolds numbers were calculated for each period, as described in Section 5.5.6. For period 1, $Re = 1749$ and for period 2, $Re = 2941$. These values would most likely increase if a physiological ejection fraction were achieved. The Reynolds number calculated for period 2 happens to be comparable to the value 3431 calculated by Krittian et al. (2010) for a human LV. It should be noted, however, that comparisons of Re for LVs of different species are not necessarily meaningful, because of differences in the sizes and pulsation rates of the LVs.

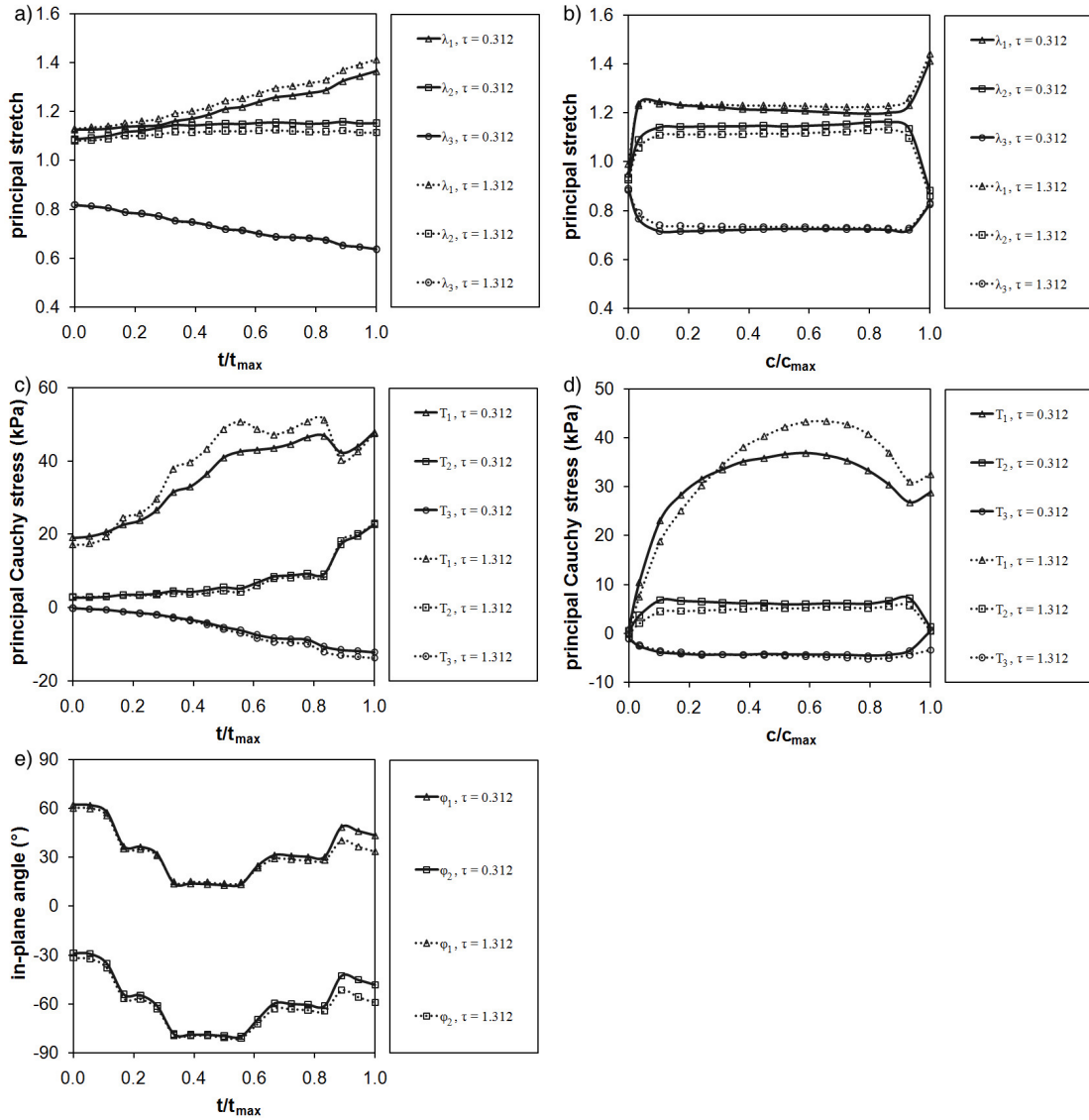


Figure 5.31: Representative transmural (a,c,e) and longitudinal (b,d) variations of the principal stretches (a,b), principal stresses (c,d), and in-plane angles (e) in the myocardium at end systole for two periods ($\tau = 0.312$ and $\tau = 1.312$), calculated as described in Section 5.5.6.

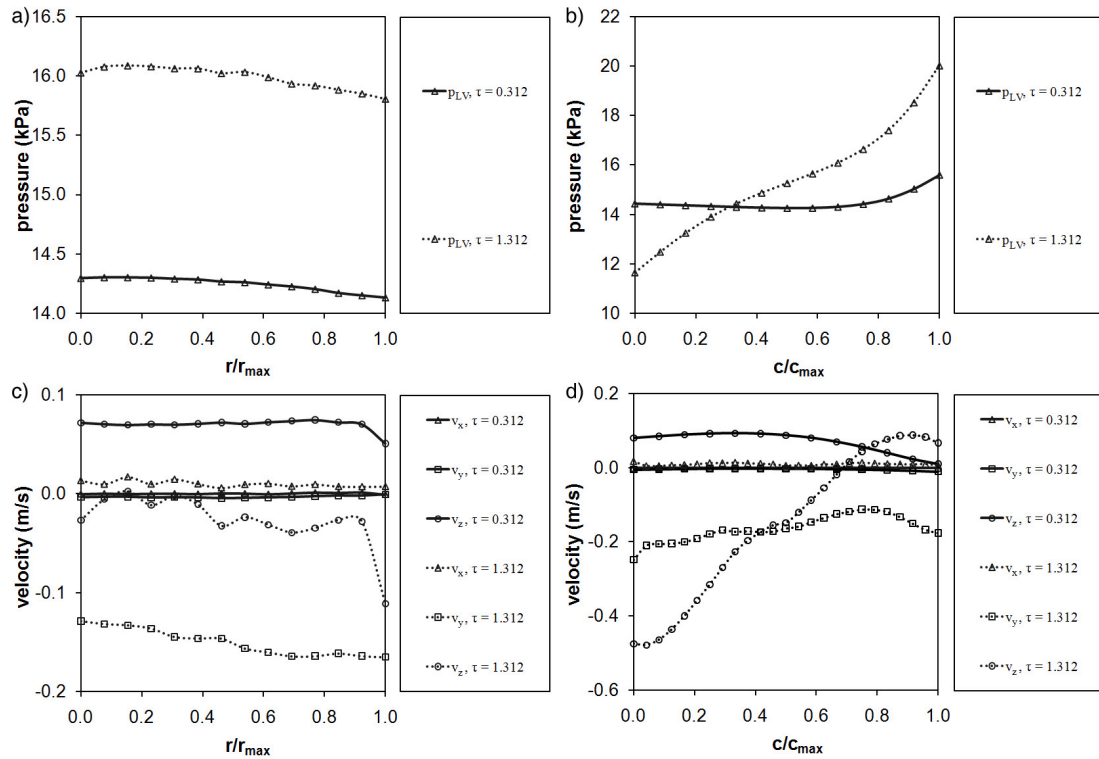


Figure 5.32: Representative radial (a,c) and longitudinal (b,d) variations of the LV cavity pressure (a,b) and blood velocities (c,d) at end systole for two periods ($\tau = 0.312$ and $\tau = 1.312$), calculated as described in Section 5.5.6.

End diastole

Figure 5.33 is a contour plot of the myocardium displacement magnitudes and effective stresses in the y - z centre-plane at end diastole for periods 1 and 2, whereas Fig. 5.34 shows the corresponding pressure contours and velocity vectors in the LV cavity. Displacement magnitudes for period 2 are more symmetric than for period 1. Stresses in the myocardium are noticeably smaller at end diastole than during systole, because, at end diastole, the muscle fibres are fully relaxed and have no active stresses. Noticeable pressure differences are visible in Fig. 5.34 within the LV cavity, however, it should be noted that the magnitudes of these differences are relatively small (pressure contours have a resolution of 0.33 kPa). Blood flow in the LV cavity at end diastole was greater for period 1 than for period 2, with higher velocities for period 1 visible in Fig. 5.34, particularly near the apex.

Figure 5.35 contains plots of the transmural and longitudinal variations of myocardium principal stretches and stresses at end diastole, along with a plot of the transmural variations of the corresponding in-plane angles, which characterize the principal stress directions. Both deformations and the magnitudes of the principal stresses increase with increasing distance from the exterior surface of the myocardium. The trends of the principal stretches are comparable to the trends found during systole as are the trends for T_2 and T_3 ; however, the trends for T_1 differ between systole and diastole due to the presence of the active stress during systole, which have a functional form that is different from that of the passive stresses. Longitudinally, the principal stretches were nearly constant, with small variations near the apex and near the base. The corresponding values of T_2 and T_3 were also nearly constant, with T_2 increasing from the apex towards the midpoint and

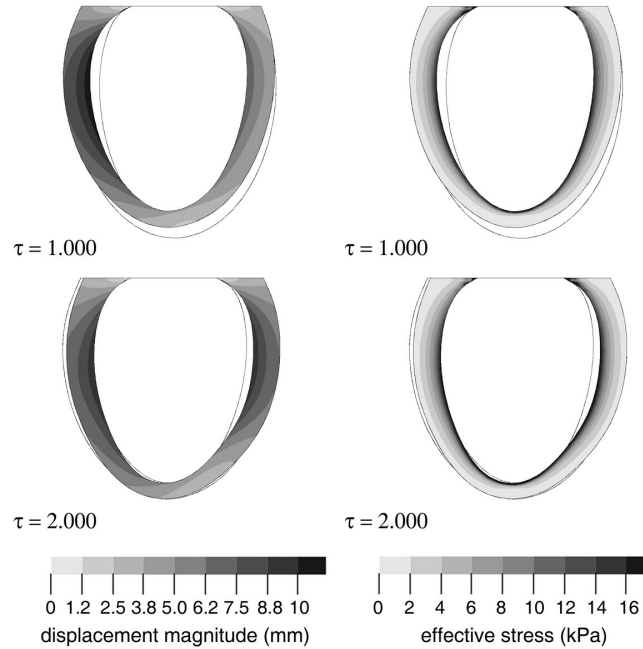


Figure 5.33: Displacement and effective stress contours for the myocardium in the y - z centre-plane at end diastole for two periods ($\tau = 1.000$ and $\tau = 2.000$).

then decreasing near the base. T_1 increased substantially from the apex until it reached a maximum near $c/c_{\max} = 0.6$ and then decreased towards the base. At end diastole, the maximum value of T_1 occurred at roughly the same value of c/c_{\max} for periods 1 and 2, while during systole there was a noticeable shift in the corresponding locations of the maximum value of T_1 between periods. Lastly, the in-plane angles in Fig. 5.35e showed very small variations through the myocardium, and were nearly constant for the inner half of the wall. This is in contrast with the behaviour of the in-plane angles during systole, which showed large apparent discontinuities through the wall, due to the presence of the active stresses which primarily act in the fibre direction.

Figure 5.36 contains plots of the radial and longitudinal variations of p_{LV} and the x -, y - and z -components of the blood velocity at end diastole ($\tau = 1.00$ and 2.00). For

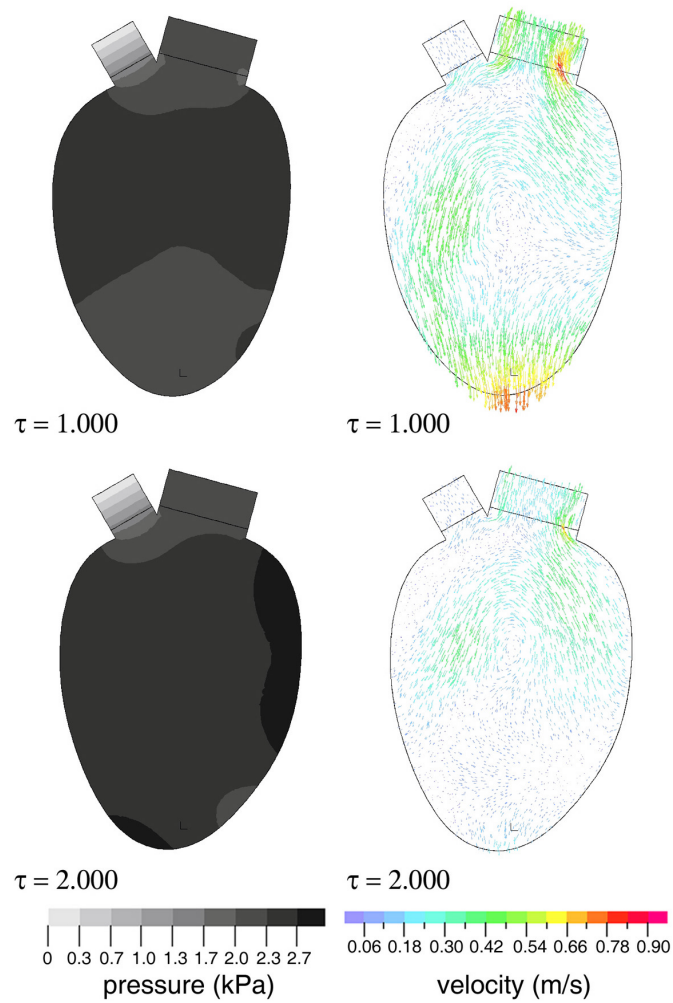


Figure 5.34: Pressure contours and velocity vectors for the LV cavity in the $y-z$ centre-plane at end diastole for two periods ($\tau = 1.000$ and $\tau = 2.000$).

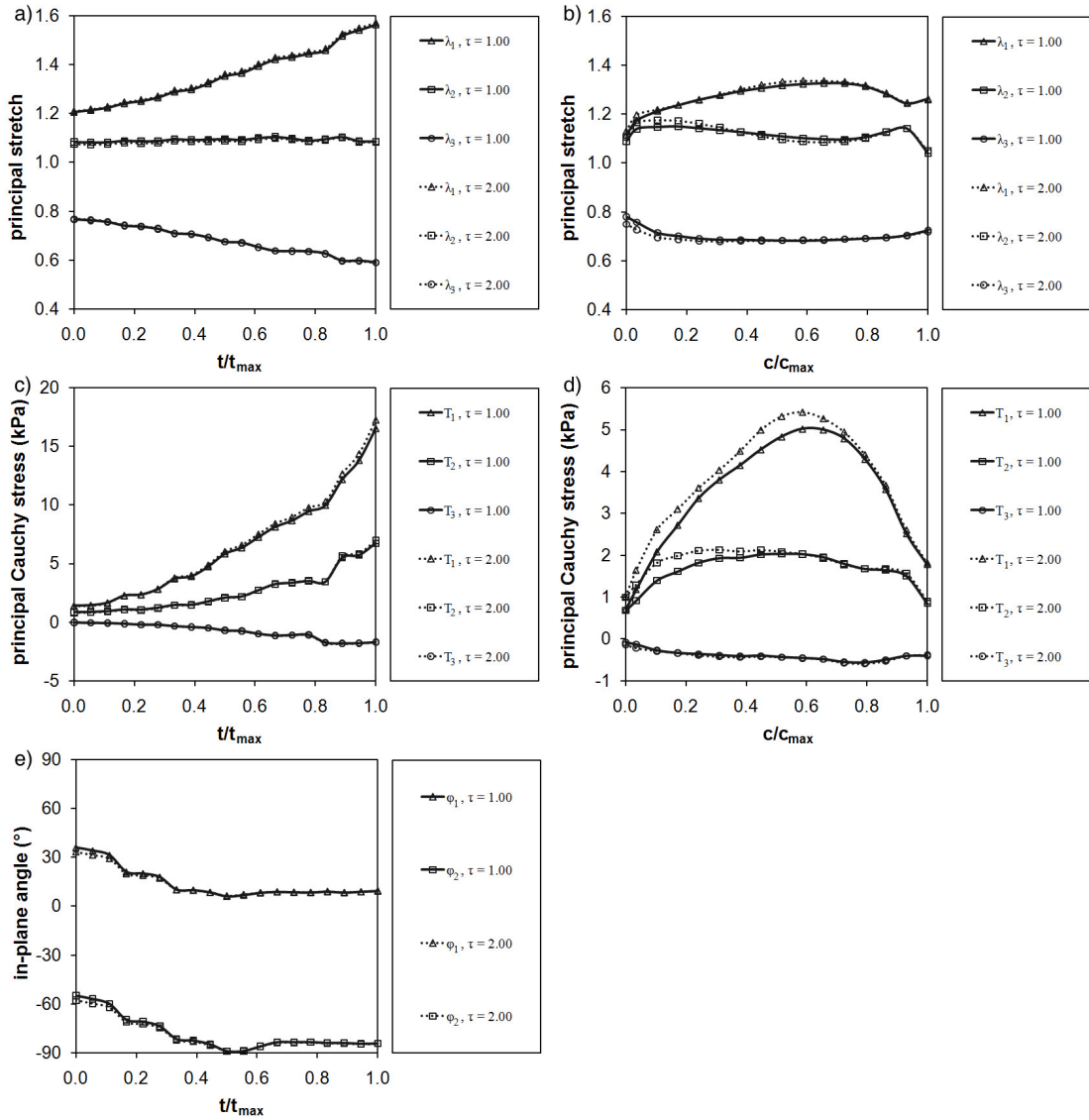


Figure 5.35: Representative transmural (a,c,e) and longitudinal (b,d) variations of the principal stretches (a,b), principal stresses (c,d), and in-plane angles (e) in the myocardium at end diastole for two periods ($\tau = 1.00$ and $\tau = 2.00$), calculated as described in Section 5.5.6.

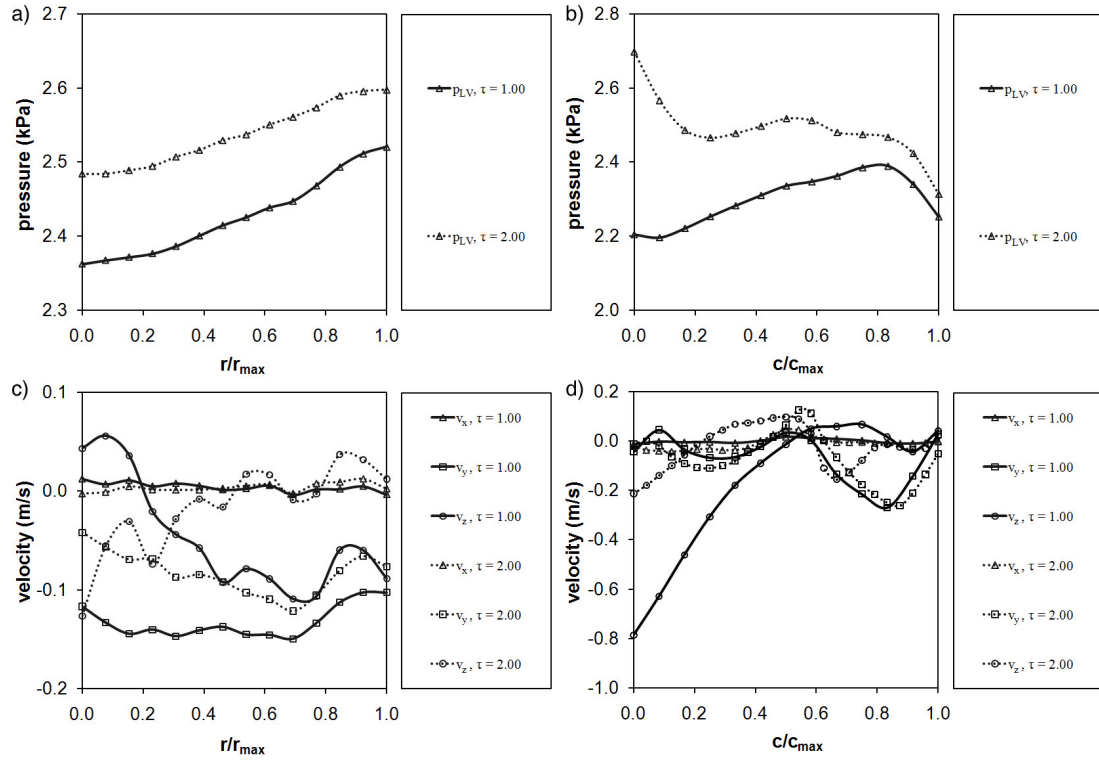


Figure 5.36: Representative radial (a,c) and longitudinal (b,d) variations of the LV cavity pressure (a,b) and blood velocities (c,d) at end diastole for two periods ($\tau = 1.00$ and $\tau = 2.00$), calculated as described in Section 5.5.6.

both periods 1 and 2, p_{LV} increased slightly from the centre to the outer edge of the LV cavity, as shown in Fig. 5.36a, while, as shown in Fig. 5.36b, it decreased longitudinally from the apex to the base for period 2 and increased then decreased for period 1. As for systole, the velocity components at end diastole, shown in Figs. 5.36c and d, were small and relatively constant, with the exception of v_z for both periods 1 and 2.

For diastole, Reynolds numbers were calculated as described in Section 5.5.6 and were found to be $Re = 193$ and 359 for periods 1 and 2, respectively. As with the systolic values, it is anticipated that these values of Re would be larger for a physiological ejection

fraction. For diastole, Krittian et al. (2010) calculated $Re = 2288$ for a human LV, which is much larger than the values for the canine LV calculated in the present study, however, as with systole, the significance of this difference is unclear.

5.6 Discussion

In this section, the successes of the present study are discussed along with future challenges in the modelling of the mechanics of the heart with FSI effects. Additionally, evaluations of several model inputs are presented.

5.6.1 Geometry and mesh

In the present study, an average canine LV geometry was chosen rather than a specimen-specific one to allow for the use of average data from the literature instead of specimen-specific data in consideration of the large variability of data from one specimen to the next and the difficulty in obtaining all necessary model inputs from a single specimen. Using an average geometry and average input data, the present simulations were successfully performed. One of the challenges in defining an average canine LV geometry was to determine appropriate diameters for the LV inflow and outflow tracts, based on diameters of the MV and AV found in the literature. As described in Appendix D, the diameters chosen in the present study were calculated from average data in the literature. However, it is possible that the assumed sizes of the valve diameters contributed to the low ejection fraction achieved in the present study. Had the diameter of the LV outflow tract been larger, more blood may have been able to exit the LV during ejection, which would increase EF .

The calculated Reynolds numbers for systole and diastole further suggest that modification of the LV inflow and outflow diameters may be appropriate. The ratio of systolic to diastolic Re for human LVs, calculated from the values proposed by Krittian et al. (2010) was approximately 1.5, while, for the present study, this ratio was approximately 9 for period 1 and 8 for period 2. An increase in D_{AV} and a corresponding decrease in D_{MV} may serve to decrease the systolic Reynolds number and increase the diastolic one, which would in turn decrease the ratio of the two towards the value calculated for humans. Although it is not anticipated that these ratios should be equal for different species, these calculations coupled with the low ejection fraction suggest that revisiting the dimensions of the LV inflow and outflow tracts may be appropriate. However, it should be mentioned that preliminary simulations were performed with an earlier version of the LV model, in which the valves were reversed such that flow exited through the inflow tract, which has a larger diameter than the outflow tract. Results of these simulations showed little difference in EF compared to the baseline case. Moreover, the assumption that the LV inflow and outflow tracts were rigid may have contributed to a reduced EF . Additional details on muscle fibre orientation and wall thickness for the LV inflow and outflow tracts, not presently available in the literature, would be required in order for one to model the upper part of the fluid geometry as deformable.

The lengths of the LV inflow and outflow tracts may also play a role in the development of the flow into and out of the LV geometry. Previous FSI simulations (Watanabe et al. (2004); Cheng et al. (2005); Krittian et al. (2010); Tang et al. (2010)) have considered inflow and outflow tracts of comparable lengths to the ones considered in the present

study. It is important to remember that the geometries of the aorta and LA are complex and should not be represented by long cylindrical tubes. Further, the flow into and out of the LV would also be complex, so including longer inlet and outlet tracts would not serve to create flows that are more physiologically correct.

Simulations in the present study have been presented for the finest fluid and solid meshes for which model convergence could be achieved and simulations could be completed in a reasonable amount of time. Using the current mesh densities, the calculation of the initial conditions for the cardiac cycle simulations required approximately two weeks of computational time, and each period of the cardiac cycle required approximately one week of computational time. From the work presented in Chapter 4, and the transmural variations of the principal stresses shown in this chapter, it is clear that additional mesh refinement is needed for the solid. However, as mentioned in Section 5.3.3, further refinement of the solid mesh led to divergence of the numerical solution. This divergence took place during the first time step of the quasi-static FSI simulations of the inflation of the passive LV, which were used to generate initial conditions for the cardiac cycle simulations. The timing of this divergence suggests that the time step used in the quasi-static FSI simulations may be the cause of this issue. Additional simulations, delegated to future work, would be required to determine if this is indeed the case. A possible solution would be to decrease the size of the time step used for the calculation of the initial conditions; however, this would substantially increase the computational time required for these calculations.

As mentioned in Section 5.4.2, additional fluid mesh refinement is also needed to study fluid mesh dependence. Any additional mesh refinement, particularly for the

fluid, would increase substantially the computational time per period, as well as the time required to generate new initial conditions for the cardiac cycle simulations. Balancing mesh refinement and computational time remains an ongoing issue in these types of numerical simulations, in particular if one was to consider a specimen-specific geometry for which even finer meshes would be required.

5.6.2 Other model inputs

During both simulated periods of the cardiac cycles, pressures in the LV cavity showed fairly good agreement with previous measurements over most of the cycle, with deviations during early filling that led to non-physiological backflow. This backflow occurred when p_{LV} exceeded p_{LA} during rapid filling. This backflow can be attributed to the combined effects of insufficient muscle fibre relaxation during this phase, crudeness of boundary conditions, and/or valve dynamics, as discussed in the following.

During rapid filling, the decrease in LV pressure due to the continuing relaxation of muscle fibres is stronger than the pressure increase caused by the incoming blood flow, such that the net effect is a decrease in p_{LV} during this phase. In the present study, the relaxation of the muscle fibres was controlled by the empirical function $F(\tau)$, which despite numerous adjustments could not be made to prevent this backflow. The objective was to select a variation $F(\tau)$, which enforces a sufficient relaxation of the muscle fibres during IVR such that the pressure drop during this phase matches physiological values, while at the same time ensuring that F is sufficiently large to allow for the necessary relaxation during rapid filling, such that p_{LV} remains less than p_{LA} during filling. In other words, the state of the muscle fibres must be such that they relax enough during IVR, but not so much that

they cannot be relaxed further during filling. In the present study, a physiological pressure drop could not be achieved during IVR without specifying a value of F at the start of filling that was too small to prevent backflow by producing the appropriate pressure drop. It is speculated that the reason why F could not be properly set in the present simulations is related to the low ejection volume achieved during systole. If EF increased, there would be less fluid inside the LV cavity during IVR, and it would be easier to decrease p_{LV} during this phase, i.e., the necessary pressure drop during IVR could be achieved with a smaller change in F than currently required. This would increase the value of F at the start of filling, which would potentially allow for a sufficient relaxation of the muscle fibres during rapid filling, such that it would prevent p_{LV} from exceeding p_{LA} and flow from entering the LV cavity.

Spikes in the pressures were evident, particularly during the second period, near the times when a valve was closed. These spikes were caused by the abrupt opening and closing of the valves. Modelling appropriately valve dynamics remains an open challenge in these types of simulations. Only recently (Wenk et al. (2010)) has a solid-only model of the mechanics of the LV been developed that included mitral valve motion. Additional work would be needed to prescribe the motion of the aortic valve in these simulations, and even more to model the valve operation with FSI. For finite element simulations, using an ALE approach to model the fluid, there is an issue with the closing of the valves in three-dimensions, related to the contact of the solid elements with each other at the tips of the valve leaflets. Even if the contact problem could be solved, including such valve motion with a sufficiently accurate solid model would require substantially more computational

time; this would likely increase the computational resources required for such simulations beyond currently available levels, especially when considering the need for computing multiple cycles.

An alternative method to address the spikes in the pressure would have been to couple the LV model with electric circuit models of the circulatory system both upstream and downstream of the LV. While this has been done by previous researchers (Watanabe et al. (2004)), in the present study, attempts were made to match the pressures without introducing this control.

Blood flow in the LV was assumed to be laminar. However, the flow, in fact, may be transitional or turbulent during parts of the cardiac cycle, particularly during phases of deceleration. By modelling the flow as laminar, we are solving the full Navier-Stokes equations and the results of these simulations could be considered to be a low order direct numerical simulation (DNS) with low spatial resolution. Further fluid mesh refinement may serve to identify small scale structures present in the flow.

One of the strengths of the present model was the inclusion of a validated myocardium material model that was transversely isotropic for both the passive and active parts, and for which the passive material properties were calculated for the species of interest. Recent studies of heart mechanics (Watanabe et al. (2002); Watanabe et al. (2004); Tang et al. (2008); Tang et al. (2010); Krittian et al. (2010)) that have included FSI effects have utilized simplified myocardium material models and/or passive material parameters adapted from species different from the ones considered in their studies. Watanabe et al. (2004) used a similar material model to the one in the present study to perform simulations

of the mechanics of the human LV, but chose their passive material parameter values to be proportional to values for rabbit LV, suggested by Lin and Yin (1998). To make matters worse, Watanabe et al. also incorrectly converted the units of one of their parameter values. Tang et al. (2010) used a modified version of the Mooney-Rivlin model to model the passive and active parts of the myocardium rather than one more suitable for modelling ventricular mechanics. Additionally, Tang et al. (2010) only included two layers in their wall, which was shown in Chapter 4 to be an insufficient number to describe the stresses in the myocardium. Krittian et al. (2010) used a transversely-isotropic material with parameter values calculated for pig LVs to model their human LV, and although it is not entirely clear in their article, it appears that they only applied active stresses in the fibre direction only. All of these previous studies presented either limited (Watanabe et al. (2002)) or no results for the myocardium.

One of the challenges in modelling the cardiac cycle using an ALE finite element approach is addressing the isovolumetric phases, for which both the aortic and mitral valves are closed and the fluid mesh is deforming. In the present study, these phases were addressed through the use a slightly compressible material model for blood, which although it led to small changes in volume during IVC and IVR, did a reasonable job of modelling these phases. In other recent FSI simulations, the issue of the isovolumetric phases was either not discussed (Krittian et al. (2010)) or neglected (Tang et al. (2008)).

5.6.3 Periodicity

Periodicity of FSI simulations in the LV has not been well documented; in fact, recent articles by Krittian et al. (2010) and Tang et al. (2010) give no mention to this issue

in their simulation results. For the present study it is unclear as to whether additional periods would lead to convergence towards a periodic state or divergence. Further, if the simulations were to converge to a periodic state, it is also unclear as to how many periods would be required to achieve periodicity.

Convergence to a periodic state is at least partially influenced by the initial conditions and convergence over a small number of cycles would only be achieved if the initial state was close to the periodic state. As the periodic state is unknown at the start of the simulations, it is unclear as to how far our initial state deviates from a periodic one. Additional cycles are required to determine the convergence or divergence of the present simulations.

5.6.4 Compressibility

In the present simulations, both blood and myocardium tissue were assumed to be slightly compressible to aid in numerical convergence, but with sufficiently high bulk moduli as to render compressibility effects essentially negligible. Although blood may be safely assumed to be incompressible, the assumption of an incompressible myocardium may not be justifiable. The coronary circulatory system is a network of blood vessels through which blood flows in myocardium. During different phases of the cardiac cycle, the blood volume in the coronary circulatory system changes. The effect of this change in blood flow is that the total volume of the myocardium changes during the cardiac cycle, so that the myocardium behaves as a compressible material, even though all of its components can be considered to be incompressible. Although the coronary circulation is well-known, it is generally not considered in numerical models of heart mechanics. For this reason, the

impact of the change in myocardium volume during the cardiac cycle on its mechanical behaviour is unknown. Additional simulations would be required to investigate this issue. These simulations could either model the myocardium as a compressible material to mimic the effects of the changing blood volume, or simulate roughly the flow of blood in the myocardium through a finite element or electric circuit approach.

5.6.5 Numerical methods

Simulations in the present study were performed using ADINA, which offers the advantage of being able to define fluid, solid, and FSI models within a single software package. Recently, other research groups (Cheng et al. (2005); Tang et al. (2010)) have also used ADINA for their FSI simulations of LV mechanics. Alternatively, we could have used other software packages such as ANSYS (ANSYS, Inc., Canonsburg, PA, USA) or Abaqus (SIMULIA, Providence, RI, USA) for the solid model and FLUENT or CFX (both from ANSYS, Inc., Canonsburg, PA, USA) for the fluid model. While ANSYS has built-in FSI coupling for its various software packages, researchers such as Krittian et al. (2010) have opted for a third-party software called MpCCI (Fraunhofer SCAI, Germany) to perform their FSI coupling. Krittian et al. (2010) coupled Abaqus and FLUENT, but MpCCI has also been used to couple ANSYS products. One advantage of MpCCI is that it allows the user to choose fluid and solid software, even if they are provided by different companies, and couple them together. As our experience in FSI simulations is limited to ADINA, we cannot comment on any specific advantages or disadvantages of using these alternative software packages, but these alternatives could be further investigated in future studies.

A different approach would have been to consider some sort of immersed method, such as the Immersed Boundary Method (IBM), which solves the fluid solution on a regular grid and does not have the mesh issues related to finite element or finite volume approaches in which the fluid mesh undergoes large deformations. However, immersed methods are somewhat limited in their solutions for the solid models and therefore do not generally allow for detailed solid and fluid results to be obtained from a single simulation. Future advancements in these methods may allow for such solutions to be obtained, potentially making these methods advantageous over finite element or finite volume methods.

5.7 Conclusions

Numerical simulations of myocardium motion and blood flow in the canine LV with FSI effects were successfully performed for two periods of the cardiac cycle. Calculated LV cavity pressures for the two periods were in good agreement with previous measurements over most of the cycle, but differed from them during rapid filling, causing backflow which is non-physiological. Trends in the cavity volume changes were consistent with physiological expectations for IVC, ejection and IVR, but the ejection volume was lower than the physiological one.

Temporal variations of the displacements and stresses in the myocardium were presented in the form of contour plots at selected times during the two cycles. Stresses were found to be much larger during ejection than during filling, in conformity with the expected effects of the contraction of the muscle fibres during ejection. Temporal variations of the LV cavity pressure and the blood velocities were presented for the same times during

the cycles as the solid results. Pressure differences in the LV cavity were visible in the contour plots for ejection for period 2, while, during filling, pressure differences were visible in the contour plots for both periods. These pressure differences emphasize the importance of performing FSI simulations of the LV operation instead of solid-only simulations of myocardium mechanics for which uniform pressures are generally assumed as boundary conditions on the inner surface of the myocardium.

Detailed spatial variations of the myocardium principal stretches, principal stresses and in-plane angles (which describe the orientation of the principal stresses) were presented at mid-ejection, end systole and end diastole, along with plots of detailed spatial variations of the pressure and velocity components in the LV cavity. The present study is the first one to report detailed spatial variations of properties for both the myocardium and the blood.

Lastly, choices of several model inputs were discussed and suggestions for future improvements to the present model were presented.

Chapter 6

Conclusions and recommendations for future work

6.1 Conclusions

The following conclusions were reached for each of the three phases of this work.

6.1.1 Myocardium material model

A material model for the canine LV myocardium has been defined for use in finite element simulations. This model was adapted from one based on measurements to make it suitable for use in numerical simulations. Specifically, additional terms were added to ensure convergence at zero stress and positive tensile stresses for small stretches. Material parameters were calculated for this model, subject to numerical constraints, which were primarily defined to ensure that both the passive and active parts of the material model were strictly convex, thus ensuring the convergence of the numerical simulations.

6.1.2 Inflation of the passive LV

To generate initial conditions for the cardiac cycle simulations, simulations of the inflation of the passive LV myocardium were performed from an unloaded stress-free state to end diastole. Dimensions of the geometry at end diastole compared well to end-diastolic measurements, thus validating the choice of end-diastolic pressure. The observed development of complex spatial variations of the stresses at end diastole justifies the present approach of generating an end-diastolic state rather than imposing an arbitrary stress distribution at end diastole. A comparison of the stresses obtained at the chosen end-diastolic pressure to stresses obtained at a lower pressure, further demonstrates that it would be inappropriate to scale stresses at a lower pressure by a constant factor to approximate end-diastolic stresses.

6.1.3 Cardiac cycle simulations

Simulations of myocardium motion and blood flow were successfully performed for two periods of the cardiac cycle. Pressure in the LV cavity showed good agreement with previous measurements over the cardiac cycle, with the exception of the rapid filling phase; differences during this phase led to non-physiological backflow. Detailed spatial and temporal variations of the principal stretches and stresses in the myocardium have been presented along with pressures and blood velocities in the LV cavity at corresponding times during the two cardiac cycles. Non-uniform pressures in the LV cavity emphasized the importance of including blood flow modelling in a study of the mechanics of the LV, rather than imposing a uniform pressure boundary condition on the inner surface of the LV cavity

for solid-only simulations. This work reports the first detailed analysis of both the solid and fluid mechanics of the LV in a single study.

6.2 Recommendations

The following recommendations for future research are made for each of the three phases of this work.

6.2.1 Myocardium material model

1. It has been shown by previous researchers that an orthotropic material model for the passive myocardium would be more appropriate than a transversely-isotropic one, as was used in the present study. To develop such a model, one would require results of biaxial tensile tests for all possible combinations of the three characteristic directions, as well as shear test results, such as those performed by Dokos et al. (2002). Once such results become available, the present simulations can be repeated using an orthotropic material model.
2. Material models for the active stresses should be extended from transversely-isotropic to orthotropic by incorporating results of corresponding biaxial tensile tests, once they become available.
3. Novak et al. (1994) showed variations in stress-stretch properties in different sections of the LV myocardium. This study should be extended to quantify differences in myocardium material properties transmurally and in different sections of the ventricles, such as the LV and RV free walls and the septum. Experiments of this nature

would allow for spatial variations in material properties to be incorporated into a myocardium material model.

4. Criscione et al. (2001) stated that the invariants of Green's strain tensor I_i , which are currently used to define the functional form of myocardium material models are not independent of each other and suggested alternative invariants that could, in conjunction with stress-stretch measurements, lead to a different functional form of myocardium material models. This idea could be developed in future research.
5. The implementation of the recommendations defined previously could potentially lead to an improved material model for the myocardium, but this model would still be only representative of an *in vitro* material. Additional research is needed to correlate these *in vitro* measurements with *in vivo* data, and use this analysis to develop a material model that it is more representative of the material behaviour of an intact heart.

6.2.2 Inflation of the passive LV

1. Stresses in the LV myocardium during filling, as well as residual stresses in the unloaded LV myocardium, have not yet been measured. The measurement of these stresses would allow for a more complete validation of numerical models to be performed.
2. If residual stresses were measured, a new material model for the LV myocardium could be developed based on the work of Hoger (1993), which could be utilized in static filling simulations as a way to account for the residual stresses in the unloaded myocardium.

3. An extension of this work to an anatomical LV/RV geometry was briefly described in Appendix C. Further work on the incorporation of varying muscle fibres angles and non-uniform myocardium material properties throughout the LV and RV could be performed to further improve these simulations.
4. It has previously been shown Yin et al. (1996) that the myocardium behaves as a compressible material due to the transfer of fluid into and out of the myocardium. To account for the variation in myocardium volume during filling, future researchers could incorporate poroelastic and viscoelastic effects into material models of the myocardium as proposed by Huyghe et al. (1991) and Yang and Taber (1991).
5. The improvements suggested previously would provide a more complete model of the myocardium behaviour during static filling. However, it would be most beneficial to establish a link between the *in vitro* data from previous experiments and *in vivo* data from living dogs. Performing measurements of pressure, cavity volume, and stresses in the intact canine myocardium and then performing the same measurements on the myocardium after it has been excised would allow for a correlation to be made between *in vitro* and *in vivo* data that would allow researchers to correct their models based on *in vitro* data to be more representative of an *in vivo* state.

6.2.3 Cardiac cycle simulations

1. The solid mesh used in the present cardiac cycle simulations was coarser than required for a mesh-independent solution. Attempts to refine the solid mesh led to model divergence. Future work should look into ways to get a convergent solution with a

finer myocardium mesh. Additionally, further mesh refinement is required for the fluid to make definitive statements on fluid mesh independence. It is recognized, however, that mesh refinement would entail a substantial increase in computational cost, which may render the implementation of this recommendation non-feasible in the near future.

2. In the current numerical model, the pressures at the LV inflow and outflow boundaries are defined as model inputs, and no mechanism is in place to adjust them during the simulations based on flow conditions. Moreover, the abrupt opening and closing of the valves generated non-physiological spikes in the cavity pressure. Future work could examine the choice of inflow and outflow boundary conditions as well as the mechanism used to open and close the valves to improve the flow at the boundaries, particularly during valve opening and closing. One way that this could be accomplished is by coupling the finite element model with electric circuit models representing the circulatory system upstream and downstream of the LV and allowing for less abrupt changes in valve geometry at these boundaries.
3. The forcing function used in the present study to model the dynamics of active muscle fibre contraction is a crude approximation of physiology. Additional work is needed to quantify the material properties of the myocardium during the contraction and relaxation of the muscle fibres and to incorporate these material properties into a material model that could be used for cardiac cycle simulations.
4. Blood is a non-Newtonian fluid and the flow of blood into, out of, and within the LV cavity may be turbulent, at least during part of the cycle. A more realistic material

model of blood as well as a model for turbulence could be included in future studies of LV mechanics.

5. Lastly, the deformation of the LV is influenced by the RV. Future work could extend the present study to one of a LV-RV geometry and perform simultaneous FSI simulations of the mechanics of the LV and the RV.

6.2.4 Extension to patient-specific models

In this section, recommendations for extending this work to patient-specific models are briefly discussed along with the information that is required to make these extensions.

Ultimately, the goal of a study of the mechanics of the LV would be to describe the behaviour of the blood and the heart wall in a specific human patient to determine the health of the patient's heart, the extent of any diseases, and/or possible treatment options for these diseases. The challenge in doing so is obtaining all of the necessary model inputs from a specific patient and incorporating them into a numerical model that can run in a reasonable amount of time and give solutions that are sufficiently accurate to aid physicians in diagnosis and treatment decisions.

To extend the present work to a patient-specific study would require a geometry based on MRI or CT data that would include not only the boundaries of the LV cavity and wall, but also muscle fibre information. Blood pressures and/or velocities would also be needed as model inputs. While a solid geometry and fluid boundary conditions allow for CFD-MRI studies to be conducted, such as those performed by Saber et al. (2003), Long et al. (2008), and Doenst et al. (2009), in order to extend these studies to fully-coupled

FSI simulations, material properties for the LV wall would be required. Developing a methodology to obtain these material properties *in vivo* and incorporating them and muscle fibre orientations into a numerical model would allow the deformation of the LV wall to be calculated along with the blood flow in an FSI simulation. This would allow physicians to observe areas of atypical behaviour within the LV wall and determine their effects on the flow of blood in the LV cavity. It would also allow treatment options to be considered by varying the LV wall properties.

In conclusion, understanding the material behaviour of the LV wall *in vivo* remains the biggest challenge to extending FSI simulations from idealized geometries to patient-specific ones in which the behaviour of the LV wall is accurately captured. The development of a method to obtain this information would be a significant step in understanding and treating heart disease.

Bibliography

ADINA R & D, Inc. (2008a). *ADINA Theory and Modeling Guide Volume I: ADINA*. ADINA R & D, Inc., Watertown, MA, USA.

ADINA R & D, Inc. (2008b). *ADINA Theory and Modeling Guide Volume III: ADINA CFD & FSI*. ADINA R & D, Inc., Watertown, MA, USA.

Baccani, B., F. Domenichini, and G. Pedrizzetti (2002). Vortex dynamics in a model left ventricle during filling. *European Journal of Mechanics B/Fluids* 21, 527–543.

Baccani, B., F. Domenichini, and G. Pedrizzetti (2003). Model and influence of mitral valve opening during the left ventricular filling. *Journal of Biomechanics* 36, 355–361.

Baccani, B., F. Domenichini, G. Pedrizzetti, and G. Tonti (2002). Fluid dynamics of the left ventricular filling in dilated cardiomyopathy. *Journal of Biomechanics* 35, 665–671.

Bathe, K. J. (1996). *Finite Element Procedures*. Prentice Hall, Englewood Cliffs, NJ, USA.

Bertsekas, D. P. (1999). *Nonlinear Programming*. Athena Scientific, Belmont, MA,

USA.

- Bovendeerd, P. H. M., T. Arts, T. Delhaas, J. M. Huyghe, D. H. van Campen, and R. S. Reneman (1996). Regional wall mechanics in the ischemic left ventricle: Numerical modeling and dog experiments. *American Journal of Physiology* 270, H398–H410.
- Chapelle, D., M. Fernández, J.-F. Gerbeau, P. Moireau, J. Sainte-Marie, and N. Zemzemi (2009). Numerical simulation of the electromechanical activity of the heart. In N. Ayache, H. Delingette, and M. Sermesant (Eds.), *Lecture Notes in Computer Science*, Volume 5528, pp. 357–365. Springer, Heidelberg, Germany.
- Cheng, Y., H. Oertel, and T. Schenkel (2005). Fluid-structure coupled CFD simulation of the left ventricular flow during filling phase. *Annals of Biomedical Engineering* 33, 567–576.
- Costa, K. D., J. W. Holmes, and A. D. McCulloch (2001). Modelling cardiac mechanical properties in three dimensions. *Philosophical Transactions of the Royal Society of London A* 359, 1233–1250.
- Costa, K. D., P. J. Hunter, J. S. Wayne, L. K. Waldman, J. M. Guccione, and A. D. McCulloch (1996). A three-dimensional finite element method for large elastic deformations of ventricular myocardium: II - Prolate spheroidal coordinates. *Journal of Biomechanical Engineering* 118, 464–472.
- Costa, K. D., K. May-Newman, D. Farr, W. G. O’Dell, A. D. McCulloch, and J. H. Omens (1997). Three-dimensional residual strain in midanterior canine

- left ventricle. *American Journal of Physiology* 273, H1968–H1976.
- Coudiere, Y. (2005). Personal communication.
- Criscione, J. C., A. S. Douglas, and W. C. Hunter (2001). Physically based strain invariant set for materials exhibiting transversely isotropic behavior. *Journal of the Mechanics and Physics of Solids* 49, 871–897.
- Criscione, J. C., A. D. McCulloch, and W. C. Hunter (2002). Constitutive framework optimized for myocardium and other high-strain, laminar materials with one fiber family. *Journal of the Mechanics and Physics of Solids* 50, 1681–1702.
- DeAnda, Jr., A., M. Komeda, M. R. Moon, G. R. Green, A. F. Bolger, S. D. Nikolic, G. T. Daughters, II, and D. C. Miller (1998). Estimation of regional left ventricular wall stresses in intact canine hearts. *American Journal of Physiology* 275, H1879–H1885.
- Deserranno, D., Z. B. Popovic, N. L. Greenberg, M. Kassemi, and J. D. Thomas (2003). Axisymmetric fluid-structure interaction model of the left ventricle. In K. J. Bathe (Ed.), *Computational Fluid and Solid Mechanics 2003*, pp. 1669–1672. Elsevier Science Ltd., Oxford, UK.
- Doenst, T., K. Spiegel, M. Reik, M. Markl, J. Hennig, S. Nitzsche, F. Beyersdorf, and H. Oertel (2009). Fluid-dynamic modeling of the human left ventricle: Methodology and application to surgical ventricular reconstruction. *Annals of Thoracic Surgery* 87, 1187–1195.
- Dokos, S., B. H. Smaill, A. A. Young, and I. J. LeGrice (2002). Shear properties of passive ventricular myocardium. *American Journal of Physiology* 283, H2650–

H2659.

- Domenichini, F., G. Pedrizzetti, and B. Baccani (2005). Three-dimensional filling flow into a model left ventricle. *Journal of Fluid Mechanics* 539, 179–198.
- Domenichini, F., G. Querzoli, A. Cenedese, and G. Pedrizzetti (2007). Combined experimental and numerical analysis of the flow structure into the left ventricle. *Journal of Biomechanics* 40, 1988–1994.
- Doyle, M. G., S. Tavoularis, and Y. Bourgault (2010a). Adaptation of a rabbit myocardium material model for use in a canine left ventricle simulation study. *Journal of Biomechanical Engineering* 132, 041006–1–041006–12.
- Doyle, M. G., S. Tavoularis, and Y. Bourgault (2010b). Application of parallel processing to the simulation of heart mechanics. In D. J. K. Mewhort, N. M. Cann, G. W. Slater, and T. J. Naughton (Eds.), *Lecture Notes in Computer Science*, Volume 5976, pp. 30–47. Springer-Verlag Berlin Heidelberg, Germany.
- Gresho, P. M. and R. L. Sani (1998). *Incompressible Flow and the Finite Element Method Volume 2: Isothermal Laminar Flow*. John Wiley and Sons, Ltd., Chichester, UK.
- Guccione, J. M., K. D. Costa, and A. D. McCulloch (1995). Finite element stress analysis of left ventricular mechanics in the beating dog heart. *Journal of Biomechanics* 28, 1167–1177.
- Guccione, J. M., A. D. McCulloch, and L. K. Waldman (1991). Passive material properties of intact ventricular myocardium determined from a cylindrical model. *Journal of Biomechanical Engineering* 113, 42–55.

- Guccione, J. M., L. K. Waldman, and A. D. McCulloch (1993). Mechanics of active contraction in cardiac muscle: Part II - Cylindrical models of the systolic left ventricle. *Journal of Biomechanical Engineering* 115, 82–90.
- Hoger, A. (1993). The constitutive equation for finite deformations of a transversely isotropic hyperelastic material with residual stress. *Journal of Elasticity* 33, 107–118.
- Holmes, J. W. (2004). Determinants of left ventricular shape change during filling. *Journal of Biomechanical Engineering* 126, 98–103.
- Holzappel, G. A. (2000). *Nonlinear Solid Mechanics: A Continuum Approach for Engineering*. John Wiley & Sons, Ltd., Chichester, UK.
- Humphrey, J. D., R. K. Strumpf, and F. C. P. Yin (1990a). Determination of a constitutive relation for passive myocardium: I. A new functional form. *Journal of Biomechanical Engineering* 122, 333–339.
- Humphrey, J. D., R. K. Strumpf, and F. C. P. Yin (1990b). Determination of a constitutive relation for passive myocardium: II. Parameter estimation. *Journal of Biomechanical Engineering* 112, 340–346.
- Hunter, P. J. (2007). Personal communication.
- Huyghe, J. M., D. H. van Campen, T. Arts, and R. M. Heethaar (1991). A two-phase finite element model of the diastolic left ventricle. *Journal of Biomechanics* 24, 527–538.
- Kang, T. and F. C. P. Yin (1996). The need to account for residual strains and composite nature of heart wall in mechanical analyses. *American Journal of*

Physiology 271, H947–H961.

- Kerckhoffs, R. C. P., M. L. Neal, Q. Gu, J. B. Bassingthwaite, J. H. Omens, and A. D. McCulloch (2007). Coupling of a 3D finite element model of cardiac ventricular mechanics to lumped systems models of the systemic and pulmonic circulation. *Annals of Biomedical Engineering* 35, 1–18.
- Krittian, S., U. Janoske, H. Oertel, and T. Böhlke (2010). Partitioned fluid-solid coupling for cardiovascular blood flow. *Annals of Biomedical Engineering* 38, 1426–1441.
- Kroon, W., T. Delhaas, P. Bovendeerd, and T. Arts (2009). Computational analysis of the myocardial structure: Adaptation of cardiac myofiber orientations through deformation. *Medical Image Analysis* 13, 346–353.
- Lanir, Y. (1979). A structural theory for the homogeneous biaxial stress-strain relationships in flat collagenous tissues. *Journal of Biomechanics* 12, 423–436.
- LeGrice, I. J., B. H. Smaill, L. Z. Chai, S. G. Edgar, J. B. Gavin, and P. J. Hunter (1995). Laminar structure of the heart: Ventricular myocyte arrangement and connective tissue architecture in the dog. *American Journal of Physiology* 269, H571–H582.
- Li, J. K.-J. (1996). *Comparative Cardiovascular Dynamics of Mammals*. CRC Press, Inc., Boca Raton, FL, USA.
- Lin, D. H. S. and F. C. P. Yin (1998). A multiaxial constitutive law for mammalian left ventricular myocardium in steady-state barium contracture or tetanus. *Journal of Biomechanical Engineering* 120, 504–517.

- Long, Q., R. Merrifield, X. Y. Xu, P. Kilner, D. N. Firmin, and G.-Z. Yang (2008). Subject-specific computational simulation of left ventricular flow based on magnetic resonance imaging. *Proceedings of the Institution of Mechanical Engineers, Part H: Journal of Engineering in Medicine* 222, 475–485.
- Long, Q., R. Merrifield, G. Z. Yang, P. J. Kilner, D. N. Firmin, and X. Y. Xu (2003). The influence of inflow boundary conditions on intra left ventricle flow predictions. *Journal of Biomechanical Engineering* 125, 922–927.
- McCulloch, A. D., P. J. Hunter, and B. H. Smaill (1992). Mechanical effects of coronary perfusion in the passive canine left ventricle. *American Journal of Physiology* 262, H523–H530.
- McCulloch, A. D. and R. Mazhari (2001). Regional myocardial mechanics: Integrative computational models of flow-function relations. *Journal of Nuclear Cardiology* 8, 506–519.
- McCulloch, A. D. and J. H. Omens (1991). Factors affecting the regional mechanics of the diastolic heart. In L. Glass, P. Hunter, and A. McCulloch (Eds.), *Theory of Heart*, pp. 87–119. Springer-Verlag, New York, NY, USA.
- McCulloch, A. D., B. H. Smaill, and P. J. Hunter (1987). Left ventricular epicardial deformation in isolated arrested dog heart. *American Journal of Physiology* 252, H233–H241.
- McCulloch, A. D., B. H. Smaill, and P. J. Hunter (1989). Regional left ventricular epicardial deformation in the passive dog heart. *Circulation Research* 64, 721–733.

- McQueen, D. M. and C. S. Peskin (1997). Shared-memory parallel vector implementation of the immersed boundary method for the computation of blood flow in the beating mammalian heart. *Journal of Supercomputing* 11, 213–236.
- McQueen, D. M. and C. S. Peskin (2000). A three-dimensional computer model of the human heart for studying cardiac fluid dynamics. *New Visualization Techniques* 34, 1–10.
- McQueen, D. M., C. S. Peskin, and L. Zhu (2001). The immersed boundary method for incompressible fluid-structure interaction. In K. J. Bathe (Ed.), *Computational Fluid and Solid Mechanics 2001*, pp. 26–30. Elsevier Science Ltd., Oxford, UK.
- Nakamura, M., S. Wada, T. Mikami, A. Kitabatake, and T. Karino (2001). Relationship between intraventricular flow patterns and the shapes of the aliasing area in color M-mode Doppler echocardiograms: A CFD study with an axisymmetric model of the LV. *JSME International Journal, Series C: Mechanical Systems, Machine Elements and Manufacturing* 44, 1013–1019.
- Nakamura, M., S. Wada, T. Mikami, A. Kitabatake, and T. Karino (2002). A computational fluid mechanical study on the effects of opening and closing of the mitral orifice on a transmitral flow velocity profile and an early diastolic intraventricular flow. *JSME International Journal, Series C: Mechanical Systems, Machine Elements and Manufacturing* 45, 913–922.
- Nakamura, M., S. Wada, T. Mikami, A. Kitabatake, and T. Karino (2003). Computational study on the evolution of an intraventricular vortical flow during

- early diastole for the interpretation of color M-mode Doppler echocardiograms. *Biomechanics and Modeling in Mechanobiology* 2, 59–72.
- Nakamura, M., S. Wada, and T. Yamaguchi (2006a). Computational analysis of blood flow in an integrated model of the left ventricle and the aorta. *Journal of Biomechanical Engineering* 128, 837–843.
- Nakamura, M., S. Wada, and T. Yamaguchi (2006b). Influence of the opening mode of the mitral valve orifice on intraventricular hemodynamics. *Annals of Biomedical Engineering* 34, 927–935.
- Nash, M. P. and P. J. Hunter (2000). Computational mechanics of the heart. *Journal of Elasticity* 61, 113–141.
- Nielsen, P. M. F., I. J. LeGrice, B. H. Smaill, and P. J. Hunter (1991). Mathematical model of geometry and fibrous structure of the heart. *American Journal of Physiology* 260, H1365–H1378.
- Nocedal, J. and S. J. Wright (1999). *Numerical Optimization*. Springer-Verlag, New York, NY, USA.
- Novak, V. P., F. C. Yin, and J. D. Humphrey (1994). Regional mechanical properties of passive myocardium. *Journal of Biomechanics* 27, 403–412.
- Oertel, H., S. Krittian, and K. Spiegel (2009). *Modelling the Human Cardiac Mechanics* (3rd ed.). Universitätsverlag Karlsruhe, Karlsruhe, Germany.
- Omens, J. H. and Y. C. Fung (1990). Residual strain in rat left ventricle. *Circulation Research* 66, 37–45.
- Omens, J. H., K. D. May, and A. D. McCulloch (1991). Transmural distribution of

- three-dimensional strain in the isolated arrested canine left ventricle. *American Journal of Physiology* 261, H918–H928.
- Opie, L. H. (2004). *Heart Physiology: From Cell to Circulation* (4th ed.). Lippincott Williams & Wilkins, Philadelphia, PA, USA.
- Parmley, W. W. and L. Talbot (1979). Heart as a pump. In R. M. Berne, N. Sperelakis, and S. R. Geiger (Eds.), *Handbook of Physiology: The Cardiovascular System, Section 2*, pp. 429–460. American Physiological Society, Bethesda, MD, USA.
- Pedley, T. J. (1980). *The Fluid Mechanics of Large Blood Vessels*, Chapter 1: Physiological Introduction, pp. 10–33. Cambridge University Press, Cambridge, UK.
- Peskin, C. S. (1977). Numerical analysis of blood flow in the heart. *Journal of Computational Physics* 25, 220–252.
- Peskin, C. S. and D. M. McQueen (1996). Fluid dynamics of the heart and its valves. In H. G. Othmer, F. R. Adler, M. A. Lewis, and J. C. Dallon (Eds.), *Case Studies in Mathematical Modeling - Ecology, Physiology, and Cell Biology*, pp. 309–337. Prentice-Hall, Inc., Englewood Cliffs, NJ.
- Pierrakos, O., P. P. Vlachos, and D. P. Telionis (2004). Time-resolved DPIV analysis of vortex dynamics in a left ventricular model through bileaflet mechanical and porcine heart valve prostheses. *Journal of Biomechanical Engineering* 126, 714–726.
- Rankin, J. S. (1980). The chamber dynamics of the intact left ventricle. In J. Bann, A. C. Arntzenius, and E. L. Yellin (Eds.), *Cardiac Dynamics*, pp. 95–106. Mar-

tinus Nijhoff Publishers, The Hague, The Netherlands.

Ross, Jr., J., E. H. Sonnenblick, J. W. Covell, G. A. Kaiser, and D. Spiro (1967).

The architecture of the heart in systole and diastole: Technique of rapid fixation and analysis of left ventricular geometry. *Circulation Research* 21, 409–421.

Sabbah, H. N. and P. D. Stein (1981). Pressure-diameter relations during early diastole in dogs. Incompatibility with the concept of passive left ventricular filling. *Circulation Research* 45, 357–365.

Saber, N. R., A. D. Gosman, N. B. Wood, P. J. Kilner, C. L. Charrier, and D. N. Firmin (2001). Computational flow modeling of the left ventricle based on *in vivo* MRI data: Initial experience. *Annals of Biomedical Engineering* 29, 275–283.

Saber, N. R., N. B. Wood, A. D. Gosman, R. D. Merrifield, G.-Z. Yang, C. L. Charrier, P. D. Gatehouse, and D. N. Firmin (2003). Progress towards patient-specific computational flow modeling of the left heart via combination of magnetic resonance imaging with computational fluid dynamics. *Annals of Biomedical Engineering* 31, 42–52.

Schenkel, T., M. Malve, M. Reik, M. Markl, B. Jung, and H. Oertel (2009). MRI-based CFD analysis of flow in a human left ventricle: Methodology and application to a healthy heart. *Annals of Biomedical Engineering* 37, 503–515.

Schmid, H., Y. K. Wang, J. Ashton, A. E. Ehret, S. B. S. Krittian, M. P. Nash, and P. J. Hunter (2009). Myocardial material parameter estimation: A comparison of invariant based orthotropic constitutive equations. *Computer Methods in Biomechanics and Biomedical Engineering* 12, 283–295.

- Stevens, C. and P. J. Hunter (2003). Sarcomere length changes in a 3D mathematical model of the pig ventricles. *Progress in Biophysics & Molecular Biology* 82, 229–241.
- Stevens, C., E. Remme, I. LeGrice, and P. Hunter (2003). Ventricular mechanics in diastole: Material parameter sensitivity. *Journal of Biomechanics* 36, 737–748.
- Streeter, Jr., D. D. and W. T. Hanna (1973). Engineering mechanics for successive states in canine left ventricular myocardium: I. Cavity and wall geometry. *Circulation Research* 33, 639–655.
- Streeter, Jr., D. D., S. M. Henry, H. M. Spotnitz, D. P. Patel, J. Ross, J., and E. H. Sonnenblick (1969). Fiber orientation in the canine left ventricle during diastole and systole. *Circulation Research* 24, 339–347.
- Sun, W. and M. S. Sacks (2005). Finite element implementation of a generalized Fung-elastic constitutive model for planar soft tissues. *Biomechanics and Modeling in Mechanobiology* 4, 190–199.
- Tang, D., C. Yang, T. Geva, and P. J. del Nito (2008). Patient-specific MRI-based 3D FSI RV/LV/patch models for pulmonary valve replacement surgery and patch optimization. *Journal of Biomechanical Engineering* 130, 041010–1–041010–10.
- Tang, D., C. Yang, T. Geva, and P. J. del Nito (2010). Image-based patient-specific ventricle models with fluid-structure interaction for cardiac function assessment and surgical design optimization. *Progress in Pediatric Cardiology* 30, 51–62.
- Tavoularis, S. (2005). *Measurement in Fluid Mechanics*. Cambridge University

Press, New York, NY, USA.

Tortora, G. J. (2002). *Principles of Human Anatomy* (9th ed.). John Wiley & Sons, Inc., New York, NY, USA.

Usyk, T. P., R. Mazhari, and A. D. McCulloch (2000). Effect of laminar orthotropic myofiber architecture on regional stress and strain in the canine left ventricle. *Journal of Elasticity* 61, 143–164.

Vetter, F. J. and A. D. McCulloch (2000). Three-dimensional stress and strain in passive rabbit left ventricle: A model study. *Annals of Biomedical Engineering* 28, 781–792.

Vierendeels, J. A., K. Rienslagh, E. Dick, and P. R. Verdonck (2000). Computer simulation of intraventricular flow and pressure gradients during diastole. *Journal of Biomechanical Engineering* 122, 667–674.

Vigmond, E. J., C. Clements, D. M. McQueen, and C. S. Peskin (2008). Effect of bundle branch block on cardiac output: A whole heart simulation study. *Progress in Biophysics and Molecular Biology* 97, 520–542.

Watanabe, H., T. Hisada, S. Sugiura, J. Okada, and H. Fukunari (2002). Computer simulation of blood flow, left ventricular wall motion and their interrelationship by fluid-structure interaction finite element method. *JSME International Journal, Series C: Mechanical Systems, Machine Elements and Manufacturing* 45, 1003–1012.

Watanabe, H., T. Sugano, S. Sugiura, and T. Hisada (2004). Finite element analysis of ventricular wall motion and intra-ventricular blood flow in heart with

- myocardial infarction. *JSME International Journal, Series C: Mechanical Systems, Machine Elements and Manufacturing* 47, 1019–1026.
- Watanabe, H., S. Sugiura, and T. Hisada (2003). Finite element analysis on the relationship between left ventricular pump function and fiber structure within the wall. *JSME International Journal, Series C: Mechanical Systems, Machine Elements and Manufacturing* 46, 1330–1339.
- Watanabe, H., S. Sugiura, H. Kafuku, and T. Hisada (2004). Multiphysics simulation of left ventricular filling dynamics using fluid-structure interaction finite element method. *Biophysical Journal* 87, 2074–2085.
- Wenk, J. F., Z. Zhang, G. Cheng, D. Malhotra, G. Acevado-Bolton, M. Burger, T. Suzuki, D. A. Saloner, A. W. Wallace, J. M. Guccione, and M. B. Ratcliffe (2010). First finite element model of the left ventricle with mitral valve: Insights into ischemic mitral regurgitation. *Annals of Thoracic Surgery* 89, 1546–1554.
- Yang, C., D. Tang, I. Haber, T. Geva, and P. J. del Nido (2007). *In vivo* MRI-based 3D FSI RV/LV models for human right ventricle and patch design for potential computer-aided surgery optimization. *Computers & Structures* 85, 988–997.
- Yang, M. and L. A. Taber (1991). The possible role of poroelasticity in the apparent viscoelastic behavior of passive cardiac muscle. *Journal of Biomechanics* 24, 587–597.
- Yin, F. C. P., C. C. H. Chan, and R. M. Judd (1996). Compressibility of perfused passive myocardium. *American Journal of Physiology* 271, H1864–H1870.
- Zhang, H. and K. J. Bathe (2001). Direct and iterative computing of fluid flows

fully coupled with structures. In K. J. Bathe (Ed.), *Computational Fluid and Solid Mechanics 2001*, pp. 1440–1443. Elsevier Science Ltd., Oxford, UK.

Appendix A

Parallel processing

A.1 Introduction

The following is an excerpt from an article (Doyle et al. (2010b)) describing the parallelization of FSI simulations of the inflation of the passive LV. These simulations were performed using an earlier version of the numerical model, which has some differences in the geometry and muscle fibre angles from those used in Chapter 4.

One of the challenges of performing fluid-structure interaction (FSI) simulations in the left ventricle (LV) is the requirement of large amounts of RAM and CPU power, which necessitate the use of a high performance computing facility. Such a facility was available for this work through membership in the High Performance Computing Virtual Laboratory (HPCVL), a consortium of Universities and Colleges in Eastern Ontario. Simulations were performed using the commercial finite element software ADINA v. 8.5.2 (ADINA R & D, Inc., Watertown, MA, USA) on 64-bit Sun computers

running the Solaris operating system.

The objective of this Appendix is to estimate the RAM and CPU time that are required for the simulations, as well as to determine an appropriate number of CPUs based on a parallelization study.

A.2 Methods

A.2.1 Geometries

The dimensions of the solid part of the geometry, representing the myocardium, are based on averages of measurements of several dog hearts (Streeter and Hanna (1973)). The outer semi-major and semi-minor axes, denoted as a and b in Fig. A.1, respectively, are 45.2 mm and 25.8 mm, whereas the thicknesses at the apex and the equator are $t_a = 5.1$ mm and $t_b = 12.1$ mm, respectively. The height of the solid geometry from the apex of the inner surface to the flat top surface is $h = 60.2$ mm. The solid wall is evenly subdivided into either three or six layers, each with a specific fibre angle. The fluid geometry consists of two parts. The lower part has an outer boundary which is identical to the inner boundary of the solid geometry to allow for FSI effects to be accounted for along the fluid-solid interface. The upper part of the fluid geometry is rigid and consists of two cylindrical tubes of length $L = 8.7$ mm with diameters $D_{MV} = 16.8$ mm and $D_{AV} = 8.7$ mm, which represent the LV inflow and outflow tracts, respectively; the inflow tract houses an idealized mitral valve, while the outflow tract houses an idealized aortic valve. The fluid geometry is completed by

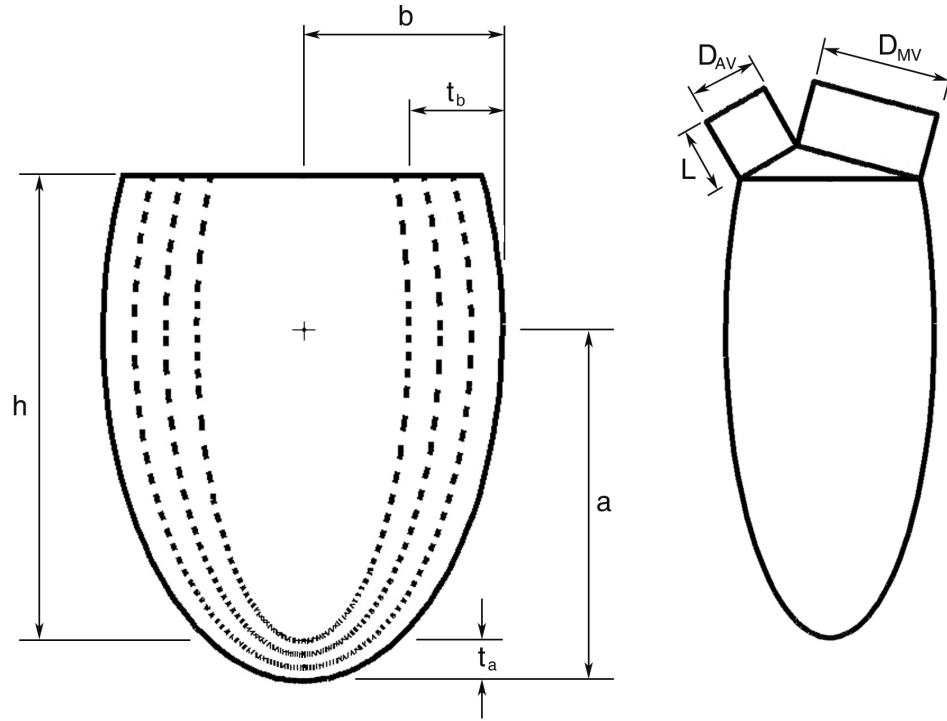


Figure A.1: Solid (left) and fluid (right) parts of the isolated LV geometry.

a section of a sphere, which joins the cylinders to the lower part of the fluid geometry.

The fluid and solid parts of the geometry are shown in Fig. A.1.

A.2.2 Meshes

The solid geometry is meshed with an unstructured grid, using ten-node tetrahedral elements, having nodes on each vertex and halfway along each edge. Higher-order elements were chosen for the solid mesh instead of lower-order ones to ensure compatibility with our material model, which requires the use of a mixed interpolation formulation. To prevent singularities at the apex of the LV, the solid geometry had

been subdivided into quarters in the vertical direction. Using the three-layer version of the solid geometry, two meshes, which will be referred to as “coarse” and “fine”, have been considered, consisting of 16,861 elements and 25,159 nodes, and 103,411 elements and 148,328 nodes, respectively.

The fluid geometry is meshed on an unstructured grid, using four-node tetrahedral elements. These elements have nodes on each vertex for velocity and pressure, and an additional node at the centre to calculate velocity and ensure stability of the solution. These elements are generally referred to as MINI elements and the velocity at the centre is called the bubble velocity (Gresho and Sani (1998)).

Three mesh densities have been considered for the fluid geometry, consisting of 28,103 elements and 5480 nodes, 193,372 elements and 34,652 nodes, and 351,378 elements and 71,915 nodes, respectively. These mesh densities will be referred to as “coarse”, “medium”, and “fine”, respectively. The FSI coupling used in ADINA does not require coincident meshes at the FSI interface, allowing the meshes for both the solid and fluid to be refined or coarsened separately. Figure A.2 shows the coarse and fine meshes for the solid and fluid models.

A.2.3 Numerical methods

Numerical methods used for the solid model are described in Chapter 4, while numerical methods for the fluid model and the FSI coupling are described in Chapter 5. In this study, FSI simulations are conducted using a direct solver, in which the fluid and solid equations, along with those on the FSI boundaries, are combined into

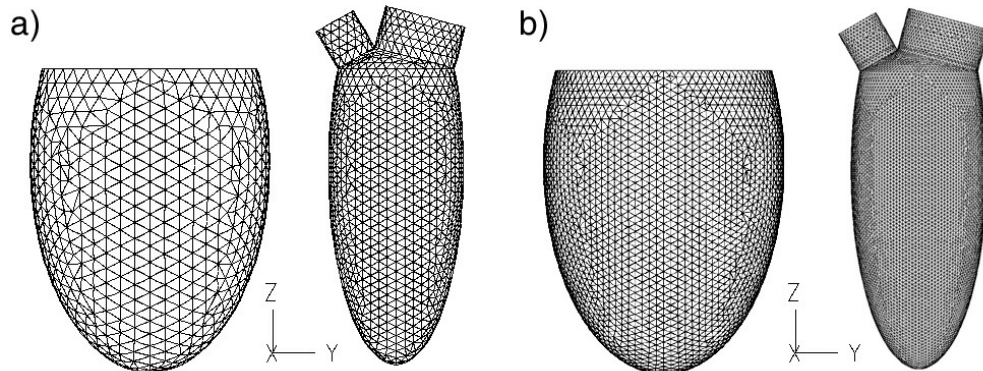


Figure A.2: Solid (left) and fluid (right) meshes with the coarse (a) and fine (b) mesh densities.

a single matrix and solved simultaneously. An alternative approach would have been the use of an iterative solver, in which the fluid and solid parts of the model are solved sequentially, with information passed between them on the FSI boundaries. Nevertheless, the direct solver approach was chosen because the iterative solver proved to be unstable, leading to a divergent solution during the first time step. Beside its advantage in reaching convergence, the direct solver yields, in general, faster results than the iterative solver (ADINA R & D, Inc. (2008b)). On the other hand, the direct solver requires more RAM than the iterative solver, because, unlike the latter, the former requires all equations to reside in RAM at any given time.

For the present FSI simulations, using the direct solver with the coarse solid mesh requires approximately 3.1 GB of RAM for the coarse fluid mesh, 6.7 GB of RAM for the medium fluid mesh, or 12.4 GB of RAM for the fine fluid mesh, with the majority of this RAM needed for the fluid model. Simulations in this study were performed on HPCVL's Sun SPARC Enterprise M9000 Servers, each consisting of 64

quad-core Sparc64 VII 2.52 GHz processors, which are capable of running 2 threads per processor.

A.3 Results and discussion

To study the effects of increasing the number of threads on wall clock time, an analysis of the parallelization performance was carried out for FSI simulations of passive LV filling using the three-layer geometry, the coarse solid mesh, and the three different fluid meshes. Simulations were performed using 2, 4, 8, 16, and 32 threads. The resulting wall clock times were compared to the wall clock time for a single thread to calculate the speed-up factor (SU), defined as the wall clock time for the single-thread simulations divided by the wall clock time for the multi-thread simulations.

The results of the calculations of the speed-up factor are presented in Fig. A.3, along with the ideal speed-up, which is equal to the number of threads. As expected, the actual speed-up factor increases with increasing number of threads, and with increasing mesh density. Moreover, the differences between the actual and ideal results increase with increasing number of threads.

To understand why the speed-up factors are much less than ideal, we will examine the parallelization procedure in ADINA. This information will be used to determine the theoretical maximum speed-up factor given by Amdahl's law

$$\text{SU}_{\max} = \frac{1}{(1 - P) + (P/N)} \quad (\text{A.1})$$

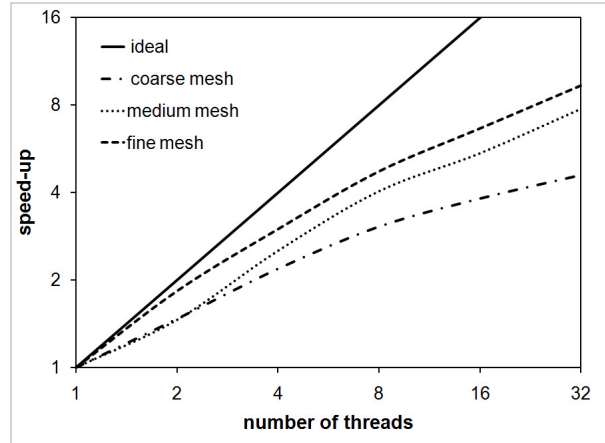


Figure A.3: Speed-up of parallel FSI simulations with three difference fluid mesh densities versus the number of threads, plotted in logarithmic axes.

where P is the fraction of the code that is parallelized and N is the number of threads.

To calculate P , the total computational time is divided into the parts that are serial and the parts that are parallel. An example of the breakdown of the computational time for one time step with the fine fluid mesh and 1 or 32 threads is given in Table A.1. In ADINA, only the sparse solver, which is a direct solver used to solve both the fluid and solid equations, is parallelized (ADINA R & D, Inc. (2008a)). As will be shown in the following, the solid solver can be assumed to be serial, so that only the fluid solver needs to be considered as parallel. Although there are differences in the CPU times from 1 to 32 threads for the “serial components” program control, solid model, fluid assembly, moving fluid mesh, and fluid output, the sum of these components is nearly constant (848 s for 1 thread and 838.91 s for 32 threads), even though the solid solver is also parallelized. In view of the relatively small change in CPU time for these components, we will assume them to be serial for the purposes

Table A.1: CPU time for the parts of the simulations with the fine fluid mesh.

Simulation part	CPU time (s), $N = 1$	CPU time (s), $N = 32$
program control	66.50	44.80
solid model	153.25	173.25
fluid assembly	497.12	560.12
fluid solver	25,274.12	1947.25
moving fluid mesh	115.88	44.62
fluid output	15.25	16.12

Table A.2: Maximum speed-up factors for the three fluid mesh densities.

Number of threads	Coarse	Medium	Fine
2	1.8	1.9	1.9
4	2.9	3.5	3.6
8	4.2	6.1	6.5
16	5.5	9.5	10.8
32	6.5	13.3	15.9
∞	7.9	21.9	30.8

of calculating SU_{\max} . P can then be calculated from the results for 1 thread as the CPU time for the fluid solver divided by the total CPU time. Using this value of P , SU_{\max} can be calculated for 2, 4, 8, 16, and 32 threads; an upper limit for SU_{\max} can be also calculated by letting $N \rightarrow \infty$. Similarly, P can be found for the other two mesh densities. The results of the calculations of SU_{\max} are presented in Table A.2. We now provide some insight on how the parallel fraction P varies for these FSI simulations. Table A.1 shows that, for our FSI simulations, the solution of the solid part of the model requires a small fraction of the total computational time, while the fluid solver uses by far the largest portion of this time. This comes from the fact that meshes for simulating flows need to be much finer than meshes used in structural mechanics, which can be coarse and fixed, as we will show in the following. Moreover, for FSI simulations, the coupling of the motions of the fluid and solid boundaries

forces repeated flow computations which could, in the worst case, amount to solving the same flow multiple times on a fixed geometry. These facts imply that, in an effort to parallelize a FSI code, one must first act on the fluid solver. As the fluid mesh is refined while the solid mesh remains fixed, the parallel fraction P of the code would increase. This is demonstrated by our calculations of P , which were 0.87, 0.95, and 0.97 for our test cases with the coarse, medium, and fine fluid meshes, respectively.

A comparison of the results in Table A.2 with those in Fig. A.3 shows that the maximum speed-up factors deduced from Amdahl's law are larger than actual speed-up factors obtained from computations. Indeed these maximum speed-up factors do not account for the increase in communication time with growing number of threads and cannot be achieved in practice. For example, with 32 threads on the fine mesh, SU_{\max} is about 16, whereas the speed-up factor observed in practice is only about 9. As for any parallel computations, additional threads improve the performance of our FSI simulations, and even more so with growing problem size, but the large amounts of memory and inter-process communications required for FSI severely limit the scalability of these parallel simulations. We used the direct fluid-structure solution method from ADINA. This method reduces the number of flow computations compared to the iterative fluid and solid solver described in Section A.2.3, but at the expense of requiring a larger memory and more extensive communications, which combined with a reduced parallelized fraction P explains our relatively poor speed-up obtained with a large number of threads.

In spite of their poor performance, parallel computations are necessary for FSI as they

reduce the total computational time, even if by much less than an ideal case. For example, in our passive LV filling simulations with the coarse fluid mesh, the total computational time was reduced from 120.4 h for 2 threads to 34.0 h for 32 threads. This impact is more significant when considering that for the medium and fine fluid mesh densities, passive LV filling simulations take 119.3 h and 254.4 h, respectively, with 32 threads. The computational time for the full cardiac cycle simulations is considerably longer than for the passive LV filling, which makes parallelization even more essential.

The computational times for these simulations should be viewed as lower bounds on the computational times needed for more complete simulations. Additional fluid mesh refinement, coupling of the LV geometry with other parts of the cardiovascular system, and/or the use of a patient-based LV geometry would all add substantially to the computational time required for simulations. This is clearly one of the reasons why many researchers have neglected FSI effects in their heart simulations and why performing FSI simulations in the heart remains a challenging computational problem.

A.4 Conclusions

We have demonstrated by example and by analysis that parallelization is essential to finite element simulations of the mechanics of the LV with fluid-structure interaction. In particular, we have shown the importance of parallelization of the fluid solver as this account for the majority of computational time in our FSI simulations; more specifically, for simulations on a single thread, the fluid solver requires more than 87%

of the computational time. Previous simulations of LV mechanics neglecting FSI effects avoid the significant increase in computational time required by the fluid part of the model when multiple iterations between the fluid and the solid are performed, but by doing so they miss an important aspect of the problem. We have shown that the speed-up factor increases with increasing number of threads and with increasing mesh density. Even though our speed-up factors are significantly lower than the theoretical maxima for a given problem size and number of threads, we were still able to achieve significant reductions in computational time, which would become increasingly important as we move from passive LV filling to cardiac cycle simulations, or if we were to introduce further geometric complexity to the model.

The use of high performance computing clusters, such as those available through HPCVL, will enable continuing improvements in the simulation of heart mechanics, by allowing additional details, such as an anatomically realistic geometry, to be incorporated into heart models, while still allowing researchers to obtain simulation results within acceptable time limits.

Appendix B

Additional details on inflation of the passive left ventricle

B.1 Definition of the governing equations

The following is an expansion of Section 4.2.2, which describes the governing equations for the solid model. Nodal displacements \mathbf{U} at the current load step $s + \Delta s$ were calculated using the following procedure, which is described in more detail in Bathe (1996). For non-linear static simulations, the governing equation is

$$\mathbf{R}(s + \Delta s) - \mathbf{F}(s + \Delta s) = 0 \quad (\text{B.1})$$

where \mathbf{R} is the external load vector, \mathbf{F} is the force vector equivalent to the element stresses, and $s = n\Delta s$, where n is the total number of load steps (ADINA R & D, Inc. (2008a)).

$\mathbf{R}(s + \Delta s)$ is a known quantity, which is assumed to be independent of deformation, and can be calculated as the sum of body forces, surface forces, initial stresses, and concentrated loads applied to each element (Bathe (1996)). $\mathbf{F}(s + \Delta s)$, which is unknown, can be rewritten as

$$\mathbf{F}(s + \Delta s) = \mathbf{F}(s) + \Delta\mathbf{F}(s) \quad (\text{B.2})$$

where $\mathbf{F}(s)$ is known from the previous load step and $\Delta\mathbf{F}(s)$ is the change in \mathbf{F} during the interval Δs , which can be approximated as

$$\Delta\mathbf{F}(s) \approx \mathbf{K}(s) \Delta\mathbf{U} = \mathbf{K}(s) [\mathbf{U}(s + \Delta s) - \mathbf{U}(s)] \quad (\text{B.3})$$

where $\mathbf{K}(s)$ is the stiffness matrix, which is known and has been calculated at the previous load step, $\Delta\mathbf{U}$ is the change in \mathbf{U} over the interval Δs , and $\mathbf{U}(s)$ is known from the previous load step.

Substituting Eqs. (B.2) and (B.3) into Eq. (B.1) leads to

$$\mathbf{K}(s) [\mathbf{U}(s + \Delta s) - \mathbf{U}(s)] = \mathbf{R}(s + \Delta s) - \mathbf{F}(s) \quad (\text{B.4})$$

B.2 Left ventricle cavity volume calculations

This section describes the calculation method of the LV cavity volume V_f for solid-only simulations, because in ADINA, the volume of a mesh cannot be calculated directly.

Towards this purpose, the divergence theorem

$$V = \iiint_V dV = \iint_S (xn_1) dS \quad (\text{B.5})$$

was used to relate the volume to a surface integral, which was then calculated in ADINA; in this expression, S is the surface of the closed volumic region V , \mathbf{x} is a vector containing the global Cartesian coordinates of the points on the surface mesh ($\mathbf{x} = [x \ y \ z]^T$), and \mathbf{n} is a vector containing the surface normals ($\mathbf{n} = [n_1 \ n_2 \ n_3]^T$).

For solid-only simulations, the LV cavity volume cannot be calculated directly from Eq. (B.5), because the LV cavity is not meshed and its surface is not closed. To allow for the calculation of the LV cavity volume, a cylindrical tube, with a height of 0.2 mm, was added to the solid geometry, as shown in Fig. B.1, for an earlier version of the geometry, to cover the opening of the LV cavity, enclosing the LV cavity with surfaces. By isolating the surfaces that border the LV cavity, V_f was calculated from the solid geometry during solid-only simulations as

$$V_f = \iint_{S_f} |xn_1| dS_f \quad (\text{B.6})$$

where S_f are the surfaces of the mesh that border the LV cavity. In Eq. (B.6), the absolute value is used because the sign of the actual surface normal is opposite to its conventional definition.

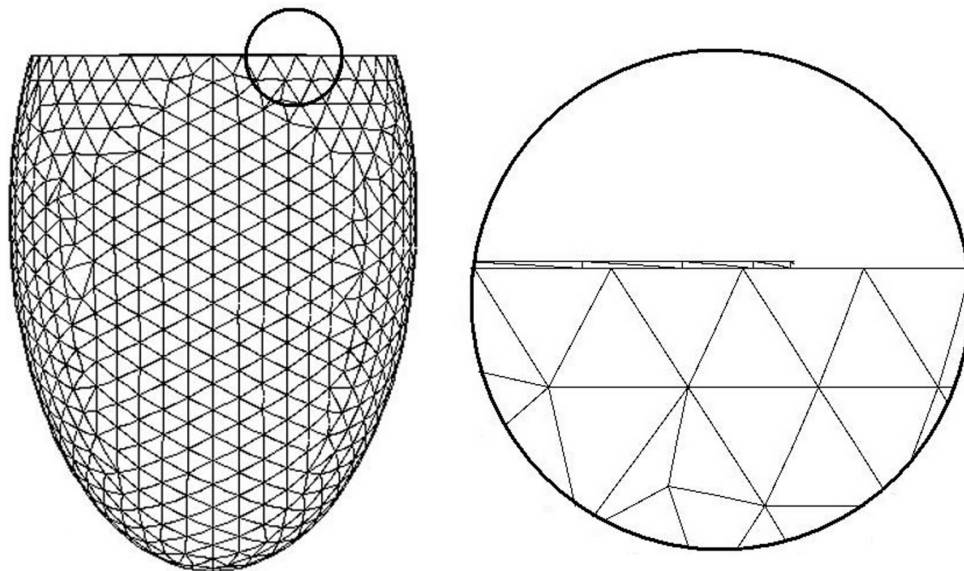


Figure B.1: Zoomed-in view (right) of the cylinder added to the top of the left ventricle cavity in the solid geometry to allow for calculations of cavity volume to be performed for the results of solid-only simulations.

Appendix C

Extension to anatomical geometry

C.1 Introduction

This appendix briefly describes the extension of this work to an anatomical geometry consisting of a left and a right ventricle (LV-RV) . In view of limitations described in the following, simulations were only performed for quasi-static filling of the passive LV. The methodology for these simulations is described along with the limitations of the present approach. Preliminary results are presented and challenges that must be met before extending this work are discussed.

C.2 Methods

C.2.1 Geometry and mesh

The canine LV-RV geometries used in this study were based on measurements performed by Nielsen et al. (1991) at the University of Auckland in New Zealand. Point data from these measurements for four dogs are available for downloading from http://www.cmiss.org/data/heart_data/ (Hunter (2007)). These data have not been used to generate geometries for the present study, but one set was used to obtain rough measurements of dimensions in the canine LV as described in Section D.1.

Researchers at INRIA Rocquencourt in France used the point data obtained from Professor Hunter to generate four different versions of surface geometries for the canine LV-RV (Coudiere (2005)). Three of these versions were scaled by identical, although unspecified, scaling factors in the x , y , and z directions. The fourth version, shown in Fig. C.1, has the same scale as the original geometry. The original geometry of Nielsen et al. (1991) used relatively few nodes, and higher order elements in its mesh. In order to perform simulations with this geometry using lower order elements, researchers at INRIA introduced additional nodes, and applied smoothing techniques to improve the quality of the surfaces, reducing sharp edges (Coudiere (2005)).

The geometries obtained from INRIA only contained a mesh for the solid part and were meshed using an in-house format. To make use of these geometries in ADINA, it was necessary to perform several conversions. The mesh was first converted to vtk format, which was opened in ParaView (Kitware, Inc., Clifton Park, NY, USA).

In ParaView, the volume mesh was converted to a surface mesh, and surface normals were defined. From ParaView, the mesh was converted to stl format using a converter in the vtk library. The stl files were then imported into SolidWorks (Dassault Systèmes SolidWorks Corp., Concord, MA, USA) where they were converted to parasolid bodies that could be imported into ADINA. Although slight changes in the geometries have occurred during the conversion processes, they are of little consequence because the smoothed INRIA geometries were also somewhat different from the original measurements.

Once the solid geometry was imported into ADINA, fluid geometries for the LV and RV cavities were generated. The first step was to truncate the top of the solid geometry to form a basal plane, which was the same in the fluid and solid geometries. This simplification may be justified by the fact that the plane containing the valve openings was not resolved in the original geometry and, consequently, each ventricle in the model has a single opening rather than the two separate ones found in the actual heart. The next step was to define solid blocks that approximated the shape of the LV and RV cavities. Separate fluid geometries of the LV and the RV were generated by removing the solid geometry from the two blocks. The two cavities can be seen in Figs. C.1a and c, whereas the solid geometry is shown in Figs. C.1b and d.

To conform with the definition of the material model, fibre orientation information may be incorporated into the present simulations by defining layers within the wall and assigning a fibre orientation to each layer. However, in its present form, the wall in the geometry in Fig. C.1 is not easy to divide into layers. For this reason, only

a single layer of muscle fibres was included in this geometry. Moreover, because of this limitation with the muscle fibre orientation, no attempt has been made to include valve openings in this geometry.

The meshes for the LV-RV geometry are illustrated in Fig. C.1. They consisted of 50,741 nodes and 33,729 elements for the solid, and 20,853 nodes and 107,231 elements for the fluid.

C.2.2 Boundary conditions

Coincident FSI boundary conditions were applied to all outer surfaces of the fluid geometry and inner surfaces of the solid geometry with the exception of the top surfaces in both cases. For the solid, the top surface was fixed in all three directions to anchor this geometry during FSI simulations. For the fluid, uniform pressure boundary conditions were applied to the top surfaces of the LV and RV cavities. The LV pressure increased linearly from 0 to 2 kPa, while the RV pressure increased linearly from 0 to 0.4 kPa, which is equal to one fifth of the LV range, in conformity with the suggestion by Nash and Hunter (2000).

C.2.3 Numerical methods

Details on the governing equations for the solid and fluid models have been described in Chapters 4 and 5. Simulations were performed using the “lower” material parameter values for the myocardium material model, defined in Table 4.2, under the assumption that material properties in the LV and RV myocardia were equal.

C.3 Results

Figure C.2a shows a central cross-section of the undeformed LV-RV geometry and Fig. C.2b shows the same cross-section at the end of the simulations, when $p_{LV} = 2$ kPa. In this figure, bands of nodal pressure are depicted in the LV and RV cavities and bands of effective stress are depicted in the myocardium. The bands of effective stress have been smoothed and truncated at a maximum value of 5 kPa to separate regions of higher and lower stresses. The maximum stresses were much larger than 5 kPa and were found along the edge of the LV cavity. It should be noted that the white lines visible in Figs. C.2a and b between the LV and RV cavities are artifacts from ADINA and do not represent any physical structures. Figure C.3 is plot of $\Delta V_f/V_{f,0}$ vs. pressure for the LV-RV model along with the results for an early version of the isolated LV geometry with the lower material parameter values, and results from previous experimental and computational studies. The parameter $\Delta V_f/V_{f,0}$ was chosen instead of $\Delta V_f/m_s$ because it was not possible to separate the LV and RV geometries in order to determine the mass of the isolated LV myocardium.

Large increases in LV and RV cavity volumes are visible in Fig. C.2b. The cavities of both ventricles expanded more in the horizontal directions than in the vertical direction, causing the LV cavity to become more spherical and decreasing the distance between the LV and RV cavities. This directional preference for the deformation can be partially attributed to the alignment of muscle fibres with this direction. As expected, the pressure inside each cavity was uniform and matched the pressure applied to the top surface of each cavity as a boundary condition. The stresses in the

myocardium were largest along the inner edge of the LV cavity and they decreased with increasing distance from this edge. Higher stresses are also visible in the top left corner and bottom edge of the RV cavity. The magnitudes of $\Delta V_f/V_{f,0}$ in Fig. C.3 are larger for a given pressure for the LV-RV geometry compared to the isolated LV geometry, and the trend for the results with the LV-RV geometry is steeper than the trend for the isolated LV geometry, especially for pressures lower than 0.5 kPa. Considering the crudeness of the assumptions used for this study, the results of these simulations have not been considered for drawing any conclusions about passive filling of actual ventricles.

C.4 Discussion

Because of the drastic simplifications made when constructing this LV-RV model, the results presented in this appendix are not sufficiently reliable. To improve the model, additional data would be required. Although the present LV-RV geometry is based on measurements of excised canine ventricles, it is unsuitable for FSI simulations, because it lacks LV and RV inflow and outflow tracts. One of the versions of the geometry available from Professor Hunter contains point data of the inflow and outflow tracts, but this geometry has not yet been converted into a usable form. Related to the geometry is the definition of muscle fibre angles within the myocardium. One of the advantages of the geometries from Professor Hunter is that they are accompanied by muscle fibre angle measurements. However, a straightforward method for incorporating these muscle fibre angles in ADINA does not exist.

In these simulations, material properties were assumed to be uniform throughout the LV and RV geometries. Novak et al. (1994) measured the stress-stretch behaviour in the septum and three sections of the LV free wall and found differences in the results. Such differences should be incorporated into material models governing the LV and RV myocardia. Measurements of stress-stretch behaviour of the RV have yet to be published in the literature, and previous solid-only LV-RV studies, such as Nash and Hunter (2000), have assumed uniform properties in both ventricles.

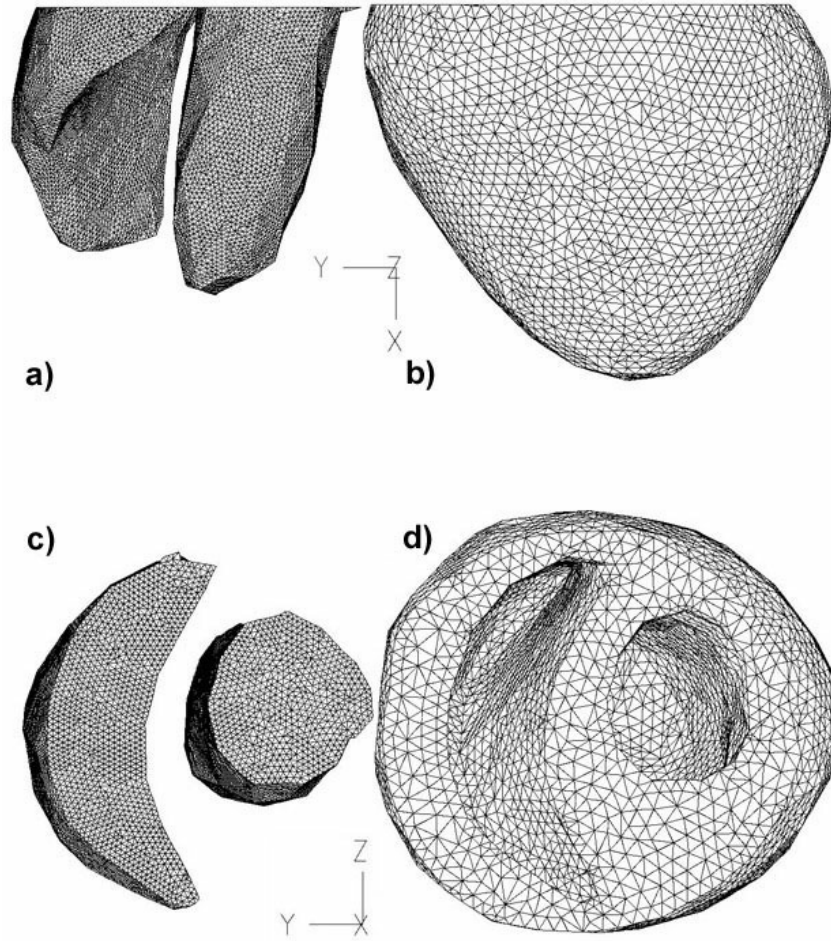


Figure C.1: Front (a-b) and top (c-d) view of the fluid (left) and solid (right) LV-RV geometry based on surface geometries obtained from researchers at INRIA Rocquencourt in France (Coudiere (2005)), based on the measurements of Nielsen et al. (1991).

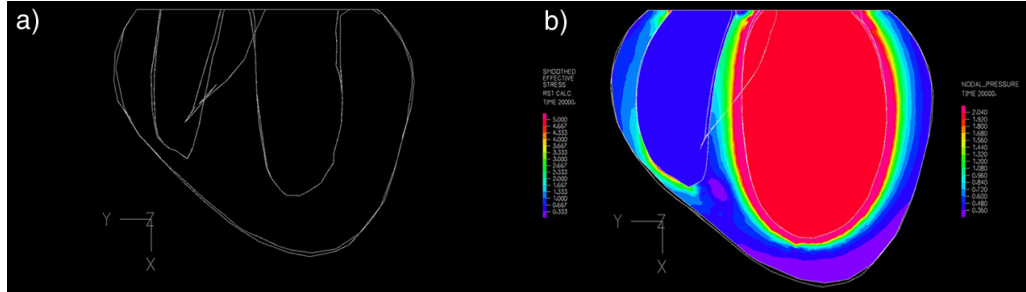


Figure C.2: Cut plane through the centre of the left and right ventricle geometry. The leftmost image (a) is for the undeformed case, and the rightmost image (b) is for the case where $p = 2$ kPa, and depicts bands of nodal pressure in the fluid part of the geometry and bands of effective stresses in the solid part of the geometry.

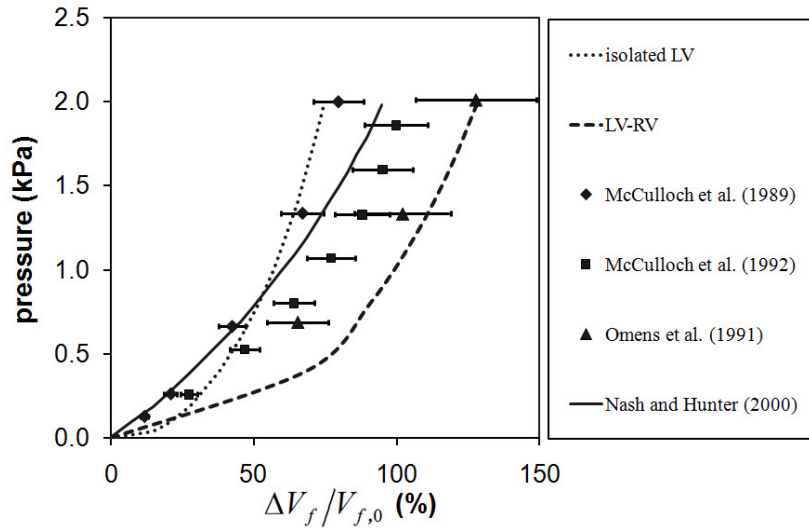


Figure C.3: Percentage volume change results for the left and right ventricle geometry, the first isolated left ventricle geometry, three previous experimental studies (points), and a previous computational study (solid line).

Appendix D

Additional details on cardiac cycle simulations

D.1 Fluid geometry definition

This section describes the equations used to define the rigid part of the fluid geometry. Three assumptions have been made in defining the cylindrical tubes that represent the LV inflow and outflow tracts. First, the diameter of the inflow tract was assumed to be greater than the diameter of the outflow tract. This assumption is consistent with diameters of $D_{MV} = 23$ mm and $D_{AV} = 10$ mm, approximated from Hunter's canine LV-RV geometry (Hunter (2007)), and $D_{MV} = 23$ mm and $D_{AV} = 14$ mm, calculated from cross-sectional area measurements made by Ross et al. (1967) using the average of their systolic and diastolic measurements and the assumption that the valves are circular. Second, the highest point on the lower surface of both tubes is

the same, such that a triangle is formed by the lower edge of each tube and the top of the LV cavity, as shown in Fig. 5.2. Third, the length of the cylindrical tubes L_1 was chosen to be equal to D_{AV} to ensure that the tubes are long enough to allow flow to develop, but not too long that they lead to unnecessary computations. Using these assumptions, D_{MV} and D_{AV} were calculated using the sine law as

$$D_{MV} = \frac{\sin(90^\circ - \alpha)}{\sin(\theta)} w_1 \quad (\text{D.1})$$

$$D_{AV} = \frac{\sin(90^\circ - \beta)}{\sin(\theta)} w_1 \quad (\text{D.2})$$

where α is the angle between the outflow tract and the basal plane, β is the angle between the inflow tract and the basal plane, θ is the angle between the two valves ($\theta = \alpha + \beta$), and w_1 is the width at the top of the LV cavity.

Nakamura et al. (2003) proposed that $\theta = 140^\circ$. Approximations of values α , β , as well as other possible values of θ were obtained from figures of LV geometries in several papers, as well as measurements of the Hunter LV-RV geometry, are presented in Table D.1. These values are very rough approximations, because it was difficult to accurately determine the horizontal and vertical directions in each figure. Because the value of $\theta = 140^\circ$ is the only value explicitly taken from the literature, this value of θ , along with the corresponding values of α and β approximated from Nakamura et al. (2003), were used as a starting point for determining appropriate angles for the current geometry.

Based on the dimensions of the solid geometry defined in Chapter 5, $w_1 = 26.7$ mm. Using this value of w_1 , $\theta = 140^\circ$, $\alpha = 60^\circ$, and $\beta = 80^\circ$ in Eqs. (D.1) and (D.2) gives

Table D.1: Approximations of valve angles from several LV geometries.

source	α ($^\circ$)	β ($^\circ$)	θ ($^\circ$)
Nakamura et al. (2003)	60	80	140
Cheng et al. (2005)	52	80	132
Peskin and McQueen (1996)	50	80	130
Pierrakos et al. (2004)	65	60	125
Hunter LV-RV geometry	71	78	149

$D_{MV} = 20.8$ mm and $D_{AV} = 7.2$ mm. Two observations can be made from these diameters; they are each smaller than the diameters from both the Hunter LV-RV geometry and the paper of Ross et al. (1967), and the ratio of $D_{AV}/D_{MV} = 0.35$ is also smaller than the values of 0.43 and 0.60 from the Hunter LV-RV geometry and the paper of Ross et al. (1967), respectively. To increase the diameter ratio to a value between 0.43 and 0.60, either α must be increased or β must be decreased, which would in turn increase or decrease the value of θ , respectively. The average of the values of θ in Table D.1 is 135° , which suggests that β should be decreased. By setting $\beta = 75^\circ$, while maintaining $\alpha = 60^\circ$, $\theta = 135^\circ$, $D_{MV} = 18.88$ mm, $D_{AV} = 9.78$ mm, and $D_{AV}/D_{MV} = 0.52$, which is the average of the two previous diameter ratio values. These values were deemed to be sufficient to be used in the current geometry.

To determine suitable values of R and z_c , equations governing chord length in a circle were used. Starting from the desired chord w_i , the perpendicular distance from the chord to the centre of the circle is r_i , and the perpendicular distance from the chord to the outer edge of the circle is h_i . In this case, there are two known chord lengths w_1 and w_2 that need to be accounted for to fit the circle through all three points of the triangle shown in Fig. 5.2, where w_1 is known based on the lower part of the geometry,

and w_2 can be calculated as twice the horizontal distance from the highest point of the proximal end of the LV outflow tract to the centre of the geometry. Using the Pythagorean Theorem, the variables w_i , r_i , and R are related to each other through the following equation

$$R^2 = r_i^2 + \left(\frac{1}{2}w_i\right)^2, \quad i = 1, 2 \quad (\text{D.3})$$

Substituting $r_i + h_i = R$ into Eq. (D.3) and rearranging leads to

$$r_i = \frac{w_i^2 - 4h_i^2}{8h_i}, \quad i = 1, 2 \quad (\text{D.4})$$

Setting $i = 1$ and $i = 2$ in Eq. (D.4) leads to two equations and four unknowns (r_1, h_1, r_2 , and h_2). Two additional equations that are needed to solve the system of equations are

$$r_1 + h_1 = r_2 + h_2 \quad (\text{D.5})$$

$$h_1 = h_2 + h_3 \quad (\text{D.6})$$

where h_3 is a known quantity, which can be determined from the geometry as the difference in height of the two endpoints on the proximal end of either cylinder. Substituting the right-hand side of Eq. (D.4) into both sides of Eq. (D.5), and then substituting Eq. (D.6) into the new equation leads to

$$h_3 + \frac{w_1^2 - 4(h_2 + h_3)^2}{8(h_2 + h_3)} = \frac{w_2^2 - 4h_2^2}{8h_2} \quad (\text{D.7})$$

Using $w_1 = 26.7$ mm, $w_2 = 9.78$ mm and $h_3 = 4.88$ mm, Eq. (D.7) was solved by iteration to get $h_2 = 0.643$ mm. This value of h_2 was then substituted into the other equations to find $R = 18.88$ mm and $z_c = 46.78$ mm.

D.2 Time integration

The ADINA composite time integration method used in the present study consists of two sub-time steps, which allows for fewer time steps to be used than those required by the available first-order method, which does not have sub-time steps. This approach leads to a reduction in overall computational time. The ADINA composite time integration method is defined as

$$\begin{aligned} u(t + \gamma\Delta t) &= u(t) + \gamma\Delta t \frac{du(t + \frac{1}{2}\gamma\Delta t)}{dt} \\ u(t + \Delta t) &= u(t + \beta\gamma\Delta t) + (1 - \alpha)\Delta t \frac{du(t + \Delta t)}{dt} \end{aligned} \quad (\text{D.8})$$

where t is time, $u(t + \beta\Delta t) = (1 - \beta)u(t) + \beta u(t + \gamma\Delta t)$, $\gamma = 2 - 1/\alpha$, $\beta = \alpha^2/(2\alpha - 1)$, and $\alpha = 1/\sqrt{2}$ (ADINA R & D, Inc. (2008b)).

D.3 Fluid-structure interaction

This section describes details on the boundary conditions enforced by ADINA along the FSI boundary as well as the coupling method used to solve the system of governing equations for the fluid and the solid.

Two compatibility conditions, the kinematic and the dynamic condition, must be satisfied on the FSI boundaries. These conditions are defined, respectively, as

$$\underline{\mathbf{d}}_f = \underline{\mathbf{d}}_s \quad (\text{D.9})$$

$$\mathbf{n} \cdot \underline{\boldsymbol{\sigma}}_f = \mathbf{n} \cdot \underline{\boldsymbol{\sigma}}_s \quad (\text{D.10})$$

where \mathbf{d} is the displacement vector (ADINA R & D, Inc. (2008b)). The underlines in the above relations represent the FSI boundary, while the subscripts f and s representing the fluid and solid, respectively. From Eq. (D.9), the fluid velocity at the FSI interface can be calculated as

$$\underline{\mathbf{v}}_f = \dot{\underline{\mathbf{d}}}_s \quad (\text{D.11})$$

From Eq. (D.10), the force on the solid boundary can be calculated as

$$\underline{\mathbf{F}}(t) = \int \mathbf{H}^{S^T} \underline{\boldsymbol{\sigma}}_f \cdot dS \quad (\text{D.12})$$

where \mathbf{H}^S contains the element shape functions (Zhang and Bathe (2001)).

Enforcement of both of the above relations, in which the fluid affects the solid and the solid affects the fluid is known as two-way coupling, which is the type of coupling required for the present study. ADINA has two methods of two-way coupling, direct and partitioned. In the direct method, the fluid and solid parts are lumped into a single system of linearized equations, which can be written in matrix form as

$$\begin{bmatrix} \mathbf{A}_{ff} & \mathbf{A}_{fs} \\ \mathbf{A}_{sf} & \mathbf{A}_{ss} \end{bmatrix} \begin{bmatrix} \Delta \mathbf{X}_f^k \\ \Delta \mathbf{X}_s^k \end{bmatrix} = \begin{bmatrix} \mathbf{B}_f \\ \mathbf{B}_s \end{bmatrix} \quad (\text{D.13})$$

where \mathbf{X}_f is the fluid solution vector, \mathbf{X}_s is the solid solution vector, the superscript k represents the iteration number, $\mathbf{X}^{k+1} = \mathbf{X}^k + \Delta \mathbf{X}^k$, and assuming the simulations are solved using the Newton-Raphson method

$$\mathbf{A}_{ij} = \frac{\partial \mathbf{F}_i^k}{\partial \mathbf{X}_j}, i, j = f, s \quad (\text{D.14})$$

$$\mathbf{B}_f = -\mathbf{F}_f^k = -\mathbf{F}_f \left[\mathbf{X}_f^k, \lambda_d \mathbf{d}_s^k + (1 - \lambda_d) \mathbf{d}_s^{k-1} \right] \quad (\text{D.15})$$

$$\mathbf{B}_s = -\mathbf{F}_s^k = -\mathbf{F}_s \left[\mathbf{X}_s^k, \lambda_\sigma \underline{\boldsymbol{\sigma}}_f^k + (1 - \lambda_\sigma) \underline{\boldsymbol{\sigma}}_f^{k-1} \right] \quad (\text{D.16})$$

where λ_d and λ_σ are relaxation factors for the displacement and stress, respectively, which are chosen in the present study to both be equal to the default value of 1 (ADINA R & D, Inc. (2008b)).

Using the direct method, the system of equations defined in Eq. (D.13) is solved simultaneously for each iteration. After each iteration, the displacement and stress residuals are calculated. If they are not lower than a specified threshold, additional iterations, up to a user-defined maximum, are performed.

In the partitioned method, the fluid and solid equations are solved sequentially rather than simultaneously. First, the fluid equations are solved, then the stress residual is computed, then the solid equations are solved, and then the displacement residual is computed. If either residual is not satisfied, additional iterations of the four steps, up to a user-defined maximum, are performed until convergence is reached.